

The Haemodynamics of a Stented Arteriovenous Fistula through Experiments and Flow Modelling

Author:

Gunasekera, Sanjiv

Publication Date:

2022

DOI:

<https://doi.org/10.26190/unsworks/24119>

License:

<https://creativecommons.org/licenses/by/4.0/>

Link to license to see what you are allowed to do with this resource.

Downloaded from <http://hdl.handle.net/1959.4/100412> in <https://unsworks.unsw.edu.au> on 2024-04-20

The Haemodynamics of a Stented Arteriovenous Fistula through Experiments and Flow Modelling

Sanjiv Gunasekera

A thesis in fulfillment of the requirements for the degree of
Doctor of Philosophy in Mechanical Engineering



School of Mechanical and Manufacturing Engineering
Faculty of Engineering
The University of New South Wales

June 2022

Originality, Copyright and Authenticity Statements

Thesis Title and Abstract	Declarations	Inclusion of Publications Statement	Corrected Thesis and Responses
---------------------------	--------------	-------------------------------------	--------------------------------

ORIGINALITY STATEMENT

☒ I hereby declare that this submission is my own work and to the best of my knowledge it contains no materials previously published or written by another person, or substantial proportions of material which have been accepted for the award of any other degree or diploma at UNSW or any other educational institution, except where due acknowledgement is made in the thesis. Any contribution made to the research by others, with whom I have worked at UNSW or elsewhere, is explicitly acknowledged in the thesis. I also declare that the intellectual content of this thesis is the product of my own work, except to the extent that assistance from others in the project's design and conception or in style, presentation and linguistic expression is acknowledged.

COPYRIGHT STATEMENT

☒ I hereby grant the University of New South Wales or its agents a non-exclusive licence to archive and to make available (including to members of the public) my thesis or dissertation in whole or part in the University libraries in all forms of media, now or here after known. I acknowledge that I retain all intellectual property rights which subsist in my thesis or dissertation, such as copyright and patent rights, subject to applicable law. I also retain the right to use all or part of my thesis or dissertation in future works (such as articles or books).

For any substantial portions of copyright material used in this thesis, written permission for use has been obtained, or the copyright material is removed from the final public version of the thesis.

AUTHENTICITY STATEMENT

☒ I certify that the Library deposit digital copy is a direct equivalent of the final officially approved version of my thesis.

Inclusion of Publications Statement

Thesis Title and Abstract	Declarations	Inclusion of Publications Statement	Corrected Thesis and Responses
---------------------------	--------------	-------------------------------------	--------------------------------

UNSW is supportive of candidates publishing their research results during their candidature as detailed in the UNSW Thesis Examination Procedure.

Publications can be used in the candidate's thesis in lieu of a Chapter provided:

- The candidate contributed **greater than 50%** of the content in the publication and are the "primary author", i.e. they were responsible primarily for the planning, execution and preparation of the work for publication.
- The candidate has obtained approval to include the publication in their thesis in lieu of a Chapter from their Supervisor and Postgraduate Coordinator.
- The publication is not subject to any obligations or contractual agreements with a third party that would constrain its inclusion in the thesis.

☒ The candidate has declared that **some of the work described in their thesis has been published and has been documented in the relevant Chapters with acknowledgement**.

A short statement on where this work appears in the thesis and how this work is acknowledged within chapter/s:


Chapter 3 contains work that I published in the Experiments in Fluids journal. The chapter also includes content that I published and presented at the 9th Australian Conference on Laser Diagnostics.

Chapter 4 contains work that I published and presented at the 22nd Australasian Fluid Mechanics Conference.

Chapter 5 contains work that I published in the International Journal of Heat and Fluid Flow.

Acknowledgement of the work of other authors has been made in the list of publications and at the beginning of each of the relevant chapters.

Candidate's Declaration

 I declare that I have complied with the Thesis Examination Procedure.

Acknowledgements

The last four years have been a journey filled with challenges that have opened my eyes to many new experiences. Numerous people have helped me on this venture, distracting me from the temporary hardship and ensuring my unwavering trajectory towards completion.

First on this list would be Prof. Tracie Barber, without whom I would have not known the applicability of mechanical engineering in the medical field. Your approachability made the work environment a very enjoyable one filled with conversations on fluid dynamics, wildlife, and the ocean. I aspire to have the vision to look at the bigger picture and generate ideas the way you do.

I am very grateful that Dr. Charitha de Silva joined my supervisory team and almost immediately helped me make gains not only with the PIV measurements but also with the CFD analyses. I am especially thankful for the many meetings we had late on Fridays where you helped guide my interpretation of results. I never imagined that I could create this level of graphics and I am very grateful for all the tips and tricks you provided along the way. You have redefined my view on attention to detail' and I hope to carry this forward with me.

I am very appreciative of the guidance and support of Prof. Ramon Varcoe and Dr. Shannon Thomas who helped draw the gap between the engineering findings and the clinical implications. Your enthusiasm and medical knowledge have been great assets to our research. I am also thankful to you and Debbie Knagge for your assistance in obtaining clinical data at the weekly dialysis clinics at the Prince of Wales Hospital.

I am very grateful for the technical support provided by the staff in the School of Mechanical Manufacturing Engineering, particularly, Benjamin Willis, Joe Tscherry, Martyn Sherriff, Alexander Chariyekkara, and Subash Puthanveetil. The guidance provided by these highly skilled people have helped me think practically about my design steps, thereby helping me become a better engineer. I am also very thankful for the software and HPC support provided by Minh Ha and Lachlan Simpson respectively. Minh, your communication was very valuable in deciphering hardware issues in our tracking system. Lachlan, your quick responses ensured that I could get my work across to the new on-demand HPC platform with minimal interruptions.

I'd also like to remember some of the past students from our research group who helped shape some of the initial work in this space, especially Dr. John Carroll and Dr. Eamonn Colley who sacrificed time during their final year to give us a crash-course on the ultrasound tracking system that they developed. I am also grateful for Dr. Dave Fulker who spent a lot of time with me in the lab in my undergrad years helping me setup and understand PIV measurements.

It has been delightful to share an office with Joseph Kim, Yani Zhang, Dr. Pujith Vijayaratham, Dr. Bac Dang, Jie Yie, Xinxing Chen, Andre Aquino, and Alexander Bateman. You all created an environment where I could reach out for feedback regarding any technical problem I was facing. I will miss our lunch time chats and laughing at Bac's antiques at our end-of-term catch-ups. I am very grateful to have the opportunity to work alongside Olivia Ng. Whether it was scanning patients during an exceptionally long clinic or troubleshooting the occasional CFD related issues, your positive attitude helped persevere through difficult situations. It was amazing to see someone so organised even with so many varied responsibilities.

The trivia nights, cycle rides, snorkelling sessions, camping trips, and online chats with my friends and relatives in Sydney and Colombo have helped by not only taking my mind off my work but also providing a broader perspective of everyone's varied journeys. My family has been a pillar of support throughout my life. I am forever indebted to my parents for their hard work without which I would not have had the opportunity to gain these valuable experiences. Amma and Thaathi, along with Anisha, have shown immense understanding during my worst times and been there to celebrate during my best times. I look forward to finally flying across and reuniting with all of you.

Finally, Sumudu, I wouldn't have gotten this far without the love and support you have given me. Your encouragement during the gruelling stages of writing up the thesis kept me pushing through, while your persuasion to balance work with leisure has kept me sane. I'll put this down in writing to promise to do the dishes for the next three months.

Abstract

The arteriovenous fistula (AVF) is a vasculature created for end-stage renal disease patients who undergo haemodialysis. This vasculature is often affected by stenosis in the juxta-anastomotic (JXA) region and the presence of disturbed haemodynamics within the vessel is known to initiate such diseased conditions. A novel treatment involving the implantation of a flexible stent in the JXA region has shown potential for retaining healthy AVFs. Only a limited number of experimental studies have been conducted to understand the disturbed flow conditions, while the impact of stent implantation on the haemodynamics within the AVF is yet to be explored.

The study was initiated by developing a benchtop patient-specific AVF model to conduct a Tomographic Particle Image Velocimetry (Tomo-PIV) measurement. The subsequent temporally resolved volumetric velocity field was phase-averaged to quantify fluctuations occurring over the inlet pulsatile conditions. It was noted that high turbulent kinetic energy (TKE) was generated at the JXA region.

To study the effects of the stent implantation, Large Eddy Simulations (LES) comparing the AVF geometry with and without the presence of the stent implantation were conducted. The trajectory of the flow in the stented case was funnelled within the stent encapsulated region which in turn, contained the disturbed flow within the stent lumen while mitigating the generation of turbulence. Consequently, the distribution of adverse wall shear stress (WSS) in the stented region was much lower compared to that of the ‘stent-absent’ case.

Simulations were also conducted on the diseased patient AVF, before the stent implantation, to make an overall assessment of the effect of treatment. Larger and persistent regions of high TKE were noted in the vessel downstream of the stenosis despite the lower velocity of flow in the diseased model.

In summary, the stent implantation in the patient AVF showed the ability to funnel flow disturbances away from the vessel wall, thereby leading to lower adverse WSS distributions. The presence of the stent also mitigated turbulence generation. These findings provide valuable insight into the favourable haemodynamic effects of this novel endovascular procedure, thus, substantiating this treatment strategy to treat vascular disease in AVFs.

List of Publications

Journal Papers

- **Sanjiv Gunasekera**, Olivia Ng, Shannon Thomas, Ramon Varcoe, Charitha de Silva, Tracie Barber. Tomographic PIV analysis of physiological flow conditions in a patient-specific arteriovenous fistula. *Experiments in Fluids*, (61) 2020.
 - As the primary author, I conducted the experiments and analysed the results by simultaneously incorporating feedback from the co-authors. The original draft was prepared by me and the ensuing reviewer comments were addressed by consulting with the co-authors. The content from this publication has been included mainly in chapter 3 with some of the results shown in chapter 6.
- **Sanjiv Gunasekera**, Olivia Ng, Shannon Thomas, Ramon Varcoe, Charitha de Silva, Tracie Barber. Impact of juxta-anastomotic stent implantation on the haemodynamics within a single representative patient AVF. *International Journal of Heat and Fluid Flow*, (92) 2021.
 - As the primary author, I conducted the simulations and analysed the results by simultaneously incorporating feedback from the co-authors. The original draft was prepared by me and the ensuing reviewer comments were addressed by consulting with the co-authors. The content from this publication has been included in chapter 5.
- Olivia Ng, **Sanjiv Gunasekera**, Shannon Thomas, Ramon Varcoe, Tracie Barber. The effect of assumed boundary conditions on the accuracy of patient-specific CFD arteriovenous fistula model. *Computer Methods in Biomechanics and Biomedical Engineering: Imaging & Visualization*, 2022.
 - I was involved in retrieving the patient data for this study. Additionally, I reviewed the manuscript in the submission process. Content in this publication has been reflected in chapter 2.

Conference Papers

- **Sanjiv Gunasekera**, Olivia Ng, Shannon Thomas, Ramon Varcoe, Charitha de Silva, Tracie Barber. Towards 3D PIV measurements of a patient-specific arteriovenous fistula. *Proceedings of the 9th Australian Conference on Laser Diagnostics*, Adelaide, Australia, 2019.
 - As the primary author, I conducted the experiments and analysed the results by simultaneously incorporating feedback from the co-authors. The original draft was prepared by me and the ensuing reviewer comments were addressed by consulting with the co-authors. The results described in this publication were used to make comparisons in chapter 3.
- **Sanjiv Gunasekera**, Olivia Ng, Shannon Thomas, Ramon Varcoe, Charitha de Silva, Tracie Barber. A numerical investigation of a stented arteriovenous fistula. *The 22nd Australasian Fluid Mechanics Conference*, Brisbane, Australia, 2020.
 - As the primary author, I conducted the simulations and analysed the results by simultaneously incorporating feedback from the co-authors. The original draft was prepared by me and the ensuing reviewer comments were addressed by consulting with the co-authors. The content from this publication has been included in chapter 4.
- Olivia Ng, **Sanjiv Gunasekera**, Shannon Thomas, Ramon Varcoe, Tracie Barber. A clinical predictive indicator for arteriovenous fistula (AVF) failure. *The 22nd Australasian Fluid Mechanics Conference*, Brisbane, Australia, 2020.
 - I was involved in retrieving the patient data for this study. Additionally, I reviewed the manuscript in the submission process. The resistance calculation detailed in this publication was employed for the analysis contained in chapter 7.
- Sam Mallinson, Geordie McBain, Olivia Ng, **Sanjiv Gunasekera**, Shannon Thomas, Ramon Varcoe, Tracie Barber. Hydraulic resistance and inertance of multi-port vessels. *The 22nd Australasian Fluid Mechanics Conference*, Brisbane, Australia, 2020.
 - I was involved in retrieving the patient data for this study. Additionally, I reviewed the manuscript in the submission process. The resistance calculation detailed in this publication was employed for the analysis contained in chapter 7.

Conference Abstracts

- **Sanjiv Gunasekera**, Olivia Ng, Shannon Thomas, Ramon Varcoe, Charitha de Silva, Tracie Barber. Flow through a malapposed flexible stent within an arteriovenous fistula. *26th Congress of the European Society of Biomechanics*, Milan, Italy, 2021.
- **Sanjiv Gunasekera**, Olivia Ng, Shannon Thomas, Ramon Varcoe, Charitha de Silva, Tracie Barber. Flow analysis in a patient-specific arteriovenous fistula. *Australian Biomedical Engineering Conference*, Melbourne, Australia, 2019.
- Olivia Ng, **Sanjiv Gunasekera**, Shannon Thomas, Ramon Varcoe, Tracie Barber. CFD-derived resistance as a clinical indicator for problematic AVFs. *26th Congress of the European Society of Biomechanics*, Milan, Italy, 2021.
- Olivia Ng, **Sanjiv Gunasekera**, Shannon Thomas, Ramon Varcoe, Tracie Barber. Regular Non-Invasive Surveillance of Arteriovenous Fistula (AVF). *5th Annual 3DMed Australia Conference*, Melbourne, Australia, 2019.
- Olivia Ng, **Sanjiv Gunasekera**, Shannon Thomas, Ramon Varcoe, Tracie Barber. Arteriovenous Fistula (AVF) failure prediction through patient-specific (PS) modelling. *Australian Biomedical Engineering Conference*, Melbourne, Australia, 2019.

Contents

1	Introduction	1
1.1	Vascular access for kidney replacement treatment	2
1.2	Features of an Arteriovenous Fistula	4
1.3	Complications encountered by the AVF	5
1.4	AVF Treatment	6
1.5	Thesis outline	8
2	Literature Review	10
2.1	Impact of haemodynamics on the AVF vessel wall	11
2.2	Haemodynamic studies of AVFs	13
2.3	Influence of stent implantations on haemodynamics	20
2.4	Thesis objectives	23
3	Development of a volumetric flow measurement for a benchtop AVF model	25
3.1	Patient Data Retrieval	26
3.1.1	Overview of the freehand 3D ultrasound scanning methodology . . .	26
3.1.2	Patient scanning procedure	27
3.1.3	Extracting the vessel geometry	29
3.1.4	Obtaining the inlet boundary conditions	29

3.2	Experimental Setup	30
3.2.1	Benchtop model fabrication	30
3.2.2	Working Fluid	31
3.2.3	Physiological boundary conditions	33
3.2.4	Laser and Camera specifications	35
3.3	PIV procedure	38
3.3.1	Calibration	38
3.3.2	Image pre-processing	38
3.3.3	Volume Self-Calibration	39
3.3.4	Volume Reconstruction and Correlation	41
3.3.5	Stereoscopic PIV processing methodology	41
3.4	Validation of vector field	42
3.4.1	Volume reconstruction comparison	42
3.4.2	Comparison with the Stereoscopic PIV measurement	43
4	Flow modelling of the stented AVF	48
4.1	Geometry preparation	49
4.2	CFD domain settings	51
4.3	Adjustments for Large Eddy Simulation	55
4.4	Comparison of the flow field across the different measurement methodologies	60
5	Impact of the stent implantation on the bulk flow	67
5.1	Introduction	68
5.2	Study-specific geometry preparation	68
5.3	Flow features within the vein	70
5.4	Flow rate ratios across stent and vessel lumen slices	72

5.5	Impact of the malapposition on the wall shear stress	73
5.6	Conclusion	75
6	Impact of the stent implantation on turbulence generation	77
6.1	Phase-averaged flow field in the treated AVF geometry	78
6.2	TKE generation within the AVF	84
6.3	Turbulence generation at the end of the stent implantation	90
6.4	Impact of the turbulence generation on the wall shear stresses	94
6.4.1	Behaviour of the WSS at the distal artery	96
6.4.2	Behaviour of the WSS in the juxta-anastomotic vein	100
6.4.3	WSS behaviour proximal to the stent implantation	105
6.5	Conclusion	105
7	Comparison between the stented and diseased AVF	107
7.1	Introduction	108
7.2	Flow behaviour at the anastomosis	112
7.3	Flow behaviour at the stenosis	118
7.4	Pressure drop across regions of the AVF	123
7.5	Comparison of WSS imparted on vessel walls	127
7.5.1	WSS characteristics at the distal artery	127
7.5.2	WSS characteristics at the proximal vein	132
7.6	Conclusion	137
8	Conclusions and Future Research	139
8.1	Key outcomes	140
8.2	Future research avenues	142

Bibliography	144
RANS CFD spatial and temporal discretization assessments	159
A.1 Mesh quality	159
A.2 Grid Convergence Index assessment	160
A.3 Time-step verification	162

List of Figures

1.1	Location of the radial-cephalic arteriovenous fistula. Reprinted from Allon and Robbin (2002).	3
1.2	Configurations of the AVF anastomosis. a) Side-to-side, b) end-to-end, c) side-to-end and d) end-to-side AVFs.	4
1.3	Overview of haemodialysis. a) General components of a dialysis machine and b) the approximate locations of the cannulation points. Adapted from Les Laboratoires Servier.	5
1.4	Illustration of the difference between a healthy remodelled vein of AVF and a diseased vein facing intimal hyperplasia with proliferation of smooth muscle cells towards the inner layers of the vessel wall. Adapted from Browne et al. (2015a).	6
1.5	An angiogram of a juxta-anastomic stent implanted arteriovenous fistula with malapposition of the stent. Adapted from Thomas et al. (2019).	7
2.1	Alignment of endothelial cells with the direction of laminar flow. Reprinted from Topper and Gimbrone Jr (1999).	12
2.2	Regions of the AVF that are most prevalent to disease with a) retrograde and b) antegrade inlet flow conditions. The proximal artery (PA), distal artery (DA) and proximal vein (PV) of the AVF, along with the sections of the anastomosis (toe, heel and floor)	14
2.3	Vortical turbulent structures visualized using Q-criterion. Diastole (minimum inlet flow time-point) in the left column, systole (maximum inlet flow time-point) in the right column. (a) Arterial needle placed 3cm from the anastomosis, (b) arterial needle placed 4cm from the anastomosis, and (c) arterial needle placed 5cm from the anastomosis. Adapted from Fulker et al. (2018)	16

2.4	Pulsatile flow patterns at four points in a cycle. Adapted from Sivanesan et al. (1999)	18
2.5	Shear rate (1/s) contours for flow across stent struts with gaps of a) $L/D = 3.53$ in a 4 mm vessel, b) $L/D = 5.88$ in a 2 mm vessel, and a) $L/D = 10.55$ in a 4 mm vessel where L represents the length of the strut gap and D represents the diameter of the strut. Adapted from Berry et al. (2000)	22
3.1	The sequence of steps followed to setup the Tomographic Particle Image Velocimetry measurement.	26
3.2	Overview of the freehand ultrasound scanning methodology. Reprinted from Colley et al. (2018).	28
3.3	Comparison of the virtual geometry with the benchtop model. (a) The STL file resulting from the segmentation of the stack of ultrasound scans of the AVF. (b) The PDMS benchtop model phantom created with a 3D print of the AVF as the positive.	31
3.4	Refractive index matching. (a) The benchtop model filled with water. (b) The benchtop model filled with the working fluid which is a mixture comprising mainly of glycerol and NaCl solution.	31
3.5	Experimental flow profile at the inlets. The red curve shows the average flow rate obtained at the patient's proximal artery. The red filled region shows the range of flow rates captured at the proximal artery of the patient. The black line imposed on the red region is the flow rate at the proximal artery in the experimental setup. The green curve shows the average flow rate obtained at the patient's distal artery. The green filled region shows the range of flow rates captured at the distal artery of the patient. The black line imposed on the green region is the flow rate at the distal artery in the experimental setup. The patient flow rates were measured using Doppler ultrasound and the experimental setup inlet flow rates were measured using ultrasound flowmeters.	35
3.6	The general experiment setup inclusive of the model, tubing components and the approximate camera positions. The annotations on the inset image explain the various regions of the model.	36
3.7	The comparison of the calibration plate holder and the PDMS model. The thickness of the holder and the PDMS model (denoted in red) are both 25 mm. The calibration plate thickness (denoted by the blue outline) is wider than the laser volume thickness (denoted by the green solid region).	39

3.8	Comparison of the disparity maps after various Volume Self-Calibration (VSC) steps. The first two images show the difference between the spread of the peaks in the sub-volumes before and after applying the Intensity Correlation based VSC (VSC-IC). The final image shows the refinement of the disparity peaks after five iterations of the standard disparity map based VSC.	40
3.9	Comparison of slices of the Tomographic PIV vectors (shown with the colourmap) and slices of the original STL (shown with the black band at each vector slice region).	43
3.10	Comparison of the velocity field between the Stereo-PIV measurement and the Tomo-PIV measurement. The in-plane velocity vector field is overlaid on the velocity magnitude contour plot in sub-figures a) , b) , d) , and e) . The relative error between the Stereo-PIV and Tomo-PIV measurements are shown in sub-figures c) and f) . The velocity field has been compared at a high-flow decelerating time-point and a low-flow accelerating time-point as seen in the inset waveform images on the right.	45
3.11	Comparison of the turbulent kinetic energy (TKE) between the Stereo-PIV measurement and the Tomo-PIV measurement. The TKE has been represented at a high-flow decelerating time-point and a low-flow accelerating time-point as seen in the inset waveform images on the right.	47
4.1	The sequence of steps followed to setup the domain and boundary conditions for the Large Eddy Simulations.	49
4.2	Comparison of a scan image of the stented patient AVF obtained using B-mode ultrasound against a scan image of the stented silicone AVF model obtained using ultra-focus micro-CT.	50
4.3	a) A segment of a stent strut with the centerline imposed across the strut. b) The physiological inlet flow waveforms imposed on the proximal artery (red) and distal artery boundaries (green). c) The AVF geometry with the stent implantation and annotations of important regions.	51
4.4	Circumferential averaged wall shear stress values along the vein of the stented and stent-absent geometries at the peak inlet flow rate timepoint. .	54
4.5	The tetrahedral meshes used for both the stented and stent-absent cases. The inset figures give further detail of the mesh elements close to the stent strut and the vessel wall.	58
4.6	Detail of cells at the vessel and stent wall boundaries near the anastomosis.	58

4.7	Convergence of the phase-averaged quantities: Turbulent Kinetic Energy and Turbulent Wall Shear Stress, for both stented and stent-absent model simulations.	59
4.8	Comparison of velocity magnitude contours across Reynolds-Averaged Navier-Stokes (RANS) simulations, Large Eddy Simulations (LES) and Tomographic Particle Image Velocimetry (Tomo-PIV) measurements at the maximum time-point of the inlet flow.	61
4.9	Comparison of velocity magnitude contours across Reynolds-Averaged Navier-Stokes (RANS) simulations, Large Eddy Simulations (LES) and Tomographic Particle Image Velocimetry (Tomo-PIV) measurements at the minimum time-point of the inlet flow.	62
4.10	Comparison of velocity magnitude across Reynolds-Averaged Navier-Stokes (RANS) simulations, Large Eddy Simulations (LES) and Tomographic Particle Image Velocimetry (Tomo-PIV) measurements using rakes across the vessel at the maximum time-point. The rake numbers correspond to the locations denoted in the bottom left sub-figure. The circle at the end of each rake denotes the starting point of each rake ($d/D = 0$).	63
4.11	Comparison of turbulent kinetic energy contours across Reynolds-Averaged Navier-Stokes (RANS) simulations, Large Eddy Simulations (LES) and Tomographic Particle Image Velocimetry (Tomo-PIV) measurements at the maximum time-point of the inlet flow.	64
4.12	Comparison of turbulent kinetic energy contours across Reynolds-Averaged Navier-Stokes (RANS) simulations, Large Eddy Simulations (LES) and Tomographic Particle Image Velocimetry (Tomo-PIV) measurements at the minimum time-point of the inlet flow.	64
4.13	Comparison of TAWSS, OSI and transWSS from across the vessel wall of the stent-absent AVF case using LES and RANS simulations.	65
5.1	Stented (left) and stent-absent (right) cases with lumen slice locations. The stent lumen slices have been shaded in red while the vessel lumen slices have been shaded in dark grey.	69
5.2	Velocity streamlines coloured with the velocity magnitude at the maximum (subfigures a) and b)) and minimum points (subfigures c) and d)) of the inlet flow profile. The subfigures a) and c) are of the stented geometry while the subfigures b) and d) are of the stent-absent geometry.	70

5.3	Velocity magnitude contours at the 5 vessel lumen slices at the maximum (subfigures a) and b) and minimum points (subfigures c) and d) of the inlet flow profile. The subfigures a) and c) are of the stented geometry while the subfigures b) and d) are of the stent-absent geometry.	71
5.4	Cycle-averaged ratios of flow rate across the stent lumen slice and the vessel lumen slice at five locations in the vein in both stented and stent-absent geometries along with the area ratios of the stent lumen slice and vessel lumen slice.	73
5.5	WSS metrics across the stented (a , c and e) and stent-absent AVFs (b , d and f). The distribution of TAWSS is shown in the contour plots of subfigures a and b . The distribution of OSI is shown in the contour band plots of subfigures c and d . The cycle-averaged WSS vectors are displayed using surface streamlines in subfigures e and f	75
6.1	Phase-averaged velocity magnitude contours across the central XY plane. The contours have been displayed at the (a) accelerating, (b) maximum, (c) decelerating and (d) minimum inlet flow time points of the cardiac cycle.	78
6.2	Streamlines of flow coloured with the phase-averaged velocity magnitude. The streamlines have been displayed at the (a) accelerating, (b) maximum, (c) decelerating and (d) minimum inlet flow time points of the cardiac cycle.	80
6.3	Phase-averaged velocity magnitude contours across the five YZ planes. The contours have been displayed at the (a) accelerating, (b) maximum, (c) decelerating and (d) minimum inlet flow time points of the cardiac cycle.	81
6.4	Ratios of flow rate across the stent lumen slice and the vessel lumen slice at five locations in the vein in both stented and stent-absent geometries obtained using the numerical methods. The procedure followed to calculate the ratios have been described in section 5.2 of chapter 5	82
6.5	Spectral decomposition of the flow rate ratio time-traces at slice locations 1 (closest to the anastomosis), 3 and 5 (furthest from the anastomosis) for the stented and stent-absent cases.	83
6.6	Spectral decomposition of the velocity magnitude at a point near the floor of the anastomosis. The location of the monitor point has been visualised on a contour plot of the Tomo-PIV stent-absent data-set.	84
6.7	Contour plots of turbulent kinetic energy (TKE) on the central plane of the anastomosis. The distribution of the TKE is illustrated at the minimum, acceleration, maximum and deceleration inlet flow time-points for both stented (left) and stent-absent (right) cases.	85

6.8	Comparison of the velocity magnitude ($ \overline{U} $) at monitor points in the anastomosis of the stented and stent-absent cases. The first two rows show the average and range of $ \overline{U} $, while the last two rows show the instantaneous $ \overline{U} $ at the maximum and deceleration time-points of each cycle.	87
6.9	Contour plots of velocity magnitude ($ \overline{U} $) on the central plane of the anastomosis. The distribution of $ \overline{U} $ is illustrated at the minimum, acceleration, maximum and deceleration inlet flow time-points for both stented (left) and stent-absent (right) cases.	89
6.10	Contour plots of vorticity magnitude (left) and turbulent kinetic energy (right) on the central plane at the edge of the stent. The distributions have been plotted at the minimum, acceleration, maximum and deceleration inlet flow time-points for the stented case.	91
6.11	Contour plots of vorticity magnitude and turbulent kinetic energy at cross-sectional slices near the stent edge. The distributions have been plotted at the maximum and deceleration inlet flow time-points for the stented case. . .	93
6.12	Example of unwrapping the 3D vessel wall locations onto a 2D space using local vectors constructed from centerline node locations. The colour bar of the cross-sectional slices assist with understanding the 3D location of the wall element on the corresponding 2D plots.	95
6.13	Wall shear stress metrics on vessel wall at the distal artery.	97
6.14	Turbulent Wall Shear Stress distribution at the maximum and deceleration time-points.	98
6.15	Turbulent Wall Shear Stress distribution at the minimum and acceleration time-points.	99
6.16	Wall shear stress metrics on vessel wall at the distal artery.	101
6.17	Turbulent Wall Shear Stress distribution at the maximum and deceleration time-points.	103
6.18	Turbulent Wall Shear Stress distribution at the minimum and acceleration time-points.	104

7.1	Comparison of the geometry and boundary conditions of the stented and diseased AVF cases. The diseased patient AVF inlet flow rates and geometry. a), b), and c) have been reproduced from figure 4.3 and display the stent strut details, stented case inlet flow rate profiles and the stented AVF geometry. The diseased case inlet boundary conditions d) and the diseased AVF geometry e) , with the annotated stenosis location, is displayed in the bottom half of the figure.	109
7.2	The sequence of steps followed to setup the domain and boundary conditions for the Large Eddy Simulations of the diseased AVF.	110
7.3	Contour plots of velocity magnitude ($ U $) on the central plane of the anastomosis. The distribution of $ U $ are shown at the minimum, acceleration, maximum and deceleration inlet flow time-points for both stented (left) and diseased (right) cases.	112
7.4	Contour plots of velocity magnitude and normalised TKE on vessel slices close to the anastomosis in both stented and diseased AVF geometries. The maximum and deceleration time-points have been used for these contour plots. The locations of the slices have been illustrated in the first row. . . .	114
7.5	Streamline plots of the stented and diseased AVF cases at the maximum and minimum time-point. The streamlines are coloured with the velocity magnitude.	115
7.6	Contour plots of normalised TKE on the central plane of the anastomosis. The distribution is illustrated at the minimum, acceleration, maximum and deceleration inlet flow time-points for both stented (left) and diseased (right) cases.	116
7.7	Isosurfaces of normalised TKE of value 0.2 at the a) acceleration, b) maximum, c) deceleration and d) minimum time-points of the diseased AVF. . .	117
7.8	Isosurfaces of velocity magnitude ($ U $) of value 1 m s^{-1} at the a) acceleration, b) maximum, c) deceleration and d) minimum time-points of the diseased AVF.	119
7.9	Contour plots of velocity magnitude ($ U $) on the central plane of the stenosis and stent edge. The distribution of $ U $ is illustrated at the maximum and deceleration inlet flow time-points for both stented (left) and diseased (right) cases.	119
7.10	Contour plots of vorticity magnitude and turbulent kinetic energy at cross-sectional slices along the vein of the diseased AVF. The distributions have been plotted at the maximum and deceleration inlet flow time-pointse. . . .	121

7.11	Contour plots of normalised TKE on the central plane of the stenosis. The distribution is illustrated at the maximum and deceleration inlet flow time-points for both stented (left) and diseased (right) cases.	122
7.12	Location of pressure drop measurements for both the stented and diseased AVF geometries.	124
7.13	Graph of the hydraulic resistance (in mmHg / L / min) calculated at the locations stipulated in figure 7.12 for the stented and diseased AVF cases. The graph displays the mean resistances along with the range.	125
7.14	Example of unwrapping the 3D vessel wall locations onto a 2D space using local vectors constructed from centerline node locations. The colour bar of the cross-sectional slices assist with understanding the 3D location of the wall element on the corresponding 2D plots.	127
7.15	Distribution of TAWSS, OSI and transWSS across the distal artery close to the anastomosis of both stented and diseased AVF geometries.	129
7.16	Turbulent Wall Shear Stress (TWSS) and normalised TWSS distribution across the distal artery at the minimum and acceleration time-points for both stented and diseased AVF geometries.	130
7.17	Turbulent Wall Shear Stress (TWSS) and normalised TWSS distribution across the distal artery at the maximum and deceleration time-points for both stented and diseased AVF geometries.	131
7.18	Distribution of TAWSS, OSI and transWSS across the proximal vein of both stented and diseased AVF geometries.	132
7.19	Turbulent Wall Shear Stress (TWSS) and normalised TWSS distribution across the proximal vein at the minimum and acceleration time-points for both stented and diseased AVF geometries.	134
7.20	Turbulent Wall Shear Stress (TWSS) and normalised TWSS distribution across the proximal vein at the maximum and deceleration time-points for both stented and diseased AVF geometries.	135
A.1	Mesh quality statistics of the stented (top row) and stent-absent (bottom row) geometries. Sub-figures a) and c) show the spread of the mesh elements with the corresponding aspect ratios while sub-figures b) and d) show the spread of the mesh elements with the corresponding skew values. .	160
A.2	Locations of slice planes in the vein of the AVF.	161
A.3	Circumferential averaged WSS values at the peak inlet timepoint along the vein.	163

List of Tables

3.1	Summary of the experimental conditions and equipment.	37
3.2	Comparison of the domain extent from the stereoscopic and tomographic PIV measurements.	42
7.1	Comparison of the stented AVF with the diseased AVF.	110
7.2	Hydraulic resistance.	125
A.1	Slice averaged velocity magnitude values used for the GCI calculation of the stented case.	161
A.2	Slice averaged velocity magnitude values used for the GCI calculation of the stent-absent case.	162

Abbreviations

Symbols

α	Womersley number
Δ	Subgrid length
μ	Dynamic viscosity
ρ	Density
τ_{wall}	Wall Shear Stress
τ'	Reynolds Stresses
ω	Angular frequency
C_S	Smagorinsky constant
D	Hydraulic Diameter
Re	Reynolds number
U	Velocity

Acronyms

AVF	Arteriovenous Fistula
CAD	Computer Aided Design
CFD	Computational Fluid Dynamics
CFI	Cross Flow Index
CFL	Courant-Friedrichs-Lewy Condition
CKD	Chronic Kidney Disease

CT	Computerised Tomography
DA	Distal Artery
DNS	Direct Numerical Simulation
ECG	Electrocardiogram
ESRD	End Stage Renal Disease
FFT	Fast-Fourier Transform
GCI	Grid Convergence Index
GUI	Graphical User Interface
IH	Intimal Hyperplasia
JXA	Juxta-Anastomotic
LDA	Laser Doppler Anemometry
LES	Large Eddy Simulation
LNH	Localized Normalized Helicity
MART	Multiplicative Algebraic Reconstruction Technique
OSI	Oscillatory Shear Index
PA	Proximal Artery
PDMS	Polydimethylsiloxane
PEG	Polyethylene Glycol
PIV	Particle Image Velocimetry
PSD	Power Spectral Density
PV	Proximal Vein
RANS	Reynolds Averaged Navier-Stokes
RI	Refractive Index
ROI	Region of Interest
RRT	Renal Replacement Treatment
SGS	Subgrid Scale
Stereo-PIV	Stereoscopic PIV
SST	Shear Stress Transport

TAWSS	Time-averaged WSS
TKE	Turbulent Kinetic Energy
Tomo-PIV	Tomographic PIV
transWSS	Transverse WSS
TWSS	Turbulent Wall Shear Stress
VSC	Volume Self-Calibration
VSC-IC	VSC - Intensity Correlation
VSMC	Vascular Smooth Muscle Cell
WSS	Wall Shear Stress

Chapter 1

Introduction

An arteriovenous fistula is a vascular structure that is surgically created by joining a vein and an artery in the forearm of patients with renal disease. The resulting vessel enlargement and increase in blood flow enables easy and efficient haemodialysis. However, this unnatural structure is faced with disease occurring most commonly at the junction (known as the anastomosis) and along the nearby venous section (also referred to as the juxta-anastomotic region). The disease onset constricts the vessel lumen area, restricting blood flow. Of the many factors known to be involved in the initiation of AVF diseases, the dynamics of the blood flow plays a crucial role. A novel treatment that has seen clinical success involves the implantation of a flexible metallic scaffolding, known as a stent, across the anastomosis to hold open the blood vessel.

This thesis is an investigation of the unsteady haemodynamics within a physiological AVF and an assessment of the role the stent implantation plays in the flow dynamics of the AVF. A combination of computational (flow modelling) and experimental methods will be employed to understand the bulk flow behaviour, turbulent fluctuations and vessel wall forces within the AVF. Subtleties of the stenting procedure will be assessed using patient-specific models of the treated AVF, while overall changes will be detailed by drawing comparisons of the flow field to that of the diseased AVF model.

This chapter provides an overview of kidney disease and the necessity of the AVF. Characteristics, disease conditions and treatment methodologies of the AVF will be detailed along with subsequent blood flow behaviour. The chapter will conclude with the structure of the thesis.

1.1 Vascular access for kidney replacement treatment

Approximately 1.7 million Australians, 10% of the population, have biomedical indicators of Chronic Kidney Disease (CKD), with the prevalence increasing after the age of 65 (Australian Institute of Health and Welfare). CKD is the progressive decrease of filtration ability of the kidneys, and is usually accompanied by underlying risk factors such as diabetes, obesity and hypertension. The last stage of CKD is known as End Stage Renal Disease (ESRD). At this stage, patients require some form of Renal Replacement Treatment (RRT) substitute for the deteriorated kidneys. Data from 2012 showed that an estimated \$4.1 billion was spent on treating CKD and the cost of treating ESRD from 2009 to 2020 is estimated to be \$12 billion (Cass et al., 2006).

The optimum treatment of ESRD is a kidney transplant, due to its higher survival rates and subsequent improved quality of life among other advantages (McDonald and Russ, 2002; Tonelli et al., 2011), but the number of patients that are deemed eligible for a transplant significantly outnumbers the available donor kidneys (Australia et al., 2018). This has led to the use of a points system for transplant candidates, which factors in tissue typing, age and health among other considerations (Browning and Thomas, 2001) and results in an average waiting period of three years (Wright and Narayan, 2016). Additionally, the general requirement to be wait-listed for a deceased donor kidney in Australia is the commencement of dialysis (TSANZ, 2019) which is an artificial method of filtering the blood outside the body. Therefore, undergoing dialysis as an alternate renal replacement treatment is an eventuality and can be done either by peritoneal dialysis or haemodialysis. Peritoneal dialysis is an ongoing process where a catheter is placed in the abdomen and the filtration occurs within the body. However, haemodialysis requires the

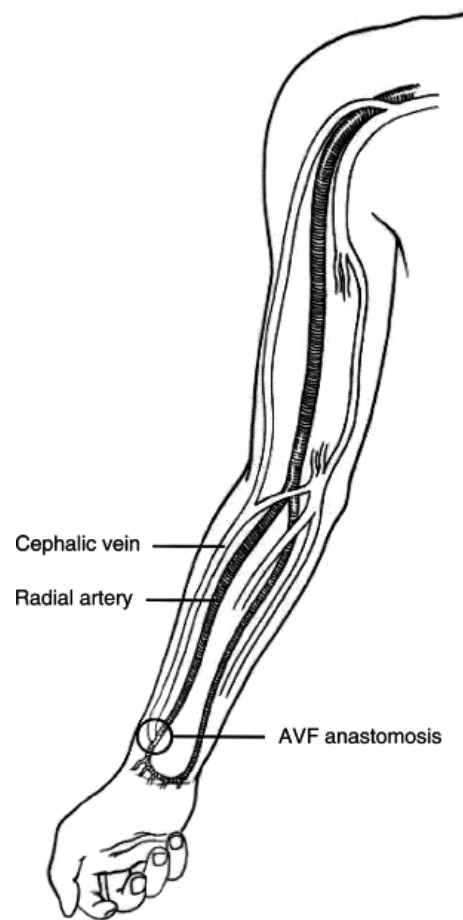


Figure 1.1: Location of the radial-cephalic arteriovenous fistula. Reprinted from Allon and Robbin (2002).

blood to be filtered outside the body in a dialysing machine and patients usually attend four-hour sessions, about three times a week. Haemodialysis, opted for by the majority of dialysis patients (Australia et al., 2018), requires vascular access that can take place either across an arteriovenous fistula, an arteriovenous graft or a catheter. Because of the complications that are associated with grafts and catheters, the arteriovenous fistula (AVF) is considered the preferred option for vascular access (Santoro et al., 2014).

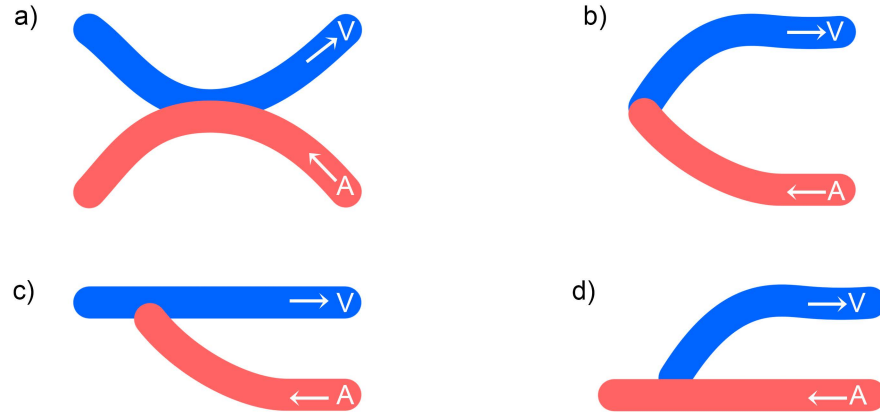


Figure 1.2: Configurations of the AVF anastomosis. **a)** Side-to-side, **b)** end-to-end, **c)** side-to-end and **d)** end-to-side AVFs.

1.2 Features of an Arteriovenous Fistula

The AVF is a surgical anastomosis of a vein to an artery with the primary goal of increasing blood flow in the vein. It is frequently created at the lower end of the fore-arm by connecting the radial artery and the cephalic vein (as illustrated in figure 1.1), however, the brachial artery and the cephalic vein can also be connected higher up in the arm for patients that have unsuitable vessels in the fore-arm (Allon and Robbin, 2002). The anastomosis between the two vessels can be created from one of four general configurations illustrated in figure 1.2. The original AVF, referred to as the ‘Brescia-Cimino’ fistula (Brescia et al., 1966), was created in the side-to-side configuration. However, due to better clinical performance (Stanziale et al., 2011; Wedgwood et al., 1984) and the less technically demanding nature of the surgical procedure (Bashar et al., 2018), the end-to-side AVF configuration has been the preferred option.

After creation, the AVF goes through a period of ‘maturation’ where the vein enlarges (or remodels) due to the significant increase in flow rate. The larger blood vessel makes it easier to cannulate and link the circulatory network to the external dialysing unit that replaces the function of the diseased kidneys (figure 1.3). The increase in flow rate ensures

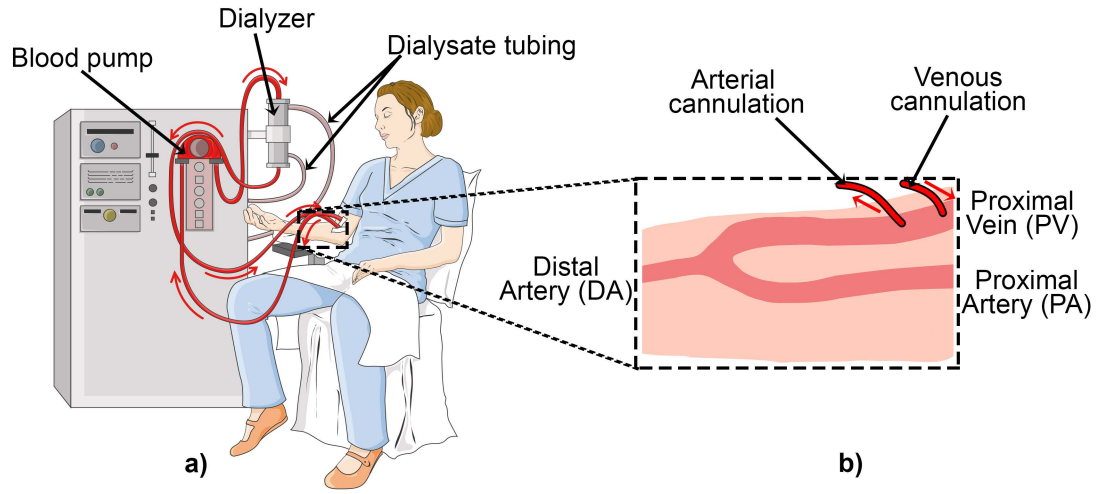


Figure 1.3: Overview of haemodialysis. **a)** General components of a dialysis machine and **b)** the approximate locations of the cannulation points. Adapted from Les Laboratoires Servier.

the dialysis session can be completed effectively within 3 to 5 hours (Jun et al., 2013). Early guidelines suggested the assessment of AVF readiness using the ‘rule of 6s’, which requires the AVF to have a flow rate larger than 600 mL/min , a venous diameter larger than 6 mm and a depth of less than 6 mm . However, clear criteria for the suitability of an AVF for dialysis is still an area being widely researched (Lok et al., 2020).

1.3 Complications encountered by the AVF

Obstacles that prevent AVFs from reaching dialysis suitability come in multiple forms of vascular diseases such as stenosis, thrombosis and ischaemia (Beathard, 2017). Stenosis, which is a narrowing of the blood vessel, frequently occurring in the juxta-anastomotic (JXA) region of the vein is the most common process that threatens AVF patency (Stolic, 2013), and is often caused by intimal hyperplasia (IH) (Duque et al., 2017). The propagation and proliferation of vascular smooth muscle cells and extra-cellular matrices (Jennette and Stone, 2014) to the innermost vessel wall layer (intima), illustrated in figure 1.4, is known as Intimal Hyperplasia (IH) and it is linked to vascular activation mechanisms

that can be initiated due to many reasons such as injury and inflammation (Newby and Zaltsman, 2000). Haemodynamic forces causing injury to the endothelial cells lining the vessel wall are known to be one of the many pathways that initiate IH (Roy-Chaudhury et al., 2006). Observations of vasoprotective cell processes in the presence of laminar flow, contrary to inflammatory cell responses in the presence of disturbed flow, have been made in studies (Gimbrone Jr and García-Cardena, 2016), which restate the impact of the flow behaviour on the disease initiation.

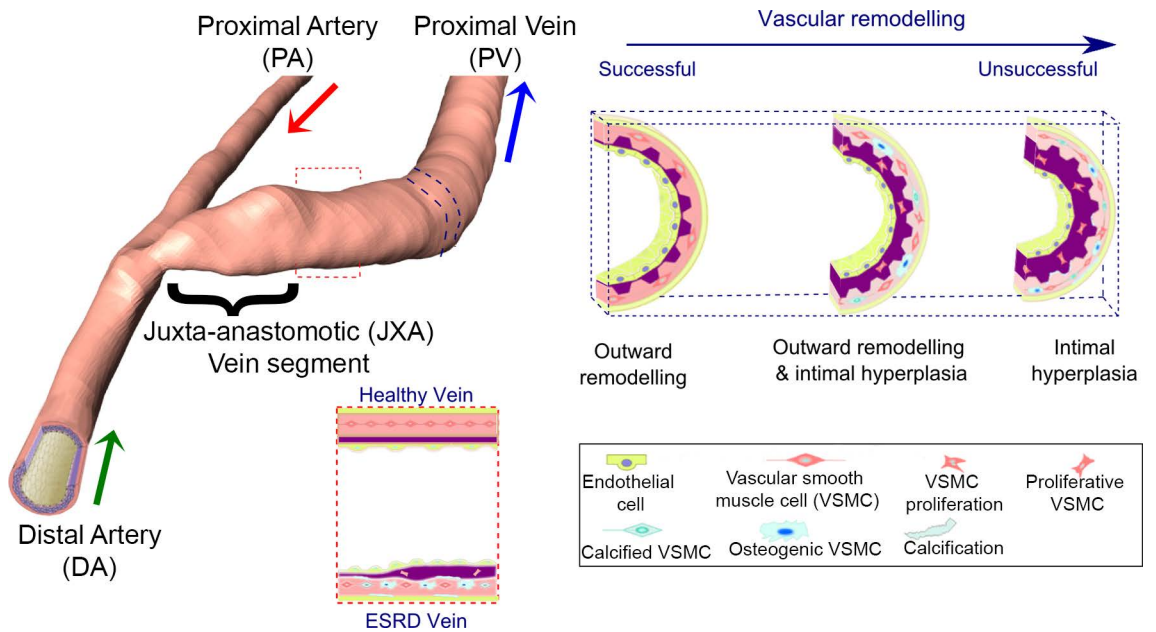


Figure 1.4: Illustration of the difference between a healthy remodelled vein of AVF and a diseased vein facing intimal hyperplasia with proliferation of smooth muscle cells towards the inner layers of the vessel wall. Adapted from Browne et al. (2015a).

1.4 AVF Treatment

Treatment of AVFs can be separated into two overarching fields which are surgical salvation and endovascular management. Relocation of the anastomosis site and restructuring the vessel are some methods of surgical salvation, whilst balloon angioplasty and stent implantation are well known endovascular options (Bharat and Shenoy, 2010; Tessitore et al., 2006). The endovascular methods are commonly used due to the minimally inva-

sive procedures and the potential to use the resulting treated AVF immediately (Williams and Stone, 2010). Stents, which are metallic mesh-like scaffolding devices that hold open vessels, have been used sparingly in AVFs due to the concerns associated with the device hindering cannulation (Mallik et al., 2011) and the potential for an undersized stent to migrate to the anastomosis and occlude the artery (Anwar and Vachharajani, 2017).

Although stent implantation was initially a contested method of treating diseased AVFs, current studies have shown that the advancement in stent technology has yielded better clinical outcomes in comparison to angioplasty alone (Fu et al., 2015). Higher patency rates were noted in AVFs treated with nitinol stents when compared to those treated with balloon angioplasty alone (Kakisis et al., 2012). Nitinol stents are known for their elasticity thereby increasing the shape conformity to various sections of the vessel (Stoeckel et al., 2004) reducing the potential for stent migration. Particularly, the use of flexible nitinol stents across the anastomosis has yielded high unassisted patencies (Swinnen et al., 2015; Thomas et al., 2019) retaining a large proportion of functioning AVFs. However, a side-effect of implanting the flexible stent across the sharp-angled anastomosis is the malapposition of the stent (sometimes referred to as the incomplete stent apposition), where the device is not completely embedded against the wall of the vessel as seen in figure 1.5.

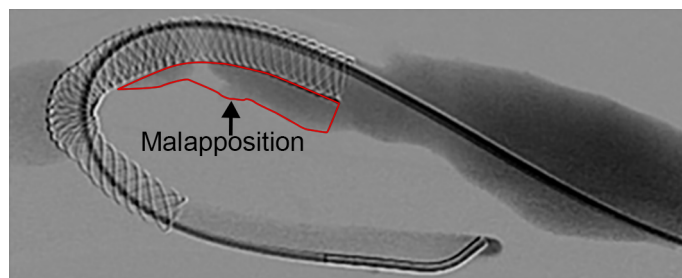


Figure 1.5: An angiogram of a juxta-anastomotic stent implanted arteriovenous fistula with malapposition of the stent. Adapted from Thomas et al. (2019).

1.5 Thesis outline

This thesis reports an investigation of the impact of stent implantation on the flow environment within an AVF by developing a benchtop experimental measurement methodology that will complement high-resolution numerical simulations of flow within *in silico*¹ AVF models.

The relationship between disease onset and disturbances in the AVF flow environment will be elaborated in **chapter 2**. To this end, the current understanding of the complex flow behaviour within the AVF will be documented. Furthermore, the varied impact of stent implantation on blood vessels will be covered.

Chapter 3 contains the procedure involved in obtaining the patient data and setting up the benchtop model of the patient-specific AVF. The detail involved in matching the physiological flow conditions and obtaining spatially and temporally resolved volumetric flow measurements has been recorded in this chapter.

The procedure followed to obtain the stent geometry within the *in silico* patient-specific AVF model is described in **chapter 4**. Additionally, the methodology to conduct high-resolution numerical simulations within the AVF domains has been included in this chapter with further supplementary details (such as temporal and spatial refinements) in Appendix A.

The effect of the stent placement on the bulk flow and the cycle-averaged wall shear stress measurements of the AVF is detailed in **chapter 5** by comparing the flow field with and without the presence of the stent. These findings are further enhanced by assessing the effect of the stent implantation on turbulent fluctuations in **chapter 6**.

A realistic assessment of the differences in the flow dynamics brought upon by the treatment procedure will be detailed by comparing the flow field of the treated AVF with that of the diseased AVF in **chapter 7**. Finally, the thesis will conclude with **chapter 8**

¹Studies performed via computer simulations

which summarises the main outcomes, thereby providing a comprehensive fluid dynamic assessment of the stent implantation procedure in an AVF.

Chapter 2

Literature Review

This chapter begins by providing an overview of the cellular mechanisms that are influenced by haemodynamic behaviour. This overview leads to a detailed discussion of the current literature on the AVF flow environment that has been mainly explored using in silico approaches but also with a few in vitro and in vivo measurements. Subsequently, strategies for assessing the haemodynamic impact of vascular treatment avenues will be detailed, which provides context to the assessment of the AVF stent implantation procedure in this thesis.

2.1 Impact of haemodynamics on the AVF vessel wall

The AVF vasculature is an environment that is faced with multiple unfavourable events such as endothelial injury (from surgical trauma and haemodynamic influences), endothelial dysfunction (due to excess urea in the blood) and the ensuing inflammatory responses (Gameiro and Ibeas, 2020) that lead to disease and the failure of the vascular access. In spite of these factors which are further confounded by variables, such as the patient's background (Fitts et al., 2014), a general theory that is currently accepted is that preceding events responsible for endothelial cell injury influence complex adverse cell responses (Roy-Chaudhury et al., 2006). Variations in wall shear stress are known to be one key event that initiates the pathways for intimal thickening (Tarbell et al., 2014).

There is a general understanding that in the presence of disturbed flow with low wall shear stress, there is increased activity of endothelial cell genes that promote venous inflammation (Chiu and Chien, 2011). *In vitro* studies of cell layers provided the valuable insight that endothelial cells conformed to the direction of laminar steady flow (as illustrated in figure 2.1) without cell division (Topper and Gimbrone Jr, 1999) which replicated observations made *in vivo*. Laminar steady flow was seen to promote cell quiescence and alignment whereas low shear stress in recirculating flow regions was noted to initiate proliferation and apoptosis (a type of cell death) (Paszkwiaak and Dardik, 2003). An *in vitro* study examining the effect of flow disturbances emanating from the dialysis needle flow found the endothelial cells to be sheared off the vessel walls (Huynh et al., 2007). The cell alignment with the graft flow direction was lost in the presence of the disturbed flow from the needle and there was a significant decrease in nitric oxide production which is a key factor in inhibiting inflammation and smooth muscle cell proliferation. In a study involving an arteriovenous graft geometry, *in vivo* vein-wall vibration measurements, using Laser Doppler Vibrometry, were observed to be consistent with the transitional flow noted using experimental and numerical *in vitro* methods (Loth et al., 2003). Importantly, preliminary biological studies of the geometry noted the elevated activity levels of proteins, commonly involved in the signalling pathways of cell migration and proliferation, at regions of high vein wall vibration. Studies of canine arteriovenous grafts have also noted the correlation

of intimal-medial thickening with the increase in vibration, suggesting that the energy of the flow disturbances are transferred to the vessel wall in the form of vibrations which initiate disease propagation (Fillinger et al., 1990).

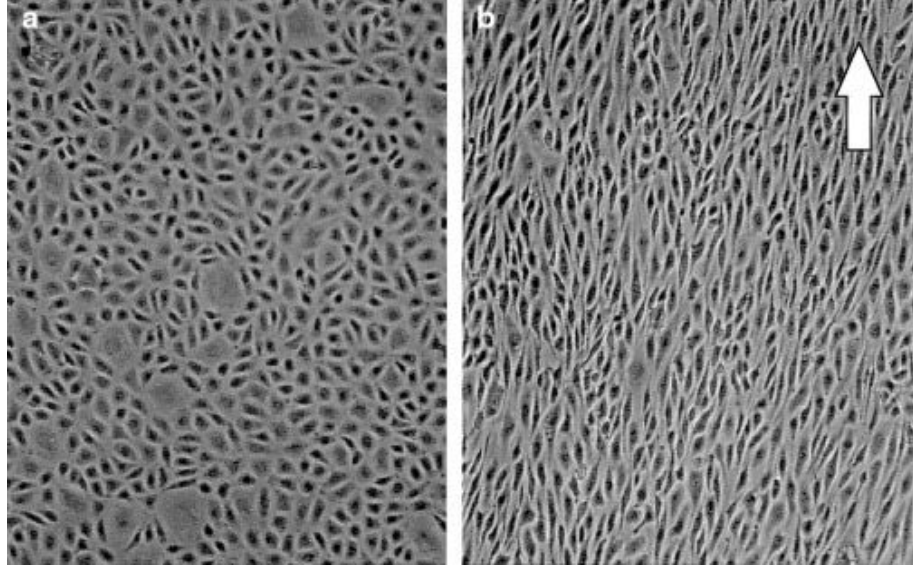


Figure 2.1: Alignment of endothelial cells with the direction of laminar flow. Reprinted from Topper and Gimbrone Jr (1999).

The ensuing wall shear stress behaviour resulting from the disturbed flow field has also been studied in relation to its effects on cell behaviour. For instance, various haemodynamic environments were imposed on porcine vein samples and the extent of intimal hyperplasia was noted to decrease with lower levels of shear stress (Gusic et al., 2005). Similarly, an *in vivo* study of the haemodynamics within carotid arteries of mice noted a negative correlation between vessel wall lesion growth and time-averaged wall shear stress measurements (De Wilde et al., 2016). The inverse correlation of wall shear stress with the intimal hyperplasia has been consistently noted in AVF models as well (Boghossian et al., 2014; Jia et al., 2015; Krishnamoorthy et al., 2008). However, studies have also noted connections between venous lesions and regions of elevated wall shear stress (Carroll et al., 2009) and temporal gradients of wall shear stress (Carroll et al., 2009; Rajabi-Jagahrgh et al., 2013). Therefore, it is quite evident that shear stresses have an impact on the disease initiation in vessel walls, however, there is still a lack of understanding linking the exact shear stress behaviours to the adverse vessel wall mechanisms.

2.2 Haemodynamic studies of AVFs

To understand the haemodynamic environment in detail, spatially and temporally resolved measurements of the AVF blood flow are required. One tool used to obtain two and three dimensional, high resolution *in vivo*¹ data is phase-contrast magnetic resonance imaging (PC-MRI) (He et al., 2018; Suqin et al., 2020), however, this technology is still emerging (Wymer et al., 2020). Meanwhile, MRI and CT (computerised tomography) scanning methodologies that use contrast agents to capture blood flow measurements, increase the likelihood of secondary complications in dialysis patients with compromised renal systems and hence are rarely utilised (Collidge et al., 2007). Therefore, many haemodynamic studies have been conducted by recreating the geometry and the boundary conditions with *in silico* methods (Ene-Iordache and Remuzzi, 2017), and to a lesser degree with *in vitro*² methods (Drost et al., 2017).

These include studies that have used idealised AVF geometries to examine features such as the anastomosis size (Van Canneyt et al., 2010) and inlet artery curvature (Iori et al., 2015). One important key geometrical feature that surgeons had some control over was the anastomosis angle. Initially, an acute-angled anastomosis (of 30°) was thought to yield a haemodynamic environment suitable for a patent AVF (Ene-Iordache et al., 2013). Simulations assuming laminar flow in idealised geometries replicating patient AVF geometries have concluded that a shallow angle (of approximately 45°) would be ideal for AVF health (Yang et al., 2020).

However, low-resolution simulations (with larger grid sizes, longer time-steps and modelled turbulent behaviour) (Carroll et al., 2019; Lee et al., 2016) and high-resolution simulations (with smaller grid sizes, shorter time-steps and partially or completely resolved turbulent behaviour) (Prouse et al., 2020) have consistently noted that larger anastomosis angles create a haemodynamic environment that is more conducive to a healthy AVF. Furthermore, larger reintervention rates have been required for patients with anastomotic angles

¹Studies performed within the living organism

²Studies performed in a controlled environment replicating the conditions of the living organism

less than 30° (Sadaghianloo et al., 2015) and smaller neointimal thickening was noted with obtuse-angled AVF anastomoses in mice (Bai et al., 2021).

A crucial component of replicating the velocity field in the AVF is the application of the appropriate boundary conditions. Simulations varying the ratios of the two steady inlet flow rates while holding a constant outlet flow rate in arteriovenous graft geometries have noted contrasting flow behaviour at the anastomosis and beyond (Broderick et al., 2015; Lee et al., 2007). Employing pulsatile flow conditions at the proximal artery inlet and imposing outlet flow conditions at the distal artery resulted in capturing important high-frequency pressure fluctuations (Browne et al., 2015b) that were not observed with steady inlet flow. The distal artery of the AVF has the characteristic of either having antegrade flow, where the blood flow direction is away from the anastomosis and towards the palmar arch, or retrograde flow where the blood flow is directed back towards the fistula further supplementing the flow from the proximal artery (illustrated in figure 2.2). Clinical observations have noted a significant number of retrograde flow conditions (Kwun et al., 1979; Sivanesan et al., 1998) possibly due to the significantly lower hydraulic resistance at the ‘shunt’ in comparison to that at the extremity of the vascular network of the hand (Beathard and Spergel, 2013). The common occurrence of retrograde flow which in effect involves two inlet flow boundaries would further aggravate the flow behaviour in the anastomosis.

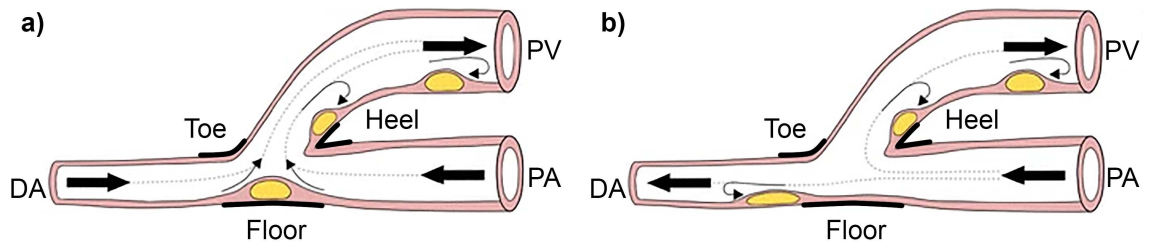


Figure 2.2: Regions of the AVF that are most prevalent to disease with **a)** retrograde and **b)** antegrade inlet flow conditions. The proximal artery (PA), distal artery (DA) and proximal vein (PV) of the AVF, along with the sections of the anastomosis (toe, heel and floor) have been annotated. Adapted from Cunnane et al. (2017).

The initiation of transitional flow behaviour at the anastomosis of the vasculature has been

observed in numerous CFD simulations of patient-specific AVF models. Using the statistical skewness calculation of velocity time series data at points along the AVF, Browne et al. (2015b) observed a significant increase in flow instabilities at the centre of the anastomosis and this deduction was confirmed with the power spectral density (PSD) of the velocity. Decomposing the velocity trace of a turbulent field yields three distinct bandwidths, namely the energy containing range, inertial subrange, and dissipation range (Pope, 2001; Richardson, 2007). These characteristics were noted in the frequency distribution of the velocity obtained at the monitor points placed at the anastomosis. Other simulations have also noted the cascade of high-frequency velocity fluctuations, attributed to turbulent behaviour, at points close to the anastomosis (Bozzetto et al., 2016; Fulker et al., 2018). Bozzetto et al. (2016) used localized normalized helicity (LNH), an indicator of helical flow, to show the nature of the transitional flow field at the anastomosis. Similarly, McGah et al. (2013) used isosurfaces Q-criterion to illustrate the vortical flow generation from the anastomosis region along the vein. Stella et al. (2019) computed the turbulent kinetic energy (albeit using only four cycles) across the geometry and noted high variances at the anastomosis. All these studies have noted the dissipation of the anastomotic disturbances as the flow traverses along the vein. Along these lines, Fulker et al. (2018) have assessed the interactions of these disturbances with dialysis needles and surmised that needle placement further than 3 *cm* would enable improved blood extraction that is not inhibited by turbulent structures emanating from the anastomosis as seen in figure 2.3.

Therefore it is crucial to establish experiments that capture the three-dimensional transitional effects directly in contrast to simulations that are aided by turbulence models. However, experimental studies of flow within AVFs have been largely restricted to CFD validation studies (Drost et al., 2017). End-to-end (Kharboutly et al., 2010), end-to-side (Botti et al., 2013; Browne et al., 2015b; Decorato et al., 2014a; Sivanesan et al., 1999) and side-to-side (Lwin et al., 2014) configurations of AVFs have been used for pressure and velocity field comparisons with most examined at steady flow boundary conditions.

An end-to-side AVF was analysed with a steady flow proximal artery inlet and an occluded

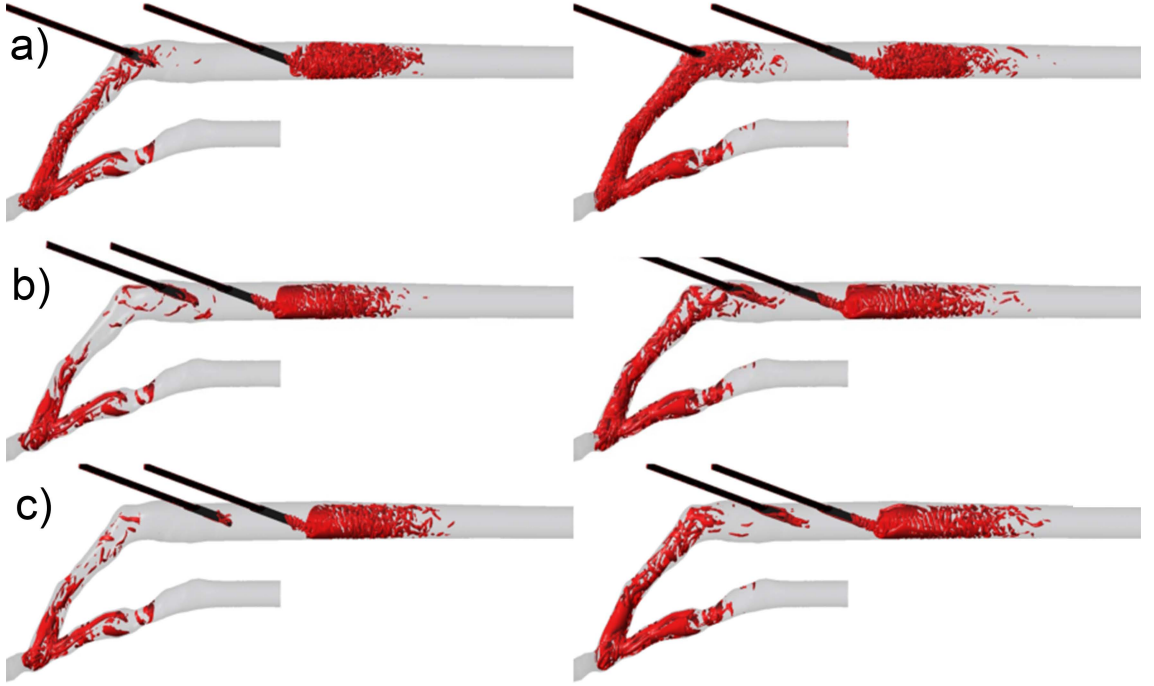


Figure 2.3: Vortical turbulent structures visualized using Q-criterion. Diastole (minimum inlet flow time-point) in the left column, systole (maximum inlet flow time-point) in the right column. (a) Arterial needle placed 3cm from the anastomosis, (b) arterial needle placed 4cm from the anastomosis, and (c) arterial needle placed 5cm from the anastomosis. Adapted from Fulker et al. (2018)

distal artery due to the complexity of establishing pulsatile conditions with three boundary nodes (Botti et al., 2013). The velocity field, which was measured using planar particle image velocimetry (PIV), was compared at two Reynolds numbers and similar flow behaviour was noted in the accompanying numerical results as well. However, the relatively coarse spatial averaging process of PIV together with the low temporal resolution led to discrepancies with the size and magnitude of the vortical regions at the heel and the toe of the anastomosis. A discrepancy between the pressure drop measured in the accelerating phase of the pulsatile inlet flow compared to the pressure drop measured using steady inlet conditions once again shows the value of replicating realistic boundary conditions. Planar PIV measurements of an end-to-end AVF with pulsatile inlet conditions (Kharboutly et al., 2010) revealed the presence of jet flow at the outer wall of the anastomosis due to the enlargement of the vessel. The large velocity gradient across the anastomosis led to a recirculation zone at the heel of the anastomosis together with vortical motion in

the plane perpendicular to the bulk flow direction. Although this experiment was more representative of a physiological AVF, the end-to-end AVF geometry is an uncommon configuration as it is more susceptible to thrombosis formation than other configurations (Galić et al., 2008; Stanziale et al., 2011).

An idealised end-to-side AVF geometry was used with pulsatile and steady conditions in the flow visualisation and laser doppler anemometry (LDA) experiments conducted by Sivanesan et al. (1999). Varying the inlet flow rate ratio (between the proximal and distal arteries) allowed the visualisation of the shift of the location of the prominent recirculating flow from the heel to the toe of the anastomosis. However, significant differences between the flow behaviour with the steady and pulsatile inlet flow were not seen in the flow visualization cases of equivalent Reynolds numbers. An advantage of an experimental setup is the ability to record large datasets with relative ease to quantify statistically converged mean and variance quantities (Buchmann et al., 2011; Gunning et al., 2014), thereby quantifying the disturbances created by the transition to turbulence. Large values of turbulent intensities, that receded along the outlet vein, were recorded at the anastomosis which complemented the vortical flow features seen using flow visualization (figure 2.4).

A key quantity useful in haemodynamics (see section 2.1) is the wall shear stress (WSS). The calculation of WSS can be described using the general equation 2.1 where the fluid dynamic viscosity, wall perpendicular unit distance and the near-wall parallel velocity component are denoted as μ , n and U_{wall} , respectively.

$$\tau_{wall} \text{ (or WSS)} = \mu \left(\frac{\delta U_{wall}}{\delta n} \right)_{wall} \quad (2.1)$$

WSS, as the name implies, quantifies the shearing stress imparted onto the vessel wall by the fluid. Although this quantity can be measured experimentally, as shown by Sivanesan et al. (1999) who quantified high varying oscillatory WSS at the floor of the anastomosis using LDA measurements and Buchmann et al. (2011) who noted low WSS at regions of flow reversal in a carotid artery geometry using tomographic PIV, it requires a high degree

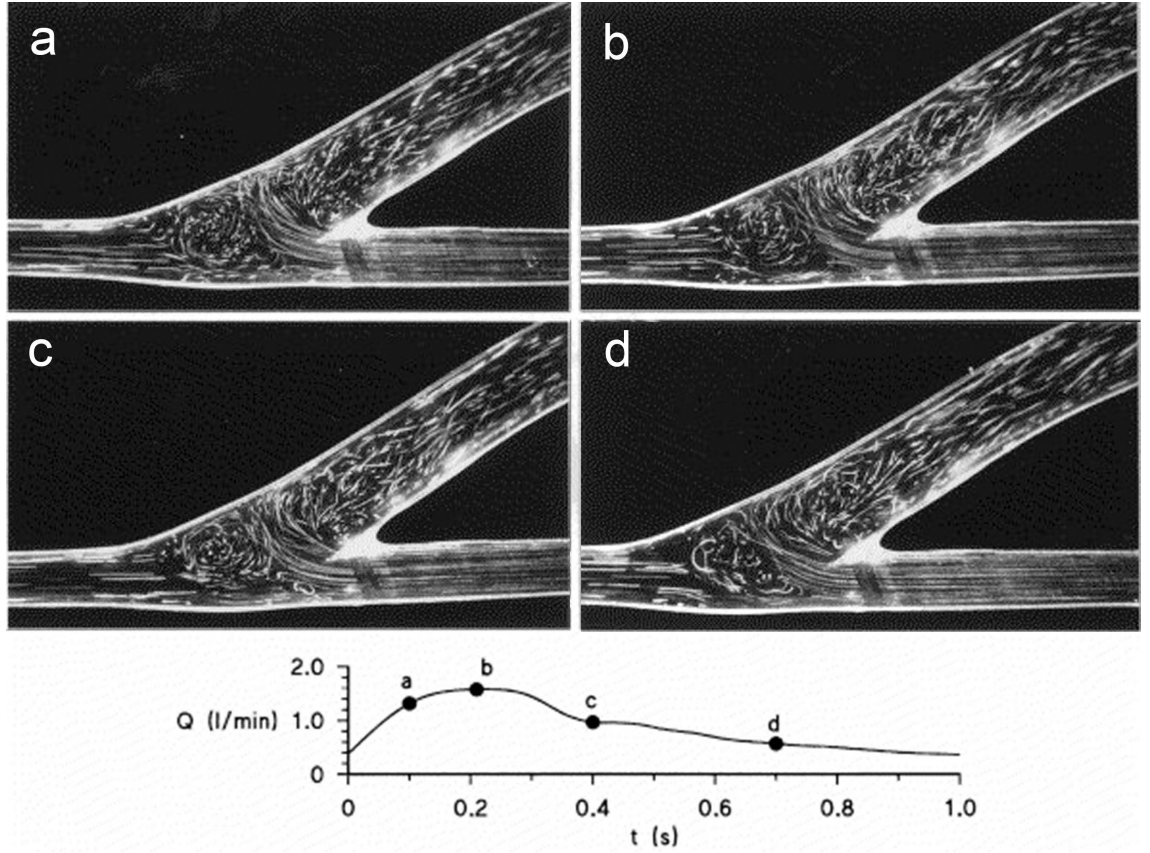


Figure 2.4: Pulsatile flow patterns at four points in a cycle. Adapted from Sivanesan et al. (1999)

of spatial resolution and near-wall flow fields, which is easier to obtain using numerical methods.

The initial postulations regarding the interplay between WSS and AVF maturation were that the blood vessel grows in diameter to compensate for the sudden increase in blood flow and WSS thereby restoring physiological levels of WSS (Humphrey, 2008). However, the WSS levels tend to remain at elevated levels that were larger than the initial WSS values in the vein (Carroll et al., 2011; McGah et al., 2013). To further understand the relationship between WSS characteristics and AVF disease initiation many cell-based biological studies, covered in section 2.1, have correlated regions of low time-averaged wall shear stress (TAWSS) and high oscillatory shear index (OSI) to locations of disease initiation. The TAWSS is a measure of the mean WSS across the cardiac cycle and

is calculated using equation 2.2 within which $\overrightarrow{\tau_{wall}}$ represents the WSS vector and T represents the time for one complete cardiac cycle.

$$TAWSS = \frac{1}{T} \int_0^T |\overrightarrow{\tau_{wall}}| dt \quad (2.2)$$

The Oscillatory Shear Index (OSI) captures the level of reversal of the WSS vector along the line of the dominant WSS vector (He and Ku, 1996) and is calculated using equation 2.3.

$$OSI = 0.5 \left(1 - \frac{\frac{1}{T} \left| \int_0^T \overrightarrow{\tau_{wall}} dt \right|}{TAWSS} \right) \quad (2.3)$$

Numerous computational studies have also noted this co-location of known common disease initiation regions with low TAWSS and high OSI (Ene-Iordache and Remuzzi, 2012; He et al., 2013). However, there are a significant amount of studies that postulate that high shear stress and large WSS gradients may be attributed to the onset of intimal hyperplasia (Carroll et al., 2009; Rajabi-Jagahrgh et al., 2013). Additionally, the TAWSS metric only provides a mean measure, while the OSI only captures the fluctuation along a single direction. Because of these deficiencies, additional WSS metrics were introduced, one of which is transverse wall shear stress (transWSS).

$$transWSS = \frac{1}{T} \int_0^T \left| \overrightarrow{\tau_{wall}} \cdot \left(\vec{n} \times \frac{\int_0^T \overrightarrow{\tau_{wall}} dt}{\left| \int_0^T \overrightarrow{\tau_{wall}} dt \right|} \right) \right| dt \quad (2.4)$$

This metric attempts to capture the multi-directional variation of the WSS vector across the cardiac cycle and is calculated by equation 2.4. This metric and its derivative (Cross Flow Index - CFI) have been shown to indicate regions of multi-directional near-wall flow and have also been linked to regions of disease initiation (Andersson et al., 2017; Carroll, 2018; Mohamied et al., 2015). Fluctuations of WSS from cycle-to-cycle have also been measured, in the same manner that turbulent kinetic energy is calculated, using higher-resolution numerical methods thereby inferring the impact of turbulent fluctuations on

the vessel wall (Andersson et al., 2019; Stella et al., 2019).

2.3 Influence of stent implantations on haemodynamics

Studies investigating the impact of treatment methodologies on AVF haemodynamics are very sparse. Some examples are the assessment of balloon angioplasty on arterial stenoses (Decorato et al., 2014b) and the impact of sildenafil on geometric and haemodynamic parameters of AVFs in rats (Northrup et al., 2021). With some treatments, such as stent implantation, the dearth of haemodynamic research can be put down to the relative novelty of the procedure in AVFs. Clinical studies have noted the safe use and good patency rates for the implantation of novel devices such as the VasQ (Chemla et al., 2016) and the optiflow (Chemla et al., 2014) in brachiocephalic AVFs. However, a detailed understanding of the impact of these devices on the flow within the AVF is yet to be explored.

Extensive fluid dynamic assessments have been conducted on other device implantations, such as artificial heart valves (Dasi et al., 2009) and ventricular assist devices (Laumen et al., 2010). Pertinently, numerous idealised and patient-specific studies have assessed the impact of stent implantations on the haemodynamics of various vessel locations including the coronary artery, cerebral vasculature and thoracic aorta to name a few.

Focused attention on strut geometries of stents showed the aggravation of flow recirculation and low shear stress zones with non-streamlined (generally rectangular cross-sectional) strut shapes which could be conducive to procoagulant and pro-inflammatory elements of blood (Jiménez and Davies, 2009). It was found that even streamlined (generally circular cross-sectional) struts with large strut heights prevented endothelialization (Nguyen et al., 2021) and increased fibrin deposition (Jiménez et al., 2014) thereby showing that both the strut shape and dimensions affect the health of the nearby vessel area.

The novel AVF treatment technique of implanting a flexible stent across the anastomosis (Swinnen et al., 2015; Thomas et al., 2019) leads to partial obstruction of the distal artery

inlet flow and malapposition at the juxta-anastomotic vein as illustrated in figure 1.5 in chapter 1. These stent implantation characteristics have been leveraged in intracranial vasculature to divert flow away from aneurysms (Brinjikji et al., 2013). The diversion of a significant portion of flow away from the aneurysm leads to occlusion in most cases (Kulcsár et al., 2012) which is a far better outcome than the converse realistic possibility of aneurysm rupture. Assessing under-sizing and over-sizing of flow-diverter stents that trap side-branches revealed that the side-branches remained patent when captured by the under-sized flow-diverters (Berg et al., 2016). The under-sized stents had lower spacing between adjacent stent struts which effectively restricted flow into trapped side branches. Using experimental and numerical methods in an idealised geometry with coronary artery physiological flow, Berry et al. (2000) noted the coalescing of vortical regions with stent struts of shorter gaps as opposed to the creation of individual recirculation zones with longer strut gaps. In addition to providing stent design guidance to avoid multiple recirculation zones, these findings also provide an additional mechanism that is potentially at play when diverting or encapsulating flow within the stent.

Stent implantations are known to reduce the overall WSS faced by the vessel with the lowest WSS regions at stent strut junctions/corners occurring due to stagnation of the flow (LaDisa et al., 2003). An increase in intimal hyperplasia within *in vivo* stented artery models has been noted at regions of low WSS and large spatial gradients of WSS (LaDisa Jr et al., 2005). Other studies have also observed the co-location of these WSS behaviour with locations of disease propagation (Murphy and Boyle, 2010) thereby highlighting the impact of the stent induced wall forces on the vessel health. Using the basis of minimizing the area exposed to low WSS, an optimisation study yielded an angle of approximately 40° regardless of the vessel size and intra-strut area (Gundert et al., 2012).

In addition to the design of the stent, studies have also assessed how the flow and WSS behaviour is affected by the degree of stent apposition, where the stent is embedded against the vessel wall, and malapposition, where the stent is not in contact with the vessel wall. An undersized stent implantation, that is not well apposed to the vessel, is known to be a predictor of stent thrombogenicity (Van Werkum et al., 2009) and the malapposition of the

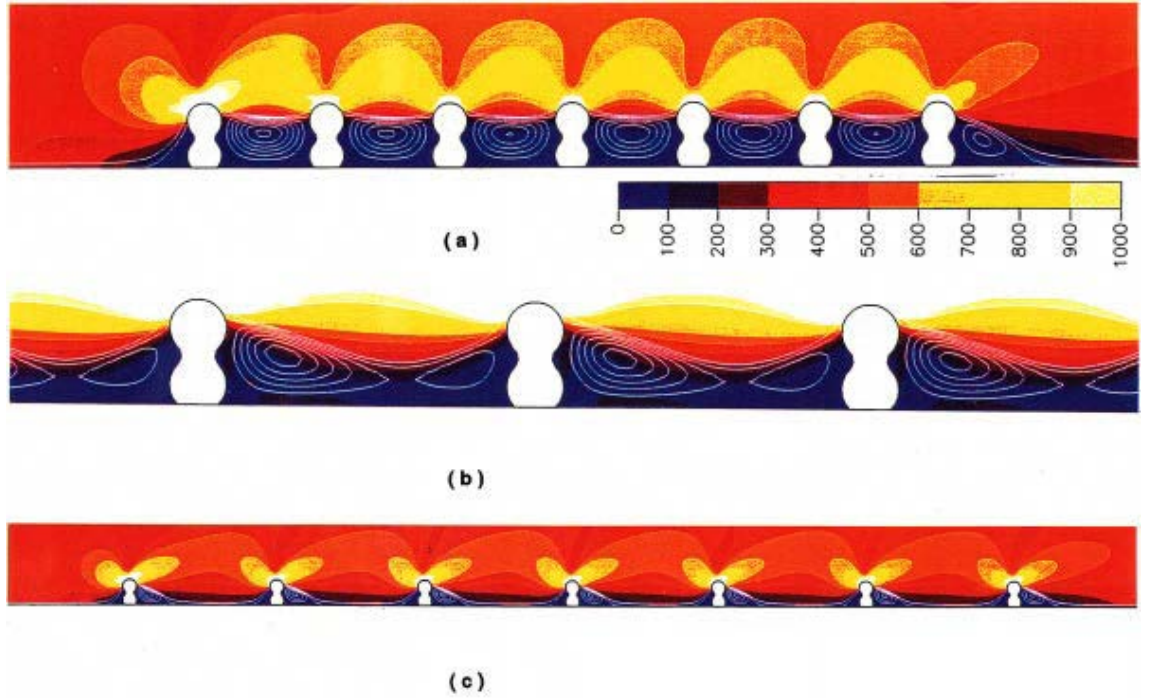


Figure 2.5: Shear rate (1/s) contours for flow across stent struts with gaps of **a)** $L/D = 3.53$ in a 4 mm vessel, **b)** $L/D = 5.88$ in a 2 mm vessel, and **c)** $L/D = 10.55$ in a 4 mm vessel where L represents the length of the strut gap and D represents the diameter of the strut. Adapted from Berry et al. (2000)

stent has shown to produce recirculation regions near stent struts, along with the increase in areas of low Time-Averaged Wall Shear Stress (TAWSS) (Beier et al., 2016; Chen et al., 2017). However, with the increase in the degree of undersizing beyond 5% of the vessel diameter (equivalent to a decrease in stent lumen area below 90.25% of the vessel lumen) a decrease in the heterogeneity of the wall shear stress (WSS) was evident across the vessel (Chen et al., 2009). Flow simulations of patient-specific models have also observed a lower coverage of adverse time-averaged wall shear stress in the presence of a malapposed stent (Wei et al., 2021). A recent study has shown that undersized stent-grafts used to treat cephalic arch stenoses associated with AVFs, have yielded higher access patency rates and a decrease in interventions (Huang et al., 2020).

2.4 Thesis objectives

This chapter has highlighted that there is an appreciable impact from the flow dynamics on AVF health, however, there remains an incomplete understanding of the nature of the adverse haemodynamics and the mechanisms it initiates in disease propagation in the vessel wall. In an attempt to treat the most commonly afflicted disease, stenosis of the juxta-anastomotic vein, clinicians have noted successful outcomes with the novel use of flexible stent implantations. Nevertheless, like other treatment strategies employed to treat AVFs, there has been an absence of investigations discerning the effect of the stent treatment on the flow environment.

Accordingly, the primary objective of this thesis is to understand the haemodynamic influence of the stent implantation within the patient AVF. This involves isolating the effect of the stent by comparing flow fields with and without the presence of the stent in the same patient AVF geometry. A key outcome of numerous AVF studies to date is the dependence of the flow environment on the physiological conditions, therefore this work attempts to replicate an exact patient AVF geometry, boundary conditions and the subtleties of the device implantation. The flow field will be quantified with bulk flow, turbulent fluctuation, and wall shear stress calculations obtained using both high-resolution computational fluid dynamics simulations and tomographic particle image velocimetry experiments. Although past works have noted the initiation of transitional flow in the anastomosis of the AVF, there is an absence of experimental studies capturing this three-dimensional behaviour in realistic AVF geometries without the influence of turbulence models. Hence, a key objective of this work is the development of a volumetric flow measurement technique that captures the highly unsteady flow in a physiological benchtop AVF model.

Beyond this, comparisons will be made between the haemodynamic environment within the treated AVF against that of the diseased AVF. This will be conducted by replicating the same numerical methodology with the (diseased) AVF geometry prior to the implantation of the stent. After normalising appropriate flow quantities, to account for the difference in inlet conditions between the diseased and treated AVFs, comparisons of the bulk flow,

turbulent fluctuations, and wall shear stresses will be made to understand the overall change the stenting procedure has had on the AVF flow environment. This comprehensive assessment of the stent implantation within a patient-specific AVF will not only provide a fundamental understanding of the potential haemodynamic factors driving the success of the treatment but would also unravel complexities at play within the unsteady flow disturbances of a realistic AVF.

Chapter 3

Development of a volumetric flow measurement for a benchtop AVF model¹

This chapter details the development of the benchtop AVF flow measurement to obtain three-dimensional volumetric flow information. The flow field within the AVF is influenced by the patient-specific geometry and boundary conditions, and the procedure followed to retrieve the relevant patient data has been outlined. Subsequently, the methodology followed to fabricate an AVF benchtop model and replicate the patient-specific inlet flow conditions have been detailed. The refinement of the Tomographic Particle Image Velocimetry measurement procedure to obtain temporally resolved velocity information has been specified and the chapter is concluded with a validation of the bounds and values of the resulting velocity field.

¹This chapter contains work that has in part been published in *Experiments in Fluids*, Vol. 61(12), 2020:

Tomographic PIV analysis of physiological flow conditions in a patient-specific arteriovenous fistula

Sanjiv Gunasekera, Olivia Ng, Shannon Thomas, Ramon Varcoe, Charitha de Silva, Tracie Barber

3.1 Patient Data Retrieval

The complex haemodynamic environment within the AVF is to be studied by obtaining detailed volumetric flow measurements using the Tomographic Particle Image Velocimetry (Tomo-PIV) methodology. In order to conduct this study, a sequence of steps, as illustrated in figure 3.1, were followed to process the patient data into valuable components of the measurement.

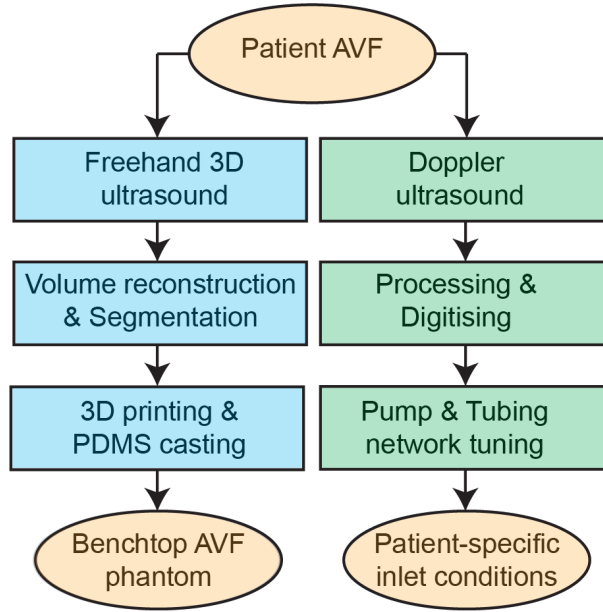


Figure 3.1: The sequence of steps followed to setup the Tomographic Particle Image Velocimetry measurement.

3.1.1 Overview of the freehand 3D ultrasound scanning methodology

The AVF of a 78-year-old male volunteer (at rest) was scanned with informed consent under the approval of the Low/Negligible Risk (LNR) application with the South Eastern Sydney Local Health District Human Research Ethics Committee number 15/063 (LNR/16/POWH/7).

A non-invasive three-dimensional freehand ultrasound scanning method was used to obtain the geometry of the AVF (Colley et al., 2018). The three main components of the

scanning methodology were the portable ultrasound machine (Mindray TE7), the infrared motion-tracking camera (Optitrack V120:Trio) and the workstation laptop (Intel(R) Core i7 2.50GHz CPU and 32-GB RAM). The scans displayed by the ultrasound machine were recorded via a video capture device (StarTech.com Ltd.) that was connected to the laptop and the B-mode ultrasound scan images were acquired by a linear transducer (Mindray L14-6NS) which was connected to the machine. A rigid body with passive reflective markers, that were detected by the motion-tracking camera, was secured to the transducer in an orientation such that it was visible during the scanning procedure and the 3D locations of the markers were relayed to the laptop within which the Motive 1.9 (Optitrack) software calculated the location and orientation of the rigid body at 100 frames per second. The location and scans were then synchronised by an in-house MATLAB (The Mathworks Inc.) script to place the scans in a 3D-volume. This overview of the scanning methodology has been illustrated in figure 3.2.

The rigid body centroid and orientation, that was relayed across to the laptop, required a transformation to align with the scan location and orientation. To accomplish this, a calibration was conducted by placing the transducer on a board with additional reflective markers placed at pre-determined positions. The transformation matrix between the scan plane location and orientation was thus calculated by comparing the location and orientation of the rigid body markers and the additional markers. A verification study of this calibration has been conducted using a cross-wire phantom submerged in water. A mean error of 2.5% was recorded after comparing the distances measured in the phantom against those in the 3D reconstruction of the scans (Carroll, 2018; Colley, 2018).

3.1.2 Patient scanning procedure

A thick layer of conductor transmission gel was placed on the forearm of the patient, to prevent the deformation of the superficial AVF vessels. The ultrasound transducer was traversed along the forearm in one smooth motion with minimal sudden rotations and translations. The motion-tracking camera was placed such that the rigid body affixed to

3. Development of a volumetric flow measurement for a benchtop AVF model

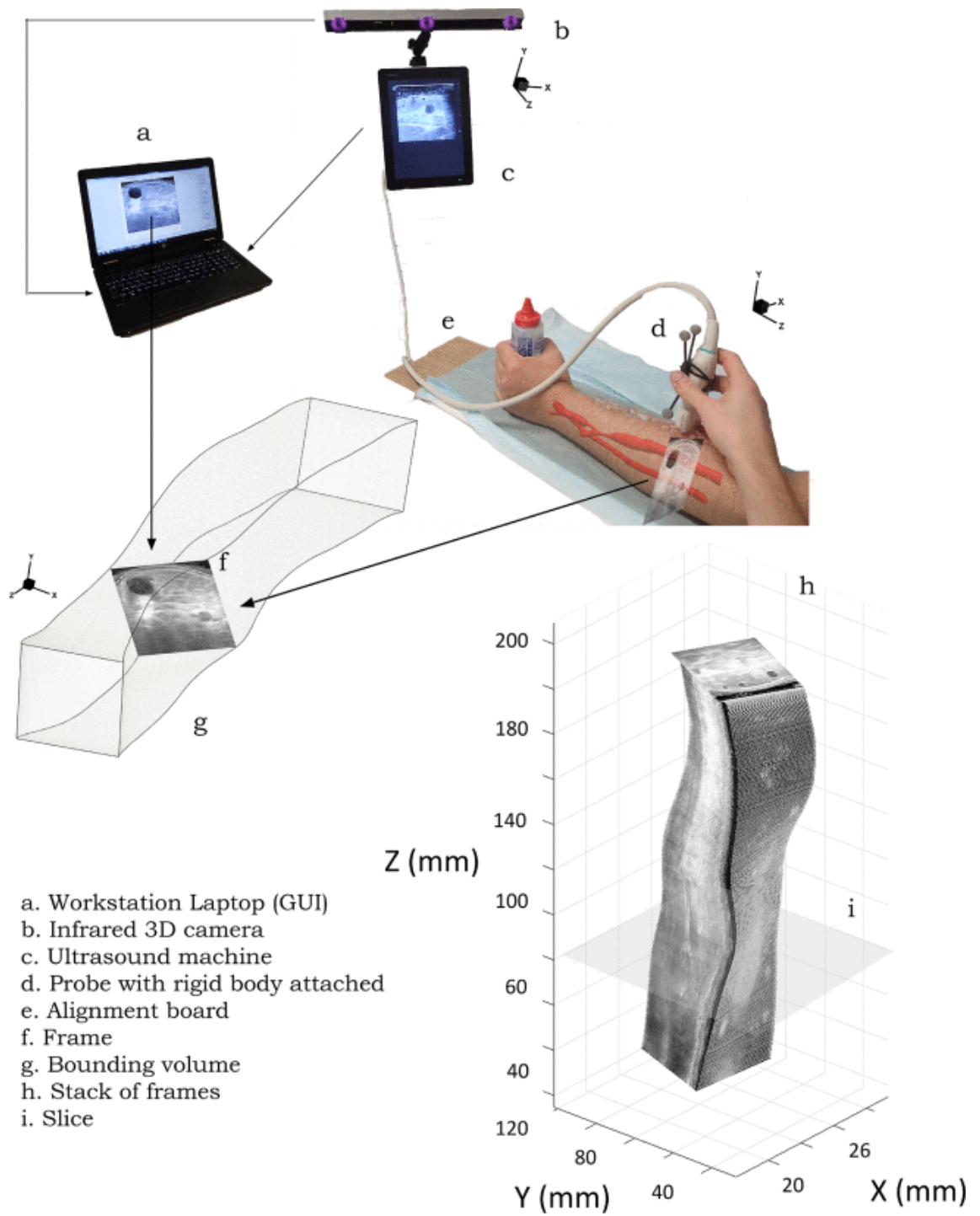


Figure 3.2: Overview of the freehand ultrasound scanning methodology. Reprinted from Colley et al. (2018).

the transducer was always in view throughout the scanning procedure. The B-mode scan image depth was fixed to 35 *mm* which equated to a pixel resolution of 0.0579 *mm/pixel*. The recorded B-mode frames placed in their respective 3D locations were visualised by a MATLAB graphical user interface (GUI) for real-time verification of the scan quality.

3.1.3 Extracting the vessel geometry

The B-mode frames located in a 3D field were then converted to a volume of scans using a voxel-based method. Although a pixel-based method would be less time-intensive, an additional strategy would need to be adopted to fill the spaces in the non-uniform scan frame field since all frames would not intersect every voxel in the final volume. The voxel-based method was conducted by traversing across every voxel and interpolating intensities of the nearest adjacent frame pixels. The resampled voxel size was set to 0.05 *mm*³.

The resulting volume of uniformly spaced scans was imported into the Simpleware ScanIP image processing software (Synopsys Inc., CA, USA). The volume was manually segmented because of the indistinct lumen boundary resulting from the low-contrast ultrasound scans. A mask around the low-intensity vessel lumen cross-section was created every five slices to reduce the duration of the segmenting procedure. The masked slices were then interpolated using a function in ScanIP. After applying 3D Gaussian smoothing functions and assessing against the scan volume, a surface mesh file in the STL format was generated.

3.1.4 Obtaining the inlet boundary conditions

In addition to obtaining the B-mode images of the AVF geometry, the spectral doppler function of the ultrasound machine was used to extract the patient-specific flow rate boundary conditions of the inlet vessels (Carroll et al., 2020). The patient AVF under consideration had a retrograde inlet flow configuration where the proximal artery and the distal artery supplied blood to the outlet vein of the AVF. Since the inlets of the two vessels were recorded individually, a simultaneous ECG trace was recorded using a 3-lead ECG.

The peak of the ‘QRS’ complex of the ECG trace was used to temporally synchronise the inlet waveforms of the two vessels. The Doppler images, which were cycle-averaged and processed using a median filter and Gaussian smoothing, were digitised using a MATLAB algorithm (Carroll et al., 2020).

3.2 Experimental Setup

The in-vitro flow experiments involving the patient-specific AVF were conducted in the Thermofluids Laser Lab in the School of Mechanical and Manufacturing Engineering at the University of New South Wales. The procedure involved casting a transparent model of the AVF, which was connected to a pulsatile pump via a tubing network, to replicate the patient-specific boundary conditions. The seeded working fluid, circulated by the pump, was illuminated by a high-speed double pulsed laser. Finally, the particle images that were captured by the cameras (placed in optimised positions), were processed using commercial PIV software.

3.2.1 Benchtop model fabrication

The surface mesh of the AVF that was generated from the segmentation of the ultrasound scan volume was used to create a 3D print of the geometry at the same scale, using the 3D systems Projet CJP 660Pro which has a minimum layer thickness of 0.1 *mm*. The model was printed in a gypsum-based material (known as Visijet PXL) without a wax infiltrant (in a ‘green’ state) and coated with three layers of PVA glue after printing. The lack of the wax infiltrant ensured that the print remained water-soluble. A clear polydimethylsiloxane (PDMS) model was created by casting around the 3D print using the Sylgard 184 (Dow Corning) silicone elastomer with the recommended 10:1, base to curing agent ratio. At this ratio, the internal walls of the silicone model remain rigid. Numerical simulations comparing compliant and rigid wall conditions have found that wall shear stress values are overestimated in the latter case, however, the general qualitative distribution of wall

shear stress is similar for both wall conditions (Decorato et al., 2014a; McGah et al., 2014). Finally, the AVF phantom, as shown in figure 3.3, was created by dissolving the 3D print in water (with the aid of a syringe and an ultrasonic bath).

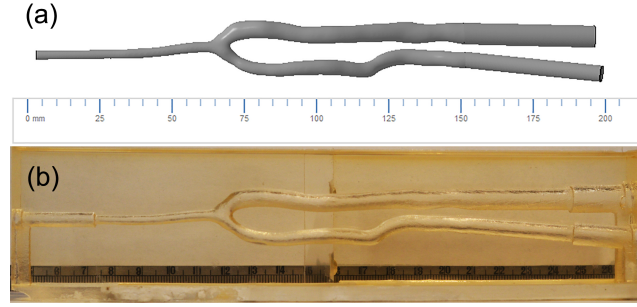


Figure 3.3: Comparison of the virtual geometry with the benchtop model. **(a)** The STL file resulting from the segmentation of the stack of ultrasound scans of the AVF. **(b)** The PDMS benchtop model phantom created with a 3D print of the AVF as the positive.

3.2.2 Working Fluid

The criteria for deciding the working fluid was predominantly based on the need for the Refractive Index (RI) of the fluid to match that of PDMS (≈ 1.42) and for the physical properties of the fluid to be similar to blood. The RI match of the benchtop model, which prevented any distortion of light at the liquid-solid interface, was scrutinised by placing a grid behind the fluid-filled benchtop model and assessing the distortion of the lines as seen in figure 3.4. The equivalent RI was obtained by creating a fluid mixture of 46.3 % of deionized water, 38.0 % of glycerol and 15.7 % of Sodium Chloride by weight.

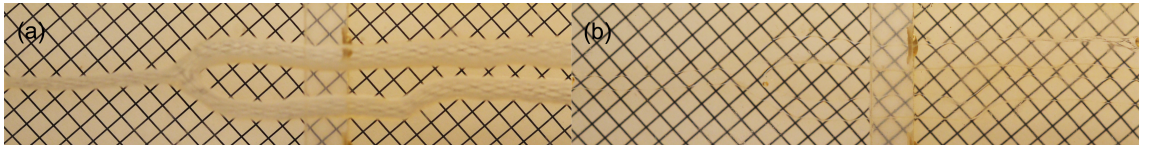


Figure 3.4: Refractive index matching. **(a)** The benchtop model filled with water. **(b)** The benchtop model filled with the working fluid which is a mixture comprising mainly of glycerol and NaCl solution.

To obtain dynamic similarity with the blood flow in the patient's AVF, both the Reynolds number (ranging between 374 - 735 in the proximal artery and 160 - 386 in the distal

3. Development of a volumetric flow measurement for a benchtop AVF model

artery) and the Womersley number (of 3.66) were matched to the physiological case. The definitions for the Reynolds number (Re) and Womersley number (α) used for these scaling calculations are,

$$Re = \frac{\rho * U * D}{\mu} \quad (3.1)$$

$$\alpha = \frac{D}{2} \sqrt{\frac{\omega * \rho}{\mu}} \quad (3.2)$$

where, ρ is the fluid density, U is the average velocity, D is the hydraulic diameter, μ is the dynamic viscosity and ω is the angular frequency. The patient heart rate was recorded as 60 bpm at the time of the scan. Blood density and dynamic viscosity values of 1060 kg/m^3 and $3.5 \text{ mPa} \cdot \text{s}$ respectively, were used for the calculations. The density and dynamic viscosity of the working fluid were measured to be 1202.7 kg/m^3 and $9.21 \text{ mPa} \cdot \text{s}$ respectively at 22°C . The density was measured using a weighing scale and a calibrated beaker while the viscosity was measured using a tuning fork vibration viscometer. With this mixture, a cycle period of 0.43 seconds was deemed necessary to meet the dynamic similarity requirement. It was possible to create a fluid with the RI matched to PDMS using a mixture of 60.75% of glycerol and 39.25% of water. However, the density and dynamic viscosity of this mixture was measured to be 1152.9 kg/m^3 and $11.6 \text{ mPa} \cdot \text{s}$ respectively, which increased the experimental inlet flow rates by 31% and decreased the cycle period to 0.3287 seconds. Ultimately, the mixture using Sodium Chloride was chosen to modify the fluid density and viscosity and enable a longer cycle period and smaller inlet flow rates (as elaborated in section 3.2.3).

A limitation of this mixture is that it is a Newtonian fluid. However, numerical studies (Vijayaratnam et al., 2015) analysing the effects of non-Newtonian and Newtonian fluid have shown that the discrepancies are negligible at high shear rates (typically seen in AVFs). The working fluid was seeded with Rhodamine-B melamine resin particles of size $5 \text{ }\mu\text{m}$ (LaVision GmbH), which were coated with Polyethylene Glycol (PEG) to minimise agglomeration, with a volume percentage of 0.06% of the total working fluid from the

aqueous solution of 2.5% w/v concentration. The calculated Stokes number for the particle in this domain was well below 0.1 confirming that the particle has a sufficient temporal response with the flow. The surfactant Tween 20 was used with a volume ratio of 1:100 to prevent seeding particles from adhering to the wall of the model. The RI matching was conducted after the surfactant was mixed, and the addition of the particles did not make a noticeable difference to the RI because of the low volume added.

3.2.3 Physiological boundary conditions

The ViVitro Superpump (ViVitro Labs Inc., BC, Canada) was used as the flow source and a network of rigid tygen tubing inclusive of valves, to simulate vascular resistance, and air-filled syringes, to simulate vascular compliance, connected the model to the pump. The Superpump, which is a piston pump with an elastic diaphragm in the output chamber, was used to produce a sinusoidal flow waveform. The eccentricity of the sinusoid can be modestly controlled by modifying the coordinates of the piston displacement with time. By varying the gain of the pump, the mean outlet flow rate can be altered while maintaining a waveform that is close to the derivative of the piston coordinate mapping. The interplay of the driven piston flow with the diaphragm and the one-way valves are some factors that restrict the user's control of the waveform via the piston displacement coordinates.

The challenge with the retrograde blood flow configuration is that two different inlet waveforms needed to be created from one source. The combination of resistance from the valves and compliance from the syringes assisted in achieving the different inlet flows. The resistances from the valves were altered to control the ratio of flow diverted to each inlet. The excessive amplitude of the inlet flow in the distal artery was dampened using an optimised ratio of fluid to air in the syringe. A downside that was seen in using this method of compliance is the presence of a secondary localised peak, due to the flow stored in compliance being ejected. An air volume of 20mL in the 40mL syringe gave the required dampening with a low secondary peak. The use of rigid tubing helped in concentrating the control of the compliance predominantly to the syringe. To avoid these complexities

in the tubing network, two pumps that are synchronised with each other would be a more direct alternative to obtain two different patient-specific profiles, provided the availability of such resources.

The suitability of the mixture with added Sodium Chloride over the mixture containing only Glycerol and Water was evident in this procedure of replicating the physiological flow by tuning the resistance and compliance of the flow-loop. The larger inlet flow rates (required with the Glycerol-Water mixture) would have led to a requirement to dampen a larger amplitude in the distal artery. Additionally, the damping response would have a shorter time duration to be enacted. Another consideration was the pump limit for the time period of each cycle that was stipulated to be 0.3 seconds (200 BPM) by the manufacturers of the Vivitro Superpump. The cycle period required with the Glycerol-water mixture (0.33 seconds - 183 BPM) was much closer to this limit than the cycle period with the addition of Sodium Chloride (0.43 seconds - 139 BPM) thereby hastening equipment wear and tear.

The flow rate was measured using a SonoFlow clamp-on ultrasonic flow sensor (Sonotec GmbH). The sensors were placed as close to the model as possible when measuring the flow rates at the inlets. Cycle-to-cycle variation of the inlet flow rates were calculated and the average standard deviations across all timesteps were found to be 0.32 ml/s ($\approx 4.79\%$) and 0.35 ml/s ($\approx 2.07\%$) at the distal artery and proximal artery respectively.

The recorded mean flow rates were compared against the scaled physiological flow rates as shown in figure 3.5. Approximately 50 cycles of the patient's cardiac flow were recorded at the vessels using Doppler ultrasound and the final mean experimental pump flow rates were compared to the range of patient flow rates. The larger range in the proximal artery could be due to the higher flow rates and therefore relatively higher disturbances were seen at the proximal artery. Additional errors in the scanning procedure would be aggravated when scaling the recorded flow rates. Upon comparison of the pump and patient scaled inlet flow rates, an average deviation of 7.57% and 21.16% was noted at the proximal artery and distal artery respectively. A sharp acceleration of the inlet flow profile in the distal artery was arduous to obtain due to the added compliance in that section of the

tubing network. Given that the flow rate was significantly higher in the proximal artery, matching the flow profile at the proximal artery with the patient data was prioritised, resulting in the higher deviation at the distal artery.

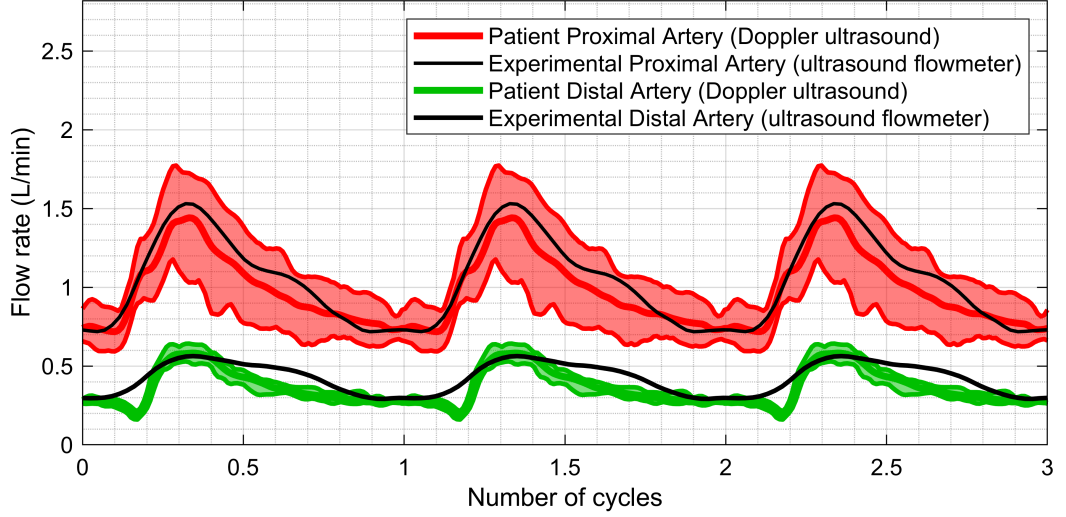


Figure 3.5: Experimental flow profile at the inlets. The red curve shows the average flow rate obtained at the patient’s proximal artery. The red filled region shows the range of flow rates captured at the proximal artery of the patient. The black line imposed on the red region is the flow rate at the proximal artery in the experimental setup. The green curve shows the average flow rate obtained at the patient’s distal artery. The green filled region shows the range of flow rates captured at the distal artery of the patient. The black line imposed on the green region is the flow rate at the distal artery in the experimental setup. The patient flow rates were measured using Doppler ultrasound and the experimental setup inlet flow rates were measured using ultrasound flowmeters.

3.2.4 Laser and Camera specifications

The region of interest (ROI) was illuminated using a 527 nm Nd:YLF (Pegasus PIV dual-head, 10 mJ at 1 kHz per cavity) laser with a volume optic at the end of the laser arm (LaVision). The anastomosis (the point where the vein meets the artery) and the region surrounding it, clinically referred to as the juxta-anastomotic (JXA) region, is most susceptible to stenosis development, therefore the illumination was focussed onto the JXA region of the model. After assessing reconstructions of varying laser volume thicknesses, it was concluded that beyond a thickness of 4 mm a significant amount of erroneous vectors

3. Development of a volumetric flow measurement for a benchtop AVF model

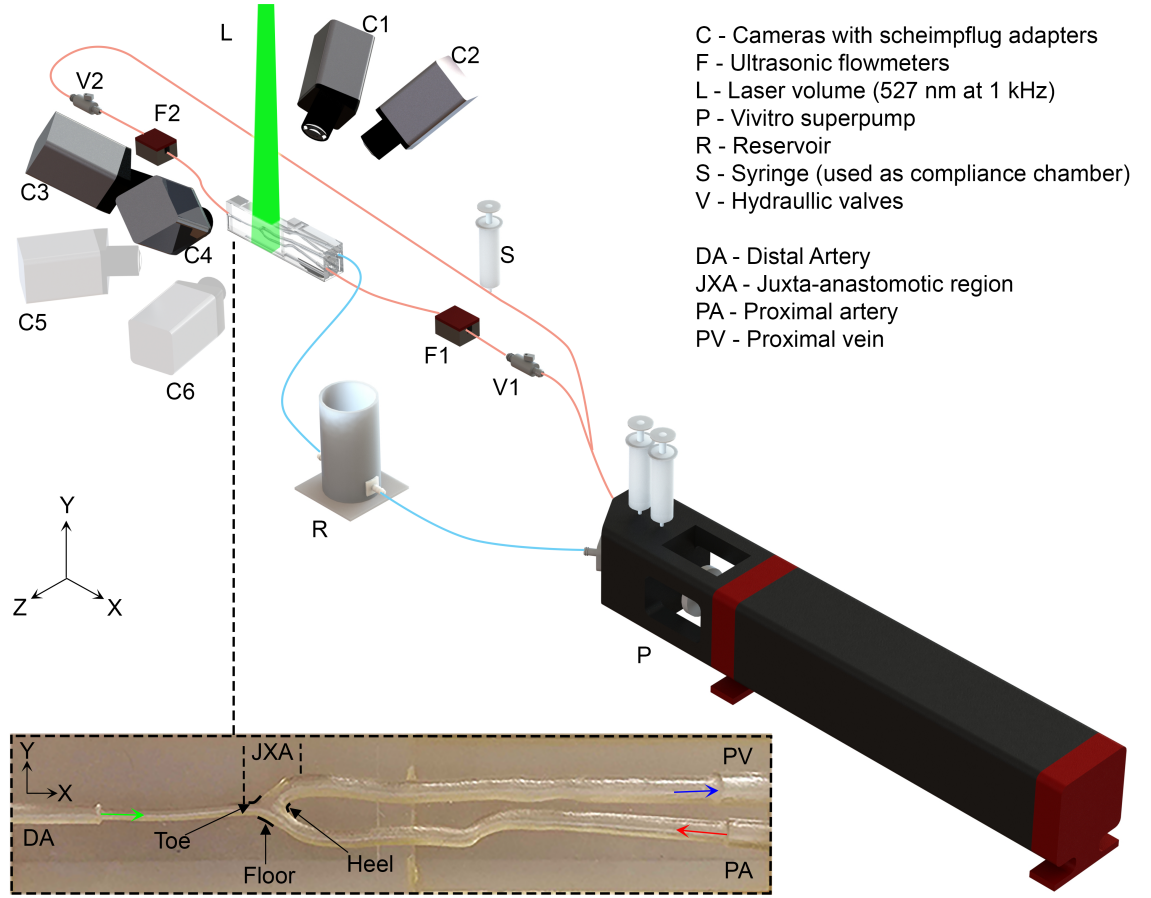


Figure 3.6: The general experiment setup inclusive of the model, tubing components and the approximate camera positions. The annotations on the inset image explain the various regions of the model.

were produced due to the increase of ghost particles and reduction in illumination intensity, therefore the laser was clipped to a thickness of 4 mm . For the preliminary stereoscopic PIV measurements used for validation, a sheet optic was used instead to illuminate the region of interest (Gunasekera et al., 2019) and the laser sheet thickness was measured to be approximately 1 mm .

Four Phantom Miro M310 high-speed cameras (with CMOS sensors), fitted with macro lenses of 100 mm focal length (Tokina AT-X M100 PRO D Macro), and 540 nm long-pass filters, recorded the double-frame particle images at 1 kHz with a $25\text{ }\mu\text{s}$ separation between the two frames (dt). The aperture set to a focal stop of 8 ensured that the 4 mm

3. Development of a volumetric flow measurement for a benchtop AVF model

Table 3.1: Summary of the experimental conditions and equipment.

PDMS model	Box dimensions	210 (<i>L</i>) \times 40 (<i>W</i>) \times 50 (<i>H</i>) mm^3
Working Fluid	Proximal Artery Diameter	≈ 4.5 <i>mm</i> near the anastomosis
	Distal Artery Diameter	≈ 4 <i>mm</i> near the anastomosis
	Proximal Vein Diameter	≈ 6.5 <i>mm</i> near the anastomosis
	Composition	Water 46.3%, Glycerol 38.0% and Sodium Chloride 15.7% (w/w)
	Surfactant	Tween 20 (1% volume ratio)
	Density	1202.7 kg/m^3
	Dynamic Viscosity	9.21 $mPa \cdot s$
Boundary conditions	Seeding type	5 μm Rhodamine-B melamine resin particles with PEG coating
	Seeding concentration	(0.06% volume ratio)
	Stokes number	4×10^{-11}
	Reynolds number (Proximal artery)	374 - 735
	Reynolds number (Distal artery)	160 - 386
	Womersley number	3.66
	Time period	0.43 <i>s</i>
Laser	Type	Nd:YLF 527 nm double pulsed
	Speed	1 kHz
	Pulse separation	25 μs
	Illuminated volume	30 (<i>L</i>) \times 4 (<i>W</i>) \times 20 (<i>H</i>) mm^3
Camera	Type	Phantom Miro M310 $\times 4$
	Resolution	1280 \times 800
	Pixel resolution	29.4 <i>pixels/mm</i>
	Aperture	f-8
	Lens filter	540 <i>nm</i> long-pass
	Azimuthal and elevation angles with respect to the perpendicular of the <i>XY</i> plane	30°

volume was in focus. Camera positions with non-zero optimised elevation (and azimuthal) angles have been shown to produce reconstructions of better quality in tomographic PIV experiments (De Silva et al., 2012); therefore the four cameras were placed in a pyramid configuration with the model at the apex and the cameras at the vertices of the pyramid as annotated C1-4 in figure 3.6. However, the Scheimpflug adapters restricted the optimisation of the azimuthal and elevation camera angles to approximately 30° each. Two cameras were previously placed on a plane perpendicular to the laser beam with only an

azimuthal angle of approximately 40° as annotated by C5-6 in figure 3.6. The images acquired from these two cameras were used to conduct preliminary stereoscopic PIV measurements of the AVF flow field. As forward scattered light has also been demonstrated to be beneficial (De Silva et al., 2012), a silver-coated front-surface mirror was placed beneath the ROI to increase the reflected particle intensity.

A summary of all the experimental values and settings is included in table 3.1.

3.3 PIV procedure

3.3.1 Calibration

As noted, the RI matched working fluid reduced the distortion across the liquid-solid interface, however, there would still be distortion due to light crossing the solid-gas interface of the transparent PDMS model to the surrounding air. A method of overcoming this obstacle is to orientate the cameras perpendicular to the solid face of the PDMS model either by placing them in orthogonal locations or by including optical devices such as prisms (Buchmann et al., 2011), however, neither method was feasible for this experiment due to the oblique camera viewing angles necessary for better quality tomographic reconstruction. Therefore, the calibration images were captured with an equivalent amount of optical distortion by embedding the calibration target (which was a LaVision 058-5 calibration plate) in a PDMS ‘holder’ of equivalent thickness to the AVF PDMS model as illustrated in figure 3.7. Since the thickness of the calibration target ($5.9mm$) was larger than the ROI thickness, one view of the target placed at the centre of the ROI was deemed sufficient.

3.3.2 Image pre-processing

The particle images were captured and processed using the commercial PIV processing software, DaVis 8.4.0 (LaVision GmbH). To improve the volume reconstruction, the raw

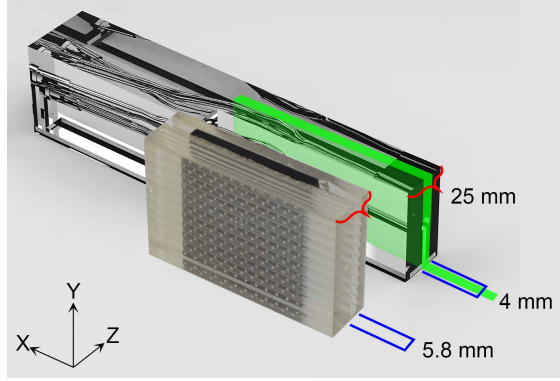


Figure 3.7: The comparison of the calibration plate holder and the PDMS model. The thickness of the holder and the PDMS model (denoted in red) are both 25 *mm*. The calibration plate thickness (denoted by the blue outline) is wider than the laser volume thickness (denoted by the green solid region).

images were first pre-processed. Although the pairing of fluorescent particles and long-pass lens filters reduce the background noise significantly, the remaining low intensity noise was eliminated by first, subtracting the minimum intensities of 1000 images at each pixel, followed by applying a sliding minimum subtraction and a constant subtraction of each image. The non-uniform spread of the laser volume intensity was mitigated by applying a local average normalisation with a large window for every image. A Gaussian smoothing step is included to combat the intensity reduction steps at particle pixel locations and to mitigate the effects of small calibration errors (Elsinga et al., 2006; Scarano, 2012).

3.3.3 Volume Self-Calibration

Although the calibration procedure was followed with care, sources of error such as misalignment of the PDMS holder to the AVF PDMS model, camera vibrations and so on would introduce disparities that are significant to the tomographic reconstruction step. Therefore, two volume self-calibration (VSC) techniques have been implemented with the first being the intensity correlation based VSC (VSC-IC) (Wieneke, 2018) to correct large disparities, followed by the standard VSC (Wieneke, 2008) which is based on comparing detected particle positions across the four cameras. The advantage of using the VSC-IC method is evident in figure 3.8 where the peaks of the disparity maps are much sharper and

are of equal intensity across all sub-volumes following the application of this method. The disparity maps were further refined by conducting five iterations of the standard disparity map based VSC method.

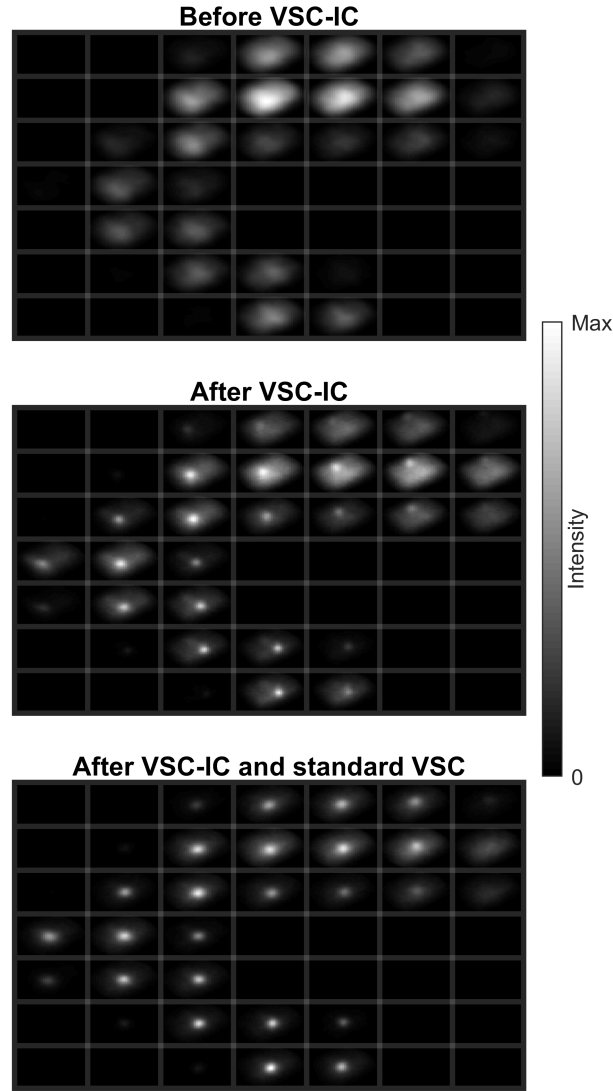


Figure 3.8: Comparison of the disparity maps after various Volume Self-Calibration (VSC) steps. The first two images show the difference between the spread of the peaks in the sub-volumes before and after applying the Intensity Correlation based VSC (VSC-IC). The final image shows the refinement of the disparity peaks after five iterations of the standard disparity map based VSC.

3.3.4 Volume Reconstruction and Correlation

The volume was reconstructed using a fast MART (multiplicative algebraic reconstruction technique) algorithm with 10 iterations (Elsinga et al., 2006) in DaVis. Before proceeding to cross-correlate the volume pairs, an internal 3D masking procedure, similar to that proposed by Im et al. (2014), was followed to minimise the effect of ghost particles affecting the correlation. The 3D masking was implemented by obtaining the summation of 150 volume reconstructions which were then subjected to a threshold elimination to null low intensity particles which is a typical characteristic of ghost particles (Scarano, 2012). Subsequently, the 3D mask was further refined using dilation, erosion and smoothing morphological operations that filled small null zones within the envelope of the geometry, eliminated spurious external spots and levelled the bounds of the mask, respectively.

The refined 3D mask was applied to the corresponding 150 volumes and correlated using a multi-step procedure starting with a window size of $64 \times 64 \times 64$ reducing to $32 \times 32 \times 32$ with an overlap of 75% for all steps. The equivalent vector spatial resolution in real world dimensions was $0.27 \times 0.27 \times 0.27 \text{ mm}^3$. Each correlation step was conducted in two passes using the universal outlier detection epsilon set to 0.1 pixels (Westerweel and Scarano, 2005) and the final vectors were post-processed using the universal outlier detection method and a median filter with a window size of 3. An overall field of view of $35 \times 22 \times 4 \text{ mm}^3$ was captured using this measurement.

3.3.5 Stereoscopic PIV processing methodology

The preliminary images acquired by the two cameras placed orthogonal to the light sheet (C5-6 in figure 3.6) were used for stereoscopic PIV measurements. These double-frame images were recorded with the same imaging speed and separation as previously mentioned. Since the viewing angle was less oblique in comparison to the Tomo-PIV configuration, only a sliding background minimisation of 3 pixels was necessary to refine the images. A multi-pass algorithm with a decreasing window size of 48×48 reducing to 24×24 with an overlap of 50% was used for cross-correlation. The equivalent vector spatial resolution

in real world dimensions was $0.25 \times 0.25 \text{ mm}^2$. The universal outlier detection algorithm along with a median filter with a window size of 3 pixels was used to filter out erroneous vectors. A mask of the ROI was created by outlining the vessel cross-section on the summation of all the particle images. This mask was used to eliminate vectors calculated outside the bounds of the ROI. An overall field of view of $33 \times 21 \text{ mm}^2$ was captured using the stereo-PIV measurement.

Table 3.2: Comparison of the domain extent from the stereoscopic and tomographic PIV measurements.

	Stereo-PIV	Tomo-PIV
Interrogation window	$48 \times 48 \rightarrow 24 \times 24$	$64 \times 64 \times 64 \rightarrow 32 \times 32 \times 32$
Interrogation window overlap	50%	75%
Resolution	$0.25 \times 0.25 \text{ mm}^2/px$	$0.27 \times 0.27 \times 0.27 \text{ mm}^3/vxl$
Field of view ($X \times Y \times Z$)	$33 \times 21 \text{ mm}^2$	$35 \times 22 \times 4 \text{ mm}^3$

3.4 Validation of vector field

3.4.1 Volume reconstruction comparison

The vectors were exported and post-processed using Matlab (The MathWorks Inc.). Before assessing the nature of the flow recorded within the AVF, the reconstruction was qualitatively assessed by comparing the recreated volume to the original STL. The global coordinates of the STL were modified manually using the Computer-Aided Design software, Netfabb (Autodesk Inc.) and then overlaid with the Tomo-PIV vector field using Tecplot 360 (Tecplot Inc.) as shown in the figure 3.9. The general reconstruction of the vector is the main focus of this figure. By assessing the outer edge of the vector field and the black band signifying the bounds of the STL, it can be seen that the reconstruction is very similar to the initial dimensions. Since relatively shallow camera viewing angles have been used, the accurate recreation of the Z dimension was the most challenging. However, the accuracy of the reconstruction in the Z direction can be seen by the fact that the circular features of the slices mimic the vessels with an insignificant amount of over-estimation (approximately 1-2 voxels). Reconstruction errors accumulated by opti-

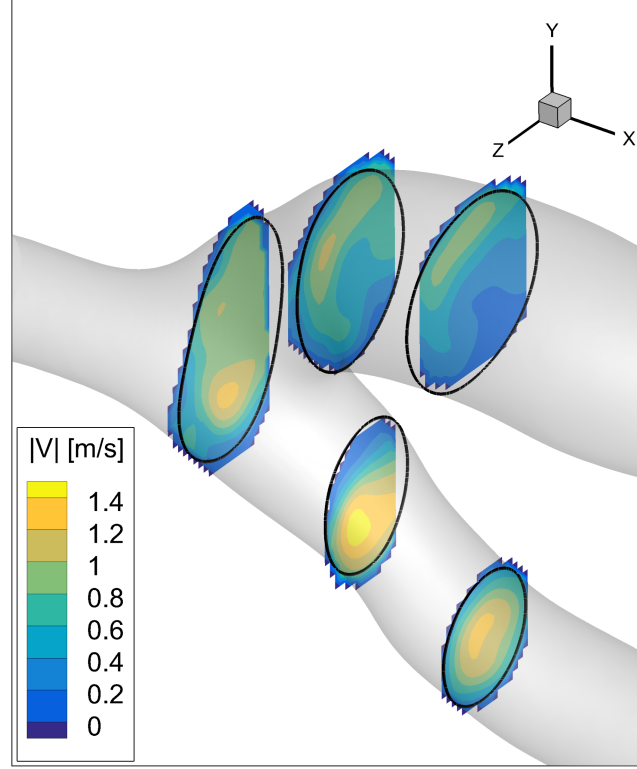


Figure 3.9: Comparison of slices of the Tomographic PIV vectors (shown with the colourmap) and slices of the original STL (shown with the black band at each vector slice region).

cal distortions and the slight imperfection of the 3D masking procedure are likely factors that lead to this subtle error. The geometry used for this experiment is patient-specific, therefore, the vessels do not align perfectly with any axis. Because of the non-alignment of the geometry, some regions were not illuminated by the 4 mm thick laser volume. The spacing between the vector field and the STL bounds in the Z direction of the first and last slice is because those regions have not been illuminated.

3.4.2 Comparison with the Stereoscopic PIV measurement

To assess the integrity of the Tomo-PIV procedure, the resulting vector field was compared to that of the Stereo-PIV measurement velocity field as shown in figure 3.10. To match the spatial averaging across the thickness of the laser sheet occurring in the Stereo-PIV

processing, adjacent Z plane slices of the Tomo-PIV vector field, amounting to an equivalent thickness of 1 *mm*, were averaged. To accurately co-locate the Tomo-PIV results, adjacent averaged Z plane slices were compared with the Stereo-PIV results and the Z-slice with the least error was selected. Both measurement methodologies were conducted with pulsatile inlet conditions; however, the procedure followed to match the waveform to the physiological inlets was refined after the Stereo-PIV measurements were completed. The inclusion of compliance into the flow-loop enabled a smaller amplitude of the waveform at the inlets which mimicked the average physiological waveform better. The decrease in the amplitude created a disparity in inlet flow conditions at the maximum and minimum points, therefore for the following velocity comparison, time-points where the inlet pump waveforms were equivalent in both measurements were selected. One time-point was at high decelerating inlet flow while the other was at low accelerating inlet flow. The comparison was made using the velocity magnitude $|\overline{U}| = \sqrt{\overline{U}_x^2 + \overline{U}_y^2 + \overline{U}_z^2}$ contour plot and the in-plane $(\overline{U}_x, \overline{U}_y)$ vector plot. The velocity components were phase-averaged across multiple cycles to obtain the general behaviour at specific flow time-points throughout the inlet cardiac cycle. 20 cardiac cycles were used for averaging the Tomo-PIV field while 10 cycles were used for averaging of the Stereo-PIV field.

The contour plots of $|\overline{U}|$ reveal that the flow fields are qualitatively in good agreement with each other. A low velocity zone is observed at the floor of the anastomosis and near the heel of the vein with the high inlet flow reaching the upper wall of the vein. The low velocity zone enlarges at the low-flow time-point in both measurements. The small discrepancies at certain locations at the heel of the vein at both time-points could be explained by transient flow effects of the two different waveforms. Another source of discrepancy is the rotational misalignment of the laser sheet relative to the principal axes of the Tomo-PIV measurement. Despite these factors, it is evident that the integrity of the flow field is retained in the progression of the experiment from stereo-PIV to Tomo-PIV.

The unsteadiness of both flow fields were quantified using Turbulent Kinetic Energy, $TKE = \frac{1}{2}(u_x'^2 + u_y'^2 + u_z'^2)$, where the velocity fluctuations, $u_x' = U_x - \overline{U}_x$, $u_y' = U_y - \overline{U}_y$, $u_z' = U_z - \overline{U}_z$ were calculated using the phase-averaged velocity components, \overline{U}_x , \overline{U}_y , \overline{U}_z ,

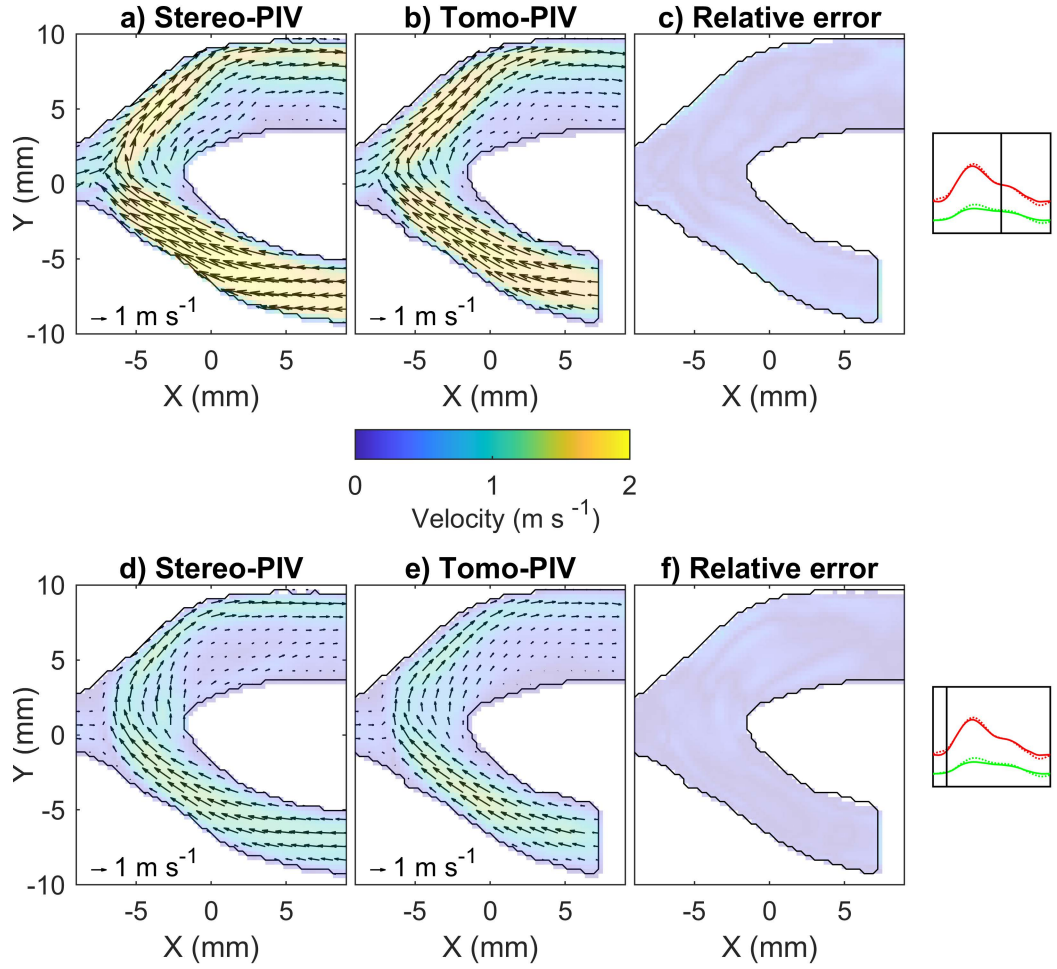


Figure 3.10: Comparison of the velocity field between the Stereo-PIV measurement and the Tomo-PIV measurement. The in-plane velocity vector field is overlaid on the velocity magnitude contour plot in sub-figures **a)**, **b)**, **d)**, and **e)**. The relative error between the Stereo-PIV and Tomo-PIV measurements are shown in sub-figures **c)** and **f)**. The velocity field has been compared at a high-flow decelerating time-point and a low-flow accelerating time-point as seen in the inset waveform images on the right.

at each time-point across the cardiac cycle. The resulting TKE was phase-averaged across all available cycles to observe persistent regions of unsteadiness. As seen in figure 3.11, the main regions of high TKE generation, at the interface of the two inlet flows and at the heel of the anastomosis, are captured in both Stereo-PIV and Tomo-PIV techniques. The high TKE region in the centre of the outlet vein is of higher values and has a sharper drop-off in the stereo-PIV derived flow field. This is owed to the lower amount of cycles available

for phase-averaging for the Stereo-PIV measurement. A larger spatial extent of high TKE at the interface of the inlet flows for the Tomo-PIV flow field at both time-points could be caused by the transient effects of the slight variations in the two inlet profiles. The volumetric averaging taking place in the Tomographic PIV correlation procedure could capture additional large in-plane disturbances leading to the higher TKE . Additionally, the relatively larger noise at the bounds of the illuminated volume contributed to the elevated TKE value at the inlet flow interface.

Although the Tomo-PIV flow field replicates the high TKE regions to that of the Stereo-PIV flow field, a latent non-zero level of TKE is noted particularly in the Tomo-PIV flow field, even in regions where the flow is expected to be undisturbed such as in the proximal artery inlet. The elevated levels of low TKE could be attributed to the overall sensitivity of the volumetric flow measurement technique to noise flow. Furthermore, the disturbances conveyed across from the multi-element tubing network although noted to be minimal (with standard deviations of approximately 4.79% and 2.07% of the proximal and distal artery inlets, respectively) could contribute to the elevated levels of TKE at the inlet.

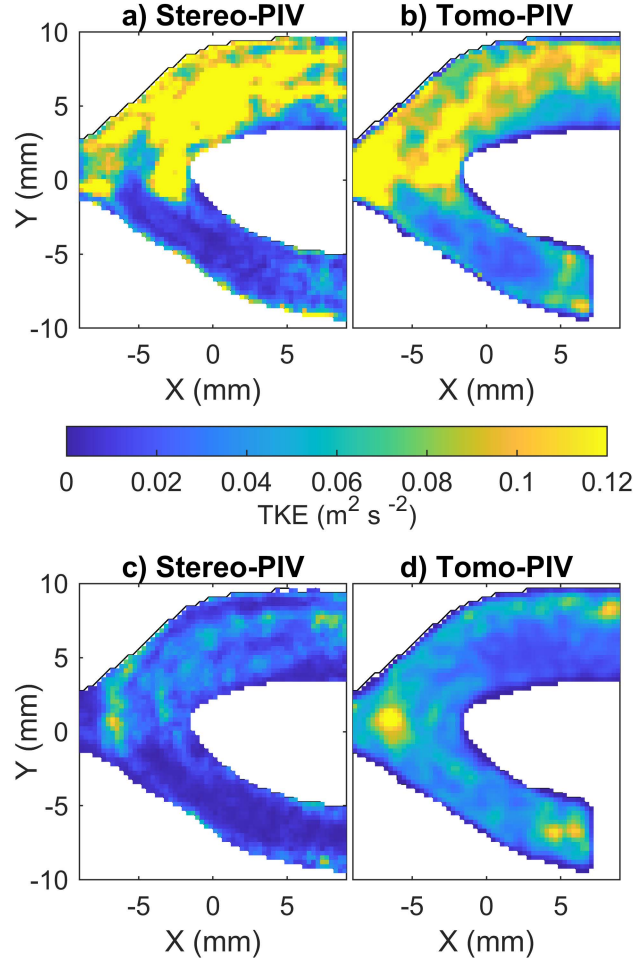


Figure 3.11: Comparison of the turbulent kinetic energy (TKE) between the Stereo-PIV measurement and the Tomo-PIV measurement. The TKE has been represented at a high-flow decelerating time-point and a low-flow accelerating time-point as seen in the inset waveform images on the right.

Chapter 4

Flow modelling of the stented AVF¹

In this chapter, the procedure followed to recreate the stent features within the AVF is detailed. Subsequently, the methodology followed to discretize both the stented and the stent-absent geometries is outlined along with other simulation settings required to conduct the Reynolds Averaged Navier-Stokes simulations and Large Eddy simulations. Accordingly, this chapter aims to set the stage for stented CFD studies in the AVF in order to understand the flow changes caused by this stenting mechanism that has been found to be clinically successful.

¹This chapter contains work that has in part been published in the *Proceedings of the 22nd Australasian Fluid Mechanics Conference*, 2020:

A numerical investigation of a stented arteriovenous fistula

Sanjiv Gunasekera, Olivia Ng, Shannon Thomas, Ramon Varcoe, Charitha de Silva, Tracie Barber

4.1 Geometry preparation

The initial ultrasound scans could not be used to segment the stent due to the presence of excessive artefacts in the scans. Therefore the steps outlined in figure 4.1 were followed to obtain the stent geometry within the patient-specific AVF domain.

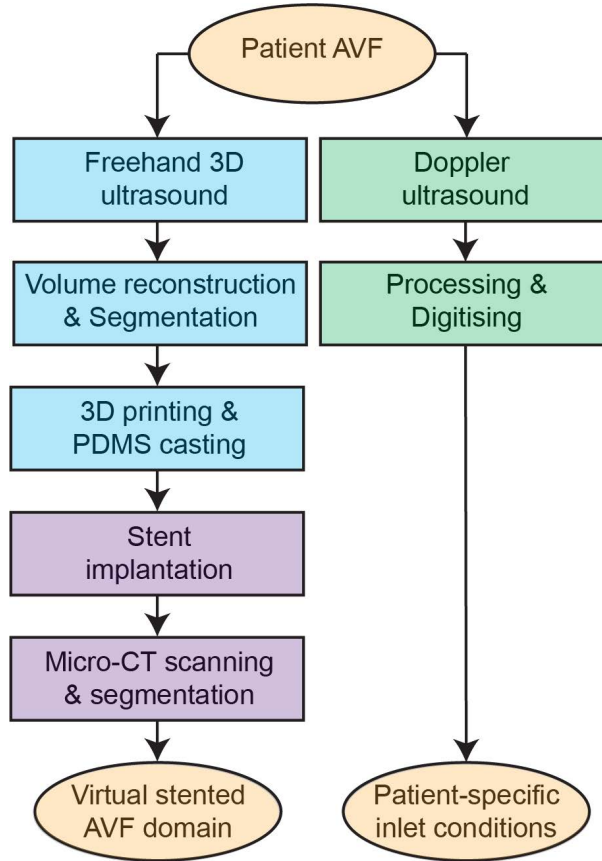


Figure 4.1: The sequence of steps followed to setup the domain and boundary conditions for the Large Eddy Simulations.

The AVF vessel geometry that was segmented, as detailed in section 3.1.3, was 3D printed using an Ultimaker 3 (Ultimaker BV) with a PVA filament. A polydimethylsiloxane (PDMS) model of the geometry was fabricated by casting the Sylgard 184 (Dow Inc.) silicone around the 3D printed model, using an elastomer to curing agent ratio of 22.5:1 to make the silicone model more elastic. The elasticity of the model allowed the stent to embed in the walls. As before, the PVA 3D print was dissolved by flushing the model with

water to create a phantom model of the patient-specific AVF vessels.

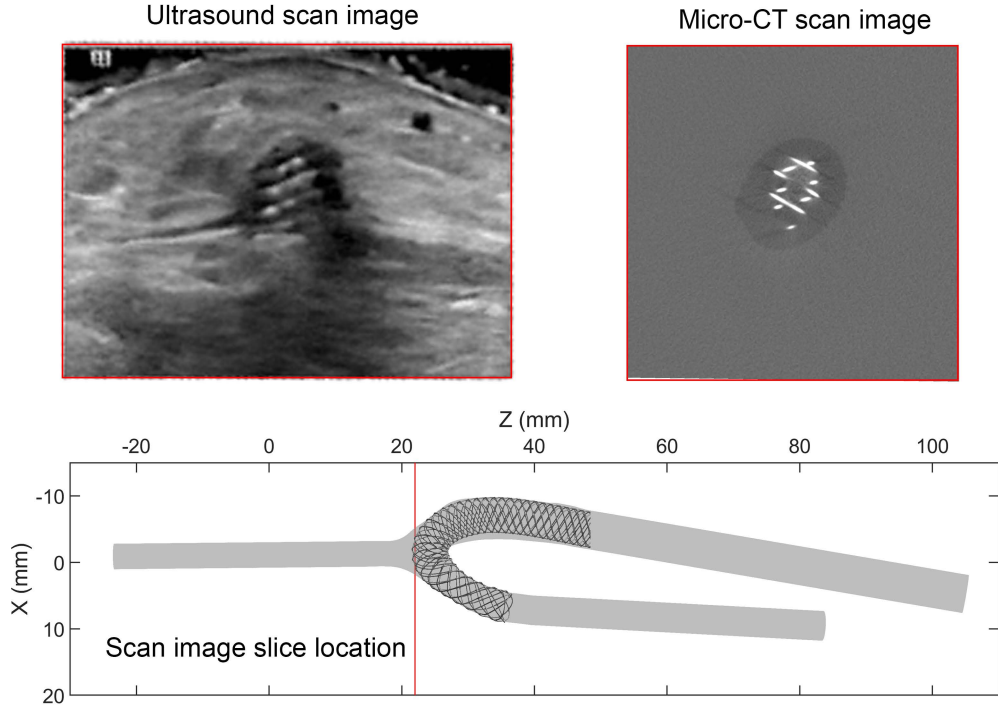


Figure 4.2: Comparison of a scan image of the stented patient AVF obtained using B-mode ultrasound against a scan image of the stented silicone AVF model obtained using ultra-focus micro-CT.

An Abbott Vascular Supera stent, the same size of which was implanted in the patient's AVF (5 mm diameter \times 60 mm length), was deployed (by a vascular surgeon) into the PDMS model. The patient scans were utilised to assess whether the placement of the stent along the vessels in the PDMS model approximately matched the corresponding location of the stent along the vessels of the patient AVF. The initial ultrasound scans could not be used to segment the stent due to the presence of excessive artefacts in the scans and the lack of resolution of the scans to pick up the detail of the stent as illustrated in figure 4.2. To obtain a precise rendering of the stented AVF model, a micro-CT scanner (MILabs U-CT at MWAC, UNSW Sydney) with a step angle of 0.25° , was used to obtain an ultra-focus scan at an approximate overall resolution of $40\ \mu\text{m}$. A comparison of approximately co-located scan slices from the two scanning modalities (ultrasound and micro-CT) in figure 4.2 illustrates the superiority of the micro-CT scan when imaging medical devices.

The resulting high-resolution scan volume was segmented to generate an STL of the stent geometry and the segmentation of the vessel geometry was repeated to locate the AVF vessels in the same local coordinate system of the stent STL as shown in figure 4.3.

The stent and vessel geometries were smoothed using several iterations of a Gaussian smoothing algorithm. To ensure the stent strut diameter was equivalent to $152\ \mu\text{m}$ (the physical stent strut diameter), sections of the segmented stent radius were measured using MATLAB (Mathworks Inc.) by calculating the distance between the stent strut centerline and the closest STL surface elements. This method was used after each smoothing iteration to ensure an appropriate level of surface smoothness was achieved whilst avoiding overly shrinking the stent STL.

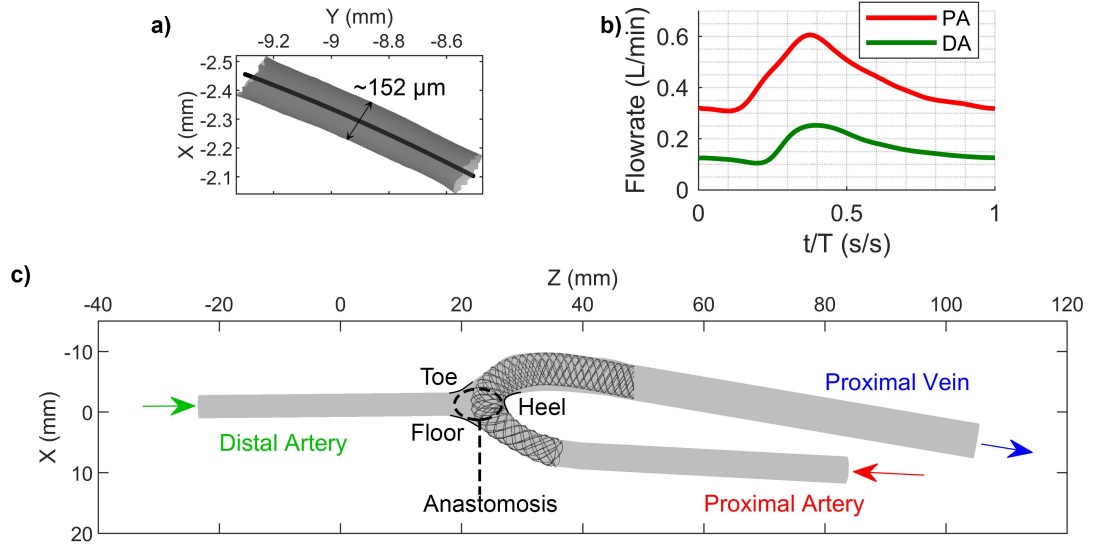


Figure 4.3: **a)** A segment of a stent strut with the centerline imposed across the strut. **b)** The physiological inlet flow waveforms imposed on the proximal artery (red) and distal artery boundaries (green). **c)** The AVF geometry with the stent implantation and annotations of important regions.

4.2 CFD domain settings

To obtain time-averaged velocity and wall shear stress quantities, the incompressible Reynolds-Averaged Navier-Stokes (RANS) equations, composed of the equations for con-

tinuity and conservation of momentum shown below in equations 4.1 and 4.2, were solved using the Fluent (version 2020 R2, ANSYS Inc.) software package.

$$\nabla \cdot \bar{U} = 0 \quad (4.1)$$

$$\rho \left(\frac{d\bar{U}}{dt} + (\bar{U} \cdot \nabla) \bar{U} \right) = -\nabla \bar{P} + \mu \nabla^2 \bar{U} - \nabla \cdot \tau' \quad (4.2)$$

The mean velocity vector, mean pressure, density, dynamic viscosity and Reynolds stresses are denoted by \bar{U} , \bar{P} , ρ , μ and τ' in the above equations. To close the equations, the values for the Reynolds stress are modelled using an appropriate turbulence model.

The pressure and velocity variables were solved using the pressure-based SIMPLE algorithm. A second order upwind scheme was used for the spatial discretization of pressure and momentum quantities while a second order implicit scheme was used for temporal discretization.

Although the Reynolds numbers (Re) of the venous outflow of the AVFs ranged from 100 to 1000, numerous studies have determined the presence of transitional flow within the AVF (Bozzetto et al., 2016; Fulker et al., 2018; Loth et al., 2008). The tortuous nature of the vessel geometries, the imposed pulsatile boundary conditions and the confluence of inlet flow from opposite directions at the anastomosis lead to a fluid domain that is more susceptible to transition to turbulence when compared to the straight pipe experiments from which the critical Re of 2000 has been derived. Therefore, to model the turbulent characteristics of the flow, the $k - \omega$ *SST* turbulence model, which is a combination of the $k - \omega$ and the $k - \epsilon$ models (Menter, 1994) built upon the Boussinesq assumption (Wilcox et al., 1998), was implemented. The standard $k - \omega$ model is known to perform well in the near-wall region of Low-Re flow while also being robust in handling the boundary layer without a damping function. However, its sensitivities in the free-stream flow make the standard $k - \epsilon$ model a better choice in this region. The $k - \omega$ *SST* combines both of these models using a blending function which allows the application of the $k - \omega$

model in the near-wall region while transitioning to the $k - \epsilon$ model in the free-stream region. The refinement of the turbulent shear stress calculation towards maintaining the assumption of proportionality of the turbulent shear stress with turbulent kinetic energy (via another blending function) advanced the performance of the two-equation model in adverse pressure gradients. Furthermore, comparison of this model's performance with a stenosed carotid bifurcation with inlet flow varying from Re from 200 to 1000 showed good agreement to the experimental findings (Tan et al., 2008).

The fluid region of the AVF geometry was discretized by creating a tetrahedral mesh in the bulk flow and boundary layer regions using ICEM CFD (ANSYS Inc.). Tetrahedral elements were used, even in the boundary layer region, because of the complexity of the geometry which incorporated the small intertwining surface of the stent within the relatively larger vessel surface. Approximately 90% of the elements were of high aspect ratio and low skew (further detail of the quality assessment is provided in appendix A). The grid convergence index (GCI) (Celik et al., 2008) was calculated by using the average of the velocity magnitude across a vessel lumen slice in the vein. 17 slices were made and the calculations were conducted for values obtained at the peak inlet flow rate timepoint. Multiple cycles of the stent-absent case were run to obtain phase-averaged velocity magnitude values at the peak inlet flow rate timepoint. This ensured that any cycle-to-cycle variations did not affect the GCI calculations. The multi-cycle simulation was carried out for stent-absent domains with coarser and finer meshes as well that were created using the same meshing strategy but adjusting the parameters to yield larger and smaller overall edge lengths respectively. The average GCI values were 0.016% and 1.95% for the stented and stent-absent geometries, respectively. Additionally, circumferentially averaged wall shear stress (WSS) values along the vein were compared against those from the coarse and fine mesh as shown in figure 4.4. The WSS values were largely seen to match the values of the fine mesh in both geometries with an average relative error of 1.86% and 1.63% for the stented and stent-absent geometries, respectively. Therefore a sufficient level of spatial discretization was achieved with 19.75 million elements for the stented geometry and 4.89 million elements for the stent-absent geometry.

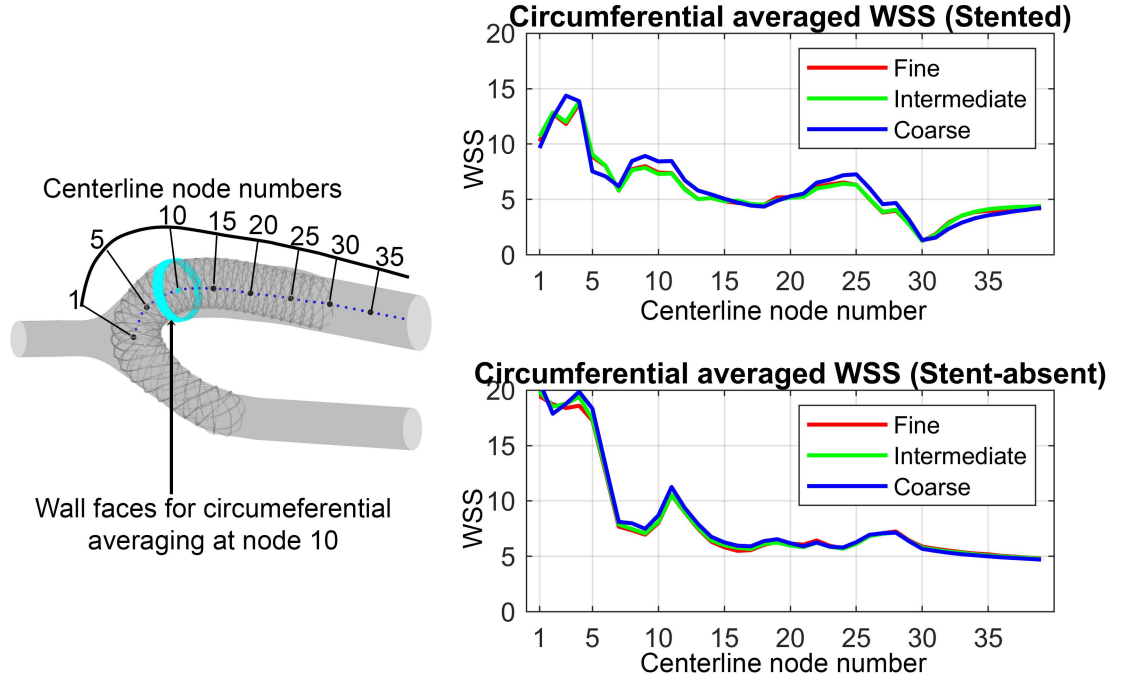


Figure 4.4: Circumferential averaged wall shear stress values along the vein of the stented and stent-absent geometries at the peak inlet flow rate timepoint.

In addition to the ultrasound scans, the flow rates of the feeding vessels of the AVF were also recorded using the Doppler function of the ultrasound machine as previously detailed in section 3.1.4. The recorded flow rates were digitized to use as pulsatile inlet flow waveforms at the proximal artery and the distal artery boundaries of the AVF geometry. A comparison of the inlet boundary conditions of the simulation with those imposed at the inlets of the experimental model has been illustrated in figure 3.5 of chapter 3. The recorded heart rate of the patient was 60 bpm which was matched in the simulations by setting the period of the inlet waveforms to 1 *s*. The proximal vein was maintained as a non-tractive outlet condition with relative pressure held at zero. To ensure the inlet flow waveforms had a developed flow profile, the ends of the vessels were extended by 10 times the diameters of the relevant vessel. The transient simulations were conducted with a fixed time-step of 0.001 *s*. Comparison of the slice-averaged velocity magnitude values between a time-step of 0.001 *s* and 0.0001 *s* showed a difference of 0.0218% and 0.166% for the stented and stent-absent cases, respectively. The difference in the circumferentially

averaged WSS measurements were 1.50% and 1.52%, respectively, therefore the time-step of 0.001 s was deemed suitable for the simulations.

The vessel and stent walls were set up with a no-slip wall condition and without compliance. A comparison between a stationary wall to a compliant wall in AVF flow simulations has shown that the resulting WSS trends remain similar with a general overestimation of the values at regions of low WSS in the case of the stationary wall (McGah et al., 2014). The fluid properties were set to replicate the average blood physical properties with a density of 1060 kg/m^3 . The effect of the non-Newtonian nature of blood, known to be minimal at the high shear rates (Vijayaratnam et al., 2015) encountered in an AVF, was modelled using the Carreau model (Cho and Kensey, 1991) provided in equation 4.3.

$$\mu = \mu_{\infty} + (\mu_0 - \mu_{\infty})[1 + (\lambda\dot{\gamma})^2]^{\frac{n_c-1}{2}} \quad (4.3)$$

The shear rate variable is denoted by $\dot{\gamma}$, and the model parameters: zero-shear rate viscosity (μ_0), infinite-shear rate viscosity (μ_{∞}), characteristic time (λ) and power-law index (n_c) were set to 0.056 $Pa \cdot s$, 0.00345 $Pa \cdot s$, 3.313 s and 0.3568, respectively.

4.3 Adjustments for Large Eddy Simulation

The presence of flow transitioning from the laminar regime, particularly in the deceleration phase of pulsatile flow, within vascular geometries have been noted in direct numerical simulations (DNS) (Valen-Sendstad et al., 2011; Varghese et al., 2007). Therefore, to understand any haemodynamic disturbances within the AVF, a simulation that is able to resolve any turbulence generation is of value. Since obtaining the spatial and temporal resolution to conduct a DNS is highly resource intensive, a Large Eddy Simulation (LES) that resolves a significant portion of the turbulence generation can provide inferences of the behaviour of larger, higher energy containing eddy disturbances while modelling the energy of the eddies smaller than the grid size.

To resolve larger scales while modelling smaller scales, an LES makes use of a spatial filter which results in the filtered Navier-Stokes equations that take a similar shape to equations

4.1 and 4.2 as shown below.

$$\nabla \cdot \tilde{\mathbf{U}} = 0 \quad (4.4)$$

$$\rho \left(\frac{d\tilde{\mathbf{U}}}{dt} + (\tilde{\mathbf{U}} \cdot \nabla) \tilde{\mathbf{U}} \right) = -\nabla \tilde{P} + \mu \nabla^2 \tilde{\mathbf{U}} - \nabla \cdot \tau_{SGS} \quad (4.5)$$

The filtered velocity and pressure variables are denoted by $\tilde{\mathbf{U}}$ and \tilde{P} , respectively. To close the filtered Navier-Stokes equations, values for the subgrid scale turbulent stresses (instead of the Reynolds stresses in the RANS simulations), denoted by τ_{SGS} , are modelled. For the simulations in this thesis, the dynamic Smagorinsky subgrid scale (SGS) model was chosen to capture the lower energy disturbances and contribute to the dissipation of turbulent energy. The original Smagorinsky SGS model is based on the assumption that small scale turbulent energy (contained within the grid) is isotropic. The Smagorinsky constant (C_S) is used to estimate the subgrid energy which is proportional to the grid length scale. Therefore the model had a tendency to be overly dissipative at regions close to the wall. Improvements of the model, such as the use of a mixing length (instead of the grid length alone) and a dynamically varying C_S value based on an additional filter length, twice the size of the grid length, has made the model more robust in applications of wall bounded flow (Germano et al., 1991; Lilly, 1992). However, the subgrid viscosity does not go to zero in laminar shear flow regions, thereby still maintaining the behaviour of being overly dissipative in regions of separating flow (Nicoud and Ducros, 1999; Nicoud et al., 2011). Despite this drawback of the SGS model, studies of stenotic flow have shown that the model replicates the mean flow and turbulent statistics well when compared with results from DNS (Jabir and Lal, 2016; Pal et al., 2014; Tan et al., 2011). Similarly, a patient-specific study of a stenosed region in a carotid artery demonstrated that LES with the dynamic Smagorinsky model was able to replicate the mean flow and turbulent features with pulsatile inlet conditions (Mancini et al., 2019), thereby showing the applicability of the SGS model in the current AVF study as well.

The fluid domain was initialised using the $k - \omega$ *SST* turbulence model based simulation

that was detailed in section 4.2. The mesh was further refined using a mesh adaption algorithm which refined elements, with a value of the gradient of subgrid dynamic viscosity, greater than a stipulated value. The chosen value was altered such that 1 – 5% of the total cells were marked at each mesh adaption step. Basing the mesh adaption on the gradient of the subgrid viscosity lead to marking regions where sudden changes in dissipative scales were present (such as in the anastomotic region and the along the vein) thereby providing the opportunity to further resolve these regions to avoid overly dissipating the turbulence generated in important regions. Four mesh adaption steps were conducted (two each at the maximum and minimum point of the cycle) to refine a sufficient amount of elements to capture behaviour across the cycle. Application of this targetted mesh refinement methodology resulted in meshes composed of 24.60 million (increasing from 19.75 million) and 6.91 million (increasing from 4.89 million) elements for the stented and stent-absent cases, respectively (illustrated in figure 4.5), with much of the refinement taking place at areas of concern. The average cell edge length on the stent wall was $32.5 \mu m$ which resulted in approximately 17 cells back-to-back across the circumference of a $152 \mu m$ stent strut. The average cell edge length on the vessel wall was $103 \mu m$ which resulted in approximately 176 cells back-to-back across the circumference of a vessel segment that is $5 mm$ in diameter. Using the stent strut diameter and the average outlet velocity (as the malapposed stent struts faced high velocities), flow with a Reynolds number of 25 would be the maximum faced at the stent struts. The detail of the mesh at the stent wall and vessel wall have been illustrated in figure 4.6.

It is recommended that an LES is capable of resolving 80% of the turbulent kinetic energy (TKE) (Pope, 2001). This requirement was assessed to determine the appropriateness of the level of spatial resolution. The resolved turbulent kinetic energy was calculated using a phase-averaged approach to account for the pulsatile nature of the flow domain. Phase-averaged turbulent kinetic energy, $TKE_{resolved} = \frac{1}{2}(u'^2_x + u'^2_y + u'^2_z)$ was calculated at seven specific time points of the cycle. Here, $u'_x = U_x - \overline{U_x}$, $u'_y = U_y - \overline{U_y}$, $u'_z = U_z - \overline{U_z}$ correspond to the instantaneous velocity fluctuations, where $\overline{U_x}$, $\overline{U_y}$, $\overline{U_z}$ are the phase-averaged velocities. In addition to the maximum and minimum time points, $TKE_{resolved}$ was calculated at two points in the acceleration phase and three points in the deceleration

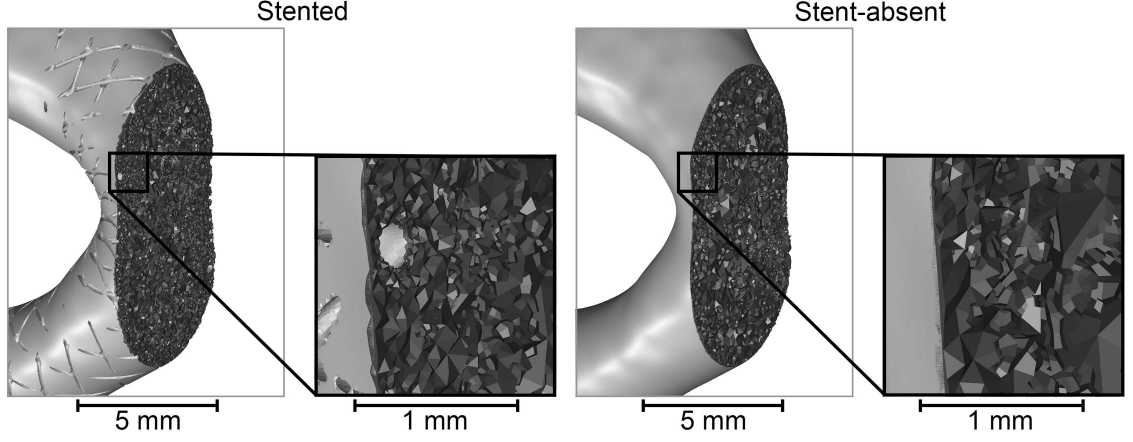


Figure 4.5: The tetrahedral meshes used for both the stented and stent-absent cases. The inset figures give further detail of the mesh elements close to the stent strut and the vessel wall.

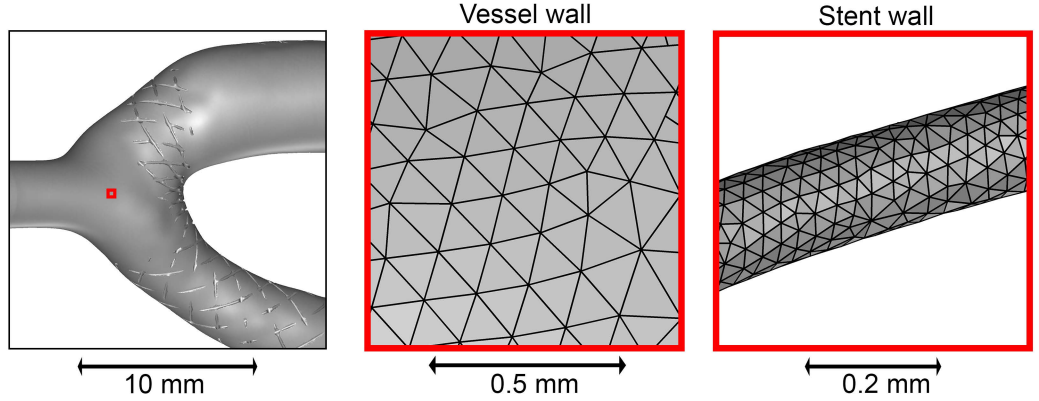


Figure 4.6: Detail of cells at the vessel and stent wall boundaries near the anastomosis.

phase. This approach was necessary as calculating $TKE_{resolved}$ for all time points would have overwhelmed the storage resources due to the small time-step and grid size. The $TKE_{resolved}$ was phase-averaged over 12 cycles to ensure that the quantity was converged as shown in figure 4.7. A user-defined function was employed to update the phase-averaged quantities on each passing cycle in an efficient manner. The unresolved turbulent kinetic energy (contained within the subgrid) was estimated using the following equations,

$$TKE_{unresolved} = \frac{(C_S \Delta S)^2}{0.3} \quad (4.6)$$

$$\Delta = (6\sqrt{2}(\text{cell-volume}))^{1/3} \quad (4.7)$$

$$\text{ratio of } TKE_{\text{resolved}} = \frac{TKE_{\text{resolved}}}{TKE_{\text{resolved}} + TKE_{\text{unresolved}}} \quad (4.8)$$

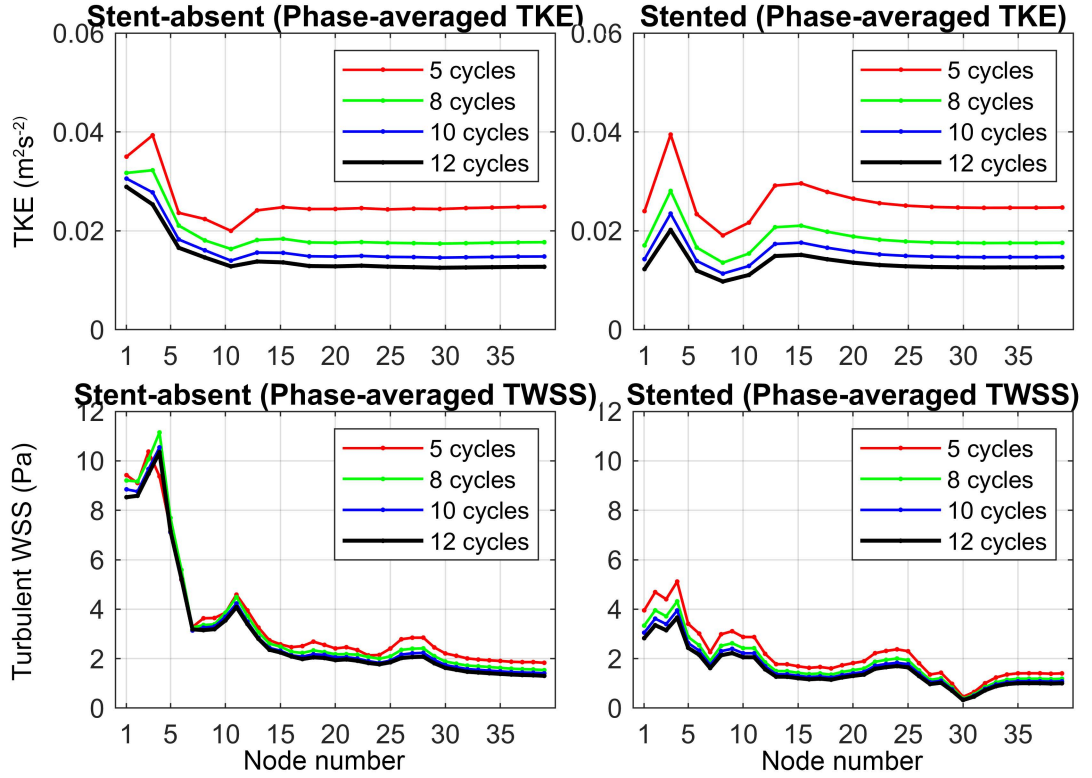


Figure 4.7: Convergence of the phase-averaged quantities: Turbulent Kinetic Energy and Turbulent Wall Shear Stress, for both stented and stent-absent model simulations.

where Δ is the subgrid length of the tetrahedral elements and S is the strain rate magnitude as calculated within the solver (Menter, 2012). The average ratio of TKE_{resolved} across the domain, calculated at the maximum inlet flow time point, was 96.8% and 97.03% for the stented and stent-absent models, respectively, thereby showing that the spatial resolution of the mesh was largely sufficient. The average y^+ from the vessel wall across the domain at the maximum time point was 0.51 and 0.45 for the stented and stent-absent cases. Therefore, an overwhelming majority of the near-wall cells were placed well within the viscous sub-layer, thereby accurately calculating the wall shear stresses.

With the increased resolution of the spatial discretization, the temporal discretization requires refinement as well to maintain the Courant-Friedrich-Lewy (CFL) (defined in equation 4.9) below 1, such that the distance travelled by the flow within a time-step, remains within the bounds of the cell (Courant et al., 1967).

$$CFL = \frac{U\Delta t}{\Delta x} \quad (4.9)$$

The velocity magnitude, time-step and grid length are denoted by U , Δt and Δx , respectively. Although the Fluent solver employs an implicit solver (which remains stable for Courant numbers larger than 1), it is recommended that this aforementioned condition is maintained to accurately resolve the LES temporally (Menter, 2012). After decreasing the time-step to 0.0002 s (from 0.001 s), the average Courant numbers across the domain at the maximum inlet time points were 0.45 and 0.51 for the stented and stent-absent models, respectively.

In a similar fashion to the calculation of phase-averaged TKE, the phase-averaged turbulent fluctuations of WSS were also calculated at the same 7 time points in the cycle. The fluctuations for each component of the WSS vector, $wss'_x = WSS_x - \overline{WSS_x}$, $wss'_y = WSS_y - \overline{WSS_y}$, $wss'_z = WSS_z - \overline{WSS_z}$. The magnitude of the WSS fluctuations were subsequently calculated, $TWSS = \sqrt{(wss'^2_x + wss'^2_y + wss'^2_z)}$, and shall be referred to as Turbulent Wall Shear Stress $TWSS$. Figure 4.7 shows that the circumferentially averaged $TWSS$ values sufficiently converges after 12 cycles.

4.4 Comparison of the flow field across the different measurement methodologies

As detailed in sections 4.2 and 4.3, both RANS simulations and LES were conducted to obtain understanding of the temporally averaged quantities and flow disturbances in the vasculature. To make a comparison of these methodologies with the Tomo-PIV measuring

technique, additional simulations were conducted with matching boundary conditions and fluid properties.

The velocity magnitude at the maximum and minimum time-point were compared using contour plots on the central XY -plane and a sequence of YZ -planes as shown in figures 4.8 and 4.9. Care was taken to rotate and translate the CFD geometry such that it is aligned well with the Tomo-PIV field (as shown in 3.9 in Chapter 3). All methodologies show a low velocity zone in the heel region of the anastomosis that extends along the vein. However, the RANS model shows that the lower velocity magnitude zone (below 0.5 m s^{-1}) extends well beyond the near wall region and towards the center of the vessel particularly at the maximum inlet flow time-point. The results from the LES however, show that the same region in the vein is of slightly higher velocity magnitude similar to the behaviour seen in the Tomo-PIV field. The characteristics of the low velocity magnitude zone were more similar across the methodologies at the minimum inlet flow time-point.

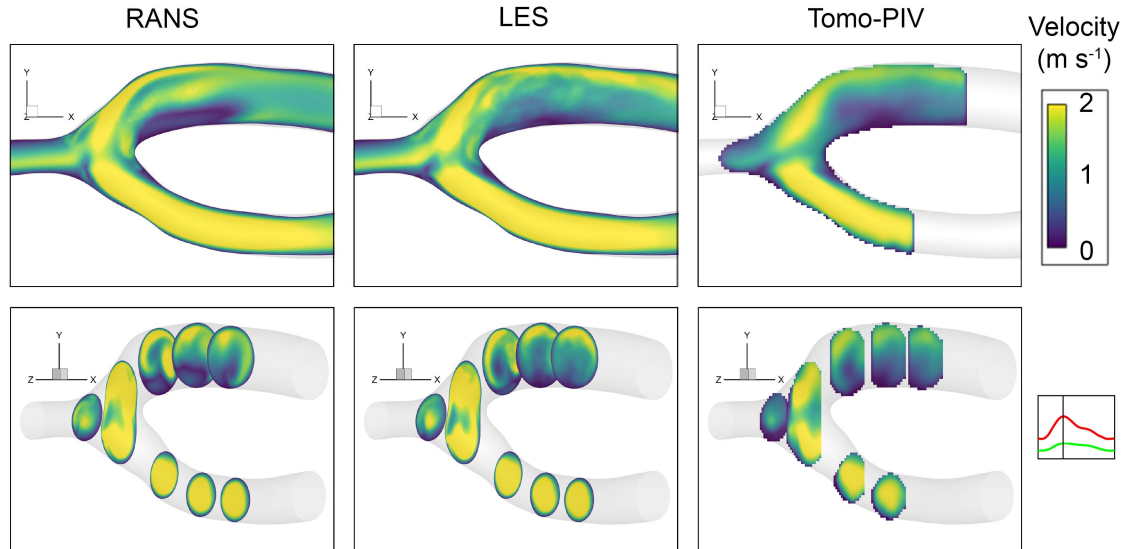


Figure 4.8: Comparison of velocity magnitude contours across Reynolds-Averaged Navier-Stokes (RANS) simulations, Large Eddy Simulations (LES) and Tomographic Particle Image Velocimetry (Tomo-PIV) measurements at the maximum time-point of the inlet flow.

At the maximum inlet time-point, the high velocity portion of the flow moving across the vein is initially seen to hug the upper wall of the vein, however, the RANS captures a

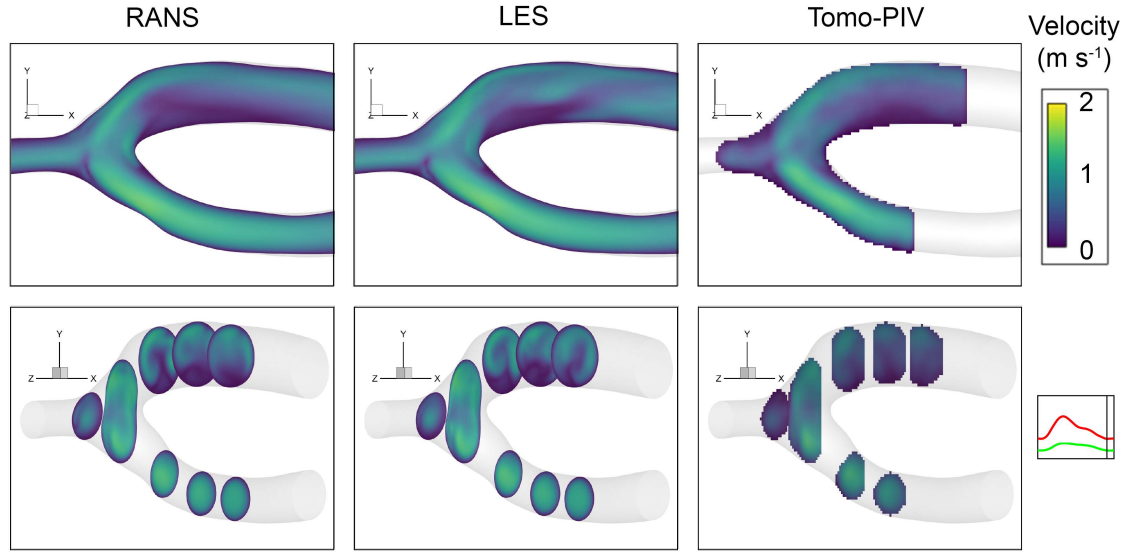


Figure 4.9: Comparison of velocity magnitude contours across Reynolds-Averaged Navier-Stokes (RANS) simulations, Large Eddy Simulations (LES) and Tomographic Particle Image Velocimetry (Tomo-PIV) measurements at the minimum time-point of the inlet flow.

secondary high velocity region in the vein. This feature possibly arises from the momentum of the distal artery inlet. The detail of the velocity magnitude values across the vessel depicted in figure 4.10, reveals that the LES also captures a secondary high velocity region (at rake 3) which is lower in magnitude than that of the RANS flow field. A key similarity is the angle of the interface of the two inlet flow at the floor of the anastomosis in the LES and Tomo-PIV results, suggesting that there is a combination of the inlet flow which is then transported to the vein. However, the angle of the interface in the RANS suggests that the proximal artery interface dominates, leading to the momentum of the distal artery to create another secondary flow transport across to the vein. The interface is a sharp region which faces a large pressure gradient and this might be a reason for the LES to be able to capture this complex region in a similar manner to the Tomo-PIV as opposed to the RANS. Yet again, the characteristics at the interface of the two inlet flow are more similar across the methodologies at the minimum inlet time-point.

Another feature that can be seen in the contour plots of figures 4.8 and 4.9 is that the velocity gradient at the near-wall region in the inlet proximal artery is much sharper in the

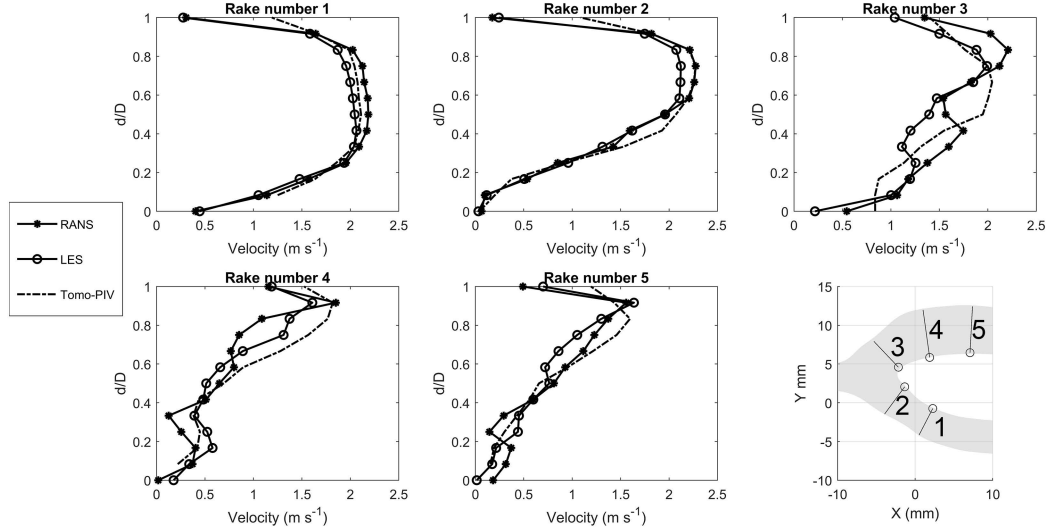


Figure 4.10: Comparison of velocity magnitude across Reynolds-Averaged Navier-Stokes (RANS) simulations, Large Eddy Simulations (LES) and Tomographic Particle Image Velocimetry (Tomo-PIV) measurements using rakes across the vessel at the maximum time-point. The rake numbers correspond to the locations denoted in the bottom left sub-figure. The circle at the end of each rake denotes the starting point of each rake ($d/D = 0$).

CFD results as opposed to the results from the Tomo-PIV. The plots in figure 4.10 reveal this difference within the outlet vein as well where there is a larger gradient from the high velocity regions to the wall in rakes 3, 4, and 5. However, this is to be expected as the PIV procedure involves averaging over an interrogation volume size of $0.27 \times 0.27 \times 0.27 \text{ mm}^3$ as opposed to the average CFD near-wall grid length of 0.025 mm (in the stent-absent model). The low resolution of the PIV procedure would hinder derivative calculations (especially with limits towards the wall for WSS) making it less suitable for WSS measurements compared to the numerical methods that have high near-wall resolution (as detailed in section 4.3).

In addition to the velocity comparison, the *TKE* (modelled in the RANS and resolved in the LES) were compared between the simulations and the experimental results using contour plots at the maximum and minimum time-point of the inlet cycle as seen in figures 4.11 and 4.12. All methodologies show three general locations where *TKE* is generated, which are the floor region near the distal artery, the toe and the heel of the anastomosis.

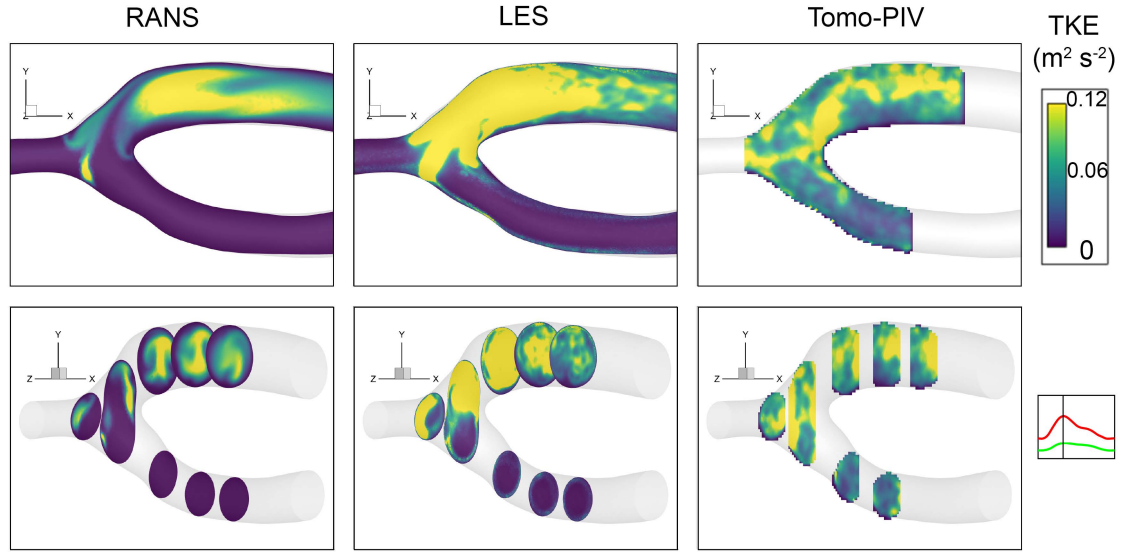


Figure 4.11: Comparison of turbulent kinetic energy contours across Reynolds-Averaged Navier-Stokes (RANS) simulations, Large Eddy Simulations (LES) and Tomographic Particle Image Velocimetry (Tomo-PIV) measurements at the maximum time-point of the inlet flow.

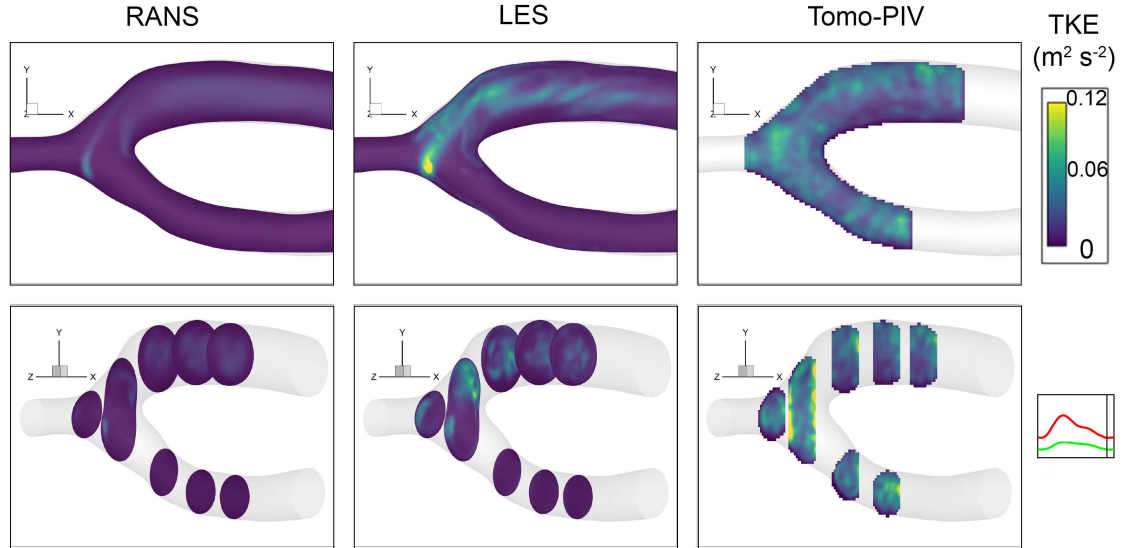


Figure 4.12: Comparison of turbulent kinetic energy contours across Reynolds-Averaged Navier-Stokes (RANS) simulations, Large Eddy Simulations (LES) and Tomographic Particle Image Velocimetry (Tomo-PIV) measurements at the minimum time-point of the inlet flow.

However, the LES seems to capture a much broader spatial extent of high TKE when compared with the other methodologies. All the results show the transport of the TKE along the vein but the experimental results particularly show that the high TKE flow is transported away from the lower vein wall (close to the heel of the anastomosis). The high levels of TKE generated in the LES dissipate much quicker than in the experiment, however this is to be expected with a Smagorinsky-Lilly SGS model (as detailed in section 4.3). The contour plots of the TKE at the minimum time-point show generation at the same three regions as stated before; however, the level of TKE is significantly lower in the RANS results. At both time-points, non-zero TKE has been noted in the Tomo-PIV derived field which has been attributed to the noise flow captured in this volumetric measurement technique (as detailed in section 3.4.2 in chapter 3).

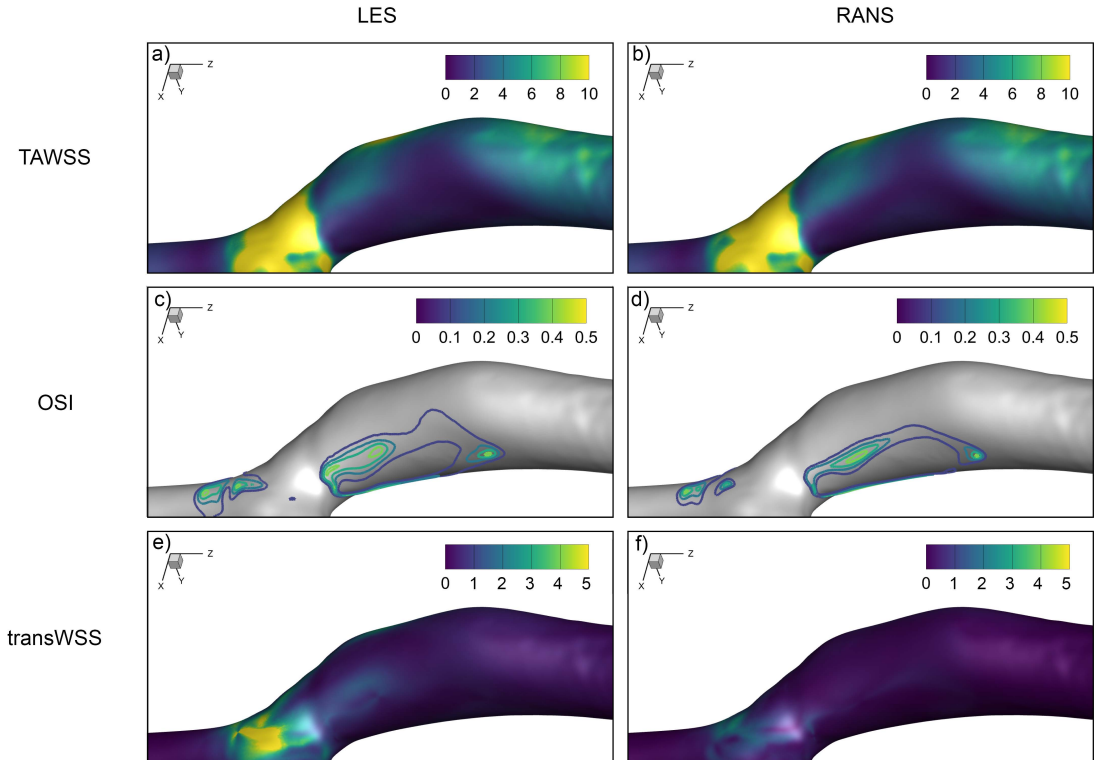


Figure 4.13: Comparison of TAWSS, OSI and transWSS from across the vessel wall of the stent-absent AVF case using LES and RANS simulations.

Finally the cycle-averaged WSS metrics: TAWSS, OSI, and transWSS, calculated using both numerical strategies across the vessel wall of the stent-absent case, were compared in figure 4.13. As expected, the distribution of the time-averaged WSS obtained from the LES was very similar to the distribution from the RANS methodology. Similarly, the large ring of OSI at the heel of the anastomosis is equivalent in spatial extent across both methodologies. The LES tends to capture unstructured behaviour at the downstream end of the OSI ring. The OSI features at the toe of the anastomosis are also equivalent with the behaviour spread across a slightly larger space in the LES derived contours. transWSS attempts to capture multi-directional intra-cycle variations in the WSS vector, hence leading to larger values measured via the LES in the anastomosis. The transWSS distribution from the RANS simulation is located in similar regions to that of the LES but is far more understated in magnitude.

In summary, the RANS simulations have matched other methodologies in time-averaged quantities such as velocity magnitude and TAWSS, however disparities were noted at locations where complex behaviour within the flow took place. The unsteady behaviour of the velocity field was better captured with the LES, although this methodology was subject to larger dissipation of TKE . Even though regions of high TKE in the LES were reflected in the Tomo-PIV measurement, a foreseeable increase in noise was noted in the experimental measurement, thereby showing the value of complementing the experimental volumetric flow measurement with the high-resolution numerical simulation.

Chapter 5

Impact of the stent implantation on the bulk flow¹

In this chapter, a controlled study of the effects of the stent implantation on the bulk flow of the AVF has been detailed. The study isolates the effects of the stent by conducting simulations on the same geometry with and without the stent implantation. Quantification of the ratio of flow held within the stent compared to flow across the whole vessel yielded the finding of funnelling flow through the stent lumen in malapposed regions of the AVF. This behaviour, in turn, is seen to affect the wall shear stress distribution across the cardiac cycle.

¹This chapter contains work that has in part been published in the *International Journal of Heat and Fluid Flow*, Vol. 92, 2021:

Impact of juxta-anastomotic stent implantation on the haemodynamics within a single representative patient AVF

Sanjiv Gunasekera, Olivia Ng, Shannon Thomas, Ramon Varcoc, Charitha de Silva, Tracie Barber

5.1 Introduction

Recent investigations of the clinical impact of stent implantation (Huang et al., 2020; Thomas et al., 2019) have shown benefits of the procedure despite the occurrence of malapposition of the device. However, malapposition in other regions of the vascular network is known to be a predictor for stent thrombogenicity (Cook et al., 2007; Van Werkum et al., 2009). *In silico* assessments of flow in idealised coronary (Beier et al., 2016; Chen et al., 2017; Poon et al., 2014) and patient-specific carotid arteries have shown that incomplete stent apposition leads to a haemodynamic environment composed of disturbed flow, resulting in atheroprone WSS behaviour. Conversely, the significant increase in space between the malapposed stent and the vessel wall has also resulted in a decrease in the heterogeneity of the WSS levels across the vessel (Chen et al., 2009). A controlled study of stent malapposition in a patient-specific coronary artery revealed a lower percentage area of adverse WSS in the malapposed case, with the differences in other WSS metrics being minimal (Wei et al., 2021). This finding suggests that the malapposition might not be the initiator of stent thrombogenicity. In fact, the lack of contact between the stent and the vessel wall provide a means to treat cerebral aneurysms by harnessing the flow diverting ability of the stent (Wang et al., 2016), thereby also eluding to another potential flow mechanism that could affect malapposed stented vessels. Accordingly, this chapter details the study of stent malapposition in a patient-specific arteriovenous fistula and by examining its impact on the funnelling (or diversion) of the bulk flow and the subsequent effects on the WSS.

5.2 Study-specific geometry preparation

As detailed in section 4.1, a virtual stent model was recreated by segmenting a micro-CT scan of a stent-implanted PDMS model of an AVF. Simultaneously, the AVF geometry was also segmented in the same 3D coordinate space. It was apparent that there was a level of malapposition of the stent in the venous segment close to the anastomosis. This

occurrence has also been observed in clinical cases where the vein is of a large diameter (Thomas et al., 2019), as can be seen in the example angiogram shown in figure 1.5.

To isolate the impact of the stent, two cases were used, with and without the stent present for the simulations as depicted in figure 5.1. The stent implanted vessel geometry without the physical stent present is referred to as the ‘stent-absent’ case whereas the geometry with the stent present will be referred to as the ‘stented’ case.

To assist with visualising the flow within the vein of the AVF, cross-sections of the vessel lumen were created by extracting planes perpendicular to the centerline such that the slices conformed with the tortuous nature of the patient-specific geometry. The vessel lumen slices were spaced 5 mm away from adjacent slices and located in the region where the malapposition was highest. To understand the effect of the malapposition of the stent in the vein, additional slices were manually created to represent the subspace of the slices that were encompassed by the stent, referred to as the stent lumen slices. Figure 5.1 illustrates the two types of lumen slices and their locations in both geometries.

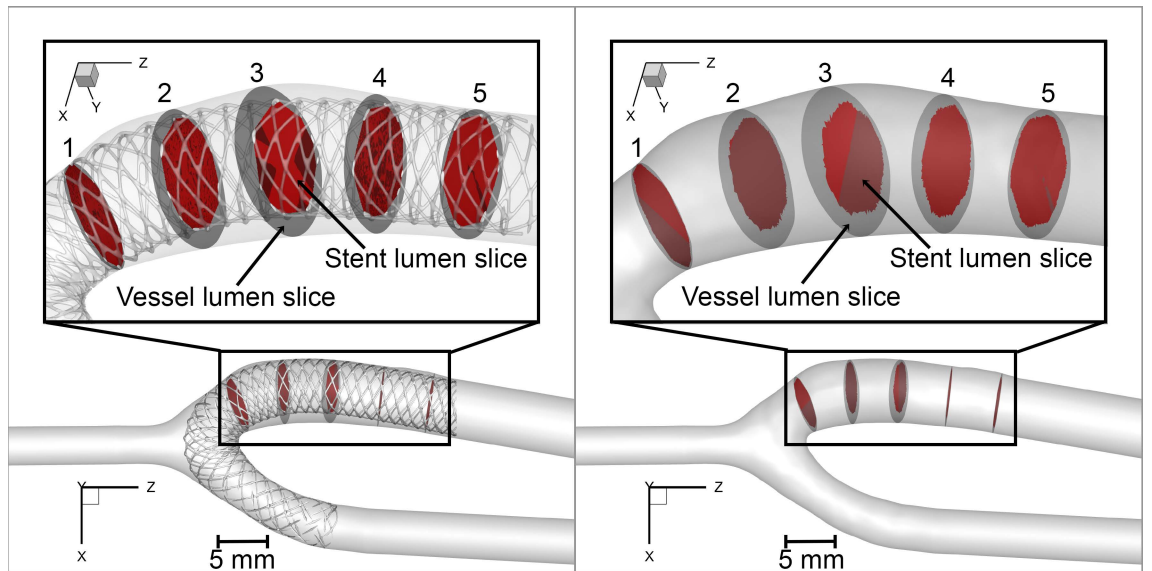


Figure 5.1: Stented (left) and stent-absent (right) cases with lumen slice locations. The stent lumen slices have been shaded in red while the vessel lumen slices have been shaded in dark grey.

5.3 Flow features within the vein

Each simulation was run for four cycles and the flow features were analysed using the data from the final cycle. Velocity streamlines coloured with the velocity magnitude were plotted at the maximum and minimum points of the inlet flow profile for both the stented and stent-absent geometries, and is shown in figure 5.2. In both geometries and at both time points, a central region of high-speed flow enveloped by a spiralling region of low-speed flow is observed. The results reveal that the initial spiralling streamlines in the stented geometry realigns with the outflow direction, closer to the anastomosis than in the stent-absent geometry. The delay in reattachment could be related to the extent of the recirculating region seen in the vein close to the heel of the anastomosis. Specifically, the recirculating flow in the stent-absent geometry at both time points are much larger compared to those in the stented geometry. The Tomo-PIV study of the stent-absent geometry in this thesis (further detailed in section 6.1 in chapter 6) also showed similar behaviour where the flow in the anastomosis was enveloped by spiralling flow (Gunasekera et al., 2020). A recirculation zone was also noted in the lower region of the vein, further aligning with the observations in the Tomo-PIV study.

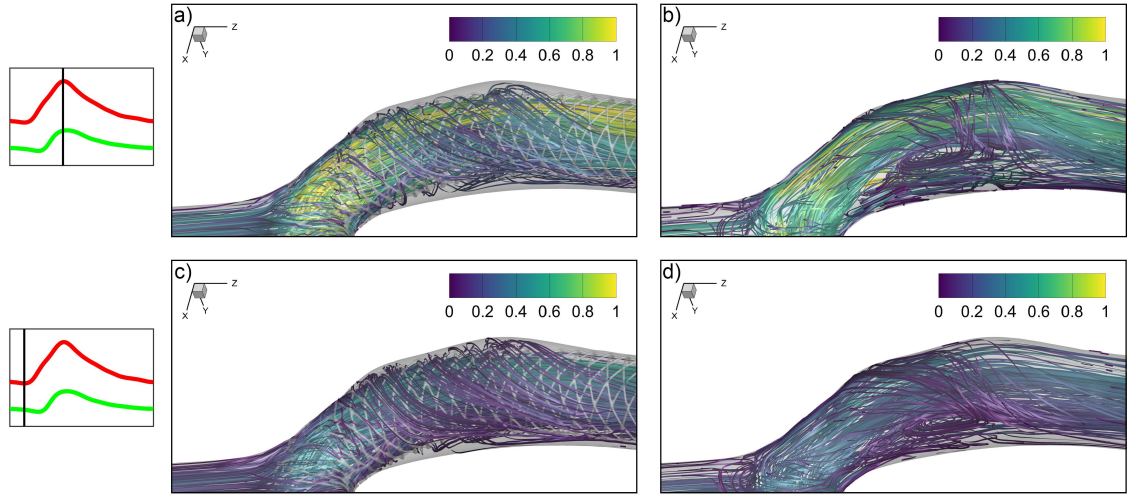


Figure 5.2: Velocity streamlines coloured with the velocity magnitude at the maximum (subfigures **a**) and **b**) and minimum points (subfigures **c**) and **d**) of the inlet flow profile. The subfigures **a**) and **c**) are of the stented geometry while the subfigures **b**) and **d**) are of the stent-absent geometry.

Contour plots of the velocity magnitude are plotted on the vessel lumen slices to better observe the central flow features of the vein as illustrated in figure 5.3. The high velocity is distributed in the upper outer regions of the slices in both geometries. A low velocity region is seen at the lower border of the vessel lumen slices. Much like the observations made with the streamlines, the low velocity region is of a larger span in the stent-absent geometry where it reaches the fourth slice, whereas the region is not visible beyond the second slice in the stented geometry. The low velocity region coincides with the region of recirculating flow in the stent-absent geometry.

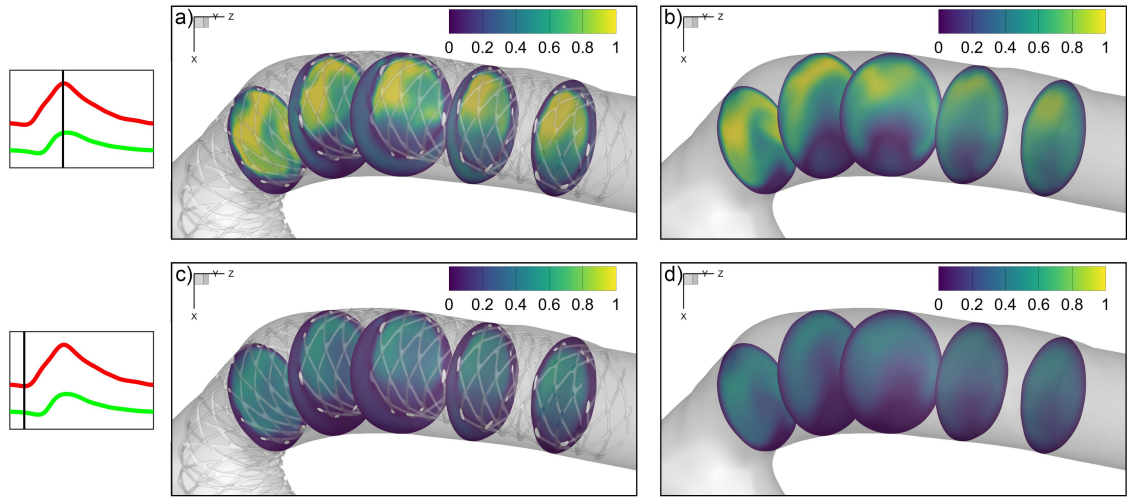


Figure 5.3: Velocity magnitude contours at the 5 vessel lumen slices at the maximum (subfigures **a**) and **b**) and minimum points (subfigures **c**) and **d**) of the inlet flow profile. The subfigures **a**) and **c**) are of the stented geometry while the subfigures **b**) and **d**) are of the stent-absent geometry.

The counter-rotating spirals of flow are created in the anastomosis as the flow is forced through the curved juxta-anastomotic vein. The flow in the outer regions of the curve accelerate in order to traverse across the curve which results in the lower velocity observed at the heel. The flow at the outer regions of the curved vessel cross-sections eventually traverse the near wall regions towards the inner edge of the curved vessel resulting in the flow spirals (or helicals). The low velocity region at the heel coincides with the region of recirculating flow in the stent-absent geometry. Previous studies have postulated that low velocity recirculating flow could be related to the onset of vascular disease (Gimbrone Jr

and García-Cardena, 2016; Ishibashi et al., 1995; Remuzzi and Ene-Iordache, 2013).

Another less distinct feature that can be seen in the slices of the stented geometry is the presence of a second low velocity region at the lower section of the stent lumen slices. This secondary low flow section extends towards the third slice as well. The high velocity central region is maintained for a longer distance within the stented geometry as opposed to the high flow in the stent-absent geometry which spreads throughout the vessel after slice two. Furthermore, the high flow region in the stented geometry is encapsulated by the bounds of the stent, hence the flow is concentrated within the stent. These findings suggest that the stent funnels a portion of the flow which increases the velocity magnitude (due to a decrease in the effective cross-sectional area) and contains recirculating flow behaviour.

5.4 Flow rate ratios across stent and vessel lumen slices

To quantify the concentration of flow within the stent encapsulated region of the flow domain, stent lumen slices were created in the subspace of vessel lumen slices at five locations as seen in figure 5.1. The flow rate across both the vessel lumen slice and the stent lumen slice was measured for both the stented and stent-absent geometry at the five locations. The ratio of the flow rates across the stent lumen slice and the vessel lumen slice at each location was averaged over time and compared against each other in figure 5.4. Along with the flow rate ratio, the area ratio between the stent lumen slices and the vessel lumen slices were also calculated to provide an indication of the level of malapposition at these locations. There is a significant level of malapposition at slice number three, where only 54% of the vessel lumen is captured by the stent; the flow rate ratios also are lowest at slice number 3. The trend of the flow rate ratios decreasing with the increase in malapposition (i.e. slices 1 and 2) and vice versa (i.e. slices 4 and 5) is seen with both geometries. However, the most important finding is that the flow rate ratio of the stented geometry incurs a decrease from 99% to 84% ($\approx 15\%$ change) in the first three slices whereas the decrease in the stent-absent geometry is much larger where the flow

rate ratios drop from 92% to 68% ($\approx 24\%$ change). On average across all slices, the flow rate ratios in the stented geometries are higher by 12%. The disparity is the highest at slice number 3 where 17% more flow passes through the stented lumen slice in the stented geometry.

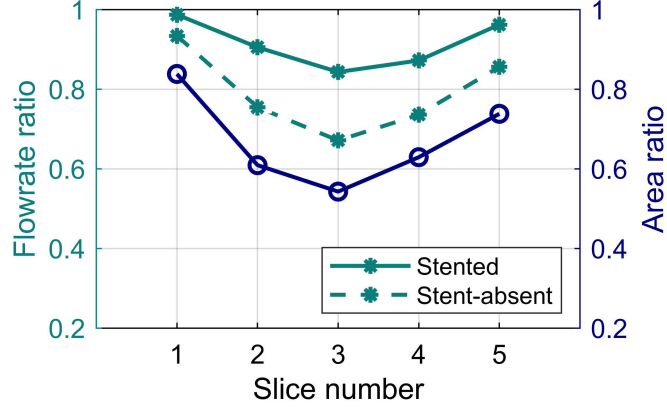


Figure 5.4: Cycle-averaged ratios of flow rate across the stent lumen slice and the vessel lumen slice at five locations in the vein in both stented and stent-absent geometries along with the area ratios of the stent lumen slice and vessel lumen slice.

These ratio differences clearly show that although the stent is porous in structure it significantly ‘funnels’ the flow within its bounds similar to flow-diverter devices, which are used in the treatment of intracranial aneurysms (Brinjikji et al., 2013). In addition to funnelling the bulk flow within the stent, the flow dynamics such as the secondary low velocity region and the high velocity magnitude at the outer edge of the curved vessel appears to be also contained within the stent encapsulated region thereby containing the adverse haemodynamic flow conditions away from the vessel wall in the malapposed region.

5.5 Impact of the malapposition on the wall shear stress

To understand the effect of the funnelling of flow within the malapposed stent on the wall shear stress (WSS) of the vessel wall, various cycle-averaged WSS metrics were plotted on the surface of the vessel as shown in figure 5.5. The TAWSS contour distribution is generally similar in both the stented and stent-absent geometries. A large high TAWSS

region occurs at the sides of the anastomosis region due to the confluence of the two inlets. These high TAWSS values on the sides of the vessels continue to reduce as the flow reaches the venous outlet. Both geometries show a low TAWSS region in the vein close to the heel of the anastomosis, however, the low TAWSS region is larger in the stent-absent geometry compared to that of the stented geometry. When comparing the TAWSS contours with the velocity magnitude slices shown in figure 5.3, the reason for the larger low TAWSS region becomes clearer. As noted with the velocity contours in figure 5.3, the low velocity region in the heel of the vein of the stent-absent geometry is much larger than that of the stented geometry and this behaviour translates to the extent of the low TAWSS region in both cases.

The distribution of OSI across both geometries largely remains at zero except at the heel of the vein where there is a region of high OSI. This region is much larger in the stent-absent geometry, within which a large ring of high OSI occurs. Another location that shows high OSI is at the toe of the anastomosis region close to the DA (see figure 5.1 for annotated locations of the AVF) in both geometries, however, the region is much narrower in the stent-absent case.

Finally, the cycle-averaged WSS vectors were used to plot surface streamlines on the AVFs as seen in figure 5.5. Both cases show a separation node at the heel where recirculation begins to take place. A node of attachment (annotated with red arrows) is seen in both geometries, and it coincides with the point at which the high OSI is observed. A noteworthy aspect of the attachment node in the stent-absent geometry is that it is encountered much further down the vein (approximately 6 *mm* further) in the stent-absent geometry resulting in a larger recirculation zone. Furthermore, a streamline focus (annotated with a blue arrow) is noted closer to the heel of the vein, only in the stent-absent geometry. A streamline node point (annotated with a green arrow) coincides with the high OSI region in the DA of both geometries. The alignment of these critical points of near wall flow patterns (Ethier et al., 2000; Perry and Chong, 1987) with the high OSI regions asserts the idea that the complex near wall flow behaviour (such as recirculation) varies in space throughout the inlet cardiac cycle.

The funnelling effect of the stent decreases the extent of vessel wall regions with high OSI and low TAWSS while also reducing other complex WSS behaviour. Regions of high OSI coupled with low TAWSS are known to encounter intimal thickening (Ku et al., 1985) and disturbed flow in these regions could be promoting inflammatory cell responses (Wang et al., 2013), leading to non-uniform remodelling and stenosis development (Cunnane et al., 2017). Therefore, the malapposed stent implantation alleviates the aforementioned adverse conditions within the vein, reducing the risk of initiating intimal thickening.

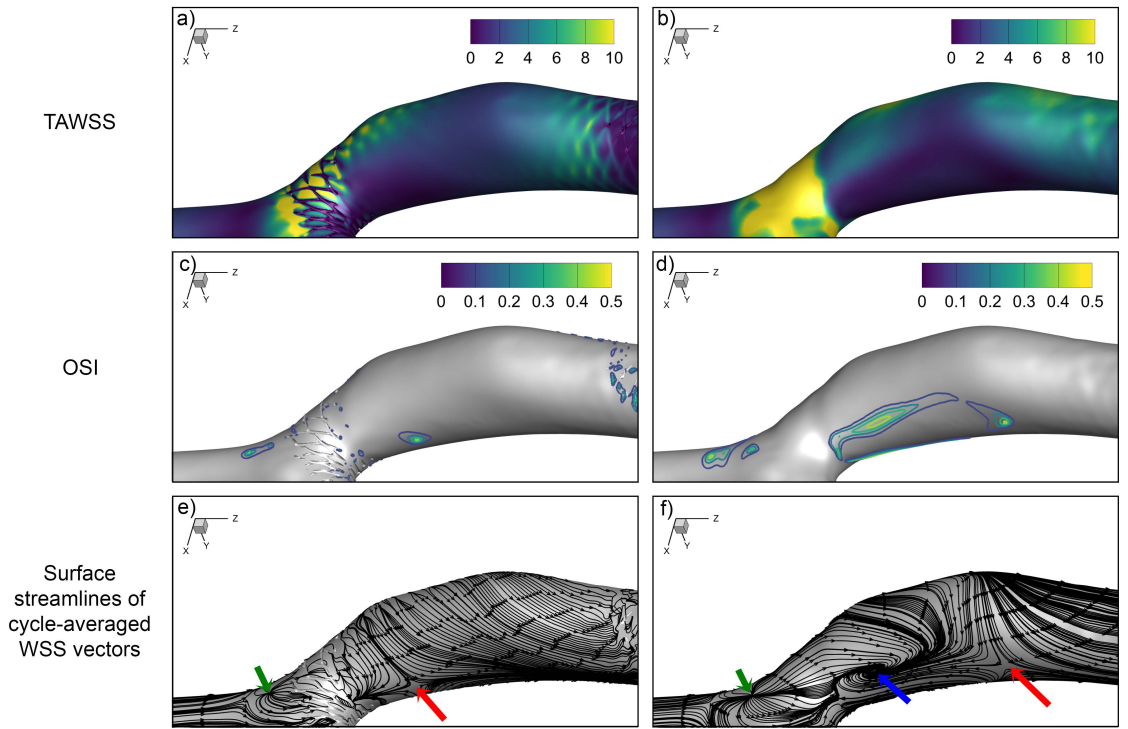


Figure 5.5: WSS metrics across the stented (**a**, **c** and **e**) and stent-absent AVFs (**b**, **d** and **f**). The distribution of TAWSS is shown in the contour plots of subfigures **a** and **b**. The distribution of OSI is shown in the contour band plots of subfigures **c** and **d**. The cycle-averaged WSS vectors are displayed using surface streamlines in subfigures **e** and **f**.

5.6 Conclusion

A numerical simulation was conducted of the blood flow within a patient-specific AVF, to assess the impact of the juxta-anastomotic stent implantation treatment on the bulk

flow. Micro-CT imaging of the stented benchtop AVF phantom was used to gain the stent features and the vessel lumen. An important feature that was apparent in the stented geometry was the malapposition of the stent close to the heel of the anastomosis; the impact of the stent malapposition was compared for the flow in an AVF model with and without the presence of a stent.

Visualisation of the flow streamlines and the velocity magnitude contours showed spiralling flow features in the anastomosis region of both models. A large recirculating low velocity region was observed at the heel of the anastomosis in the stent-absent geometry, which has also been observed and predicted in other studies. The equivalent region in the stented geometry is much smaller. A second low velocity region was present at the lower regions in the stent encapsulated area, coupled with a high velocity region which was sustained further down the vein. These observations suggested the funnelling of flow within the stent encapsulated region which was further confirmed by assessing flow rate ratios between the stent lumen and the vessel lumen. The ratios were significantly higher in the stented geometry. The funnelling effect of the stent on the WSS was clearly evident, with a larger high OSI - low TAWSS region present in the stent-absent geometry along with more complex WSS behaviour in the vein.

The findings of this study show that, in this single patient-specific case, the severe malapposition of a stent yields favourable haemodynamic conditions that could prevent the initiation of inflammatory vessel wall mechanisms. The adverse flow behaviour is seen to be contained in the stent encapsulated region, thereby offsetting its impact away from the near-wall region. The suppression of adverse vessel wall forces potentially being the corollary of the degree of stent malapposition suggests that similar detailed studies on larger cohorts could lead to better understanding of the complex effects of endovascular treatment.

Chapter 6

Impact of the stent implantation on turbulence generation

This chapter extends the findings from the previous chapter and details the impact the stent implantation has on the generation of oscillatory flow behaviour and turbulent kinetic energy (TKE) within the AVF. Locations of significant TKE generation have been identified and compared between the stented and the stent-absent cases. The chapter is concluded by assessing the impact of the high TKE regions on the fluctuations of the WSS.

6.1 Phase-averaged flow field in the treated AVF geometry

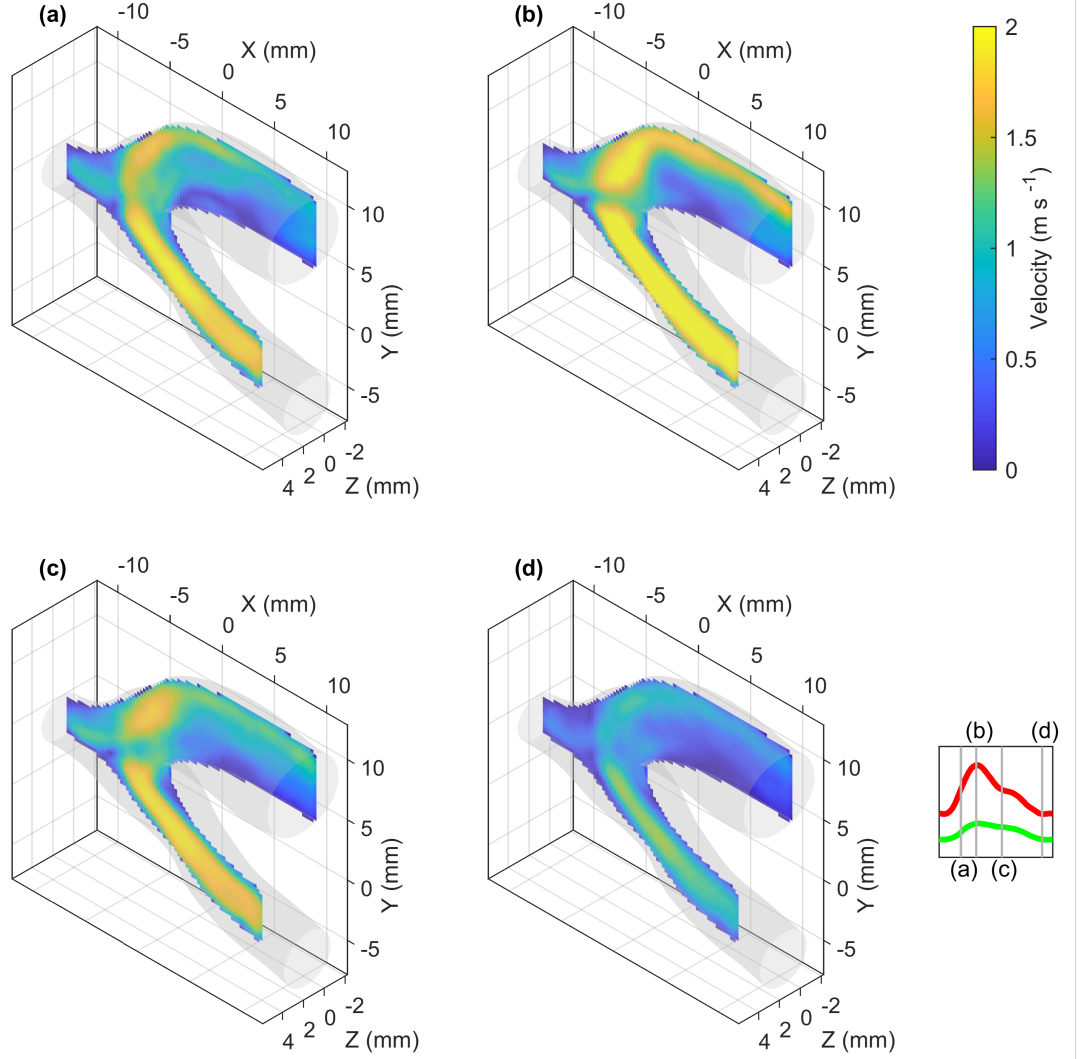


Figure 6.1: Phase-averaged velocity magnitude contours across the central XY plane. The contours have been displayed at the **(a)** accelerating, **(b)** maximum, **(c)** decelerating and **(d)** minimum inlet flow time points of the cardiac cycle.

The Tomo-PIV measurement provides the opportunity to understand the flow field of the treated AVF geometry without the presence of the stent implantation. The flow field is initially assessed by plotting the velocity magnitude $|\overline{U}| = \sqrt{\overline{U}_x^2 + \overline{U}_y^2 + \overline{U}_z^2}$ colour contours across the central XY plane at the maximum, minimum, accelerating and decelerating time points of the inlet profile as illustrated in figure 6.1. To assess the general

behaviour at these time points, the velocities were phase-averaged across 20 pump profiles of the experimental data before calculating $\overline{|U|}$. A significant feature that can be seen in the venous region close to the heel is a low velocity zone that extends well beyond the juxta-anastomotic region and persists across the cycle albeit with slight differences in its spatial extent at the various time-points. The streamlines illustrated in figure 6.2 show the presence of a recirculation zone at certain time points in the low velocity zone mentioned previously. This temporal non-uniformity suggests continually varying flow features in the low velocity zone. The postulation that a low velocity zone would, in turn, lead to a small velocity gradient and persistent low wall shear stresses in this region has been shown in section 5.5. The low wall shear stresses when coupled with disturbed flow is known to be a factor in the onset of vascular disease (Gimbrone Jr and García-Cardena, 2016).

Another low velocity zone at the floor of the anastomosis can be seen throughout the cycle with varying spatial extent, although covering a much smaller region. However, this zone is seen to move across the floor of the anastomosis at different time points. For instance, at the accelerating time point, the low velocity zone is much closer to the centre of the anastomosis floor than at other time points. This behaviour could be caused by the two opposing inlet flows varying in momentum across the cardiac profile, thereby suppressing each inlet flow to various degrees temporally. The implications of this behaviour could be twofold: first, the varying suppression of each inlet flow could provoke disturbance in the flow field which would then propagate downstream; and second, the effect of the varying near-wall velocity could have an impact on the vessel wall at the distal end of the anastomosis floor. Vessel wall damage in the distal artery is not detrimental to the efficiency of haemodialysis in the same way that disease in the vein is; the incidence rate of disease in the distal segment of the AVF is lower (Stolic, 2013).

To assess the effect of these flow features across the Z-direction, $\overline{|U|}$ contours on YZ cross planes are plotted across the geometry at the same time points as illustrated in figure 6.3. The thickness of the low velocity zone in the vein close to the heel varies at different slice points with the zone extending beyond the laser thickness (4 mm) at the decelerating and minimum time points. The low velocity zone near the toe is seen to be much broader in

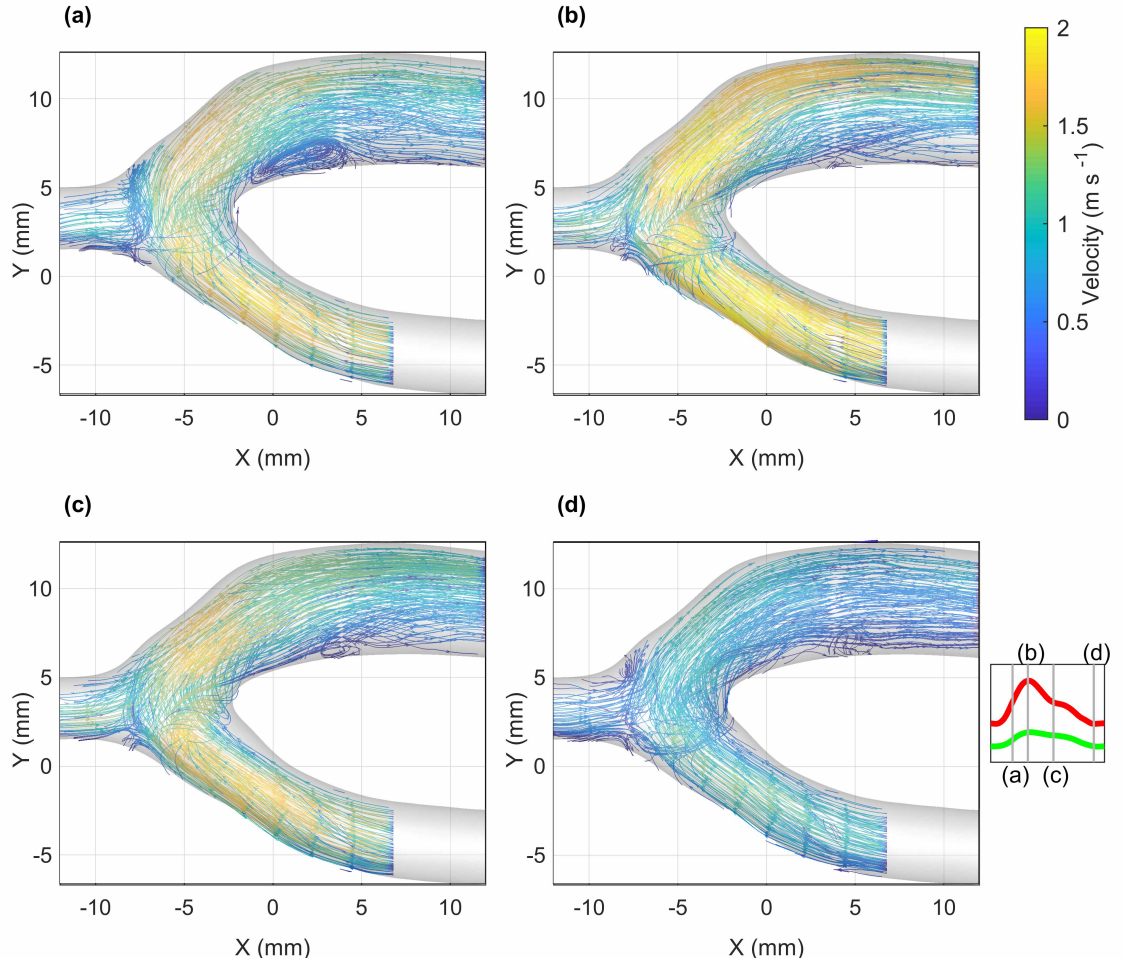


Figure 6.2: Streamlines of flow coloured with the phase-averaged velocity magnitude. The streamlines have been displayed at the **(a)** accelerating, **(b)** maximum, **(c)** decelerating and **(d)** minimum inlet flow time points of the cardiac cycle.

this cross-plane plot as opposed to the previous plots, however, this zone also is widest at the minimum time point. The momentum of the flow across the curved anastomosis is significant enough for separation to occur at the heel but is insufficient to spiral and meet the lower wall of the vessel in a short space, therefore leading to the broader low velocity magnitude regions.

The cross planes at the anastomosis region also show the discontinuity of the high flow from the proximal artery. At all profile time points, it is observed that the high velocity flow tends towards the upper and outer walls of the vessel while the low velocity flow aggregates

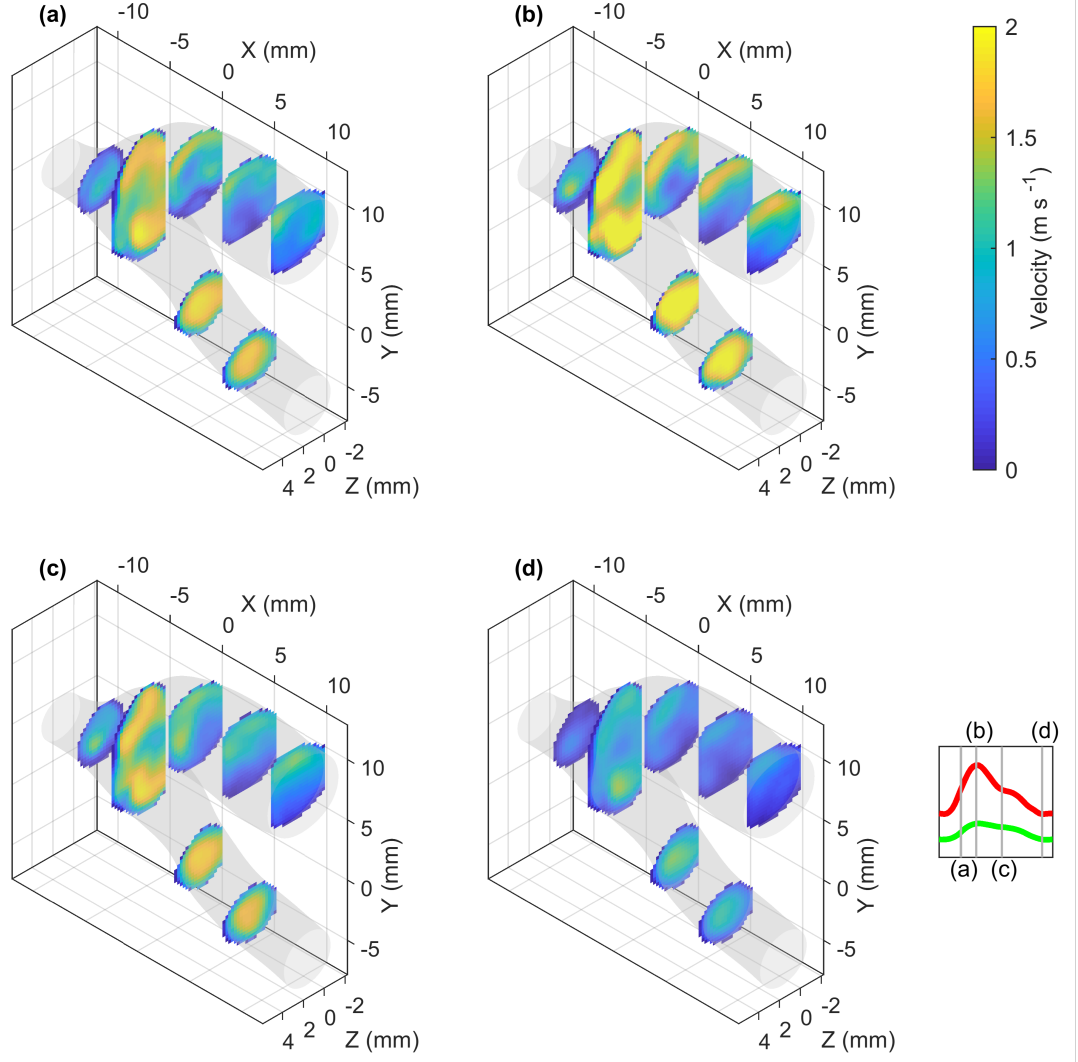


Figure 6.3: Phase-averaged velocity magnitude contours across the five YZ planes. The contours have been displayed at the **(a)** accelerating, **(b)** maximum, **(c)** decelerating and **(d)** minimum inlet flow time points of the cardiac cycle.

to the central and lower regions of the vessel, suggestive of vortical flow emanating from the anastomosis region. This flow feature, which has been seen in computational studies of AVFs (Carroll et al., 2019; Fulker et al., 2018), could be caused due to the flow being directed along a curved trajectory across the anastomosis at a high velocity, and the traditional AVF geometry (with an acute-angled anastomosis) has been seen to further aggravate this feature (Lee et al., 2016).

A common feature of the low velocity recirculation zones at the heel and the floor of the anastomosis and the connecting spiralling flow is that the spatial location varies at the various time-points. This temporal variation is captured in detail in a video of the phase-averaged velocity magnitude across the cross-planes and central plane throughout the cardiac cycle (linked [here](#) and included in the supplementary material). The low velocity zone at the floor of the anastomosis exhibits a periodic movement at the interface of the two inlet flows. This behaviour is seen to affect the high velocity flow traversing around the outer edges of the vein and finally interacts with the end of the recirculation zone at the heel of the anastomosis as well.

Expanding the measurement of the vessel-stent lumen slice flow rate ratios, detailed in section 5.2, temporally gave rise to the presence of oscillations in the time traces as shown in figure 6.4. This behaviour is caused by the flow (temporally) traversing in and out of the boundaries of the smaller stent lumen slices. The key difference between the two cases was that these oscillations only occurred for a short duration (of approximately 0.29 s) in the deceleration phase of the inlet flow in the stented case while the oscillatory behaviour persisted throughout the cardiac cycle in the stent-absent case, the same case used in the Tomo-PIV experiment.

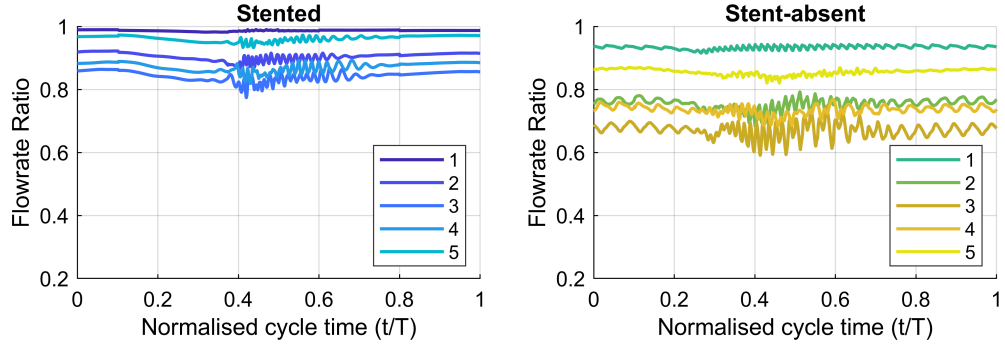


Figure 6.4: Ratios of flow rate across the stent lumen slice and the vessel lumen slice at five locations in the vein in both stented and stent-absent geometries obtained using the numerical methods. The procedure followed to calculate the ratios have been described in section 5.2 of chapter 5

These time traces were decomposed using a fast-Fourier transform (FFT) at the *in-vivo* timescale, illustrated in figure 6.5. The resulting spectral distributions facilitated a better

understanding of the differences in oscillations between the two cases. In the stent-absent case, at the first and middle slice locations, there were two clear local peaks, at approximately 22 Hz and 56 Hz, contributing to the oscillations. The amplitudes of these local peaks increased at the central slice in comparison to the first slice that was placed closer to the anastomosis. These local peaks plateaued at the final slice locations. In the stented case, a range of frequencies from approximately 10 Hz to 100 Hz was noted to have high amplitude; however, no specific local peak was observed. Like the stent-absent case, the overall amplitude increased at the central slice for the stented case as well. These observations show that there is a level of disturbed flow behaviour in both cases, however, the stent-absent case conveys across a specific oscillatory flow behaviour towards the vein. This specific oscillation could be attributed to the periodic oscillations initiating at the interface of the two inlets in the anastomosis.

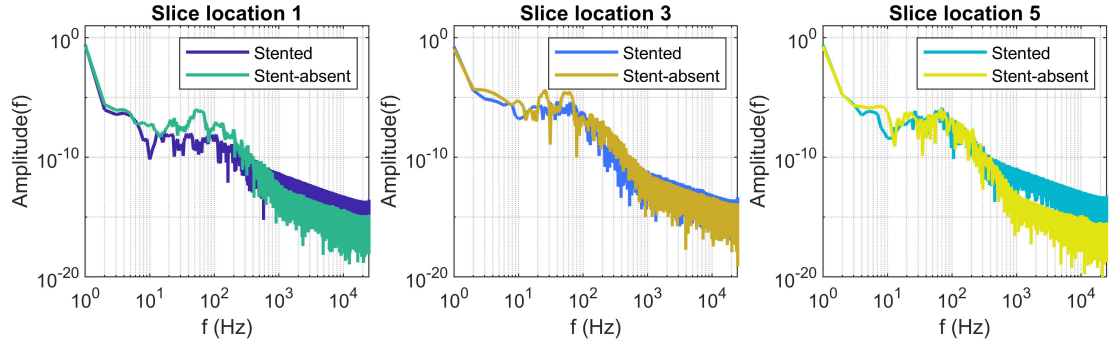


Figure 6.5: Spectral decomposition of the flow rate ratio time-traces at slice locations 1 (closest to the anastomosis), 3 and 5 (furthest from the anastomosis) for the stented and stent-absent cases.

To make a comparison of the oscillations seen at the floor of the anastomosis, as seen in the aforementioned video ([link here](#)) a spectral decomposition (at the *in-vivo* timescale) of the time-trace of the velocity magnitude values close to the floor of the anastomosis was conducted. Figure 6.6 shows the location of the monitor point used to conduct the decomposition. As seen in the spectral graph, high amplitudes were detected at 10 Hz and 20 Hz. The frequency of the second peak is very similar to those noted in the oscillations of the stent-absent case ratios as well. The high velocity spiralling flow noted in the streamlines and cross planes of figures 6.2 and 6.3, respectively, are impacted by the

oscillations generated at the floor of the anastomosis as substantiated by the similarity of the frequencies of oscillations.

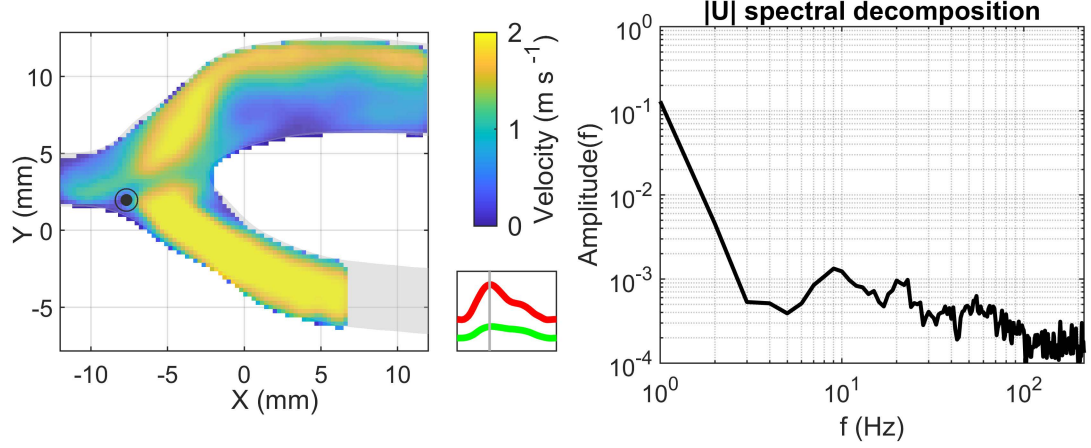


Figure 6.6: Spectral decomposition of the velocity magnitude at a point near the floor of the anastomosis. The location of the monitor point has been visualised on a contour plot of the Tomo-PIV stent-absent data-set.

In addition to these persistent oscillations noted in the stent-absent case, both cases showed an increase in disturbance of the flow rate ratios (of figure 6.4) just after the inlet conditions reached their peak. Additionally, disturbances that are initiated within the stent encapsulated region of the stented case could be contained within the bounds of the device.

6.2 TKE generation within the AVF

To quantify the fluctuations generated in the LES of the two AVF cases, TKE was calculated using equation 4.6 that was defined previously. The distribution of the TKE across a central plane cutting through all vessels at the anastomosis is illustrated in figure 6.7. The general level of turbulence generation is much lower (by approximately an order of magnitude) in the stented case when compared to the stent-absent case.

High TKE persisted throughout the cardiac cycle at the distal region of the anastomosis in the stent-absent case. This region coincides with the oscillations in velocity magnitude

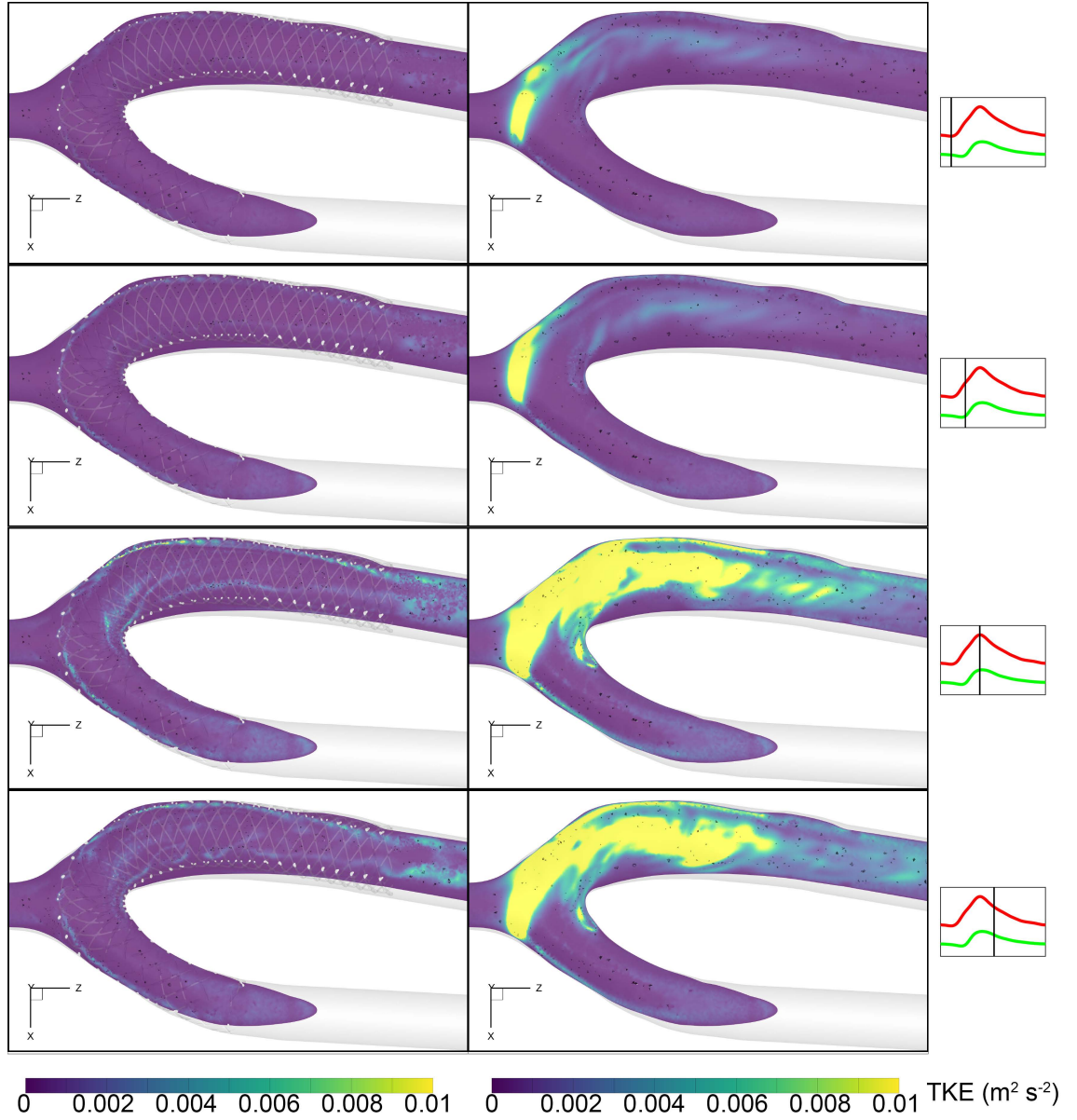


Figure 6.7: Contour plots of turbulent kinetic energy (TKE) on the central plane of the anastomosis. The distribution of the TKE is illustrated at the minimum, acceleration, maximum and deceleration inlet flow time-points for both stented (left) and stent-absent (right) cases.

noted in the stent-absent case. The variations in velocity from cycle-to-cycle, when there is a slight phase difference in the oscillations, contribute to this increase in turbulence. A parametric study using large eddy simulations of AVF geometries (without stent implantations) of varying anastomosis angles have also encountered a large standard deviation of

velocity (proportional to the square root of TKE) at the anastomosis (Stella et al., 2019). The large regions of variance were located closer to the distal region of the anastomosis, somewhat similar to the findings of the current chapter. In contrast to the stent-absent case, the TKE generation at the distal region of the anastomosis in the stented case is much lower. The oscillatory behaviour of the flow rate ratios of the stented case did not show any peaks, therefore, the contribution of disturbances from such behaviour is negated to a certain extent in the stented case. An LES study of flow across the junction of a mixing tee noted the significant reduction in temperature fluctuations with the presence of a porous interface (Lu et al., 2010). The averaged flow fields of the case with the porous junction also showed smoother velocity vectors towards the outlet. Similar dynamics could be at play with the presence of the stent (acting as the porous interface) obstructing the incoming distal flow (that could be likened to the branch of the mixing tee) yielding a smoother outlet flow with lower fluctuations.

To interrogate the disturbance levels at the interface of the two inlets, three monitor points were placed close to the heel, centre and toe of the anastomosis of both LES cases, as illustrated in the inset diagrams of figure 6.8. The phase-average and range of the velocity magnitude were computed at each time-point of the cycle for all monitor points. Compared to the monitor points at the heel and the centre (red and purple, respectively), the phase-averaged $\overline{|U|}$ oscillations are significantly higher closer to the toe (blue) in both cases. These oscillations are restricted to the deceleration phase in the stented case, however, the oscillations are persistent throughout the cardiac cycle in the stent-absent case.

Crucially, even though $\overline{|U|}$ at the toe oscillates in the deceleration phase in the stented case, there is very insignificant cycle-to-cycle variation as illustrated in the last two rows of figure 6.8. Conversely, there are consistently large fluctuations in the stent-absent case, not only at the toe but also at the centre and the heel of the anastomosis. Although it is very clear that the fluctuations at the toe are the largest.

In addition to this source of turbulence generation, the heel region of the stent-absent anastomosis was another location where high TKE flow was emanating. The spatial extent

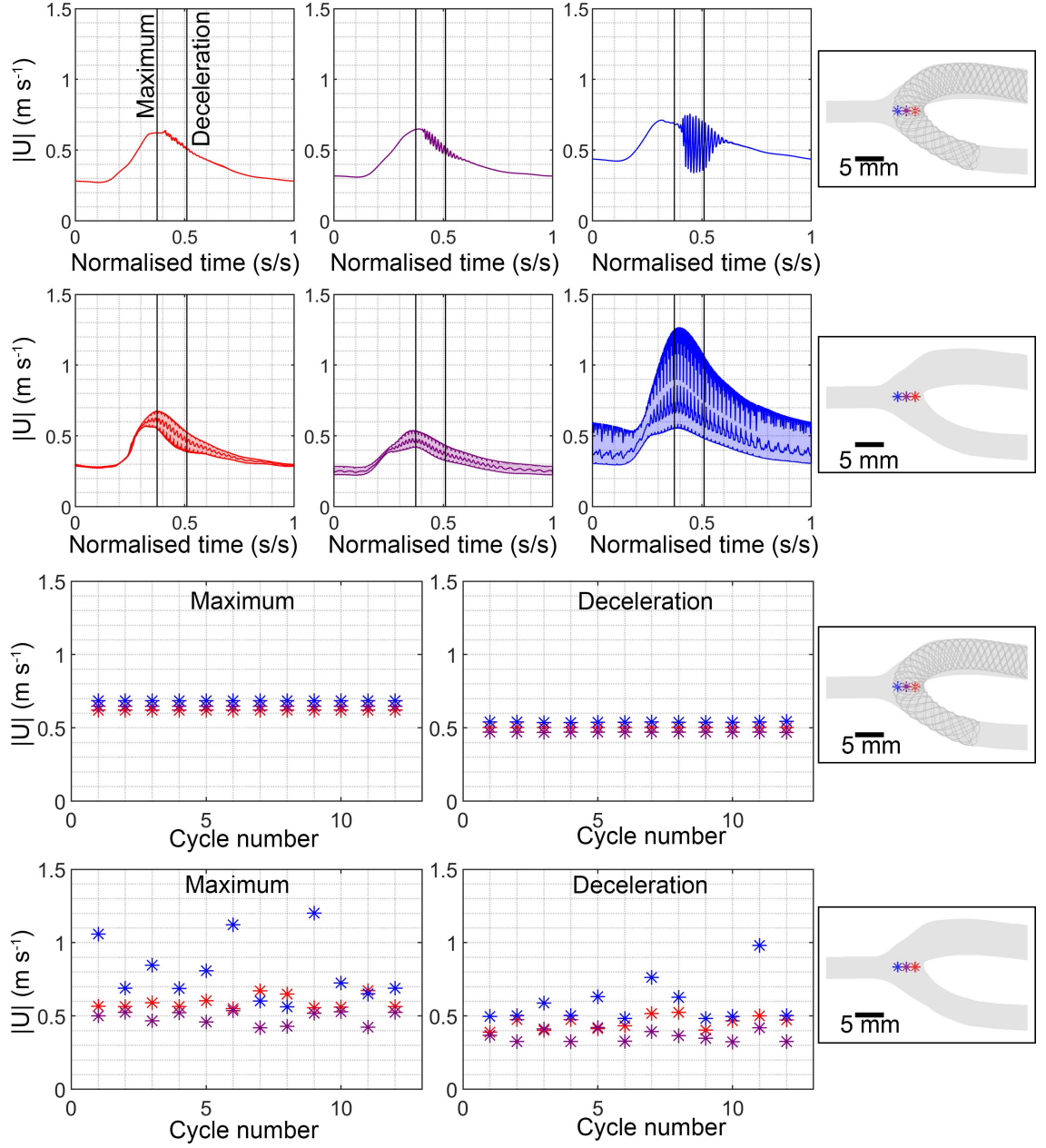


Figure 6.8: Comparison of the velocity magnitude ($|U|$) at monitor points in the anastomosis of the stented and stent-absent cases. The first two rows show the average and range of $|U|$, while the last two rows show the instantaneous $|U|$ at the maximum and deceleration time-points of each cycle.

and the magnitude of the TKE increased at the maximum inlet flow time-point and was sustained in the deceleration phase of the inlet flow. Regions of high standard deviation of velocity have been noted at the anastomosis with a further increase at the heel during the

deceleration phase (particularly with the intermediate angle) in the aforementioned LES study (Stella et al., 2019). Similar increases in disturbances at the anastomosis have been noted in other studies of AVF geometries (Bozzetto et al., 2016; Browne et al., 2015b) where it was postulated that the spiralling flow separated at the heel. Similar behaviour has been noted in the tortuous intracranial aneurysm geometries (Valen-Sendstad et al., 2014) where disturbances tended to grow in the deceleration phase.

To visualise the flow separation at the heel of the anastomosis, velocity magnitude plots have been shown on the central plane of the two AVF cases as seen in figure 6.9. A clear and persistent low velocity magnitude region is seen at the heel of the stent-absent case. Streamlines, shown in the previous chapter (figure 5.2), illustrated the presence of a recirculation zone in this low velocity region. The implication of this behaviour is the necessity of the flow to accelerate through a smaller cross-section of the vessel. The ensuing velocity gradient together with the spiralling flow in the outer regions of the vessel would further contribute to the generation of high TKE . The low velocity magnitude region noted at the heel of the stented case is much smaller due to the uneven wall surface, created by the stent struts, energising the boundary layer which in turn delays or negates flow separation (Lin et al., 1990). However, the resemblance of smooth flowing features across the vein is lost at the maximum time-point where two separate high velocity regions are seen closer to the inner stent surface. These regions of high velocity magnitude are further broken down in the deceleration phase. Although the TKE distribution is much lower in magnitude in the stented AVF, an increase in TKE is noted at the heel of the anastomosis at the maximum time-point. These features are seen to be transported along the vein in the deceleration phase in a manner mimicking the breakdown of the high velocity magnitude regions. The disturbed flow regions are conveyed through the vein of the stented case as well, however, the interaction of these disturbed flow regions with the near-wall flow is reduced due to the funnelling effect of the flow within the stent encapsulated region.

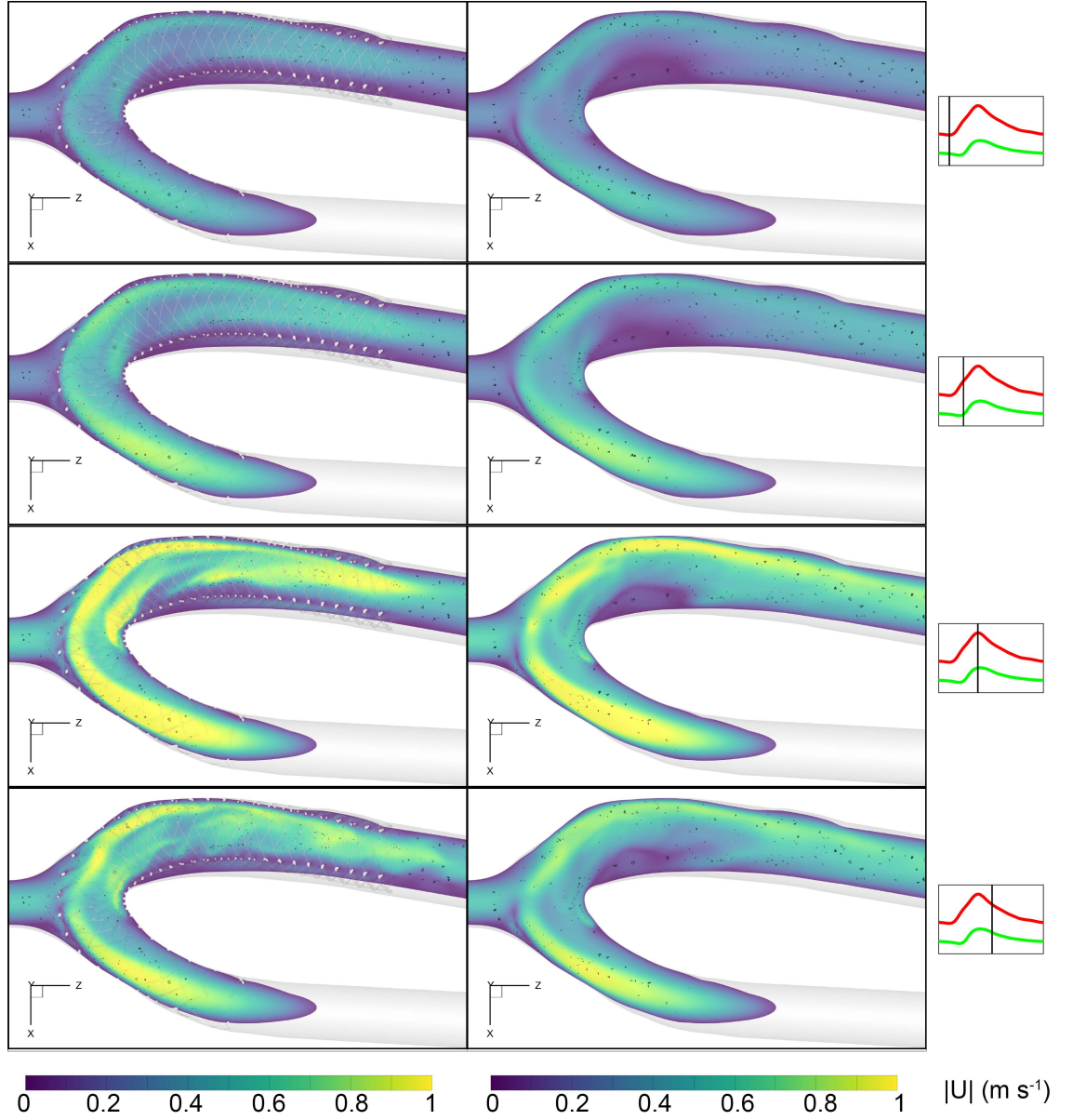


Figure 6.9: Contour plots of velocity magnitude ($|\overline{U}|$) on the central plane of the anastomosis. The distribution of $|\overline{U}|$ is illustrated at the minimum, acceleration, maximum and deceleration inlet flow time-points for both stented (left) and stent-absent (right) cases.

6.3 Turbulence generation at the end of the stent implantation

Although the noted TKE is much lower in the stented case, there is an increase in TKE magnitude (relative to other regions in the stented case) after the end of the stent. This increase in disturbance is seen most clearly in the deceleration phase of the inlet flow waveform. A study measuring shear stress of stented *in vitro* vessels noted the presence of disturbances downstream of the stent implantation (Peacock et al., 1995). The authors postulated that the struts could behave similar to a cylinder placed in a cross-flow where the oscillating vortices shed from the cylinder become unstable with flow over a certain Reynolds number. A recent PIV measurement of a stent-graft in an *in vitro* compliant model noted a recirculation zone at the trailing edge that was postulated to be caused by the compliance mismatch between the graft and the artery (Yazdi et al., 2021). Vorticity magnitude was plotted across a central plane at the stent edge, as illustrated in figure 6.10 to assess the span-wise vortical behaviour suggested in other studies. The magnitude (rather than a component) of the vorticity was used to avoid complications that arise with aligning the tortuous vessel with the principle axes.

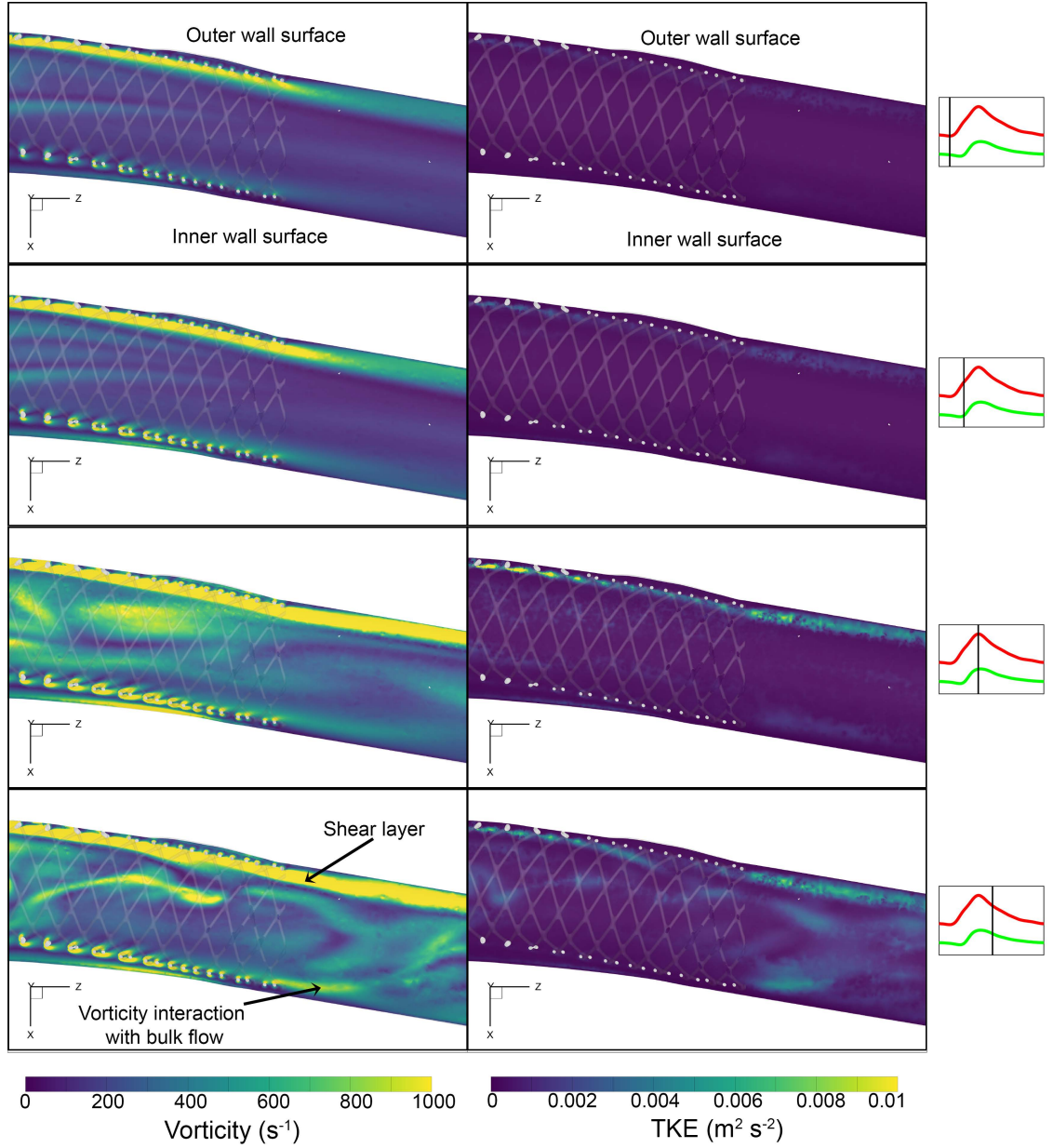


Figure 6.10: Contour plots of vorticity magnitude (left) and turbulent kinetic energy (right) on the central plane at the edge of the stent. The distributions have been plotted at the minimum, acceleration, maximum and deceleration inlet flow time-points for the stented case.

The vortical behaviour is relatively low in the bulk flow of the vessel except at the deceleration phase where there is a high vorticity region coming off of the heel of the anastomosis. The magnitude of this feature reduces as the flow approaches the edge of the stent. More complex vortical behaviour is initiated in the bulk flow past the proximal edge of the stent (at the deceleration time-point). These complex regions are co-located with regions of non-zero TKE as well.

Another striking feature is the high vorticity magnitude region at the stent struts. This behaviour is persistent throughout the cycle, however, the interaction between the vortical flow from adjacent stent struts is much higher at the outer wall surface (refer to figure 6.11 for the inner/outer wall surface localities). The coalescing vortical flow structures amount to a shear layer forming and shielding the stent encapsulated flow. The shear layer is seen to continue past the stent edge at the outer wall surface, however, the shear layer at the inner wall surface is seen to interact with the aforementioned bulk flow complexities.

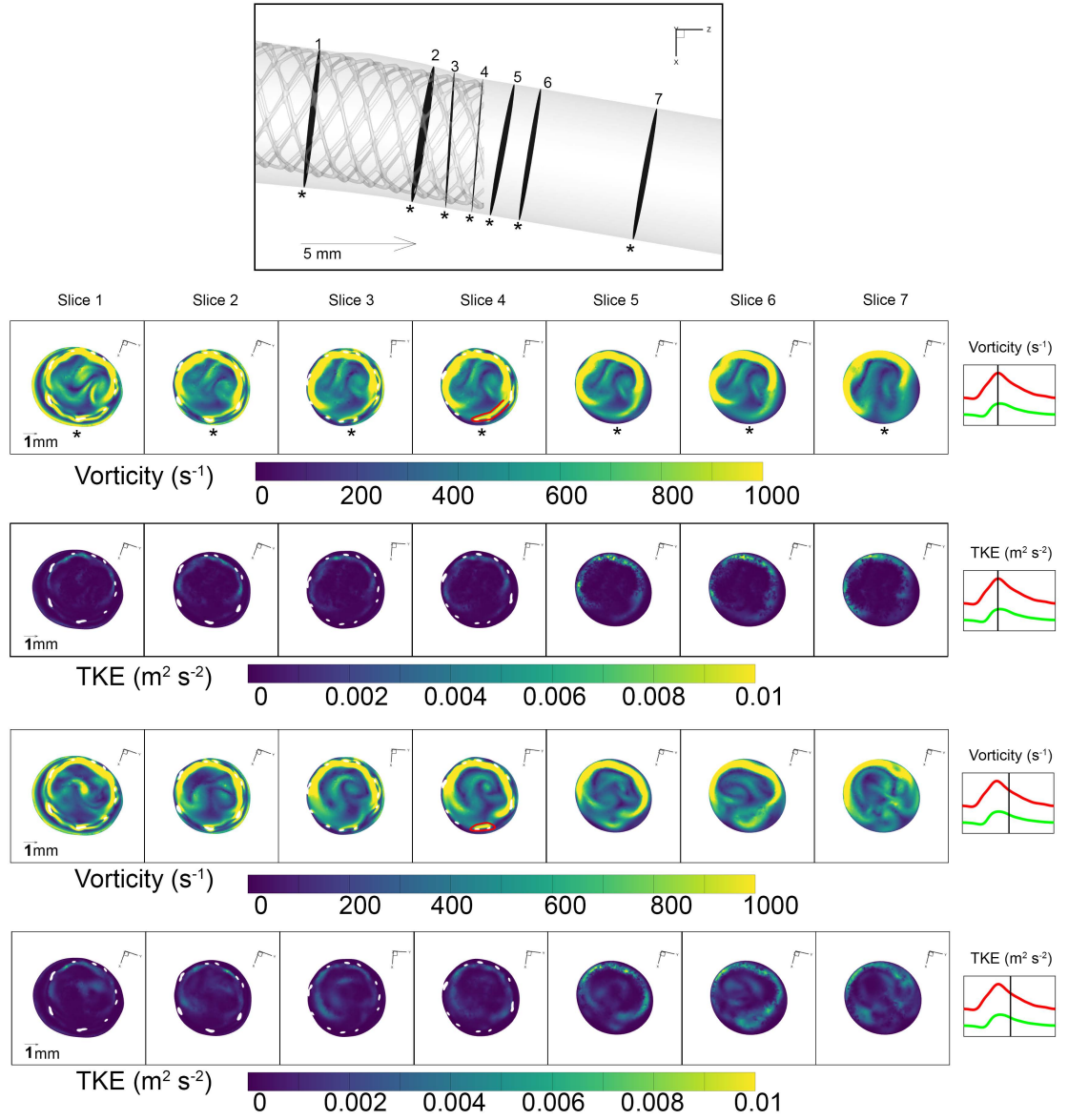


Figure 6.11: Contour plots of vorticity magnitude and turbulent kinetic energy at cross-sectional slices near the stent edge. The distributions have been plotted at the maximum and deceleration inlet flow time-points for the stented case.

To detail the distribution across the vessel, the vorticity magnitude and TKE was plotted on cross-sectional slices close to the edge of the stent at the maximum and deceleration time-points, as shown in figure 6.11. Two counter-rotating Dean vortices that are created at the anastomosis are seen to propagate along the vein at both time-points. At the maximum time-point, these vortices continue to travel beyond the stent edge with little disturbance. This is further reflected in the TKE distribution which is seen to increase only in the small region downstream of the stent struts at the outer surface.

The high vorticity magnitude circumscribes a large portion of the cross-sectional planes at the maximum time-point. However, in the deceleration phase, less of the cross-sectional circumference is covered by the high vorticity magnitude due to a decrease in the velocity of the incoming flow. Another separate high vorticity region at the strut of the inner surface of the stent edge is noted (highlighted in red in figure 6.11). This region is observed to grow in size and agitate the two counter-rotating vortices further downstream, creating disturbances that are quantified by the TKE . This increase in magnitude and traversal of vortical flow towards the bulk flow region was noted in PIV studies of flow around a spanwise cylinder close to a wall (He et al., 2017), where, at a critical gap width, the vortices created from the gap flow interact with the upper vortices.

6.4 Impact of the turbulence generation on the wall shear stresses

The previous sections detailed turbulence generation in the AVF cases. The stent-absent case showed higher levels of TKE that were generated at the interface of the two inlet flows and at the heel of the AVF. A lower magnitude of TKE generation was observed at these two locations in the stented case, however, there was an increase in turbulence generation at the end of the stent implantation. To further illustrate the effects of these disturbances on the vessel wall, a MATLAB script was developed to unwrap the vessel wall onto a 2D surface plot. This script utilised the vessel centerline node locations together with the vessel wall locations.

A local centerline node direction vector can be calculated using a central difference of the two adjacent centerline node locations. Another direction vector, perpendicular to the local centerline direction vector, was created such that it pointed to the inner surface of the vessel from the centerline node. In the case of the outlet vein, the inner half of the vessel was the half that was closest to the proximal artery vessel, and vice-versa. The inner surface of the distal artery was also determined relative to the location of the proximal artery. Following these two steps provides a local axial vector and an auxiliary in-plane (vessel cross-section) vector to calculate distances away from the anastomosis and angles relative to the inner surface, respectively, at each node.

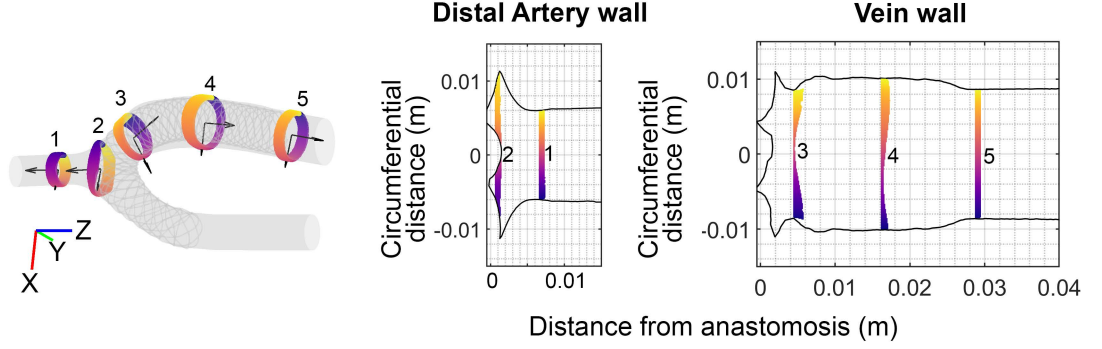


Figure 6.12: Example of unwrapping the 3D vessel wall locations onto a 2D space using local vectors constructed from centerline node locations. The colour bar of the cross-sectional slices assist with understanding the 3D location of the wall element on the corresponding 2D plots.

The next step was to assign each wall element to its closest centerline node. Using the in-plane vector, an angle was measured for each of these assigned wall elements relative to the inner surface of the vessel. Assuming that the vessel cross-sections were close to circular, a circumferential distance of the wall element from the inner surface could be calculated using the aforementioned angle and the distance of the wall element from the centerline node.

Following these steps yields an axial location along the vein and a circumferential location along the cross-section of the vessel for each wall element, thereby converting the prior 3D vessel wall surface to a 2D surface. The spacing of the centerline nodes was reduced

to 0.1 *mm* increments to decrease unnatural steps in the plot. The clarity obtained by visualising the whole tortuous vessel on 2D outweighed the effects of the circularity assumption.

6.4.1 Behaviour of the WSS at the distal artery

To understand the effect of the oscillatory flow behaviour at the distal floor of the anastomosis, cycle-averaged WSS metrics have been plotted along the distal artery using the vessel unwrapping method explained previously. There is a clear low TAWSS region in the distal artery near the anastomosis for both the stented and stent-absent cases. This is to be expected as the collision of the two inlet flows creates a recirculation zone near the floor of the anastomosis. Since the trajectory of the coalesced flow is directed towards the vein and the high velocity flow moves towards the outer wall of the vessel (relating to the maximum circumferential distances in figures 6.13 to 6.15), the TAWSS starts increasing in the anastomosis. The increase is more sudden and persistent in the stent-absent case compared to the stented case. This is due to the stent implantation inhibiting the high velocity flow from being incident on large sections of the vessel wall.

In the stent-absent case, large regions of high OSI are noted in the same regions that low TAWSS was observed. Similar patterns are noted in the stented case as well, however, the magnitude and spread of these regions are very much subdued. The generation of high *TKE* in the anastomosis of the stent-absent model could explain the high regions of oscillating wall shear stresses. However, transWSS is a better metric to assess multi-directional disturbances in the anastomosis. As expected there are much larger regions of high transWSS noted in the stent-absent case when compared to that of the stented case. An important observation is that the high transWSS and OSI regions of the stent-absent AVF case are adjacent or coincident with the band of low TAWSS.

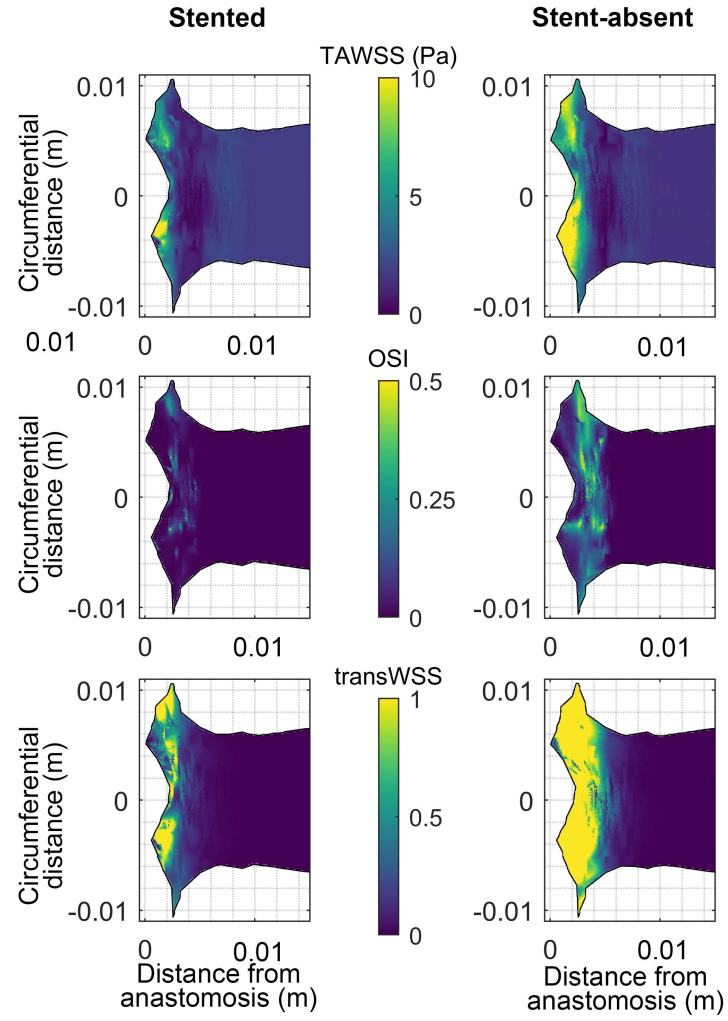


Figure 6.13: Wall shear stress metrics on vessel wall at the distal artery.

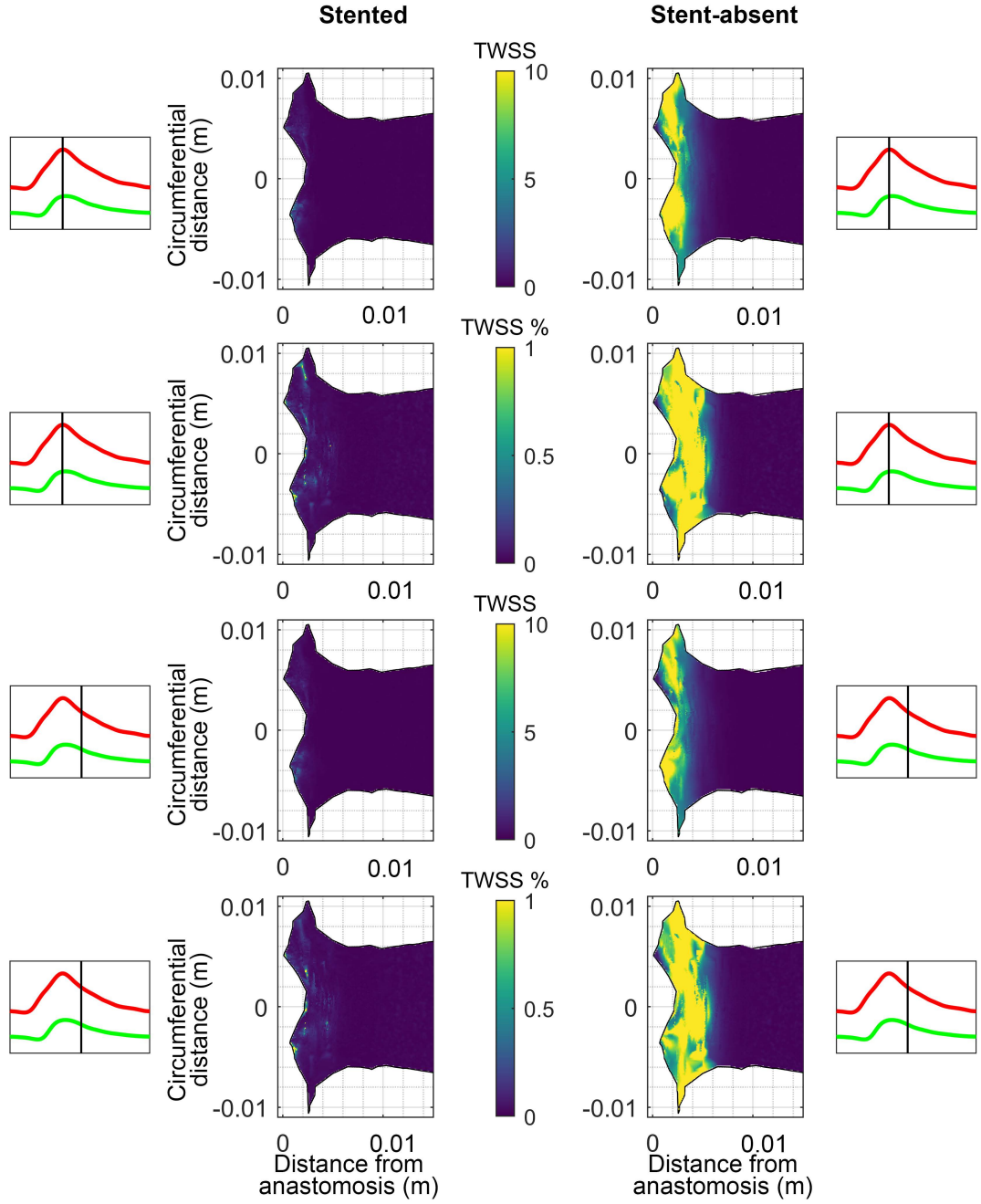


Figure 6.14: Turbulent Wall Shear Stress distribution at the maximum and deceleration time-points.

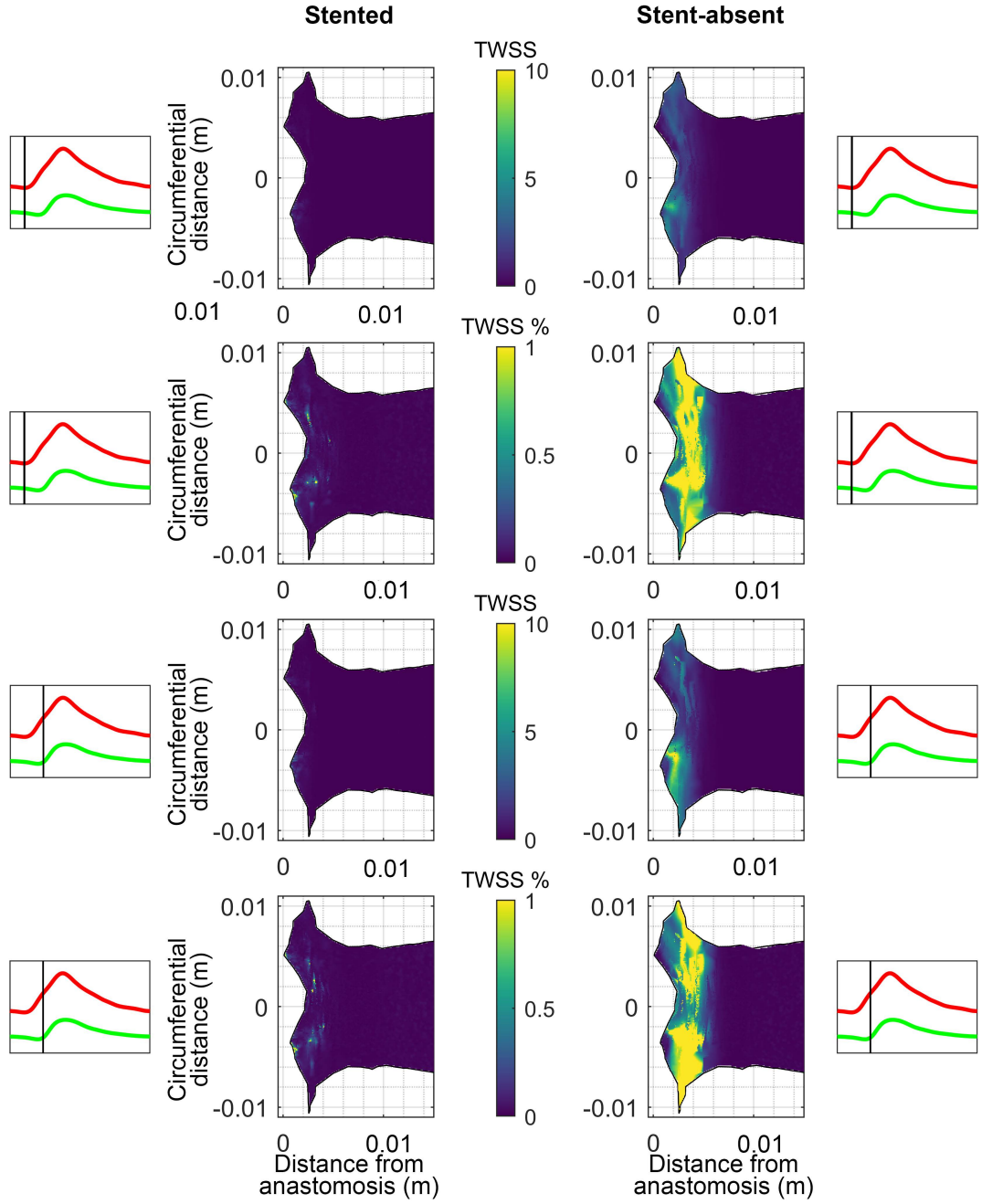


Figure 6.15: Turbulent Wall Shear Stress distribution at the minimum and acceleration time-points.

In addition to the cycle-averaged WSS metrics (such as TAWSS, OSI, transWSS), phase-averaged turbulent WSS (TWSS) were also calculated to measure the vessel wall force fluctuations. This metric provides further clarity on the relationship between the impact of the contrasting *TKE* regions noted in both cases, as it has been calculated in a similar manner. In addition, the TWSS values have also been normalised using the phase-averaged WSS to understand the level of shear stress fluctuations.

The TWSS at the anastomosis floor is of much higher magnitude in the stent-absent case in comparison to the stented case. This high level of TWSS which is persistent throughout the cardiac inlet flow profile is also mobile with the high TWSS covering a larger region at the maximum and deceleration time-points. The normalised TWSS in the same region is also of high magnitude and follows a similar behaviour of spreading across a larger region of the anastomosis of the stent-absent case at the maximum and deceleration time-points. The fluctuations are significant in comparison to the phase-averaged WSS magnitude sensed at these locations. The oscillatory flow and the ensuing high *TKE* generated at the interface of the two inlet flows in the stent-absent case are very likely to be contributors to this mobile high TWSS region. Observing converse subdued behaviour in both *TKE* and TWSS distributions in this region of the stented case further substantiates this claim.

6.4.2 Behaviour of the WSS in the juxta-anastomotic vein

As detailed previously, the proximal vein wall has been unwrapped onto a 2D surface to visualise the WSS patterns. The distribution of the cycle-averaged WSS metrics: TAWSS, OSI, and transWSS, across the vein is illustrated in figure 6.16. A clear difference between the stented and stent-absent cases is noted at the heel region of the vein. A large TAWSS accompanied by a large ring of high OSI is noted in the stent-absent case, however, the stent-absent case shows a much smaller region of high OSI. The funnelling capability of the porous stent is a major contributing factor to the decrease in OSI (detailed in section 5.5 of chapter 5). The disturbances generated in the anastomosis are kept away from the vessel wall in the malapposed region of the vessel. The impact of the shorter recirculation

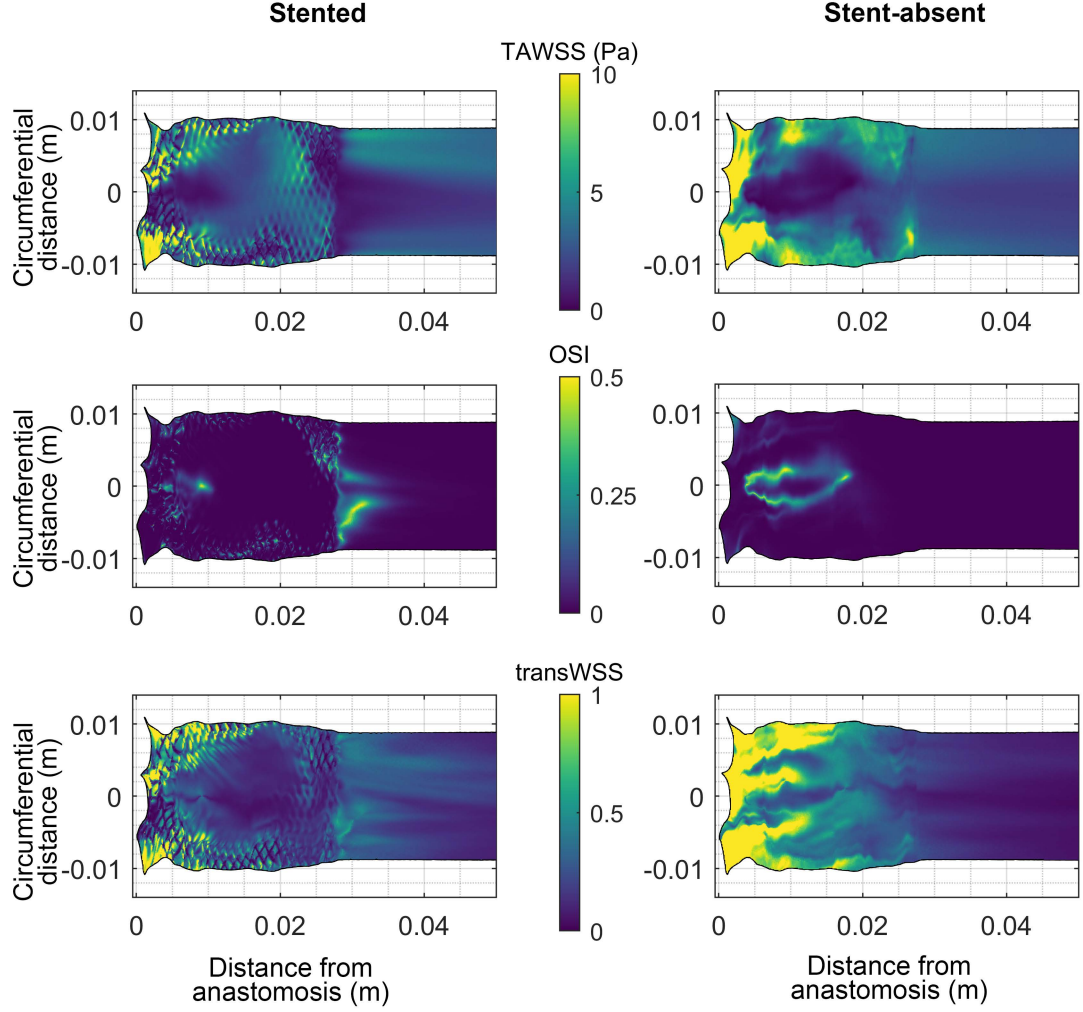


Figure 6.16: Wall shear stress metrics on vessel wall at the distal artery.

zone results in a shorter region of low TAWSS in the stented case.

There is a large distribution of high transWSS on either side of the recirculation zone in the stent-absent case, with the magnitude decreasing at the downstream edge of the recirculation zone. There is also a large distribution of high transWSS at the outer surface of the vein (relating to the maximum circumferential distances in figures 6.16 to 6.18). The oscillatory flow behaviour that was initiated at the interface and conveyed along the outer bounds of the vein (as detailed with the temporal flow rate ratios of section 6.1) would lead to the vessel wall continually sensing a high and low velocity gradient across the cycle, with variations in the WSS vector direction. These flow oscillations were very much tempered

in the stented case which resulted in a smaller distribution of the high transWSS.

As before, to better understand the impact of the *TKE* flow behaviour, the distribution of the absolute and normalised TWSS has been considered at the maximum and deceleration time-points in figure 6.17 and at the minimum and acceleration time-points in figure 6.18. A persistent high TWSS region is seen at the outer regions of the vessel wall near the anastomosis in the stent-absent case throughout the cycle. A possible contributor to these fluctuations in WSS is the *TKE* generated at the interface of the two inlets. At the maximum and deceleration time-points, the high magnitude fluctuations are seen to spread across the venous cross-section for a length of about 25 *mm* along the vessel which is a similar behaviour to the *TKE* in the vein. A high normalised TWSS ring at the heel of the stent-absent case resembles the behaviour of the OSI and transWSS. Therefore, the extent of the recirculation zone not only varies within the cycle but also fluctuates across cycles.

Conversely, the distribution of high TWSS marginally encroaches the heel region in the stented case. The main behaviour seen in the stented case is that the high TWSS (and the normalised TWSS) is concentrated to the stent strut regions. Studies have shown the presence of recirculation zones in the spaces between struts of apposed (Jiménez and Davies, 2009) and malapposed (Chen et al., 2017) stent segments. The disturbances caused in these micro-recirculation zones coupled with the high velocity flow traversing on the outer edge of the vessel yields significantly high levels of TWSS localised to the stent strut spaces. It is also clear that these dynamics localised to the strut regions are not propagated to the vessel in the malapposed region.

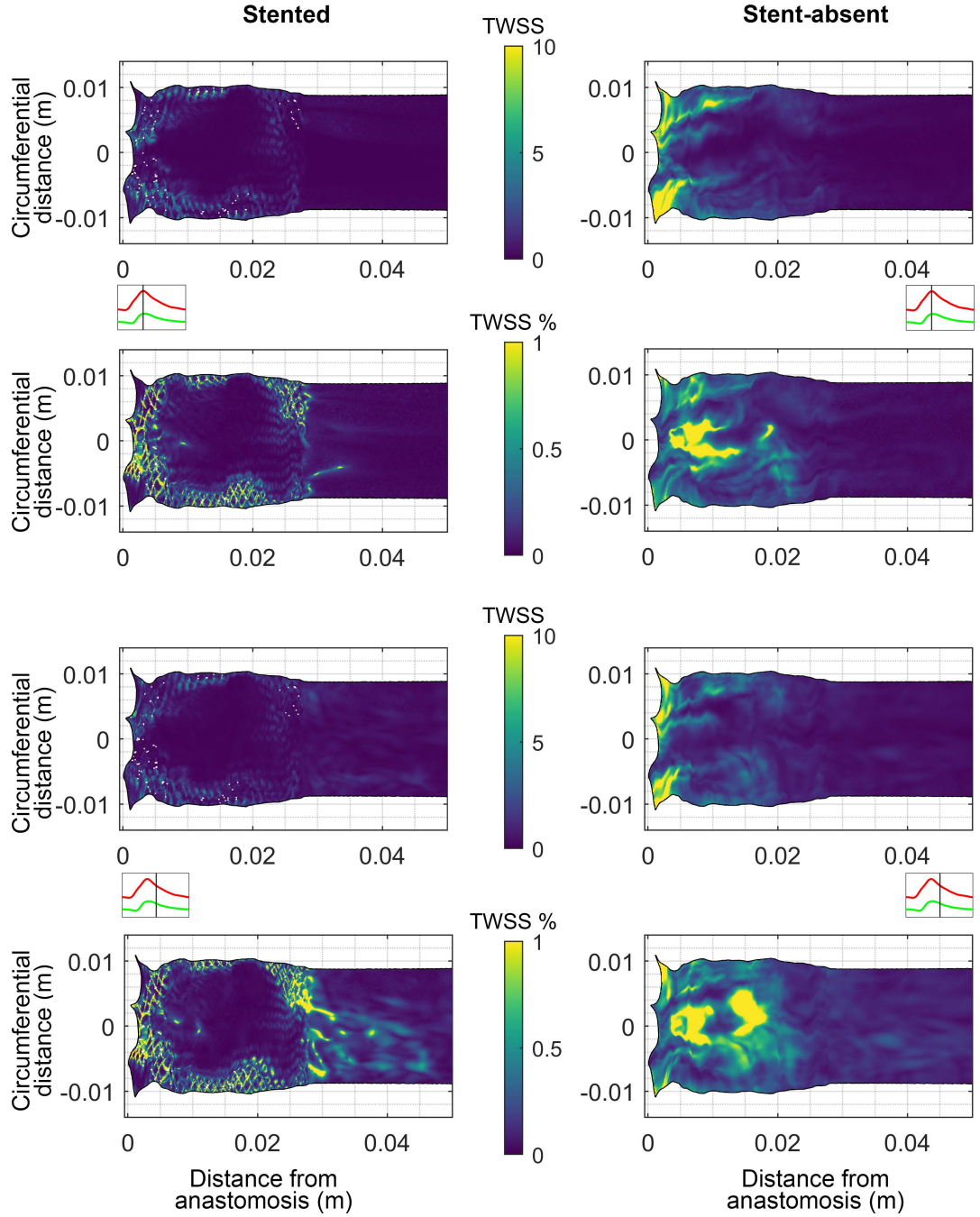


Figure 6.17: Turbulent Wall Shear Stress distribution at the maximum and deceleration time-points.

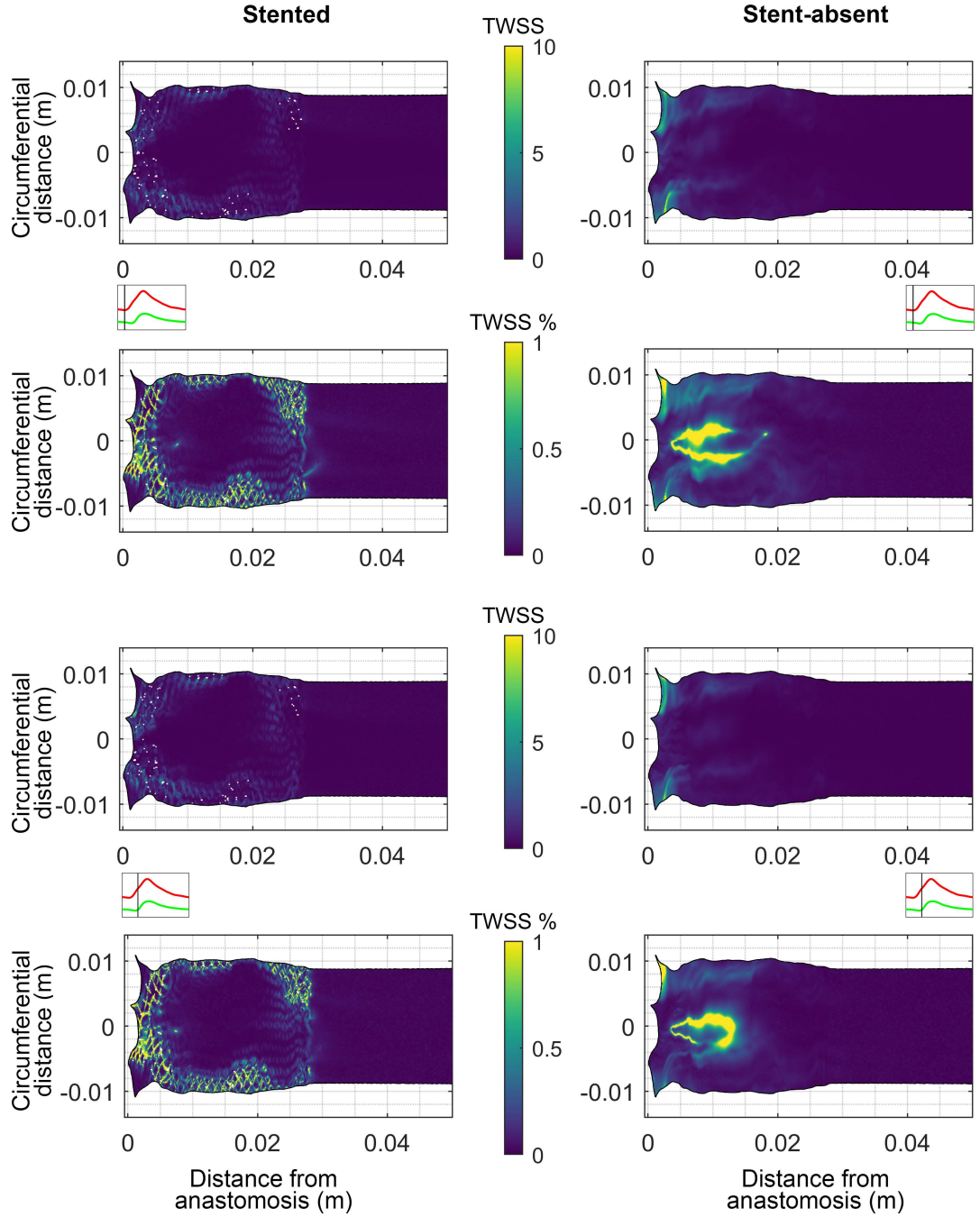


Figure 6.18: Turbulent Wall Shear Stress distribution at the minimum and acceleration time-points.

6.4.3 WSS behaviour proximal to the stent implantation

The WSS behaviour appears to be generally homogeneous in the stented case downstream of the heel until the flow reaches the stent edge. There is an increase of OSI and transWSS at the inner vessel wall (relating to a circumferential distance of zero in figures 6.16 to 6.18). The increase in these WSS measures are co-located with a decrease in TAWSS which would be caused by the recirculating flow emanating from the malapposed stent edge. The decrease in shear stress and presence of recirculatory flow has also been noted in simulations of peripheral arteries with insufficient stent-graft apposition (Al-Hakim et al., 2017). The variation of the vortical flow emanating from the stent edge leads to the increase in the transWSS and OSI which spans an extent of approximately 7.5 *mm* downstream of the stent-edge.

The absolute and normalised TWSS at the stent-edge is generally low at all analysed time-points except at the deceleration time-point. Although the absolute TWSS is not as large as what is measured around the stent struts, the normalised TWSS significantly increases up to an extent of approximately 20 *mm* downstream of the stent edge. The elevated regions of normalised TWSS are noted at approximately equal intervals which could be caused by the periodic shedding of vortices during the deceleration stage. The dynamics of the interactions of the multiple vortices (detailed in 6.3) lead to a sudden increase in the *TKE* near the wall that subsequently affects the near-wall velocity gradients as well. The increased fluctuating near-wall dynamics caused by the stent edge could lay claim to the build-up of IH downstream of stent implantations noted in aorta subjects (Barth et al., 1990) and could potentially affect stented AVFs in a similar manner.

6.5 Conclusion

The complex spiralling flow behaviour stemming from the anastomosis of the AVF was further examined using the Tomo-PIV measurement of the stent-absent case. In addition to the flow spirals, oscillatory behaviour was noted to be originating from the distal toe

of the anastomosis. The frequency peaks of the oscillatory behaviour were very similar to that measured across slices in the vein using large eddy simulations of the stent-absent case. Furthermore, a high TKE region was consistently noted at the interface of the two inlet flows at all analysed time-points in the stent-absent case. This coincidence in findings asserts that the oscillatory disturbances initiated due to the collision of the two inlet flows at the distal region of the anastomosis are conveyed towards the vein. Conversely, the levels of TKE in the anastomosis of the stented case were far lower. The presence of the stent at the location of the inlet flow interface could mitigate the flow disturbances.

An increase in TKE levels was also noted at the heel of the stent-absent AVF anastomosis at the maximum and deceleration time-points. These flow features led to a ring of high WSS fluctuations within the cycle (OSI, transWSS) and across cycles (TWSS). The increase in TKE was far less significant in the stented case and these disturbances were held within the stent encapsulated region (assisted by the funnelling feature of the stent that was detailed in chapter 5). The stent circumvented these minor disturbances away from the vessel walls thereby resulting in a smaller region of adverse WSS behaviour at the heel of the AVF. However, there were localised regions of high WSS fluctuations surrounding the stent struts due to the generation of micro-recirculation regions.

Although the fluctuating haemodynamics of the stented case were far less apparent than that of the stent-absent case, an increase in TKE was noted at the downstream edge of the stent which was malapposed from the inner vessel wall. Complex vortical flow behaviour emanating from this malapposed stent edge acted as a catalyst in the increase in flow disturbances, particularly at the deceleration time-point of the inlet flow. These observations were mirrored with the TWSS measurements which also increased downstream of the stent edge. Therefore, the stent placement mitigated the initiation of TKE and the malapposition at the heel shielded the vessel from the disturbed flow, however, the malapposition at the stent edge could potentially create adverse disease-causing flow conditions downstream of the implantation.

Chapter 7

Comparison between the stented and diseased AVF

In this chapter, the overall effect of the stenting procedure on the shape of the AVF and the subsequent haemodynamic conditions are assessed by comparing fluid dynamic quantities between the treated AVF and the diseased AVF. Accordingly, an additional LES has been conducted on the diseased AVF case to measure the turbulent flow quantities and their effects on the wall.

7.1 Introduction

The previous chapters focused on the effects of the stent device on the haemodynamic environment by isolating the impact of the stent. This strategy was employed by assessing the flow field within the same (treated) AVF geometry with or without the presence of the stent. However, after subjecting the diseased AVF to the stent implantation treatment, the geometry of the AVF changes noticeably. The flexible metallic structure alters the anastomosis from a tight-angled junction (in the diseased geometry) to an obtuse-angled smooth loop and the subsequent venous flow rates have been known to increase significantly as well (Thomas et al., 2019). Therefore, in this chapter, we will explore the progression of the AVF haemodynamic environment from the diseased condition to the stent implanted condition.

To assess this transition, the recorded geometry and boundary conditions from the same patient AVF (studied in preceding chapters) prior to the stent implantation procedure was utilised. Apart from the sharper anastomosis angle and the decreased flow rate, the main characteristic of the diseased AVF is the presence of the severe stenosis in the vein as illustrated in figure 7.1. As before, the freehand 3D ultrasound scanning methodology (Colley et al., 2018) was used to scan and then segment the diseased patient AVF geometry. Similarly, the Doppler function of the ultrasound machine was used to obtain the pulsatile inlet flow conditions (Carroll et al., 2020). This overall methodology of obtaining the patient data has been illustrated in figure 7.2 and has been detailed in chapter 4. It is worth noting that the additional steps involving device implantation and micro-CT imaging were not necessary for the diseased case as this scan was obtained before the stenting procedure was conducted. A summary comparing the diseased AVF geometry with the stented AVF geometry is shown in table 7.1. In particular, a stark difference between the two cases is the significant increase in the outlet flow rate of the vein upon stent implantation.

The segmented diseased AVF geometry was (spatially) discretized by creating a tetrahedral mesh using ICEM CFD. Care was taken to follow the same initial meshing strategy of

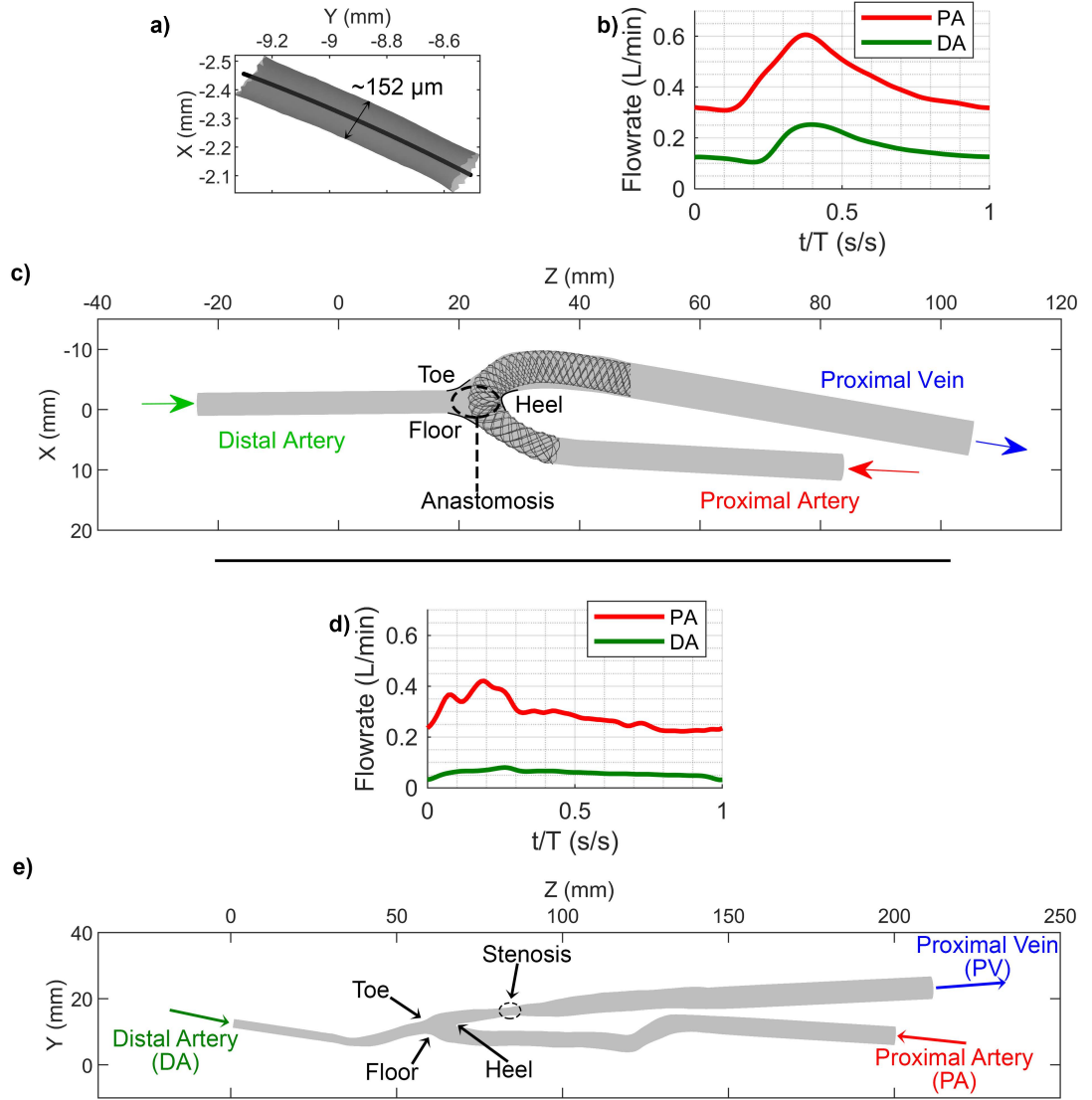


Figure 7.1: Comparison of the geometry and boundary conditions of the stented and diseased AVF cases. The diseased patient AVF inlet flow rates and geometry. **a)**, **b)**, and **c)** have been reproduced from figure 4.3 and display the stent strut details, stented case inlet flow rate profiles and the stented AVF geometry. The diseased case inlet boundary conditions **d)** and the diseased AVF geometry **e)**, with the annotated stenosis location, is displayed in the bottom half of the figure.

employing tetrahedral elements in the boundary layer as well. The average y^+ across the vessel wall at the maximum time-point was measured to be 0.28 thereby ensuring sufficient refinement to the wall. After initialising the flow domain with three simulation cycles run using the RANS turbulence model, the mesh was refined in the initial LES

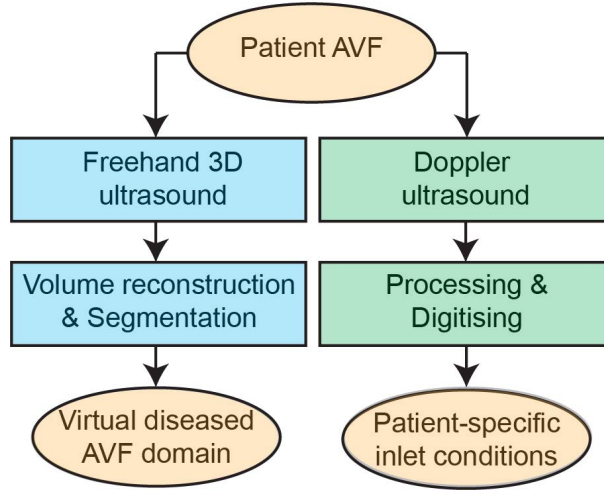


Figure 7.2: The sequence of steps followed to setup the domain and boundary conditions for the Large Eddy Simulations of the diseased AVF.

	Stented AVF	Diseased AVF
Proximal Artery - Re	451 - 884	141 - 375
Proximal Artery - Diameter (mm)	4.5	5.6
Distal Artery - Re	202 - 427	113 - 241
Distal Artery - Diameter (mm)	3.8	2.7
Proximal Vein - Re	481 - 964	242 - 363
Proximal Vein - Diameter (mm)	5.8	6.9
Outlet flow rate (L/min)	0.309 - 0.606	0.223 - 0.421
Cycle length (s)	1	1.2

Table 7.1: Comparison of the stented AVF with the diseased AVF.

cycles by using the mesh adaption strategy. As before (refer to section 4.3), the gradient of subgrid dynamic viscosity was used to mark approximately 1-5% of the total cells. This mesh adaption strategy was employed four times, i.e. twice at the maximum and minimum timepoints of the inlet pulsatile flow, which resulted in a domain consisting of 18 million elements. Further, consistent fluid physical properties were maintained across the stented and diseased cases, with the density set at 1060 kg/m^3 and the Carreau model with zero-shear rate viscosity set at $0.00345 \text{ Pa} \cdot \text{s}$.

The recorded heart rate of the patient at the time of the diseased AVF geometry scan was noted to be 50 bpm, which equated to a cycle length of 1.2 s. The same time-step

of 0.0002 s was used for the diseased AVF LES, which resulted in an average Courant number of 0.08 at the maximum inlet flow time-point.

The simulation was run for three cycles using the $k - \omega$ *SST* turbulence model to set the initial flow domain for the LES. As with the stented geometry simulations (elaborated in chapter 4), the Smagorinsky sub-grid scale model was used with a Dynamic Smagorinsky constant. After the mesh adaption was conducted using the LES, a further 12 cycles were run to ensure *TKE* and *TWSS* measurements, made throughout the domain and at specific time-points in the cycle, were sufficiently converged.

In contrast to chapter 6, to make comparisons of the quantified disturbances between the two cases, the *TKE* magnitude required a normalising procedure as the inlet flow rates of the two AVFs were different. A higher velocity field would usually generate larger *TKE*, however, normalising the disturbances will quantify the level of *TKE* relative to the general kinetic energy in each case thereby providing a more appropriate comparison. The average outlet velocity, U_{outlet} , was calculated by dividing the outlet flow rate, Q_{outlet} , by the outlet area. The average kinetic energy at the outlet, KE_{outlet} , was used to normalise *TKE* as shown in the equations (7.1) to (7.3).

$$U_{outlet} = Q_{outlet} / Area_{outlet} \quad (7.1)$$

$$KE_{outlet} = \frac{1}{2} * U_{outlet}^2 \quad (7.2)$$

$$TKE_{norm} = \frac{TKE}{KE_{outlet}} \quad (7.3)$$

Although normalisation of the WSS can be obtained following the Darcy Friction Factor (Çengel and Cimbala, 2014), absolute values are generally used even with comparisons across cases (Andersson et al., 2019; Manchester et al., 2021; Stella et al., 2019). Therefore,

the absolute $TWSS$ and the consequent normalisation with the phase averaged WSS will be used to analyse the fluctuations of the WSS as before.

7.2 Flow behaviour at the anastomosis

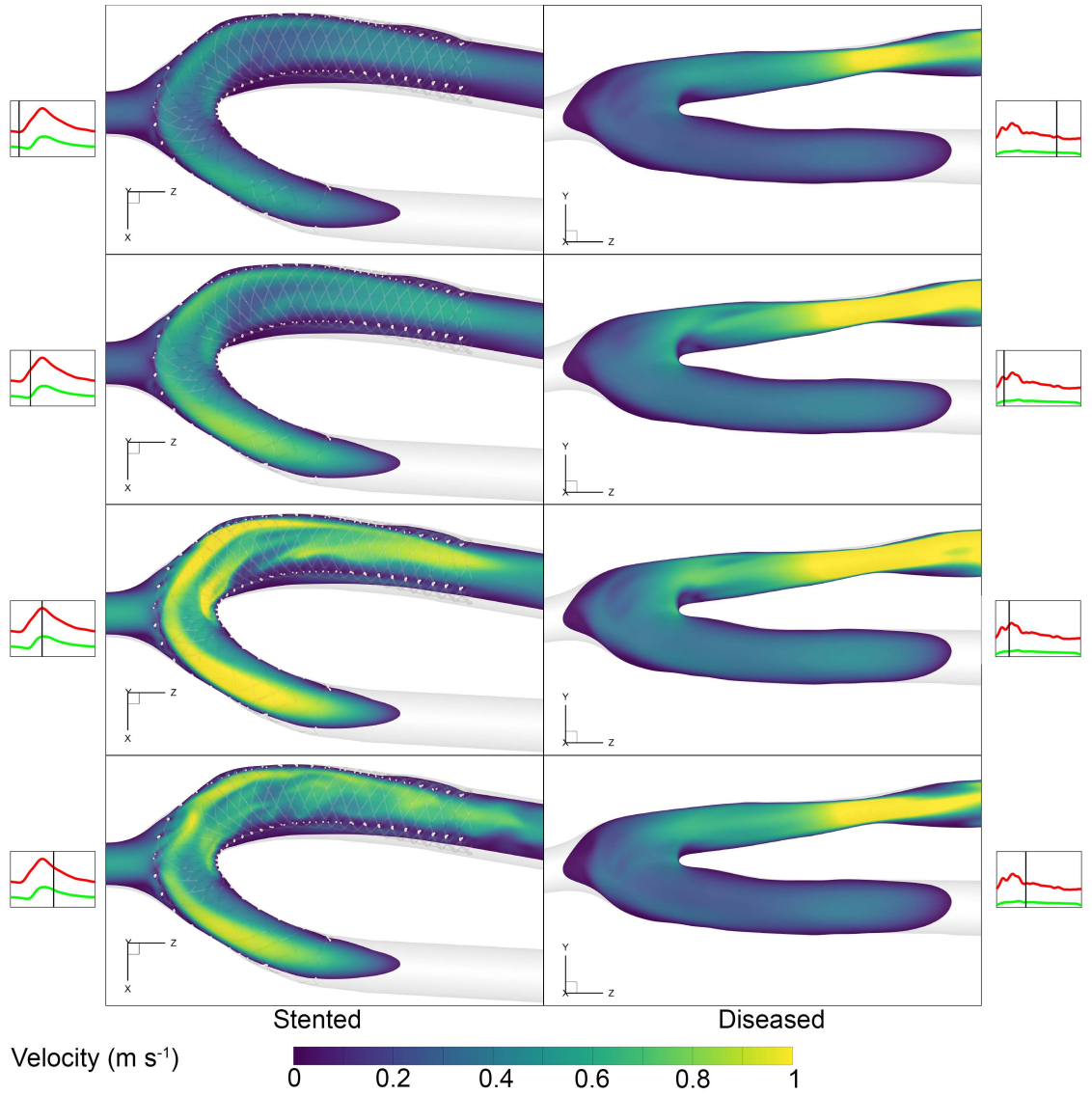


Figure 7.3: Contour plots of velocity magnitude ($|U|$) on the central plane of the anastomosis. The distribution of $|U|$ are shown at the minimum, acceleration, maximum and deceleration inlet flow time-points for both stented (left) and diseased (right) cases.

As previously outlined, the inlet flow rates of the diseased case are significantly lower in comparison to those of the stented case. To understand how these inlet conditions translate to the flow behaviour in the anastomosis region, phase-averaged velocity magnitude contour plots were created on the central plane of the anastomosis for both the stented and diseased cases. Results are presented in figure 7.3, where a clear increase in velocity magnitude can be seen in the proximal artery of the stented case, especially at the maximum time-point. A more unexpected observation in the diseased case is the presence of a low velocity magnitude region at the heel of the anastomosis that is persistent throughout the cycle. This highlights that even with the low inlet flow rate, a recirculation zone could be initiated due to the sharp angle of the anastomosis. The difference in the outlet flow is further shown on vessel cross sections close to the anastomosis (figure 7.4). At the slice closest to the anastomosis in the vein (slice 3) in the stented case, a high velocity flow region is seen to surround the central bulk flow region. Further, there is a more even spread of intermediate velocity (approximately 0.5 m s^{-1}) and a distinct low velocity region close to the heel of the equivalent slice (slice 6) of the diseased case.

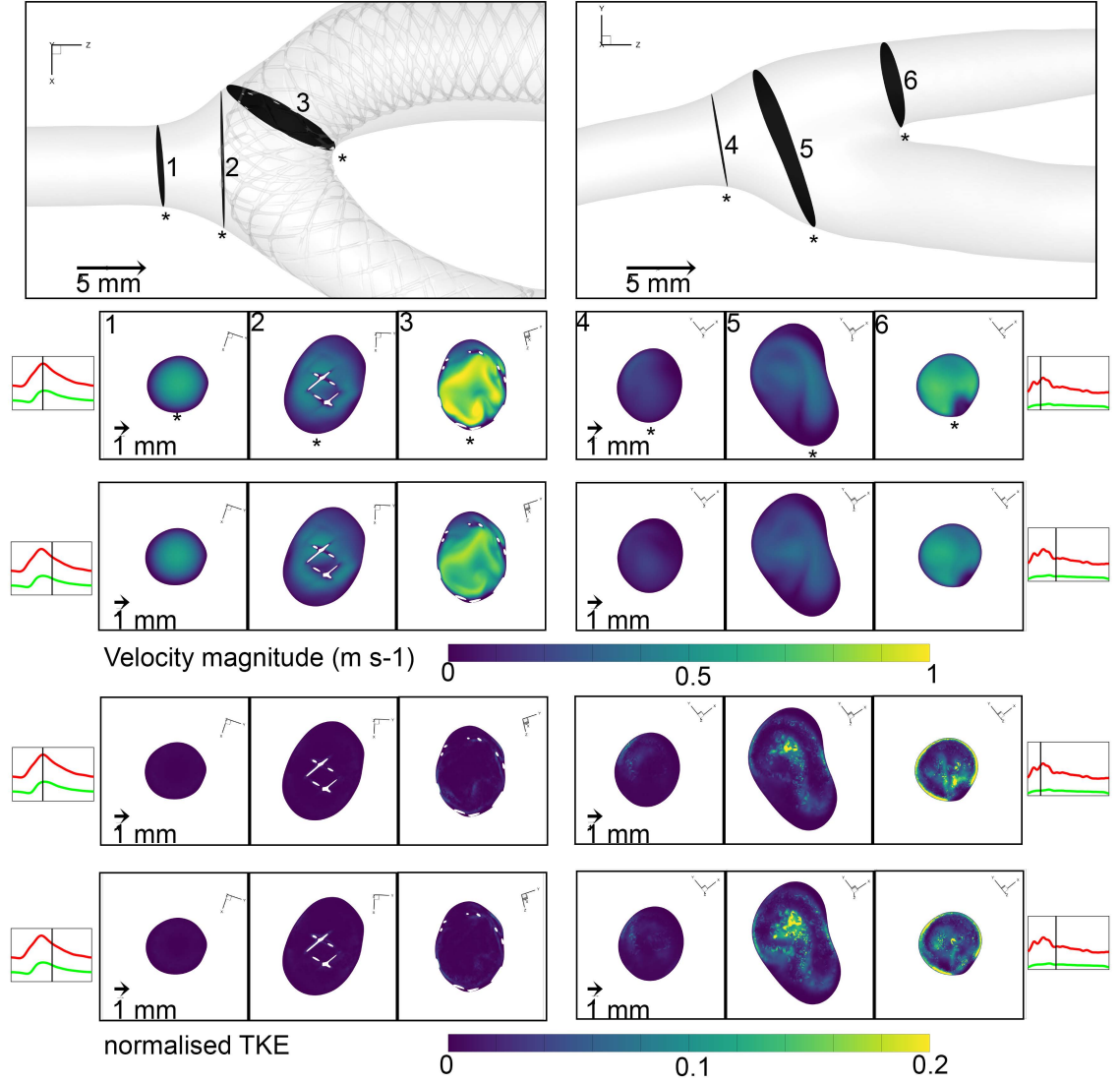


Figure 7.4: Contour plots of velocity magnitude and normalised TKE on vessel slices close to the anastomosis in both stented and diseased AVF geometries. The maximum and deceleration time-points have been used for these contour plots. The locations of the slices have been illustrated in the first row.

The streamlines of the flow in the diseased AVF, shown in figure 7.5, reveals the presence of highly disturbed behaviour within the anastomosis, albeit with a lower velocity magnitude to the stented case. The two inlet flow streams are observed to interact with one another and finally swirl towards the outlet vein. A swirling pattern of intermediate velocity magnitude is also observed in the vessel cross slice (slice 5), shown in figure 7.4, suggesting that the swirling behaviour is present in the central region of the anastomosis. This disturbed behaviour is initiated despite the lower velocity magnitude through the distal artery (see slice 4). The stented AVF case also has a moderate degree of streamlines that swirl around the central bulk flow region; however, the majority of the streamlines maintain a trajectory towards the outlet vein. The interaction between the two inlet flows is also much less understated, as seen in slice 2 in figure 7.4. This behaviour is partially attributed to the effect of the funnelling behaviour of the stent previously discussed in chapter 5. The larger anastomosis angle of the stented geometry also plays a role in reducing the swirling flow in the anastomosis.

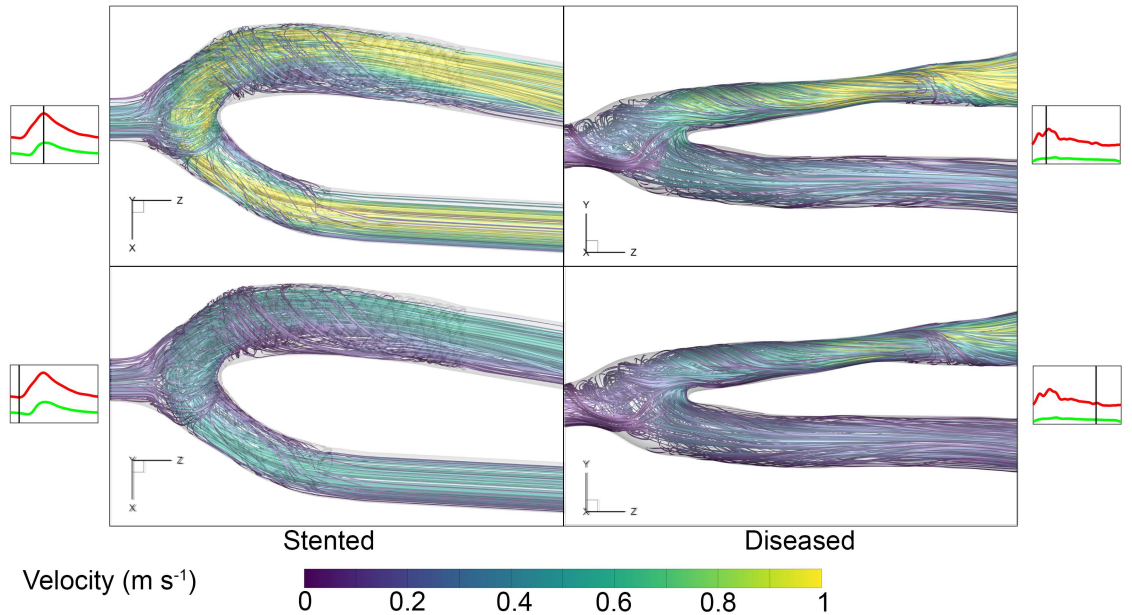


Figure 7.5: Streamline plots of the stented and diseased AVF cases at the maximum and minimum time-point. The streamlines are coloured with the velocity magnitude.

To investigate the fluctuations in the flow field, the distribution of normalised TKE on the central plane is shown in figure 7.6. The results reveal a clear difference in the dis-

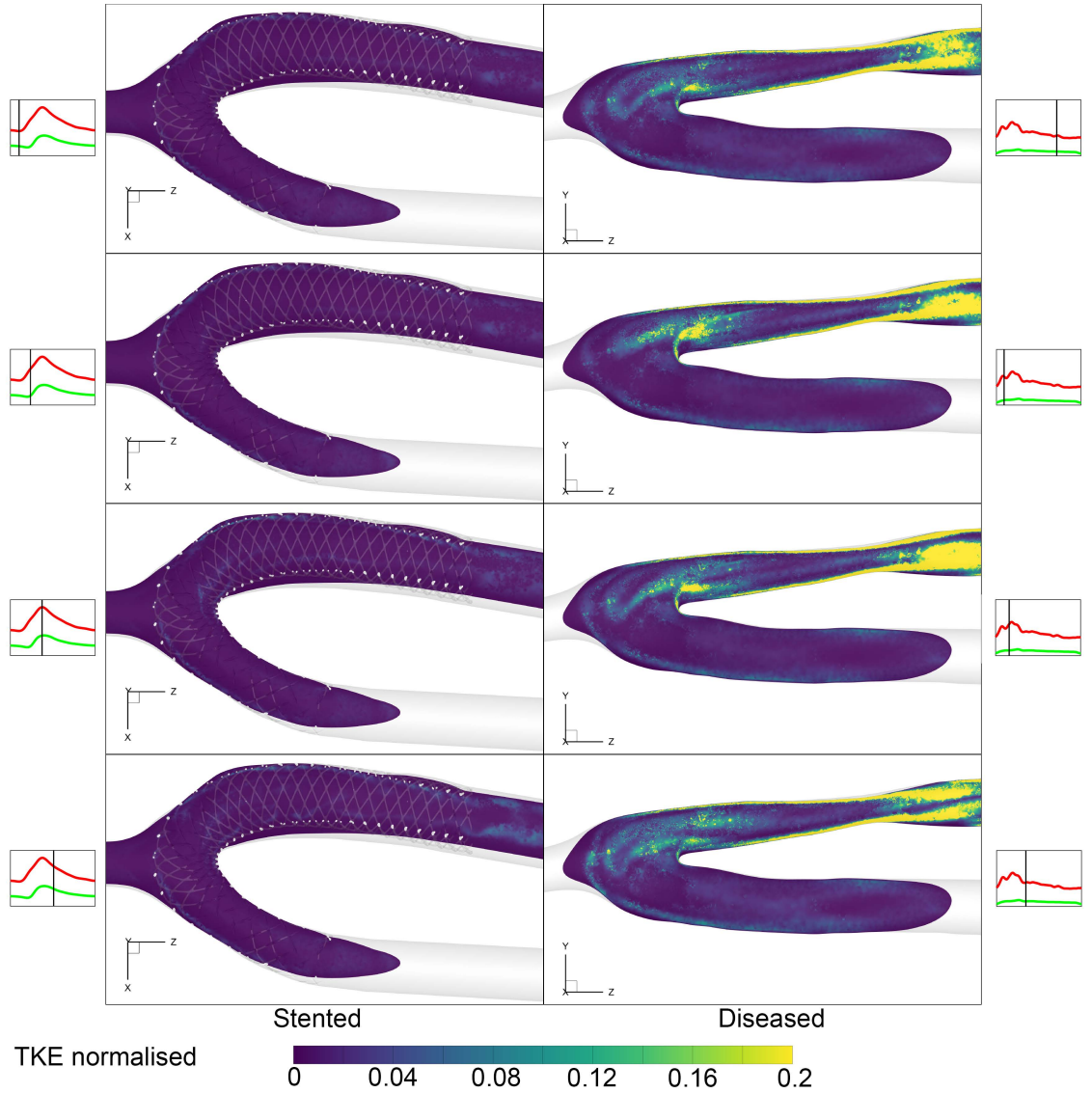


Figure 7.6: Contour plots of normalised TKE on the central plane of the anastomosis. The distribution is illustrated at the minimum, acceleration, maximum and deceleration inlet flow time-points for both stented (left) and diseased (right) cases.

turbances generated in the two AVF cases. Specifically, at the heel of the diseased AVF, where persistent recirculating flow was noted previously, a high region of normalised TKE is present. This is caused by the high velocity gradient developed due to the recirculation zone. The high normalised TKE locations, observed using isosurfaces in figure 7.7 appear close to the vessel wall at the heel region, which suggests that the shear stress at these regions would also experience a higher degree of fluctuations. The anastomosis region also

shows an intermediate level (about 0.1 of the outlet kinetic energy) of fluctuating energy. The swirling flow behaviour in the AVF leads to regions of varying velocities that contribute to the increase in disturbance. The spatial distribution of the disturbances, caused by the swirling flow in the anastomosis, is better observed in slice 5 of figure 7.4. The high normalised TKE is seen to follow a similar distribution as the swirling features of the velocity magnitude contour plots. The disturbances initiated due to the recirculation zone are noted in the normalised TKE contour plots on slice 6, however, additional regions of disturbances are also seen on this cross section which can be attributed to the transport of disturbances initiated in the anastomosis towards the outlet vein. The spatial distribution of the disturbed regions is marginally increased at the deceleration time-point of the cycle at the anastomosis (as seen in slice 5 of figure 7.4). However, the high normalised TKE regions marginally decrease in magnitude at the deceleration time-point at the heel of the diseased AVF anastomosis as seen in both slice 6 of figure 7.4 and the central plane in figure 7.6. As mentioned before, a crucial difference, further illustrated by the normalised TKE contours, on slices of figure 7.4 and the central planes of figure 7.6, is the significantly lower disturbance in the stented AVF geometry.

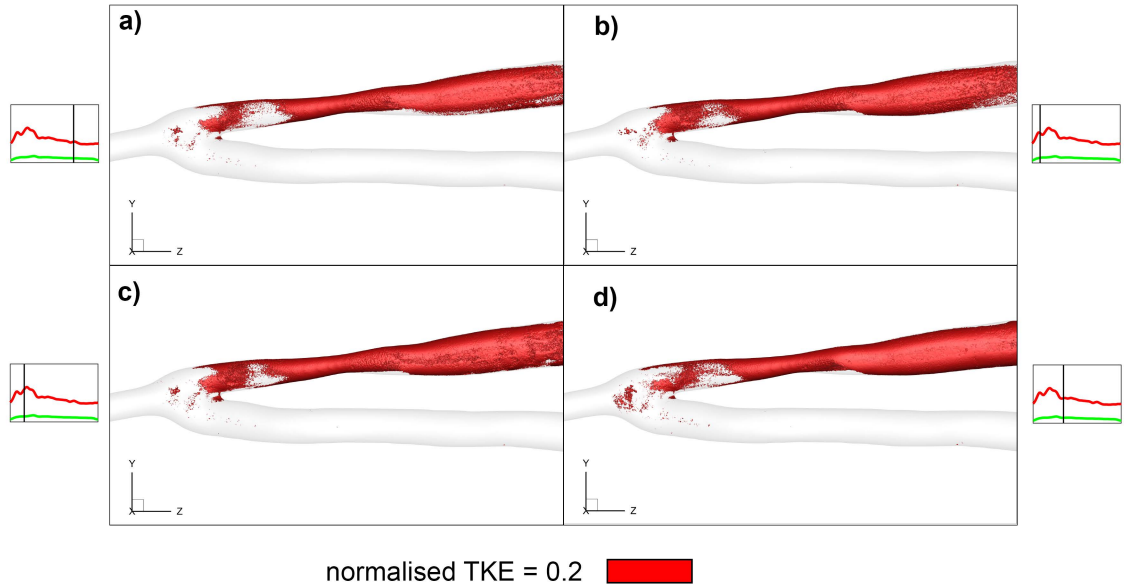


Figure 7.7: Isosurfaces of normalised TKE of value 0.2 at the a) acceleration, b) maximum, c) deceleration and d) minimum time-points of the diseased AVF.

7.3 Flow behaviour at the stenosis

The most noticeable feature of the diseased AVF is the stenosis, which underpins the diseased state. The narrowing of the blood vessel (stenosis) leads to an increase in the velocity across the stenosis as seen in the velocity magnitude contours of figure 7.3. There is a decrease in cross-sectional area by a factor of 2.5 leading to a comparable increase in the velocity at the stenosis. The increase in bulk flow velocity would subsequently lead to an increase in WSS, thereby leading to an environment where the vessel wall is faced with largely varying levels of WSS. Furthermore, the subsequent increase in velocity due to the decrease in cross-sectional area would lead to significant fluctuations in the bulk flow that would also incur fluctuations of the WSS.

As expected, the increase in velocity is consistent throughout the cycle, but importantly, it results in a high velocity jet formation proximal from the stenosis as the vessel cross-section increases. The jet flow initiating at the stenosis can be seen in the isosurfaces of velocity magnitude shown in figure 7.8. The formation of the jet leads to a swirling flow behaviour at the outer boundary of the jet as seen in the streamlines of figure 7.5.

In addition to the swirling flow, a shear layer surrounding the jet is formed due to the large velocity gradient in this region. Contour plots of vorticity at the central plane of the stenosis in figure 7.9 illustrate the formation of the shear layer. The stented AVF geometry is also susceptible to a shear layer formation due to the aggregation of the vortical flow over the stent struts across the vessel. At the deceleration time-point (second row of figure 7.9), the vortical flow in the lower regions of the stented edge is seen to interact with the bulk flow, as detailed in section 6.3 of chapter 6. There is a larger spread of high vortical regions in the diseased AVF geometry in comparison to the stented AVF geometry at both time-points. The temporally varying behaviour of the shear layer in the diseased geometry is better visualised on the vessel cross-sectional slices shown in the figure 7.10. Two clear counter-rotating vortical regions are noted in the slices proximal to the stenosis at the maximum time-point. The results reveal that Dean vortices are created due to the flow traversing across the sharp curve of the anastomosis. The Dean

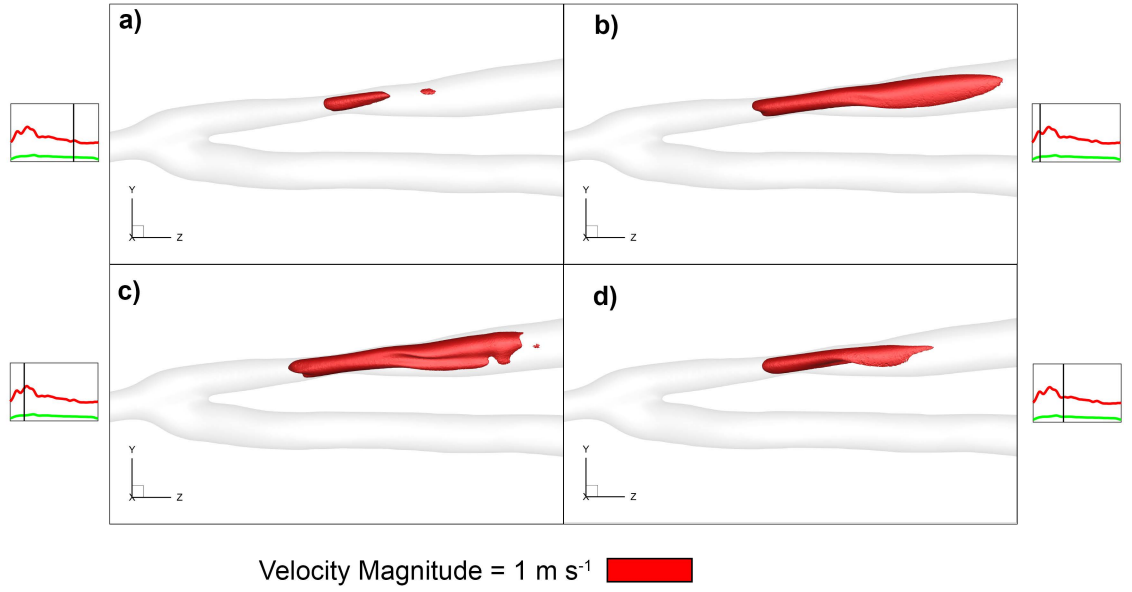


Figure 7.8: Isosurfaces of velocity magnitude ($|U|$) of value 1 m s^{-1} at the a) acceleration, b) maximum, c) deceleration and d) minimum time-points of the diseased AVF.

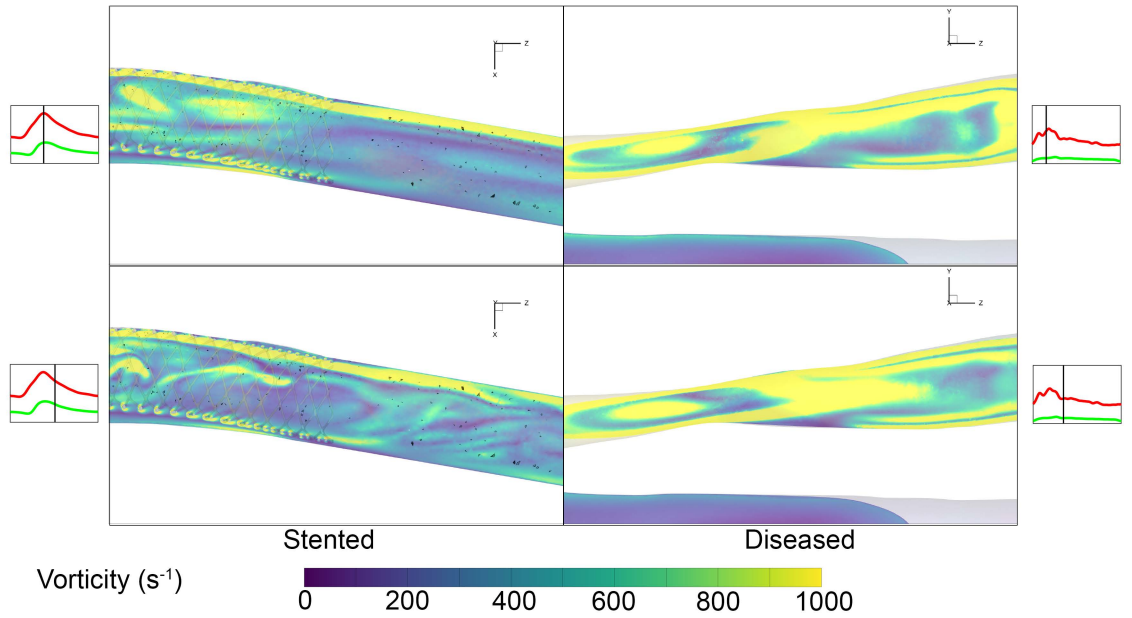


Figure 7.9: Contour plots of velocity magnitude ($|U|$) on the central plane of the stenosis and stent edge. The distribution of $|U|$ is illustrated at the maximum and deceleration inlet flow time-points for both stented (left) and diseased (right) cases.

vortices are squeezed at the stenosis and subsequently coalesced into the shear layer. The annulus shaped shear layer deforms and travels towards the vessel wall finally collapsing to dissipate the rotational energy. At the deceleration time-point, similar Dean vortical motion is detected, however, the annulus shaped shear layer breaks down much earlier (as annotated in red on slice 4 of figure 7.10). Studies conducted on an idealised eccentric stenosis model also noted the formation of a vortex ring that travelled downstream of the constriction and collapsed at the wall of the vessel (Varghese et al., 2007). The study also noted the increase in the localisation of turbulence after the peak of the inlet flow rate was reached.

7. Comparison between the stented and diseased AVF

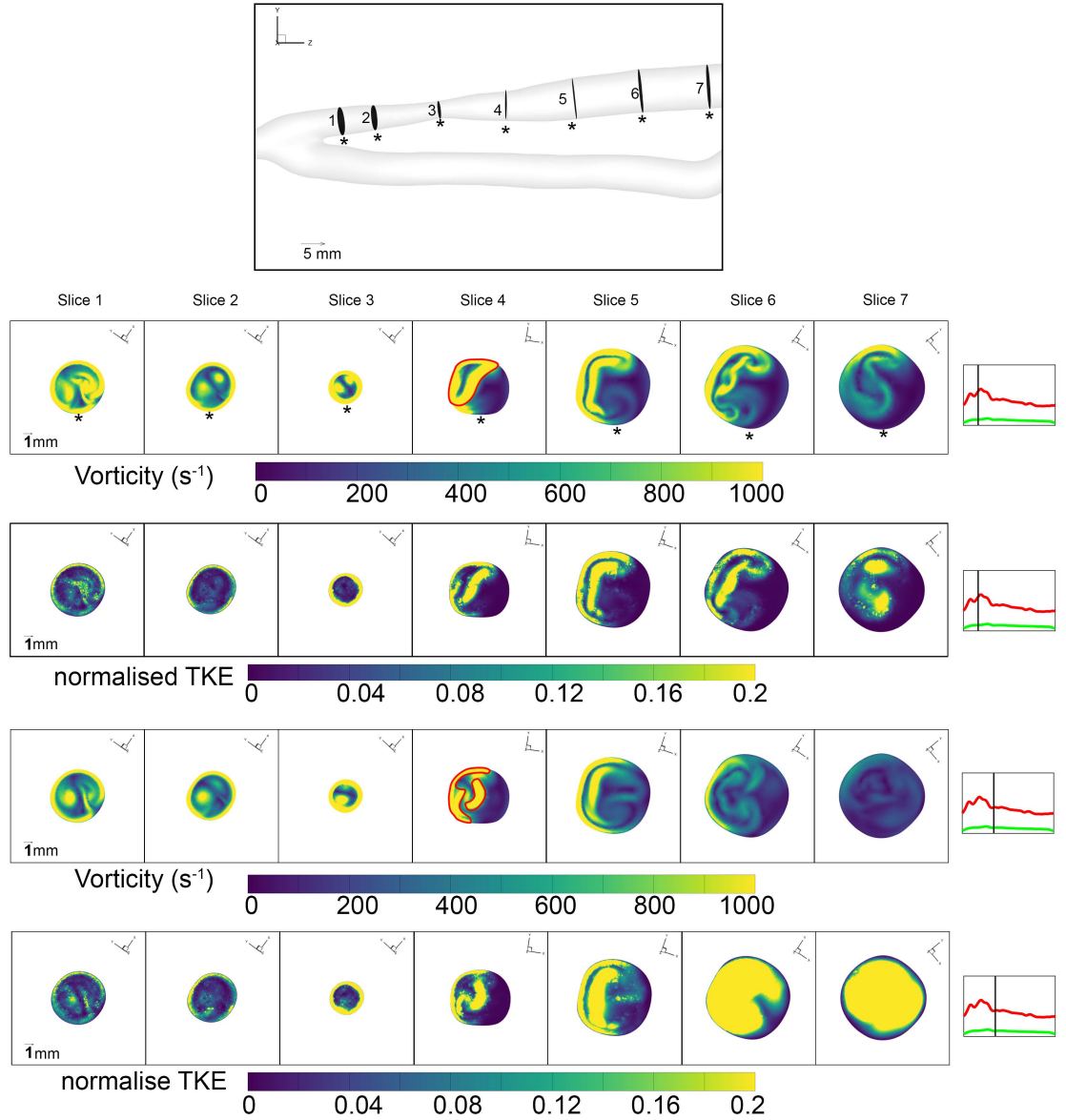


Figure 7.10: Contour plots of vorticity magnitude and turbulent kinetic energy at cross-sectional slices along the vein of the diseased AVF. The distributions have been plotted at the maximum and deceleration inlet flow time-pointse.

In comparison to the disturbances prevailing at the heel of the anastomosis, the magnitude of the normalised TKE is much larger at the stenosis as seen in the contour plots of figure 7.6. The spatial extent of the high normalised TKE is also much larger at the stenosis region as illustrated using isosurfaces of normalised TKE in figure 7.7. The location of the high normalised TKE is initially seen just proximal to the stenosis. However, after observing the contour plots on the vessel cross sections in figure 7.10, it is understood that the disturbances are primarily in the near-wall region. This is caused due to the steadily accelerating flow causing a larger velocity gradient at the wall, thereby initiating turbulent behaviour. However, proximal to the stenosis, the higher normalised TKE follows the boundaries of the shear layer.

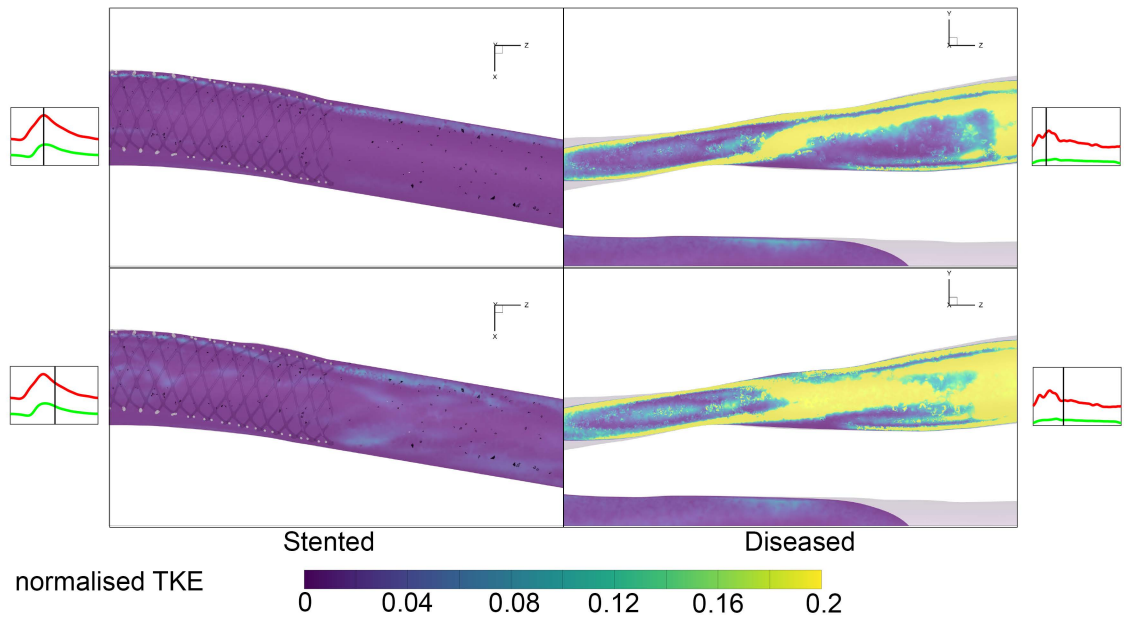


Figure 7.11: Contour plots of normalised TKE on the central plane of the stenosis. The distribution is illustrated at the maximum and deceleration inlet flow time-points for both stented (left) and diseased (right) cases.

At slice 7 at the maximum time-point, two large regions of high normalised TKE are noted to have broken away from the annulus shaped shear layer, which appears to be from the breakdown of the vortical motion. The spread of the normalised TKE at slices 6 and 7 at the deceleration time-point show a much larger spread in comparison to those at the maximum time-point. The sudden increase in turbulent energy at these slices

could be attributed to the breakdown of the shear layer emanating from the stenosis. As previously discussed in chapter 6, the elevated turbulent behaviour in the deceleration phase has been observed in other vascular geometries (Manchester et al., 2021; Valen-Sendstad et al., 2014). In this case, the rotational energy in the shear layer cannot be sustained with the decreasing inlet flow rate, potentially leading to a violent breakdown of the energy.

An important observation made in chapter 6 was that the disturbance level increased at the stent edge. However, in comparison to the disturbances created at the stenosis, the normalised TKE at the stent edge is significantly lower as shown in figure 7.11. This re-asserts the value of the stent implantation procedure which yields a far less turbulent environment in comparison to that of the diseased AVF.

7.4 Pressure drop across regions of the AVF

Although the goal of the stent implantation was to broaden the stenosed region of the vessel, the use of the interwoven nitinol stent across the anastomosis has yielded an AVF resembling the ‘smooth’ loop geometry as well. In comparison to the acute-angled geometry of the diseased AVF, the larger angle of the treated AVF is more conducive for the flow to traverse across the anastomosis. The use of pressure drop to assess the effectiveness of treatments has been used not only for AVF geometries (Carroll et al., 2020; Mallinson et al., 2020) but also in aorta models (Xu et al., 2021). Therefore, it is apt to use a similar methodology in this instance as well.

Instantaneous pressure drops at the maximum and minimum time-point have been quantified at specific cross-sectional slices. For all the ensuing calculations, the instantaneous pressure values were averaged across each slice. The calculation was conducted with the stented and diseased AVF geometries and care was taken to place the corresponding cross-sectional slices at equivalent distances from the anastomosis.

One cross-sectional slice each was created in the proximal and distal artery, approximately

5.5 *mm* away from the anastomosis. Pressure drop measurements were made from each of these two slices to the slice placed approximately 2.5 *mm* away from the anastomosis in the vein. These two measurements captured the pressure drop from both feeding vessels individually. To measure the pressure drop in the juxta-anastomotic region of the vein, a slice was created 5 *mm* away from the anastomosis in the vein and the pressure drop was calculated relative to the slice placed 2.5 *mm* away from the anastomosis in the vein. To make a comparison between the pressure drop of the stent edge and the stenosis, two slices, approximately 6 *mm* apart, were created with the stent edge and the stenosis in the centre. Finally, to compare the overall pressure drop across the vein, a slice was placed in the vein approximately 75 *mm* away from the anastomosis and the pressure drop was calculated relative to the vein slice located 2.5 *mm* away from the anastomosis. The spatial location of the slices has been illustrated in figure 7.12 with the corresponding pressure drop measurements.

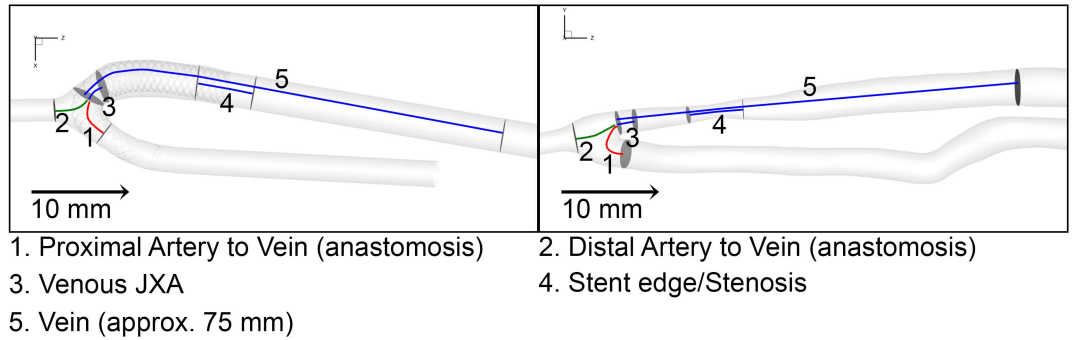


Figure 7.12: Location of pressure drop measurements for both the stented and diseased AVF geometries.

Since the two AVF geometries experience different inlet flow rates, the pressure drop (ΔP) was normalised using flow rate values which resulted in the calculation of instantaneous hydraulic resistance ($R_{hyd.}$). For locations 1 and 2, the pressure drops were divided by the inlet flow rate (Q_{inlet}) in the proximal artery and distal artery, respectively, using equation 7.4. However, all the other pressure drop measurements were divided by the outlet vein flow rate (Q_{outlet}) using equation 7.5. The resulting hydraulic resistance measurements are recorded in table 7.2 and illustrated in figure 7.13.

Table 7.2: Hydraulic resistance.

Hydraulic Resistance (mmHg / L / min)	Stented (Min./Max.)	Diseased (Min./Max.)
1. Proximal Artery - Vein (near anastomosis)	0.52/0.89	1.54/2.52
2. Distal Artery - Vein (near anastomosis)	2.67/3.32	7.95/14.12
3. Venous JXA	0.65/1.23	0.74/1.04
4. Stent edge/Stenosis	0.34/0.62	9.75/14.10
5. Vein (approx. 75 mm)	3.38/5.34	16.75/24.72

$$R_{hyd.} = \frac{\Delta P}{Q_{inlet}} \quad (7.4)$$

$$R_{hyd.} = \frac{\Delta P}{Q_{outlet}} \quad (7.5)$$

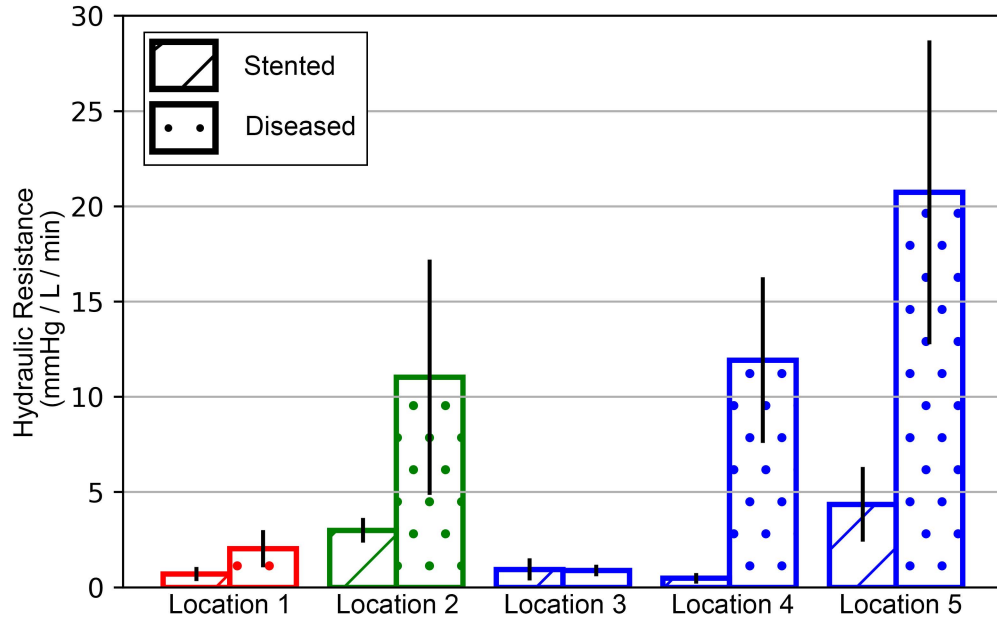


Figure 7.13: Graph of the hydraulic resistance (in mmHg / L / min) calculated at the locations stipulated in figure 7.12 for the stented and diseased AVF cases. The graph displays the mean resistances along with the range.

A consistent finding throughout all locations except location 3 is that the hydraulic resistance is higher in the diseased case when compared to the stented case. The hydraulic resistance values from the proximal artery to the vein (location 1) are approximately three times higher in the diseased AVF case while the values from the distal artery to the vein (location 2) are approximately four times higher in the diseased case. The swirling flow noted in the anastomosis of the diseased case is a major contributor to the increase in hydraulic resistance in this region. This behaviour is significantly mitigated in the stented case due to the funnelling effect caused by the stent. This enables the proximal artery inlet flow to be effectively guided towards the vein while minimising disturbances created from the interaction with the distal artery inlet flow.

The hydraulic resistance calculated at the juxta-anastomotic region of the AVF is more comparable between the two cases. More turbulent behaviour is transported in the bulk flow region of the diseased AVF case. However, the friction caused by the rotating vortical flow near the stent wall could be contributing to the pressure drop that the flow needs to overcome in the JXA thereby accounting for the similarity in hydraulic resistance values between the stented and diseased AVF cases.

The hydraulic resistance across the stenosis is more than an order of magnitude larger than that across the stent edge, once again justifying that the negative effect of the disease far outweighs the drawback of the treatment procedure. The hydraulic resistance value across the stenosis is the main contributor to the hydraulic resistance value of the diseased vein which is approximately five times larger than the hydraulic resistance of the stented vein. Assuming that the overall cardiac flow rate from the patient's heart remained the same before and after the stent implantation, it is quite evident that the increased pressure drop caused by the stenosis has led to the lower flow rates at the inlets of the AVF.

7.5 Comparison of WSS imparted on vessel walls

The previous sections were focused on assessing and comparing the behaviour in the bulk flow by not only calculating detailed metrics such as normalised TKE at specific time-points but also by measuring general metrics such as pressure drop. The impact of the discussed bulk flow characteristics on the vessel wall will be explored in this section using cycle averaged metrics such as time-averaged wall shear stress (TAWSS), oscillatory shear index (OSI) and transverse wall shear stress (transWSS) along with detailed cycle-to-cycle variance measurements such as turbulent wall shear stress (TWSS) and normalised TWSS. To clearly visualise the distribution of these metrics across the vessel wall, a vessel wall unwrapping methodology (figure 7.14), detailed in chapter 6, was utilised. The WSS behaviour will be assessed across the vessel walls of the distal artery (anastomotic and juxta-anastamotic regions) and vein (juxta-anastomotic and stenosis/stent-edge regions) of both the diseased and stented AVF.

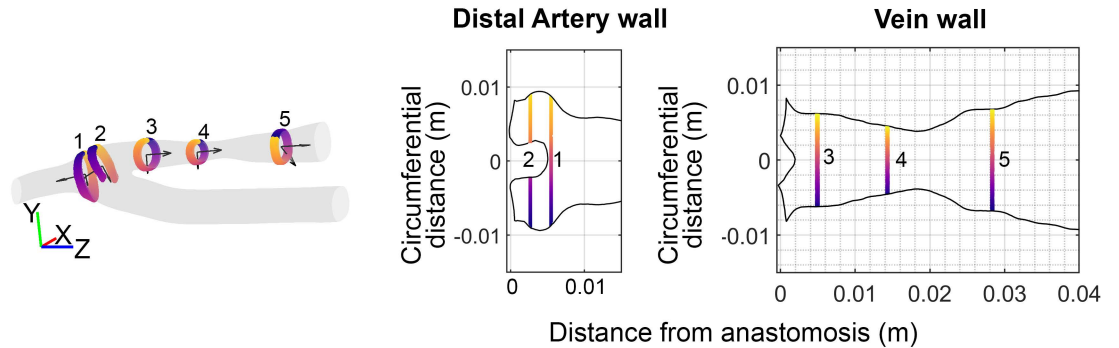


Figure 7.14: Example of unwrapping the 3D vessel wall locations onto a 2D space using local vectors constructed from centerline node locations. The colour bar of the cross-sectional slices assist with understanding the 3D location of the wall element on the corresponding 2D plots.

7.5.1 WSS characteristics at the distal artery

A clear band of low TAWSS is seen in the distal artery close to the anastomosis in the stented geometry (see figure 7.15). Conversely, a decrease in the TAWSS of the distal

artery close to the anastomosis is not apparent for the diseased AVF as the general flow velocity is low in this vessel contributing to low shear forces.

The distribution of high OSI is limited to a few isolated points in the anastomosis of the stented AVF. In contrast, a curved streak of high OSI is noticeable at the anastomosis of the diseased AVF. The swirling disturbed flow noted in figure 7.5 is evidently contributing to oscillatory shearing forces. The impact of the swirling disturbances would also cause multi-directional shearing forces throughout the cycle as illustrated by the high transWSS regions of the diseased AVF. Similar increases in transWSS are much less pronounced in the stented AVF with these regions localised closer to the heel of the anastomosis.

There is an increase in the cycle-to-cycle fluctuations of WSS at the anastomosis of the diseased AVF (figures 7.16 and 7.17). The increase is most noticeable at the maximum and acceleration time-points of the inlet cycle, however, the significant fluctuations (quantified by the normalised WSS) are present in a curved streak across the anastomosis, similar in pattern to the OSI distribution, at all recorded time-points. In this case, the highlighted feature is caused by the shear force fluctuations converging to locations where low phase-averaged WSS exist. In comparison, the distribution of TWSS and normalised TWSS at the anastomosis of the stented AVF vessel remain at low levels at all time-points.

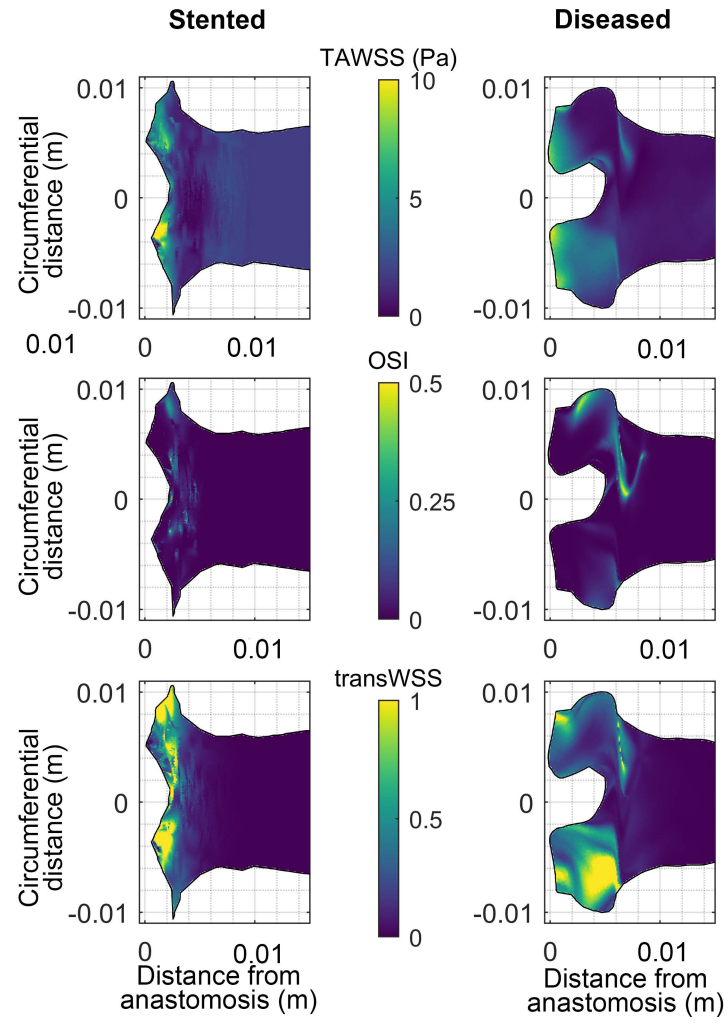


Figure 7.15: Distribution of TAWSS, OSI and transWSS across the distal artery close to the anastomosis of both stented and diseased AVF geometries.

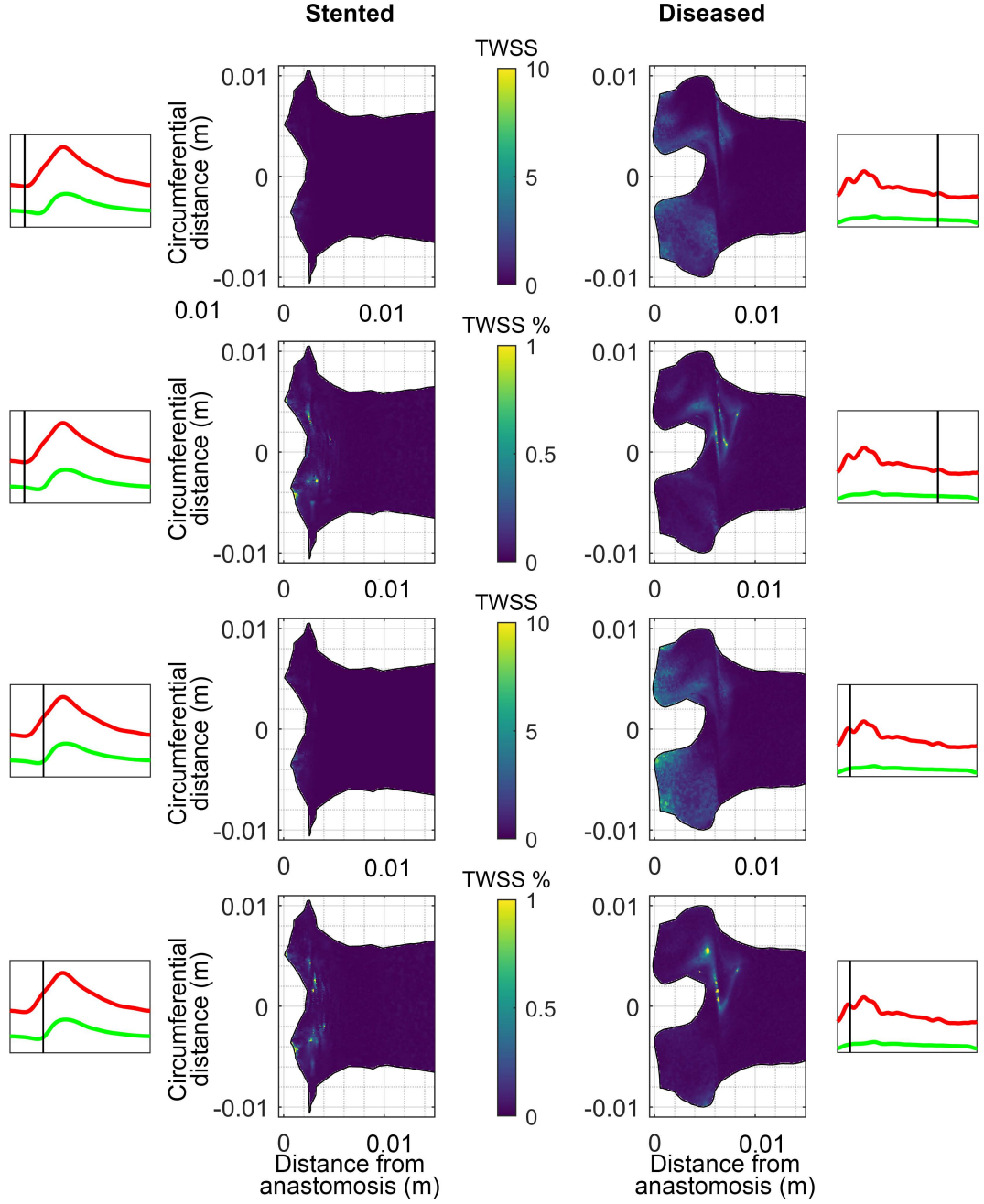


Figure 7.16: Turbulent Wall Shear Stress (TWSS) and normalised TWSS distribution across the distal artery at the minimum and acceleration time-points for both stented and diseased AVF geometries.

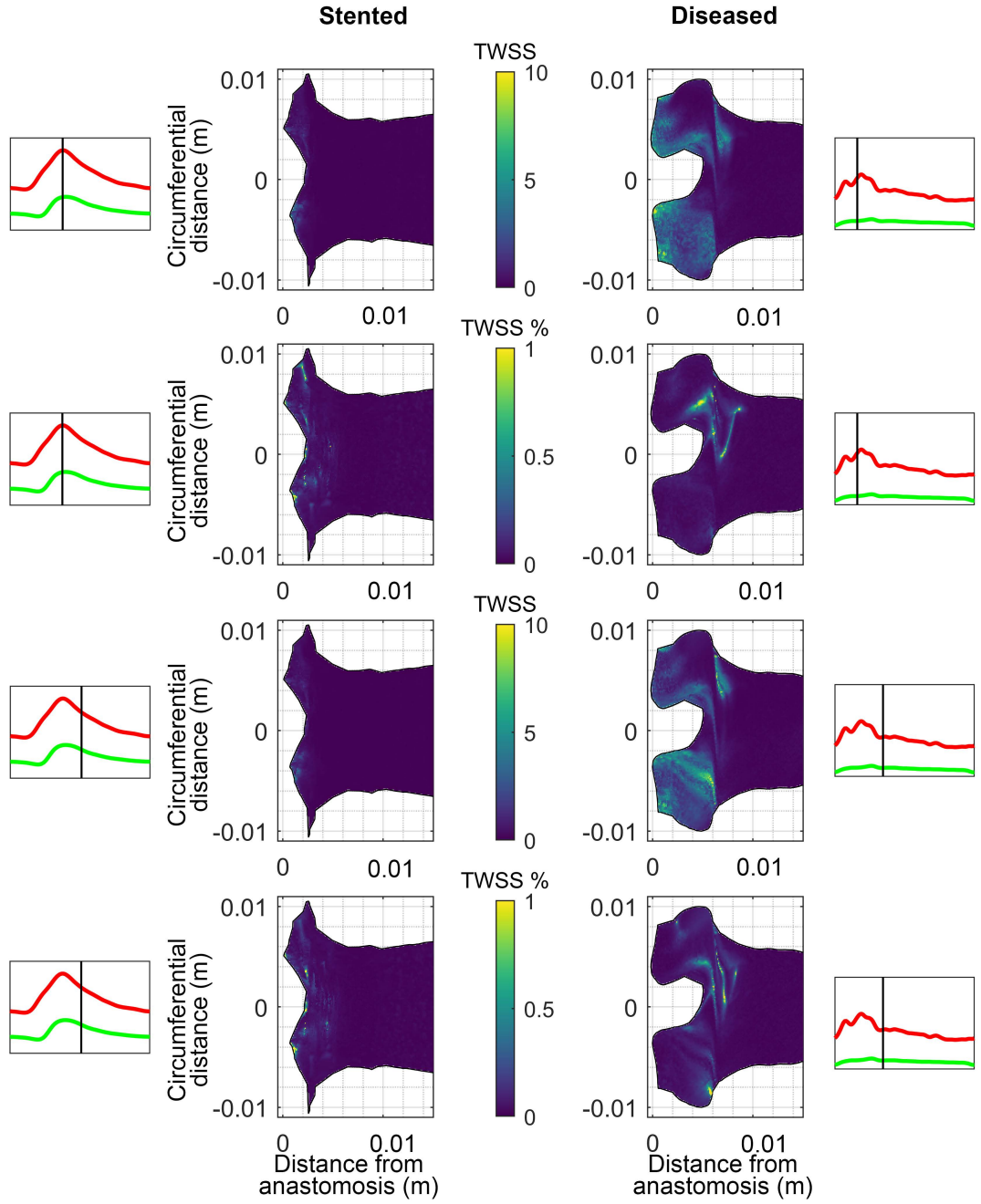


Figure 7.17: Turbulent Wall Shear Stress (TWSS) and normalised TWSS distribution across the distal artery at the maximum and deceleration time-points for both stented and diseased AVF geometries.

7.5.2 WSS characteristics at the proximal vein

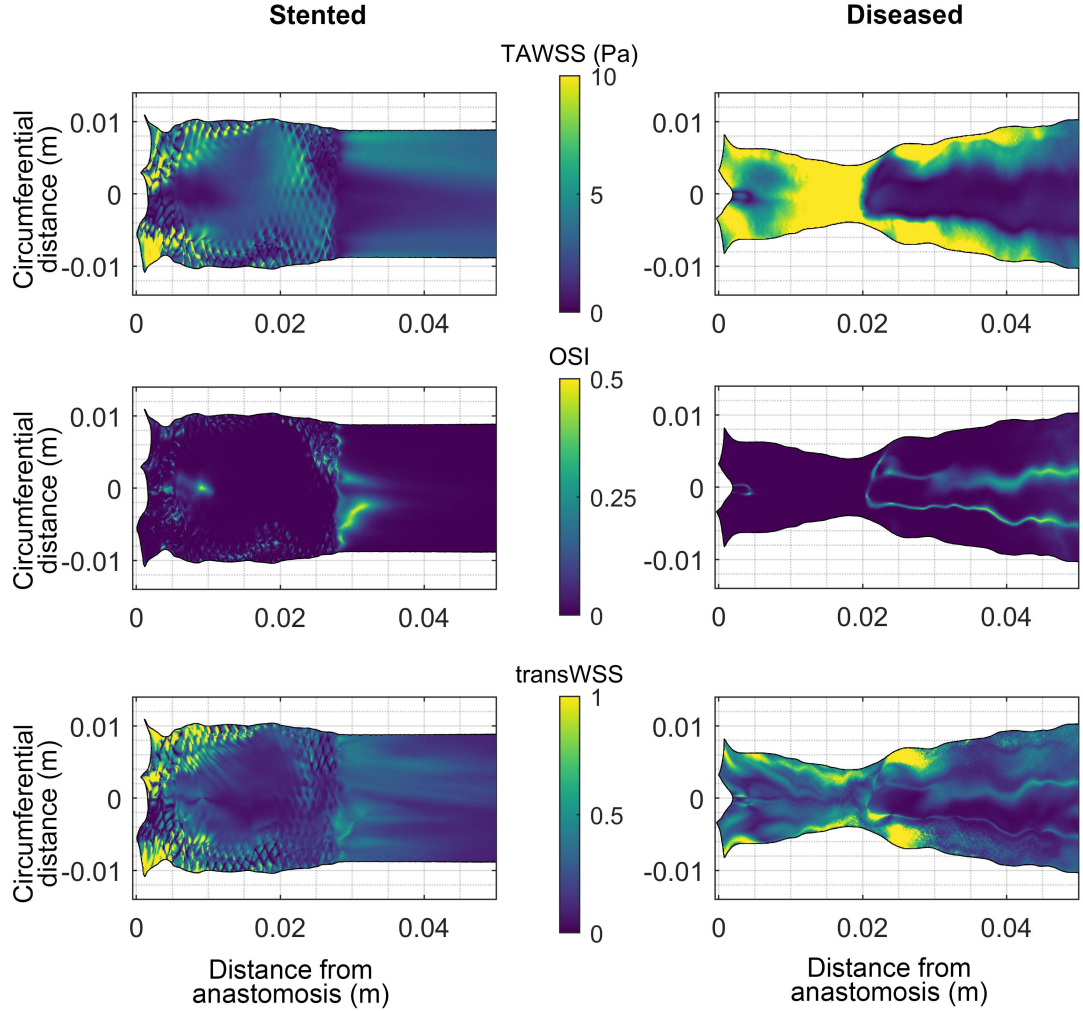


Figure 7.18: Distribution of TAWSS, OSI and transWSS across the proximal vein of both stented and diseased AVF geometries.

The distributions of the cycle-averaged WSS metrics across the vein (figure 7.18) reveal that the two main areas of concern are the juxta-anastomotic region and the stenosis region. The juxta-anastomotic region of the diseased AVF is faced with a small low TAWSS region that is surrounded by high OSI and transWSS. The recirculating flow present at the heel of the anastomosis creates a low velocity gradient leading to low TAWSS. The change in the extent of the recirculation zone across the cycle would lead to high OSI, while the general disturbance created in the vicinity leads to high levels of transWSS.

This behaviour is very similar to that seen in the stent-absent AVF of chapter 6, where the recirculation zone created a large ring of high OSI around the low TAWSS region. However, the ring of high OSI is much smaller in the diseased AVF because of the low velocity flow carrying comparatively lower momentum resulting in a shorter recirculation zone. There is a presence of a low TAWSS region at the heel of the stented AVF model as well; however, the clearly defined ring of high OSI does not present itself suggesting that the recirculation zone is more stable across the cycle. Additionally, the high transWSS regions lie predominantly adjacent to the stent struts resulting from the high vortical flow over the struts.

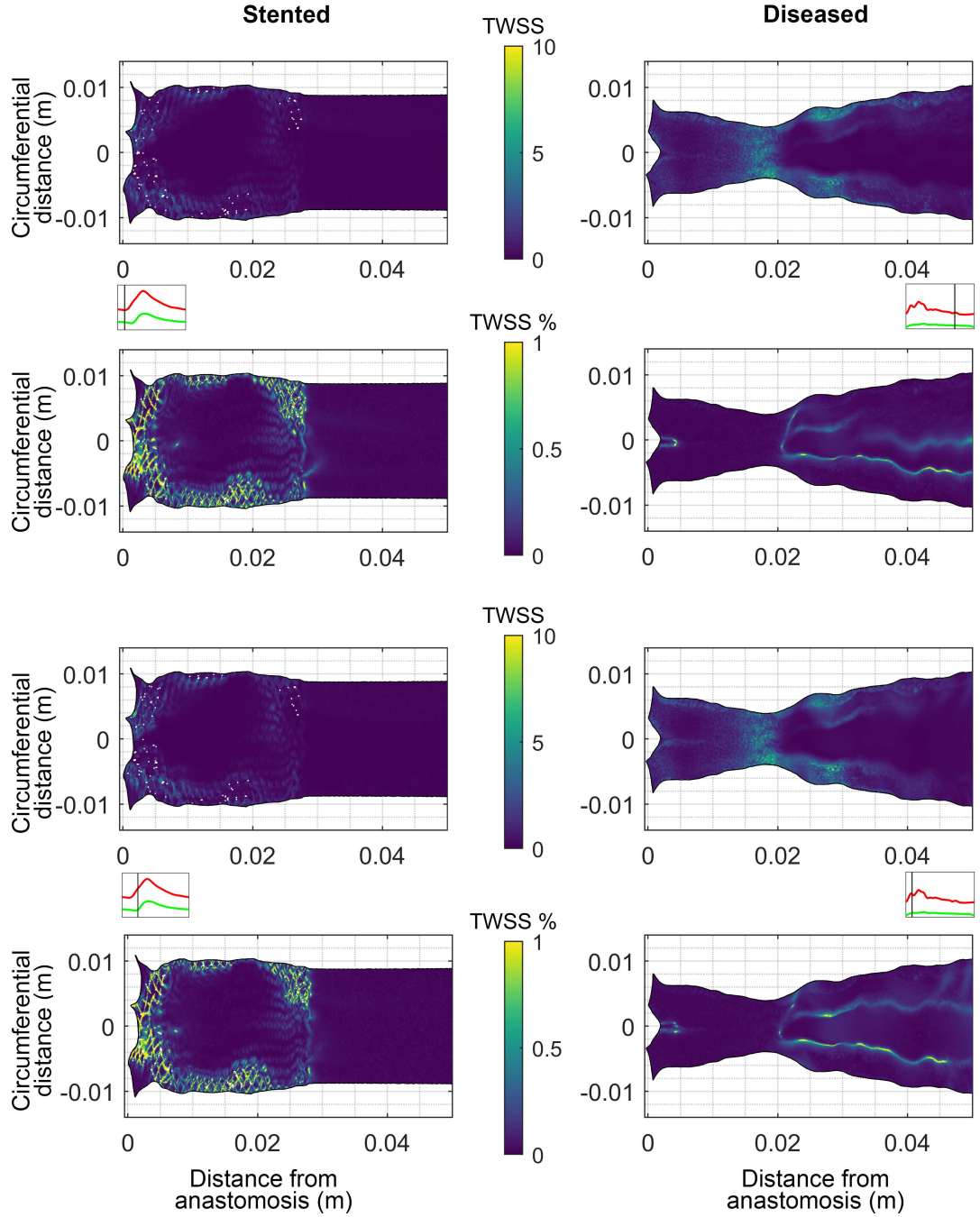


Figure 7.19: Turbulent Wall Shear Stress (TWSS) and normalised TWSS distribution across the proximal vein at the minimum and acceleration time-points for both stented and diseased AVF geometries.

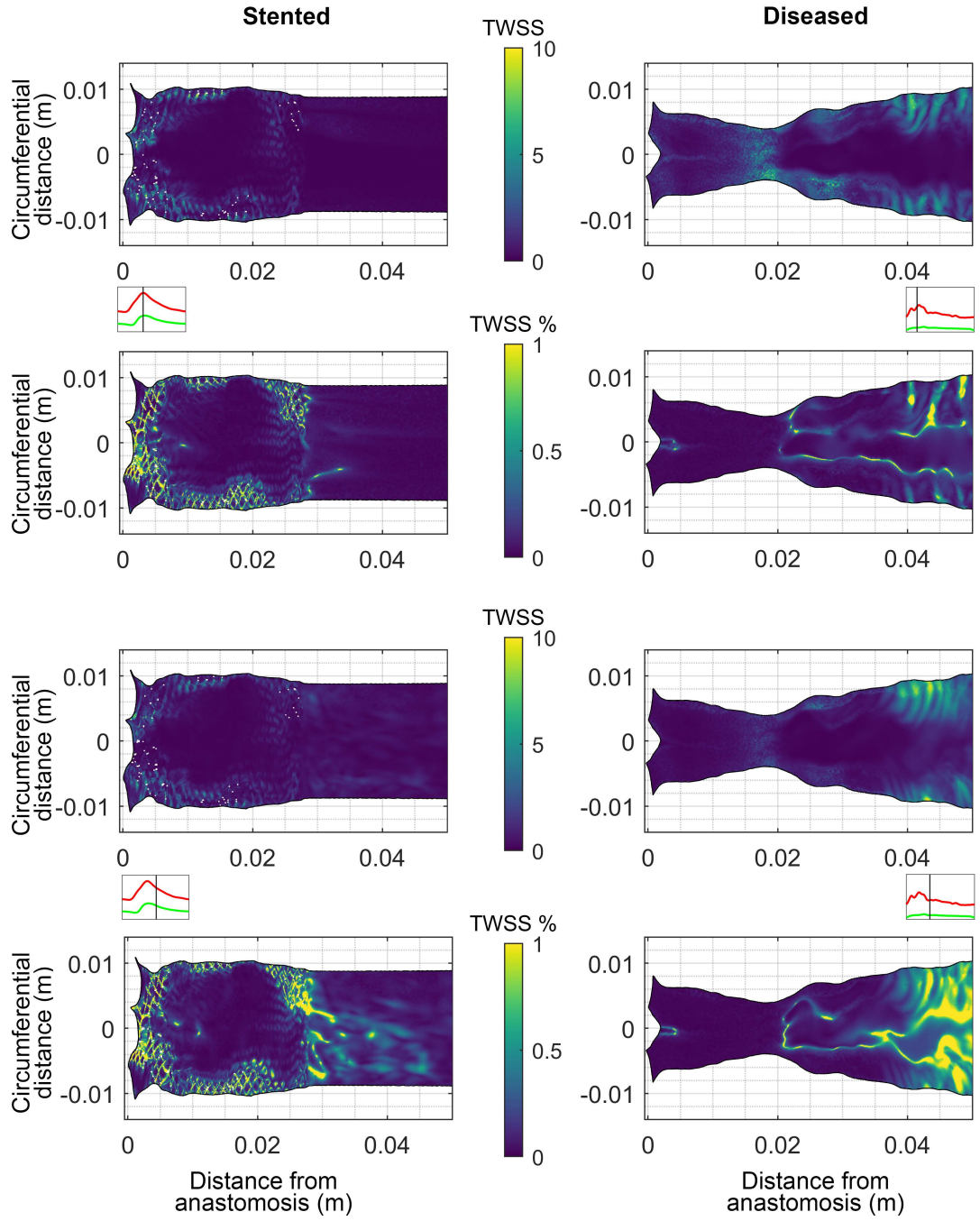


Figure 7.20: Turbulent Wall Shear Stress (TWSS) and normalised TWSS distribution across the proximal vein at the maximum and deceleration time-points for both stented and diseased AVF geometries.

In addition to the oscillatory and disturbed behaviour occurring across the cycle, fluctuations from cycle-to-cycle have also been noted at the heel of the anastomosis in the diseased AVF as illustrated in the contour plots of TWSS and normalised TWSS across the vein in figures 7.19 and 7.20. The spatial extent of the normalised TWSS at the heel is very similar to that of the OSI as the behaviour is consistent at all the recorded time-points. As before, the spread of the high fluctuations in the stented AVF close to the heel is largely at the stent strut regions. The mitigating factor of this behaviour is that the fluctuations are present in the upper layers of the vessel where higher WSS are present. Because of the stent malapposition at the lower section of the vein (closer to the heel of the anastomosis), the effects of the vortical flow near the stent struts have less impact on the vessel wall in that region.

Although the behaviour of WSS at the heel of the diseased AVF is of concern, it is outweighed by the dynamics of the WSS caused by the stenosis. A large low TAWSS region is initiated at the stenosis site and spreads for at least 30 *mm* downstream. This low TAWSS region is surrounded by high TAWSS regions on the upper side of the vessel caused by the asymmetric constriction forcing the high velocity flow closer to the upper portion of the vessel. As expected, the TAWSS continuously increases with the increasing flow velocity up to the stenosis site.

The large low TAWSS region is bordered by high OSI separating it from the high TAWSS regions of the upper vessel wall. The asymmetric jet flow that is created at the stenosis leads to a recirculating low flow region. As with the flow at the heel, the dynamic nature of this recirculation zone contributes to the back and forth movement of the WSS vectors at the boundary of the zone leading to high OSI. High levels of transWSS were also noted at the upper edge of the vessel close to the stenosis. This could be caused by the swirling flow that traverses around the jet and fills the void created in the low velocity region of the lower section of the vessel as seen in the streamline plot in figure 7.5. The high transWSS in this region suggest that this three-dimensional flow behaviour close to the vessel wall has some fluctuating characteristics that are conveyed from the boundary of the jet. There is a low TAWSS - high OSI region downstream of the stent edge in the

stented AVF, however, this region spreads for about 5 *mm* at most.

The WSS fluctuations in the diseased AVF increase at the stenosis and this corresponds to the high near-wall normalised *TKE* that was noted from figure 7.10. As with the heel, the high normalised TWSS spread at all recorded time-points was similar to that of the OSI. The importance of assessing the cycle-to-cycle WSS fluctuation comes to light with the plots at the maximum and deceleration time-points as seen in figure 7.20. Waves of high TWSS and normalised TWSS are noted approximately 20 *mm* downstream of the stenosis and the spacing of these waves are seen to decrease at the deceleration time-point. The jet flow loses momentum and breaks down, creating disturbed flow that travels further down the vein. The breakdown of the jet is worsened with the decrease in inlet flow, similar to the behaviour noted in DNS studies of symmetric (Blackburn and Sherwin, 2007) and asymmetric (Varghese et al., 2007) stenosis models with pulsatile conditions.

The TWSS levels remain low downstream of the stent edge in the stented AVF case, however, there is an increase in fluctuations noted at the deceleration time-point. Once again, the absolute and relative TWSS values were lower at the stent edge in comparison to the stenosis, thereby reassuring that the impact of the stenosis is far more detrimental than that of the stent edge.

7.6 Conclusion

Additional Large Eddy Simulations were conducted on the diseased AVF geometry (prior to stent implantation) of the same patient that underwent the treatment procedure. The diseased AVF consisted of a stenosis and the inlet flow rates were much slower than those of the stented AVF. Care was taken to follow the same methodology for patient data retrieval and computational domain setup. An additional step of normalising the turbulent kinetic energy measurements with the mean outlet kinetic energy was done to allow comparisons of the fluctuations with that of the stented AVF.

Swirling disturbed flow was noted at the interface of the two inlet flows in the diseased

AVF, and a short recirculation zone at the heel of the anastomosis was present despite relatively low inlet flow rates. The primary source of turbulence generation was caused by the behaviour associated with a jet flow formation at the stenosis site. The breakdown of the shear layer surrounding the jet flow created elevated levels of normalised TKE downstream of the stenosis which spread at the deceleration time-point of the inlet flow. The levels of flow disturbances far outweighed those noted in the stented AVF despite the diseased case having lower inlet flow rates.

Hydraulic resistance measurements yielded the fact that a significant pressure drop was built from the distal artery to the vein in the diseased AVF. However, the main reason for the additional resistance in the diseased AVF was the constriction at the stenosis site and is likely to be the main contributor to the lower inlet flow rates.

The swirling flow in the anastomosis had an effect on the shear forces on the vessel wall, where streaks of low TAWSS and high OSI were noted. Similarly, low TAWSS together with high OSI and transWSS were noted at the heel of the anastomosis, where recirculating flow was present. The normalised TWSS also followed a similar pattern asserting that variations in WSS were not only occurring throughout the cycle but also from cycle-to-cycle. As expected, a large low TAWSS region surrounded by high OSI and high transWSS was noted downstream from the stenosis. The TWSS measurements at the maximum and deceleration time-points revealed the impact of the breakdown of the jet flow on the vessel wall. A sequence of high TWSS regions was noted and the spacing decreased at the deceleration time-point.

The haemodynamic environment of the diseased AVF is one that is of high disturbances mainly caused by the stenosis site. However, the sharper angle of the anastomosis also yields recirculation zones and high pressure drops even with lower flow rates traversing across this region. The ill effects of this environment are more severe than the limited effects of the disturbances caused by the stent edge, thereby justifying the stent implantation treatment avenue from a haemodynamic standpoint.

Chapter 8

Conclusions and Future Research

The main aim of this thesis was to investigate the haemodynamic influence of a stent implantation in an arteriovenous fistula, thereby understanding an important aspect of a clinically successful treatment avenue. To this end, the effect of the stent was assessed with high-resolution simulations of a patient-specific AVF with and without the presence of the device. The simulations were complemented with tomographic particle image velocimetry measurements of the AVF with realistic flow conditions, providing much needed experimental data of the complex haemodynamic environment. Additionally, comparisons of the flow field of the diseased AVF have been made with that of the treated AVF to gain a comprehensive understanding of the alteration of the flow environment following the treatment.

8.1 Key outcomes

Disturbed blood flow is known to initiate disease pathways in vessels. Accordingly, complex transitional flow has been noted in the AVF using numerical methods, specifically noting the dependence of the flow behaviour on the geometry and boundary conditions. A benchtop model, inclusive of a silicone-based phantom of a patient-specific AVF geometry connected to a tubing network incorporating resistances and compliances that replicate the physiological flow conditions, was used for tomographic particle image velocimetry measurements. In doing so, high turbulent kinetic energy (TKE) in the order of approximately 10% of the outlet kinetic energy, calculated using 20 cardiac cycles, was found originating at the anastomosis and was conveyed along the vein. Large eddy simulations were conducted on the same geometry capturing the onset of turbulent fluctuations at the interface of the inlet flow streams and at the heel of the anastomosis using TKE measurements over 12 cycles. Oscillation frequencies noted in flow rate measurements in the vein of the stent-absent LES case were confirmed to be stemming from the distal floor of the anastomosis by observing equivalent oscillation frequencies in the time-resolved Tomo-PIV field. Additionally, a large recirculation zone at the heel of the anastomosis was noted which resulted in a region of low TAWSS surrounded by a ring of high OSI.

A key objective of this thesis was to understand the impact that stent implantation had on the haemodynamic environment within the AVF. Micro-CT images of a stented silicone AVF phantom provided the capability to capture the small stent features in the same domain as the parent vasculature, thereby also replicating the subtleties of the treatment procedure such as the occurrence of stent malapposition. The analysis revealed that the flow in the malapposed region of the stented AVF was being funnelled through the stent encapsulated region of the lumen. This behaviour was first observed when comparing contour plots of velocity magnitude between the flow field of the same AVF geometry with and without the presence of the stent. Flow rate ratios of the flow within the stent bounded cross-section over the flow rate across the whole vessel cross-section further affirmed this observation. The subsequent recirculation at the heel of the anastomosis of the stented AVF was much smaller, leading to a smaller region of low TAWSS and high OSI. However,

the stent malapposition also was a source of disturbance at the stent edge where vortical flow was emanating, which led to turbulent fluctuations (in the bulk flow and wall shear stress) that eventually dissipated further downstream.

The isolation of the stent provided insight into the flow mechanisms that the stent influenced, however, the assessment of the treatment methodology as a whole required a comparison of the flow field of the diseased AVF geometry prior to the stent implantation. Accordingly, an LES was conducted of the diseased AVF with a stenosis site in the vein, with closely matching numerical settings. Due to the lower flow rates experienced by the diseased AVF, the resulting TKE calculations were normalised to make comparisons to the flow field of the treated AVF. Despite the lower inlet flow, a short recirculation zone at the heel, together with swirling disturbed flow initiating at the interface of the two inlet flows, was observed in the diseased AVF. However, the most significant source of turbulent fluctuations was the stenosis site where the constrained flow was ejected as a jet in the expanding section of the vessel. The breakdown of the vortical shear layer surrounding the jet led to turbulent fluctuations that imparted varying wall shear stresses on the vessel, proximal to the stenosis site. This was particularly noted in the deceleration phase of the inlet cardiac cycle. The disturbances originating from the stenosed region of the diseased AVF far outweigh those that were occurring at the stent edge in the treated AVF.

The hydraulic resistance measured across the anastomosis was larger in the diseased AVF geometry (even with lower flow rates) suggesting that the larger angle that the anastomosis conformed to, following stent implantation, posed less resistance in conveying blood flow. However, it was apparent that the extremely high hydraulic resistance across the stenosis overshadowed the resistance across the anastomosis and the relief gained by placing the stent would have resulted in the considerably higher (approximately double) flow rates in the treated AVF.

In summary, it is clear that stent implantation in the AVF has transformed the haemodynamic environment to one that is faced with lower turbulent fluctuations in the bulk flow and of the wall shear stresses. Malapposition of the stent at the heel of the anastomosis assists in shielding the vessel wall from recirculating flow, which in turn leads to smaller

regions of concerning wall shear stress behaviour. However, the malapposition at the edge of the stent implantation contributed to the initiation of disturbances that could be harmful to the vessel wall. Despite this drawback of the stent implantation, the characteristics of the haemodynamic environment of a treated AVF are far less hostile than that of a diseased AVF (particularly with a stenosis).

8.2 Future research avenues

The findings of this thesis involved high-resolution numerical results that were complemented with velocity fields obtained using Tomo-PIV. However, the experimental results could not be extended to calculate wall shear stresses due to the lack of reliability in the flow field in the near-wall region. This limitation could be overcome by employing a Lagrangian particle tracking methodology which would provide a higher spatial resolution and avoid the necessity for averaging over the interrogation volumes, allowing calculations of wall shear stress. This would provide the opportunity to capture the fluctuating WSS behaviour, which would be a more direct consequence to the health of the AVF.

A shortcoming in the benchtop experiment was the absence of the physical stent implantation in the AVF phantom. The opaque medical device would have obstructed the laser beam and the view from the cameras, thereby severely undermining the three-dimensional reconstruction of the flow field. This obstacle could be overcome by implementing innovative fabrication strategies that recreate a transparent version of the stent within the benchtop AVF model. Despite the challenging nature of this objective, the resulting data-set would provide a valuable time-resolved flow field that would further unravel the mechanisms of the decrease in turbulent fluctuations with the presence of the stent.

The outcomes of this thesis were restricted to a single representative patient case due to the level of detail involved in the experimentation. Replicating turbulent fluctuation measurements (numerically and experimentally) for a larger cohort of AVF patients would be very time consuming and resource-intensive. Alternatively, the funnelling flow char-

acteristic of the stent in the malapposed region and the subsequent reduction in area of the low TAWSS - high OSI region can be captured with appropriate Reynolds-averaged Navier Stokes turbulence models, which would considerably reduce computational time. Subsequently, scaling up a methodology that captures these flow characteristics in a larger cohort would elucidate the effect of varying patient AVF geometry and flow conditions.

Another avenue of future work is to hold patient AVF geometry and boundary conditions constant, and vary parameters of the stent itself. Variations of the nominal stent diameter chosen could affect the level of malapposition at the heel of the anastomosis. Additionally, stents with larger overall diameters would better appose the vessel walls but would also lead to larger strut gaps, thereby potentially minimising the funnelling effect and increasing the turbulent fluctuations. Variations of the overall length of the stent would affect the level of apposition at the stent edge, thus, affecting the disturbance noted at this location. Furthermore, variations of the design of the stent using flexible stents from other manufacturers could provide understanding of the effects of additional stent specific parameters (strut shape, strut angle etc.).

Finally, turbulent fluctuations at the interface of the inlets were noted in both the diseased AVF geometry and the stent-absent AVF geometry suggesting that the collision of the opposing inlet flow could play a significant role in the disturbance at the anastomosis. Experimenting with vascular plug implantations that seal the distal artery inlet could further inform this view while remaining more realistic than simply ligating the distal artery or removing its inlet flow. However, implementation of this methodology, although surgically possible, could surface other clinical complications such as ischaemia (i.e. if the AVF had antegrade flow conditions) or a lack of adequate venous outflow (i.e. if the proximal artery flow rate was insufficient).

Bibliography

- R Al-Hakim, EW Lee, ST Kee, K Seals, B Varghese, A Chien, M Quirk, and J McWilliams. Hemodynamic analysis of edge stenosis in peripheral artery stent grafts. Diagnostic and Interventional Imaging, 98(10):729–735, 2017.
- Michael Allon and Michelle L Robbin. Increasing arteriovenous fistulas in hemodialysis patients: problems and solutions. Kidney International, 62(4):1109–1124, 2002.
- Magnus Andersson, Jonas Lantz, Tino Ebbers, and Matts Karlsson. Multidirectional wss disturbances in stenotic turbulent flows: A pre-and post-intervention study in an aortic coarctation. Journal of Biomechanics, 51:8–16, 2017.
- Magnus Andersson, Tino Ebbers, and Matts Karlsson. Characterization and estimation of turbulence-related wall shear stress in patient-specific pulsatile blood flow. Journal of Biomechanics, 85:108–117, 2019.
- Siddiq Anwar and Tushar J Vachharajani. Stent use for hemodialysis access: What a general nephrologist needs to know. Hemodialysis International, 2017.
- Australia, New Zealand Dialysis, and Transplant Registry. ANZDATA Registry. 40th Report, chapter Brochure - Highlights key info 2016. Australia and New Zealand Dialysis and Transplant Registry, Adelaide, Australia, 2018. Available at: <http://www.anzdata.org.au>.
- Australian Institute of Health and Welfare. Chronic kidney disease compendium. URL <https://www.aihw.gov.au/reports/chronic-kidney-disease/chronic-kidney-disease-compendium/contents/how-many-australians-have-chronic-kidney-disease>.
- Hualong Bai, Shunbo Wei, Boao Xie, Zhiwei Wang, Mingxing Li, Zhentao Qiao, Peng Sun, and Wang Wang. Endothelial nitric oxide synthase (enos) mediates neointimal thickness in arteriovenous fistulae with different anastomotic angles in rats. The Journal of Vascular Access, page 1129729821996537, 2021.
- Klemens H Barth, Renu Virmani, Ernst P Strecker, Michael A Savin, David Lindisch, Alan H Matsumoto, and George P Teitelbaum. Flexible tantalum stents implanted in aortas and iliac arteries: effects in normal canines. Radiology, 175(1):91–96, 1990.

-
- Khalid Bashar, Mekki Medani, Hiba Bashar, Khalid Ahmed, Thomas Aherne, Tony Moloney, and Stewart R Walsh. End-to-side versus side-to-side anastomosis in upper limb arteriovenous fistula for dialysis access: a systematic review and a meta-analysis. Annals of Vascular Surgery, 47:43–53, 2018.
- Gerald A. Beathard. Angiography of hemodialysis fistulas and grafts. Seminars in Dialysis, 30(4):326–337, 2017. doi: <https://doi.org/10.1111/sdi.12595>. URL <https://onlinelibrary.wiley.com/doi/abs/10.1111/sdi.12595>.
- Gerald A. Beathard and Lawrence M. Spergel. Hand ischemia associated with dialysis vascular access: An individualized access flow-based approach to therapy. Seminars in Dialysis, 26(3):287–314, 2013. doi: <https://doi.org/10.1111/sdi.12088>. URL <https://onlinelibrary.wiley.com/doi/abs/10.1111/sdi.12088>.
- Susann Beier, John Ormiston, Mark Webster, John Cater, Stuart Norris, Pau Medrano-Gracia, Alistair Young, and Brett Cowan. Hemodynamics in idealized stented coronary arteries: important stent design considerations. Annals of Biomedical Engineering, 44(2):315–329, 2016.
- Philipp Berg, Christina Iosif, Sebastien Ponsonnard, Catherine Yardin, Gábor Janiga, and Charbel Mounayer. Endothelialization of over-and undersized flow-diverter stents at covered vessel side branches: an in vivo and in silico study. Journal of Biomechanics, 49(1):4–12, 2016.
- Joel L Berry, Aland Santamarina, James E Moore, Suranjan Roychowdhury, and William D Routh. Experimental and computational flow evaluation of coronary stents. Annals of Biomedical Engineering, 28(4):386–398, 2000.
- Ankit Bharat and Surendra Shenoy. Assessment and intervention for arteriovenous fistula maturation. Vascular access: principle and practice. Philadelphia, PA: Lippincott Williams and Wilkins, pages 196–205, 2010.
- Hugh Maurice Blackburn and Spencer John Sherwin. Instability modes and transition of pulsatile stenotic flow: pulse-period dependence. Journal of Fluid Mechanics, 573: 57–88, 2007.
- M Boghosian, K Cassel, M Hammes, B Funaki, S Kim, X Qian, X Wang, P Dhar, and J Hines. Hemodynamics in the cephalic arch of a brachiocephalic fistula. Medical Engineering & Physics, 36(7):822–830, 2014.
- Lorenzo Botti, Koen Van Canneyt, Rado Kaminsky, Tom Claessens, Robrecht Nils Planken, Pascal Verdonck, Andrea Remuzzi, and Luca Antiga. Numerical evaluation and experimental validation of pressure drops across a patient-specific model of vascular access for hemodialysis. Cardiovascular Engineering and Technology, 4(4):485–499, 2013.
- Michela Bozzetto, Bogdan Ene-Iordache, and Andrea Remuzzi. Transitional Flow in the Venous Side of Patient-Specific Arteriovenous Fistulae for Hemodialysis. Annals of Biomedical Engineering, 44(8):2388–2401, 8 2016. ISSN 1573-9686. doi: [10.1007/s10439-015-1525-y](https://doi.org/10.1007/s10439-015-1525-y). URL <https://doi.org/10.1007/s10439-015-1525-y>.

-
- Michael J Brescia, James E Cimino, Kenneth Appel, and Baruch J Hurwich. Chronic hemodialysis using venipuncture and a surgically created arteriovenous fistula. New England Journal of Medicine, 275(20):1089–1092, 1966.
- Waleed Brinjikji, Mohammad H Murad, Giuseppe Lanzino, Harry J Cloft, and David F Kallmes. Endovascular treatment of intracranial aneurysms with flow diverters: a meta-analysis. Stroke, 44(2):442–447, 2013.
- Stephen P Broderick, J Graeme Houston, and Michael T Walsh. The influence of the instabilities in modelling arteriovenous junction haemodynamics. Journal of Biomechanics, 48(13):3591–3598, 2015.
- Leonard D Browne, Khalid Bashar, Philip Griffin, Eamon G Kavanagh, Stewart R Walsh, and Michael T Walsh. The role of shear stress in arteriovenous fistula maturation and failure: a systematic review. PloS one, 10(12):e0145795, 2015a.
- Leonard D Browne, Michael T Walsh, and Philip Griffin. Experimental and numerical analysis of the bulk flow parameters within an arteriovenous fistula. Cardiovascular Engineering and Technology, 6(4):450–462, 2015b.
- Colette J Browning and Shane A Thomas. Community values and preferences in transplantation organ allocation decisions. Social Science & Medicine, 52(6):853–861, 2001.
- NA Buchmann, C Atkinson, MC Jeremy, and J Soria. Tomographic particle image velocimetry investigation of the flow in a modeled human carotid artery bifurcation. Experiments in Fluids, 50(4):1131–1151, 2011.
- Gráinne T Carroll, Timothy M McGloughlin, Lucy M OKeeffe, Anthony Callanan, and Michael T Walsh. Realistic temporal variations of shear stress modulate mmp-2 and mcp-1 expression in arteriovenous vascular access. Cellular and Molecular Bioengineering, 2(4):591, 2009.
- GT Carroll, TM McGloughlin, PE Burke, M Egan, F Wallis, and MT Walsh. Wall shear stresses remain elevated in mature arteriovenous fistulas: a case study. Journal of Biomechanical Engineering, 133(2):021003, 2011.
- John Carroll. A clinical role for fluid dynamics modelling of arteriovenous fistulae. PhD thesis, Mechanical & Manufacturing Engineering, Faculty of Engineering, UNSW, 2018.
- John Carroll, Ramon L Varcoe, Tracie Barber, and Anne Simmons. Reduction in anastomotic flow disturbance within a modified end-to-side arteriovenous fistula configuration: Results of a computational flow dynamic model. Nephrology, 24(2):245–251, 2019.
- John E Carroll, Eamonn S Colley, Shannon D Thomas, Ramon L Varcoe, Anne Simmons, and Tracie J Barber. Tracking geometric and hemodynamic alterations of an arteriovenous fistula through patient-specific modelling. Computer methods and programs in biomedicine, 186:105203, 2020.
- A Cass, S Chadban, J Craig, K Howard, S McDonald, G Salkeld, and S White. The economic impact of end stage kidney disease in australia., 2006.

-
- Ishmail B Celik, Urmila Ghia, Patrick J Roache, et al. Procedure for estimation and reporting of uncertainty due to discretization in {CFD} applications. Journal of Fluids Engineering, 130(7), 2008.
- Y.A. Çengel and J.M. Cimbala. Fluid Mechanics: Fundamentals and Applications. McGraw-Hill Education, 2014.
- Eric Chemla, Afshin Tavakoli, Milind Nikam, Sandip Mitra, Tlou Malete, Jackie Evans, and Prabir Roy-Chaudhury. Arteriovenous fistula creation using the optiflow vascular anastomotic connector: The open (o ptiflow p at e ncy and maturatio n) study. The Journal of Vascular Access, 15(1):38–44, 2014.
- Eric Chemla, Carmen C Velazquez, Fabrizio D’abate, Veni Ramachandran, and Gary Maytham. Arteriovenous fistula construction with the vasq external support device: a pilot study. The Journal of Vascular Access, 17(3):243–248, 2016.
- Henry Y Chen, James Hermiller, Anjan K Sinha, Michael Sturek, Luoding Zhu, and Ghassan S Kassab. Effects of stent sizing on endothelial and vessel wall stress: potential mechanisms for in-stent restenosis. Journal of Applied Physiology, 106(5):1686–1691, 2009.
- Winson X Chen, Eric KW Poon, Vikas Thondapu, Nicholas Hutchins, Peter Barlis, and Andrew Ooi. Haemodynamic effects of incomplete stent apposition in curved coronary arteries. Journal of Biomechanics, 63:164–173, 2017.
- Jeng-Jiann Chiu and Shu Chien. Effects of disturbed flow on vascular endothelium: pathophysiological basis and clinical perspectives. Physiological Reviews, 91(1):327–387, 2011.
- Young I Cho and Kenneth R Kenney. Effects of the non-newtonian viscosity of blood on flows in a diseased arterial vessel. part 1: Steady flows. Biorheology, 28(3-4):241–262, 1991.
- Eamonn Colley. Vascular remodelling due to haemodynamics, in an arteriovenous fistula. PhD thesis, Mechanical & Manufacturing Engineering, Faculty of Engineering, UNSW, 2018.
- Eamonn Colley, John Carroll, Shannon Thomas, Ramon L Varcoe, Anne Simmons, and Tracie Barber. A methodology for non-invasive 3-d surveillance of arteriovenous fistulae using freehand ultrasound. IEEE Transactions on Biomedical Engineering, 65(8):1885–1891, 2018.
- Tara Anne Collidge, Peter Campbell Thomson, Patrick Barry Mark, James Phillip Traynor, Alan George Jardine, Scott Thomas William Morris, Keith Simpson, and Giles Hannibal Roditi. Gadolinium-enhanced mr imaging and nephrogenic systemic fibrosis: retrospective study of a renal replacement therapy cohort. Radiology, 245(1): 168–175, 2007.
- Stephane Cook, Peter Wenaweser, Mario Togni, Michael Billinger, Cyrill Morger, Christian Seiler, Rolf Vogel, Otto Hess, Bernhard Meier, and Stephan Windecker. Incomplete

-
- stent apposition and very late stent thrombosis after drug-eluting stent implantation. Circulation, 115(18):2426–2434, 2007.
- Richard Courant, Kurt Friedrichs, and Hans Lewy. On the partial difference equations of mathematical physics. IBM journal of Research and Development, 11(2):215–234, 1967.
- Connor V Cunnane, Eoghan M Cunnane, and Michael T Walsh. A review of the hemodynamic factors believed to contribute to vascular access dysfunction. Cardiovascular Engineering and Technology, 8(3):280–294, 2017.
- Lakshmi P Dasi, Helene A Simon, Philippe Sucosky, and Ajit P Yoganathan. Fluid mechanics of artificial heart valves. Clinical and experimental pharmacology and physiology, 36(2):225–237, 2009.
- CM De Silva, R Baidya, M Khashehchi, and I Marusic. Assessment of tomographic piv in wall-bounded turbulence using direct numerical simulation data. Experiments in Fluids, 52(2):425–440, 2012.
- David De Wilde, Bram Trachet, Guido RY De Meyer, and Patrick Segers. Shear stress metrics and their relation to atherosclerosis: an in vivo follow-up study in atherosclerotic mice. Annals of Biomedical Engineering, 44(8):2327–2338, 2016.
- Iolanda Decorato, Zaher Kharboutly, Tommaso Vassallo, Justin Penrose, Cécile Legallais, and Anne-Virginie Salsac. Numerical simulation of the fluid structure interactions in a compliant patient-specific arteriovenous fistula. International journal for numerical methods in Biomedical Engineering, 30(2):143–159, 2014a.
- Iolanda Decorato, Anne-Virginie Salsac, Cecile Legallais, Mona Alimohammadi, Vanessa Diaz-Zuccarini, and Zaher Kharboutly. Influence of an arterial stenosis on the hemodynamics within an arteriovenous fistula (avf): Comparison before and after balloon-angioplasty. Cardiovascular Engineering and Technology, 5(3):233–243, 2014b.
- S Drost, N Alam, JG Houston, and D Newport. Review of experimental modelling in vascular access for hemodialysis. Cardiovascular Engineering and Technology, 8(3):330–341, 2017.
- Juan C Duque, Marwan Tabbara, Laisel Martinez, Jose Cardona, Roberto I Vazquez-Padron, and Loay H Salman. Dialysis arteriovenous fistula failure and angioplasty: intimal hyperplasia and other causes of access failure. American Journal of Kidney Diseases, 69(1):147–151, 2017.
- Gerrit E Elsinga, Fulvio Scarano, Bernhard Wieneke, and Bas W van Oudheusden. Tomographic particle image velocimetry. Experiments in Fluids, 41(6):933–947, 2006.
- Bogdan Ene-Iordache and Andrea Remuzzi. Disturbed flow in radial-cephalic arteriovenous fistulae for haemodialysis: low and oscillating shear stress locates the sites of stenosis. Nephrology Dialysis Transplantation, 27(1):358–368, 2012.

-
- Bogdan Ene-Iordache and Andrea Remuzzi. Blood flow in idealized vascular access for hemodialysis: a review of computational studies. Cardiovascular engineering and technology, 8(3):295–312, 2017.
- Bogdan Ene-Iordache, Luca Cattaneo, Gabriele Dubini, and Andrea Remuzzi. Effect of anastomosis angle on the localization of disturbed flow in side-to-end fistulae for haemodialysis access. Nephrology Dialysis Transplantation, 28(4):997–1005, 2013.
- C Ross Ethier, Sujata Prakash, David A Steinman, Richard L Leask, Gregory G Couch, and M Ojha. Steady flow separation patterns in a 45 degree junction. Journal of Fluid Mechanics, 411:1–38, 2000.
- Mark F Fillinger, Emanuel R Reinitz, Robert A Schwartz, Dennis E Resetarits, Andrew M Paskanik, David Bruch, and Carl E Bredenberg. Graft geometry and venous intimal-medial hyperplasia in arteriovenous loop grafts. Journal of Vascular Surgery, 11(4):556–566, 1990.
- Michelle K Fitts, Daniel B Pike, Kasey Anderson, and Yan-Ting Shiu. Hemodynamic shear stress and endothelial dysfunction in hemodialysis access. The Open Urology & Nephrology Journal, 7(Suppl 1 M5):33, 2014.
- Ning Fu, Emily Joachim, Alexander S. Yevzlin, Jung-Im Shin, Brad C. Astor, and Micah R. Chan. A meta-analysis of stent placement vs. angioplasty for dialysis vascular access stenosis. Seminars in Dialysis, 28(3):311–317, 2015. doi: <https://doi.org/10.1111/sdi.12314>. URL <https://onlinelibrary.wiley.com/doi/abs/10.1111/sdi.12314>.
- David Fulker, Bogdan Ene-Iordache, and Tracie Barber. High-resolution computational fluid dynamic simulation of haemodialysis cannulation in a patient-specific arteriovenous fistula. Journal of Biomechanical Engineering, 140(3):031011, 2018.
- Gordan Galić, Ante Kvesić, Monika Tomić, Zoran Rebac, Zdrinko Brekalo, Vlatka Martinović, and Šime Vučkov. The advantages of end-to-side arteriovenous anastomosis over the other two types of arteriovenous anastomosis in dialysis patients. Collegium antropologicum, 32(1):109–114, 2008.
- Joana Gameiro and Jose Ibeas. Factors affecting arteriovenous fistula dysfunction: a narrative review. The Journal of Vascular Access, 21(2):134–147, 2020.
- Massimo Germano, Ugo Piomelli, Parviz Moin, and William H Cabot. A dynamic subgrid-scale eddy viscosity model. Physics of Fluids A: Fluid Dynamics, 3(7):1760–1765, 1991.
- Michael A Gimbrone Jr and Guillermo García-Cardena. Endothelial cell dysfunction and the pathobiology of atherosclerosis. Circulation Research, 118(4):620–636, 2016.
- Sanjiv Gunasekera, Olivia Ng, Shannon Thomas, Ramon Varcoe, Charitha de Silva, and Tracie Barber. Towards 3d piv measurements of a patient-specific arteriovenous fistula. In Proceedings of the 9th Australian conference on laser diagnostics. University of Adelaide, pages 87–90, 2019.

-
- Sanjiv Gunasekera, Olivia Ng, Shannon Thomas, Ramon Varcoe, Charitha de Silva, and Tracie Barber. Tomographic piv analysis of physiological flow conditions in a patient-specific arteriovenous fistula. Experiments in Fluids, 61(12):1–14, 2020.
- Timothy J Gundert, Alison L Marsden, Weiguang Yang, and John F LaDisa Jr. Optimization of cardiovascular stent design using computational fluid dynamics. Journal of Biomechanical Engineering, 134(1), 2012.
- Paul S Gunning, Neelakantan Saikrishnan, Laoise M McNamara, and Ajit P Yoganathan. An in vitro evaluation of the impact of eccentric deployment on transcatheter aortic valve hemodynamics. Annals of Biomedical Engineering, 42(6):1195–1206, 2014.
- Rebecca J Gusic, Richard Myung, Matus Petko, J William Gaynor, and Keith J Gooch. Shear stress and pressure modulate saphenous vein remodeling ex vivo. Journal of Biomechanics, 38(9):1760–1769, 2005.
- Guo-Sheng He, Jin-Jun Wang, Chong Pan, Li-Hao Feng, Qi Gao, and Akira Rinoshika. Vortex dynamics for flow over a circular cylinder in proximity to a wall. Journal of Fluid Mechanics, 812:698–720, 2017.
- Xiaoyi He and David N Ku. Pulsatile flow in the human left coronary artery bifurcation: average conditions. Journal of Biomechanical Engineering, 118(1):74–82, 1996.
- Yong He, Christi M Terry, Cuong Nguyen, Scott A Berceli, Yan-Ting E Shiu, and Alfred K Cheung. Serial analysis of lumen geometry and hemodynamics in human arteriovenous fistula for hemodialysis using magnetic resonance imaging and computational fluid dynamics. Journal of Biomechanics, 46(1):165–169, 2013.
- Yong He, Yan-Ting Shiu, Daniel B Pike, Prabir Roy-Chaudhury, Alfred K Cheung, and Scott A Berceli. Comparison of hemodialysis arteriovenous fistula blood flow rates measured by doppler ultrasound and phase-contrast magnetic resonance imaging. Journal of Vascular Surgery, 68(6):1848–1857, 2018.
- Eric Po-Yu Huang, Ming-Feng Li, Chia-Chi Hsiao, Hsin-Yu Chen, Ping-An Wu, and Huei-Lung Liang. Undersized stent graft for treatment of cephalic arch stenosis in arteriovenous hemodialysis access. Scientific Reports, 10(1):1–9, 2020.
- JD Humphrey. Vascular adaptation and mechanical homeostasis at tissue, cellular, and sub-cellular levels. Cell Biochemistry and Biophysics, 50(2):53–78, 2008.
- Thanh N Huynh, Balu K Chacko, Xinjun Teng, Brigitta C Brott, Michael Allon, Stacey S Kelpke, John A Thompson, Rakesh P Patel, and Andreas S Anayiotos. Effects of venous needle turbulence during ex vivo hemodialysis on endothelial morphology and nitric oxide formation. Journal of Biomechanics, 40(10):2158–2166, 2007.
- Sunghyuk Im, Go Eun Heo, Young Jin Jeon, Hyung Jin Sung, and Sung Kyun Kim. Tomographic piv measurements of flow patterns in a nasal cavity with geometry acquisition. Experiments in Fluids, 55(1):1644, 2014.

-
- F Iori, L Grechy, RW Corbett, W Gedroyc, N Duncan, CG Caro, and PE Vincent. The effect of in-plane arterial curvature on blood flow and oxygen transport in arterio-venous fistulae. Physics of Fluids, 27(3):031903, 2015.
- Hiroyuki Ishibashi, Makoto Sunamura, and Takeshi Karino. Flow patterns and preferred sites of intimal thickening in end-to-end anastomosed vessels. Surgery, 117(4):409–420, 1995.
- E Jabir and S Anil Lal. Numerical analysis of blood flow through an elliptic stenosis using large eddy simulation. Proceedings of the Institution of Mechanical Engineers, Part H: Journal of Engineering in Medicine, 230(8):709–726, 2016.
- J. Charles Jennette and James R. Stone. Diseases of Medium-Sized and Small Vessels. In Cellular and Molecular Pathobiology of Cardiovascular Disease, pages 197–219. Elsevier, 2014. ISBN 9780124052062. doi: 10.1016/B978-0-12-405206-2.00011-9. URL <http://linkinghub.elsevier.com/retrieve/pii/B9780124052062000119>.
- Lan Jia, Lihua Wang, Fang Wei, Haibo Yu, Hongye Dong, Bo Wang, Zhi Lu, Guijiang Sun, Haiyan Chen, Jia Meng, et al. Effects of wall shear stress in venous neointimal hyperplasia of arteriovenous fistulae. Nephrology, 20(5):335–342, 2015.
- Juan M Jiménez and Peter F Davies. Hemodynamically driven stent strut design. Annals of Biomedical Engineering, 37(8):1483–1494, 2009.
- Juan M Jiménez, Varesh Prasad, Michael D Yu, Christopher P Kampmeyer, Abdul-Hadi Kaakour, Pei-Jiang Wang, Sean F Maloney, Nathan Wright, Ian Johnston, Yi-Zhou Jiang, et al. Macro-and microscale variables regulate stent haemodynamics, fibrin deposition and thrombomodulin expression. Journal of The Royal Society Interface, 11(94):20131079, 2014.
- Min Jun, Meg J Jardine, Nicholas Gray, Rosemary Masterson, Peter G Kerr, John WM Agar, Carmel M Hawley, Carolyn Van Eps, Alan Cass, Martin Gallagher, et al. Outcomes of extended-hours hemodialysis performed predominantly at home. American Journal of Kidney Diseases, 61(2):247–253, 2013.
- John D Kakisis, Efthymios Avgerinos, Triantafyllos Giannakopoulos, Konstantinos Moulakakis, Anastasios Papapetrou, and Christos D Liapis. Balloon angioplasty vs nitinol stent placement in the treatment of venous anastomotic stenoses of hemodialysis grafts after surgical thrombectomy. Journal of Vascular Surgery, 55(2):472–478, 2012.
- Zaher Kharboutly, Valerie Deplano, Eric Bertrand, and Cecile Legallais. Numerical and experimental study of blood flow through a patient-specific arteriovenous fistula used for hemodialysis. Medical Engineering & Physics, 32(2):111–118, 2010.
- Mahesh K Krishnamoorthy, Rupak K Banerjee, Yang Wang, Jianhua Zhang, Abhijit Sinha Roy, Saeb F Khoury, Lois J Arend, Steve Rudich, and Prabir Roy-Chaudhury. Hemodynamic wall shear stress profiles influence the magnitude and pattern of stenosis in a pig av fistula. Kidney International, 74(11):1410–1419, 2008.

-
- David N Ku, Don P Giddens, Christopher K Zarins, and Seymour Glagov. Pulsatile flow and atherosclerosis in the human carotid bifurcation. positive correlation between plaque location and low oscillating shear stress. Arteriosclerosis: An Official Journal of the American Heart Association, Inc., 5(3):293–302, 1985.
- Zsolt Kulcsár, Luca Augsburger, Philippe Reymond, Vitor M Pereira, Sven Hirsch, Ajit S Mallik, John Millar, Stephan G Wetzel, Isabel Wanke, and Daniel A Rüfenacht. Flow diversion treatment: intra-aneurismal blood flow velocity and wss reduction are parameters to predict aneurysm thrombosis. Acta neurochirurgica, 154(10):1827–1834, 2012.
- KB Kwun, H Schanzer, N Finkler, M Haimov, and L Burrows. Hemodynamic evaluation of angioaccess procedures for hemodialysis. Vascular Surgery, 13(3):170–177, 1979.
- John F LaDisa, Ismail Guler, Lars E Olson, Douglas A Hettrick, Judy R Kersten, David C Warltier, and Paul S Pagel. Three-dimensional computational fluid dynamics modeling of alterations in coronary wall shear stress produced by stent implantation. Annals of Biomedical Engineering, 31(8):972–980, 2003.
- John F LaDisa Jr, Lars E Olson, Robert C Molthen, Douglas A Hettrick, Phillip F Pratt, Michael D Hardel, Judy R Kersten, David C Warltier, and Paul S Pagel. Alterations in wall shear stress predict sites of neointimal hyperplasia after stent implantation in rabbit iliac arteries. American Journal of Physiology-Heart and Circulatory Physiology, 288(5):H2465–H2475, 2005.
- Marco Laumen, Tim Kaufmann, Daniel Timms, Peter Schlanstein, Sebastian Jansen, Shaun Gregory, Kai Chun Wong, Thomas Schmitz-Rode, and Ulrich Steinseifer. Flow analysis of ventricular assist device inflow and outflow cannula positioning using a naturally shaped ventricle and aortic branch. Artificial Organs, 34(10):798–806, 2010.
- Jinkee Lee, Sunho Kim, Sung-Min Kim, Ryungeun Song, Hyun Kyu Kim, Jang Sang Park, and Sun Cheol Park. Assessing radiocephalic wrist arteriovenous fistulas of obtuse anastomosis using computational fluid dynamics and clinical application. The Journal of Vascular Access, 17(6):512–520, 2016.
- Sang-Wook Lee, David S Smith, Francis Loth, Paul F Fischer, and Hisham S Bassiouny. Importance of flow division on transition to turbulence within an arteriovenous graft. Journal of Biomechanics, 40(5):981–992, 2007.
- Les Laboratoires Servier. Servier medical art. URL <https://www.smart.servier.com>.
- Douglas K Lilly. A proposed modification of the germano subgrid-scale closure method. Physics of Fluids A: Fluid Dynamics, 4(3):633–635, 1992.
- John Lin, Floyd Howard, Dennis Bushnell, and G Selby. Investigation of several passive and active methods for turbulent flow separation control. In 21st fluid dynamics, plasma dynamics and lasers conference, page 1598, 1990.

-
- Charmaine E Lok, Thomas S Huber, Timmy Lee, Surendra Shenoy, Alexander S Yevzlin, Kenneth Abreo, Michael Allon, Arif Asif, Brad C Astor, Marc H Glickman, et al. Kdoqi clinical practice guideline for vascular access: 2019 update. American Journal of Kidney Diseases, 75(4):S1–S164, 2020.
- Francis Loth, Paul F Fischer, Nurullah Arslan, Christopher D Bertram, Seung E Lee, Thomas J Royston, Wael E Shaalan, and Hisham S Bassiouny. Transitional flow at the venous anastomosis of an arteriovenous graft: potential activation of the erk1/2 mechanotransduction pathway. Journal of Biomechanical Engineering, 125(1):49–61, 2003.
- Francis Loth, Paul F Fischer, and Hisham S Bassiouny. Blood flow in end-to-side anastomoses. Annual Review of Fluid Mechanics, 40:367–393, 2008.
- Tao Lu, PX Jiang, ZJ Guo, YW Zhang, and H Li. Large-eddy simulations (les) of temperature fluctuations in a mixing tee with/without a porous medium. International Journal of Heat and Mass Transfer, 53(21-22):4458–4466, 2010.
- N Lwin, M Wahab, J Carroll, and T Barber. Experimental and computational analysis of a typical arterio-venous fistula. In 19th Australasian Fluid Mechanics Conference (December, 2014), 2014.
- Mekhola Mallik, Rajesh Sivaprakasam, Gavin J Pettigrew, and Chris J Callaghan. Operative salvage of radiocephalic arteriovenous fistulas by formation of a proximal neoanastomosis. Journal of Vascular Surgery, 54(1):168–173, 2011.
- Sam Mallinson, Geordie McBain, Olivia Ng, Sanjiv Gunasekera, and Tracie Barber. Hydraulic resistance and inertance of multi-port vessels. In Hubert Chanson and Richard Brown, editors, Proceedings of the 22nd Australasian Fluid Mechanics Conference. The University of Queensland, Dec 2020. ISBN 978- 1-74272-341-9.
- Emily L Manchester, Selene Pirola, Mohammad Yousuf Salmasi, Declan P ORegan, Thanos Athanasiou, and Xiao Yun Xu. Analysis of turbulence effects in a patient-specific aorta with aortic valve stenosis. Cardiovascular Engineering and Technology, pages 1–16, 2021.
- Viviana Mancini, Aslak W Bergersen, Jan Vierendeels, Patrick Segers, and Kristian Valen-Sendstad. High-frequency fluctuations in post-stenotic patient specific carotid stenosis fluid dynamics: A computational fluid dynamics strategy study. Cardiovascular Engineering and Technology, 10(2):277–298, 2019.
- Stephen P McDonald and Graeme R Russ. Survival of recipients of cadaveric kidney transplants compared with those receiving dialysis treatment in australia and new zealand, 1991–2001. Nephrology Dialysis Transplantation, 17(12):2212–2219, 2002.
- Patrick M McGah, Daniel F Leotta, Kirk W Beach, R Eugene Zierler, and Alberto Aliseda. Incomplete restoration of homeostatic shear stress within arteriovenous fistulae. Journal of Biomechanical Engineering, 135(1), 2013.

-
- Patrick M McGah, Daniel F Leotta, Kirk W Beach, and Alberto Aliseda. Effects of wall distensibility in hemodynamic simulations of an arteriovenous fistula. Biomechanics and Modeling in Mechanobiology, 13(3):679–695, 2014.
- Florian R Menter. Two-equation eddy-viscosity turbulence models for engineering applications. AIAA journal, 32(8):1598–1605, 1994.
- Florian R Menter. Best practice: scale-resolving simulations in ansys cfd. ANSYS Germany GmbH, 1, 2012.
- Yumnah Mohamied, Ethan M Rowland, Emma L Bailey, Spencer J Sherwin, Martin A Schwartz, and Peter D Weinberg. Change of direction in the biomechanics of atherosclerosis. Annals of Biomedical Engineering, 43(1):16–25, 2015.
- Jonathan Murphy and Fergal Boyle. Predicting neointimal hyperplasia in stented arteries using time-dependant computational fluid dynamics: a review. Computers in Biology and Medicine, 40(4):408–418, 2010.
- Andrew C Newby and Alla B Zaltsman. Molecular mechanisms in intimal hyperplasia. The Journal of Pathology, 190(3):300–309, 2000.
- Duy T Nguyen, Alexander F Smith, and Juan M Jiménez. Stent strut streamlining and thickness reduction promote endothelialization. Journal of the Royal Society Interface, 18(181):20210023, 2021.
- Franck Nicoud and Frédéric Ducros. Subgrid-scale stress modelling based on the square of the velocity gradient tensor. Flow, turbulence and Combustion, 62(3):183–200, 1999.
- Franck Nicoud, Hubert Baya Toda, Olivier Cabrit, Sanjeeb Bose, and Jungil Lee. Using singular values to build a subgrid-scale model for large eddy simulations. Physics of Fluids, 23(8):085106, 2011.
- Hannah Northrup, Maheshika Somarathna, Savanna Corless, Isabelle Falzon, John Totenhagen, Timmy Lee, and Yan-Ting Shiu. Analysis of geometric and hemodynamic profiles in rat arteriovenous fistula following pde5a inhibition. Frontiers in Bioengineering and Biotechnology, 9, 2021.
- Abhiro Pal, Kameswararao Anupindi, Yann Delorme, Niranjana Ghaisas, Dinesh A Shetty, and Steven H Frankel. Large eddy simulation of transitional flow in an idealized stenotic blood vessel: evaluation of subgrid scale models. Journal of Biomechanical Engineering, 136(7):071009, 2014.
- Jacek J Paszkowiak and Alan Dardik. Arterial wall shear stress: observations from the bench to the bedside. Vascular and Endovascular Surgery, 37(1):47–57, 2003.
- Jon Peacock, Shelly Hankins, Travis Jones, and Robert Lutz. Flow instabilities induced by coronary artery stents: assessment with an in vitro pulse duplicator. Journal of Biomechanics, 28(1):17–26, 1995.

-
- Anthony E Perry and Min S Chong. A description of eddying motions and flow patterns using critical-point concepts. Annual Review of Fluid Mechanics, 19(1):125–155, 1987.
- Eric KW Poon, Peter Barlis, Stephen Moore, Wei-Han Pan, Yun Liu, Yufei Ye, Yuan Xue, Shuang J Zhu, and Andrew SH Ooi. Numerical investigations of the haemodynamic changes associated with stent malapposition in an idealised coronary artery. Journal of Biomechanics, 47(12):2843–2851, 2014.
- Stephen B Pope. Turbulent flows. Measurement Science and Technology, 12(11):2020–2021, oct 2001. doi: 10.1088/0957-0233/12/11/705. URL <https://doi.org/10.1088/0957-0233/12/11/705>.
- Giorgio Prouse, Simone Stella, Christian Vergara, Alfio Quarteroni, Stephan Engelberger, Reto Canevascini, and Luca Giovannacci. Computational analysis of turbulent hemodynamics in radiocephalic arteriovenous fistulas to determine the best anastomotic angles. Annals of Vascular Surgery, 68:451–459, 2020.
- Ehsan Rajabi-Jagahrgh, Mahesh K. Krishnamoorthy, Yang Wang, Ann Choe, Prabir Roy-Chaudhury, and Rupak K. Banerjee. Influence of temporal variation in wall shear stress on intima-media thickening in arteriovenous fistulae. Seminars in Dialysis, 26(4):511–519, 2013. doi: <https://doi.org/10.1111/sdi.12045>. URL <https://onlinelibrary.wiley.com/doi/abs/10.1111/sdi.12045>.
- Andrea Remuzzi and Bogdan Ene-Iordache. Novel paradigms for dialysis vascular access: Upstream hemodynamics and vascular remodeling in dialysis access stenosis. Clinical Journal of the American Society of Nephrology, 8(12):2186–2193, 2013. ISSN 1555905X. doi: 10.2215/CJN.03450413.
- Lewis Fry Richardson. Weather prediction by numerical process. Cambridge university press, 2007.
- Prabir Roy-Chaudhury, Vikas P Sukhatme, and Alfred K Cheung. Hemodialysis vascular access dysfunction: a cellular and molecular viewpoint. Journal of the American Society of Nephrology, 17(4):1112–1127, 2006.
- Nirvana Sadaghianloo, Elixène Jean-Baptiste, Khalid Rajhi, Etienne François, Serge Declemy, Alan Dardik, and Réda Hassen-Khodja. Increased reintervention in radial-cephalic arteriovenous fistulas with anastomotic angles of less than 30 degrees. Journal of Vascular Surgery, 62(6):1583–1589, 2015.
- Domenico Santoro, Filippo Benedetto, Placido Mondello, Narayana Pipitò, David Barillà, Francesco Spinelli, Carlo Alberto Ricciardi, Valeria Cernaro, and Michele Buemi. Vascular access for hemodialysis: current perspectives. International Journal of Nephrology and Renovascular Disease, 7:281, 2014.
- Fulvio Scarano. Tomographic piv: principles and practice. Measurement Science and Technology, 24(1):012001, 2012.
- S Sivanesan, TV How, RA Black, and A Bakran. Flow patterns in the radiocephalic arteriovenous fistula: an in vitro study. Journal of Biomechanics, 32(9):915–925, 1999.

-
- Sharmila Sivanesan, Thien V How, and Ali Bakran. Characterizing flow distributions in av fistulae for haemodialysis access. Nephrology, dialysis, transplantation: official publication of the European Dialysis and Transplant Association-European Renal Association, 13(12):3108–3110, 1998.
- Rodolfo Stanziale, Massimo Lodi, Enrico D’Andrea, Fulvio Sammartino, and Virgilio Di Luzio. Arteriovenous fistula: end-to-end or end-to side anastomosis? Hemodialysis International, 15(1):100–103, 2011.
- Simone Stella, Christian Vergara, Luca Giovannacci, Alfio Quarteroni, and Giorgio Prouse. Assessing the disturbed flow and the transition to turbulence in the arteriovenous fistula. Journal of Biomechanical Engineering, 141(10), 2019.
- Dieter Stoeckel, Alan Pelton, and Tom Duerig. Self-expanding nitinol stents: material and design considerations. European Radiology, 14(2):292–301, 2004.
- Radojica Stolic. Most important chronic complications of arteriovenous fistulas for hemodialysis. Medical principles and practice, 22(3):220–228, 2013.
- Li Suqin, Zhu Mingli, Suo Shiteng, Mi Honglan, Zhang Lan, Ni Qihong, and Lu Qing. Assessment of the hemodynamics of autogenous arteriovenous fistulas with 4d phase contrast-based flow quantification mri in dialysis patients. Journal of Magnetic Resonance Imaging, 51(4):1272–1280, 2020.
- John Swinnen, Kia Lean Tan, Richard Allen, David Burgess, and Irwin V Mohan. Juxta-anastomotic stenting with aggressive angioplasty will salvage the native radiocephalic fistula for dialysis. Journal of Vascular Surgery, 61(2):436–442, 2015.
- F. P. P. Tan, N. B. Wood, G. Tabor, and X. Y. Xu. Comparison of LES of Steady Transitional Flow in an Idealized Stenosed Axisymmetric Artery Model With a RANS Transitional Model. Journal of Biomechanical Engineering, 133(5), 04 2011. ISSN 0148-0731. doi: 10.1115/1.4003782. URL <https://doi.org/10.1115/1.4003782>. 051001.
- FPP Tan, G Soloperto, S Bashford, NB Wood, S Thom, A Hughes, and XY Xu. Analysis of flow disturbance in a stenosed carotid artery bifurcation using two-equation transitional and turbulence models. Journal of Biomechanical Engineering, 130(6), 2008.
- John M Tarbell, Zhong-Dong Shi, Jessilyn Dunn, and Hanjoong Jo. Fluid mechanics, arterial disease, and gene expression. Annual Review of Fluid Mechanics, 46:591–614, 2014.
- Nicola Tessitore, Giancarlo Mansueto, Giovanni Lipari, Valeria Bedogna, Stefano Tardivo, Elda Baggio, Daniela Cenzi, Giovanni Carbognin, Albino Poli, and Antonio Lupo. Endovascular versus surgical preemptive repair of forearm arteriovenous fistula juxta-anastomotic stenosis: analysis of data collected prospectively from 1999 to 2004. Clinical Journal of the American Society of Nephrology, 1(3):448–454, 2006.
- Shannon D Thomas, Samantha Peden, Phillip Crowe, and Ramon L Varcoe. Interwoven nitinol stents to treat radiocephalic anastomotic arteriovenous fistula stenosis. Journal of Endovascular Therapy, 26(3):394–401, 2019.

-
- M Tonelli, N Wiebe, G Knoll, A Bello, S Browne, D Jadhav, S Klarenbach, and J Gill. Systematic review: kidney transplantation compared with dialysis in clinically relevant outcomes. American Journal of Transplantation, 11(10):2093–2109, 2011.
- James N Topper and Michael A Gimbrone Jr. Blood flow and vascular gene expression: fluid shear stress as a modulator of endothelial phenotype. Molecular medicine today, 5(1):40–46, 1999.
- TSANZ. Clinical guidelines for organ transplantation from deceased donors. Technical Report 1.3, The Transplantation Society of Australia and New Zealand, May 2019.
- Kristian Valen-Sendstad, Kent-André Mardal, Mikael Mortensen, Bjørn Anders Pettersson Reif, and Hans Petter Langtangen. Direct numerical simulation of transitional flow in a patient-specific intracranial aneurysm. Journal of Biomechanics, 44(16):2826–2832, 2011.
- Kristian Valen-Sendstad, Marina Piccinelli, and David A Steinman. High-resolution computational fluid dynamics detects flow instabilities in the carotid siphon: implications for aneurysm initiation and rupture? Journal of Biomechanics, 47(12):3210–3216, 2014.
- Koen Van Canneyt, Thierry Pourchez, Sunny Eloot, Caroline Guillame, Alexandre Bonnet, Patrick Segers, and Pascal Verdonck. Hemodynamic impact of anastomosis size and angle in side-to-end arteriovenous fistulae: a computer analysis. The Journal of Vascular Access, 11(1):52–58, 2010.
- Jochem W Van Werkum, Antonius A Heestermans, A Carla Zomer, Johannes C Kelder, Maarten-Jan Suttorp, Benno J Rensing, Jacques J Koolen, BR Guus Brueren, Jan-Henk E Dambrink, Raymond W Hautvast, et al. Predictors of coronary stent thrombosis: the dutch stent thrombosis registry. Journal of the American college of cardiology, 53(16):1399–1409, 2009.
- Sonu S Varghese, Steven H Frankel, and Paul F Fischer. Direct numerical simulation of stenotic flows. part 2. pulsatile flow. Journal of Fluid Mechanics, 582:281–318, 2007.
- Pujith RS Vijayaratnam, Caroline C OBrien, John A Reizes, Tracie J Barber, and Elazer R Edelman. The impact of blood rheology on drug transport in stented arteries: steady simulations. PloS one, 10(6), 2015.
- Chao Wang, Zhongbin Tian, Jian Liu, Linkai Jing, Nikhil Paliwal, Shengzhang Wang, Ying Zhang, Jianping Xiang, Adnan H Siddiqui, Hui Meng, et al. Flow diverter effect of lvis stent on cerebral aneurysm hemodynamics: a comparison with enterprise stents and the pipeline device. Journal of Translational Medicine, 14(1):1–10, 2016.
- Chong Wang, Brendon M Baker, Christopher S Chen, and Martin Alexander Schwartz. Endothelial cell sensing of flow direction. Arteriosclerosis, Thrombosis, and Vascular Biology, 33(9):2130–2136, 2013.
- KR Wedgwood, PA Wiggins, and PJ Guillou. A prospective study of end-to-side vs. side-to-side arteriovenous fistulas for haemodialysis. Journal of British Surgery, 71(8): 640–642, 1984.

-
- Lingling Wei, Jiaqiu Wang, Qiang Chen, and Zhiyong Li. Impact of stent malapposition on intracoronary flow dynamics: an optical coherence tomography-based patient-specific study. Medical Engineering & Physics, 2021.
- Jerry Westerweel and Fulvio Scarano. Universal outlier detection for piv data. Experiments in Fluids, 39(6):1096–1100, 2005.
- B Wieneke. Volume self-calibration for 3d particle image velocimetry. Experiments in Fluids, 45(4):549–556, 2008.
- Bernhard Wieneke. Improvements for volume self-calibration. Measurement Science and Technology, 29(8):084002, 2018.
- David C Wilcox et al. Turbulence modeling for CFD, volume 2. DCW industries La Canada, CA, 1998.
- Russell A Williams and Kimberly S Stone. Endovascular management of dialysis graft stenosis. Vascular Access: Principles and Practice, page 155, 2010.
- Jenni Wright and Shelvin Narayan. Analysis of kidney allocation during 2015. Technical report, National Organ Matching System, 2016.
- David T Wymer, Kunal P Patel, William F Burke III, and Vinay K Bhatia. Phase-contrast mri: Physics, techniques, and clinical applications. Radiographics, 40(1):122–140, 2020.
- Huanming Xu, Jiang Xiong, Xiaofeng Han, Yuqian Mei, Yue Shi, Dianpeng Wang, Mingchen Zhang, and Duanduan Chen. Computed tomography-based hemodynamic index for aortic dissection. The Journal of Thoracic and Cardiovascular Surgery, 162(2):e165–e176, 2021.
- Chih-Yu Yang, Ming-Chia Li, Chien-Wen Lan, Wang-Jiun Lee, Chen-Ju Lee, Cheng-Hsueh Wu, Jing-Min Tang, Yang-Yao Niu, Yao-Ping Lin, Yan-Ting Shiu, et al. The anastomotic angle of hemodialysis arteriovenous fistula is associated with flow disturbance at the venous stenosis location on angiography. Frontiers in Bioengineering and Biotechnology, 8:846, 2020.
- Sina G Yazdi, Paul D Docherty, Adib Khanafer, Mark Jermy, Natalia Kabaliuk, Patrick H Geoghegan, and Petra Williamson. In-vitro particle image velocimetry assessment of the endovascular haemodynamic features distal of stent-grafts that are associated with development of limb occlusion. Journal of the Royal Society of New Zealand, 51(2): 361–374, 2021.

RANS CFD spatial and temporal discretization assessments

A.1 Mesh quality

The AVF geometries were discretized using tetrahedral elements to achieve high quality elements in regions close to the stent and the vessel wall. This meshing strategy was used in the stent-absent and diseased geometry as well to ensure uniformity in spatial discretization strategy. The quality of the meshes were assessed using the aspect ratio and the skew where a measure of 1 was ideal in both metrics. Approximately 90% of the mesh elements in the stented and stent-absent geometries had aspect ratio values larger than 0.6 and 0.65, respectively, and the skew values for more than approximately 90% of the stented and stent-absent mesh elements were larger than 0.9 and 0.85, respectively. The spread of these values has been illustrated in figure A.1.

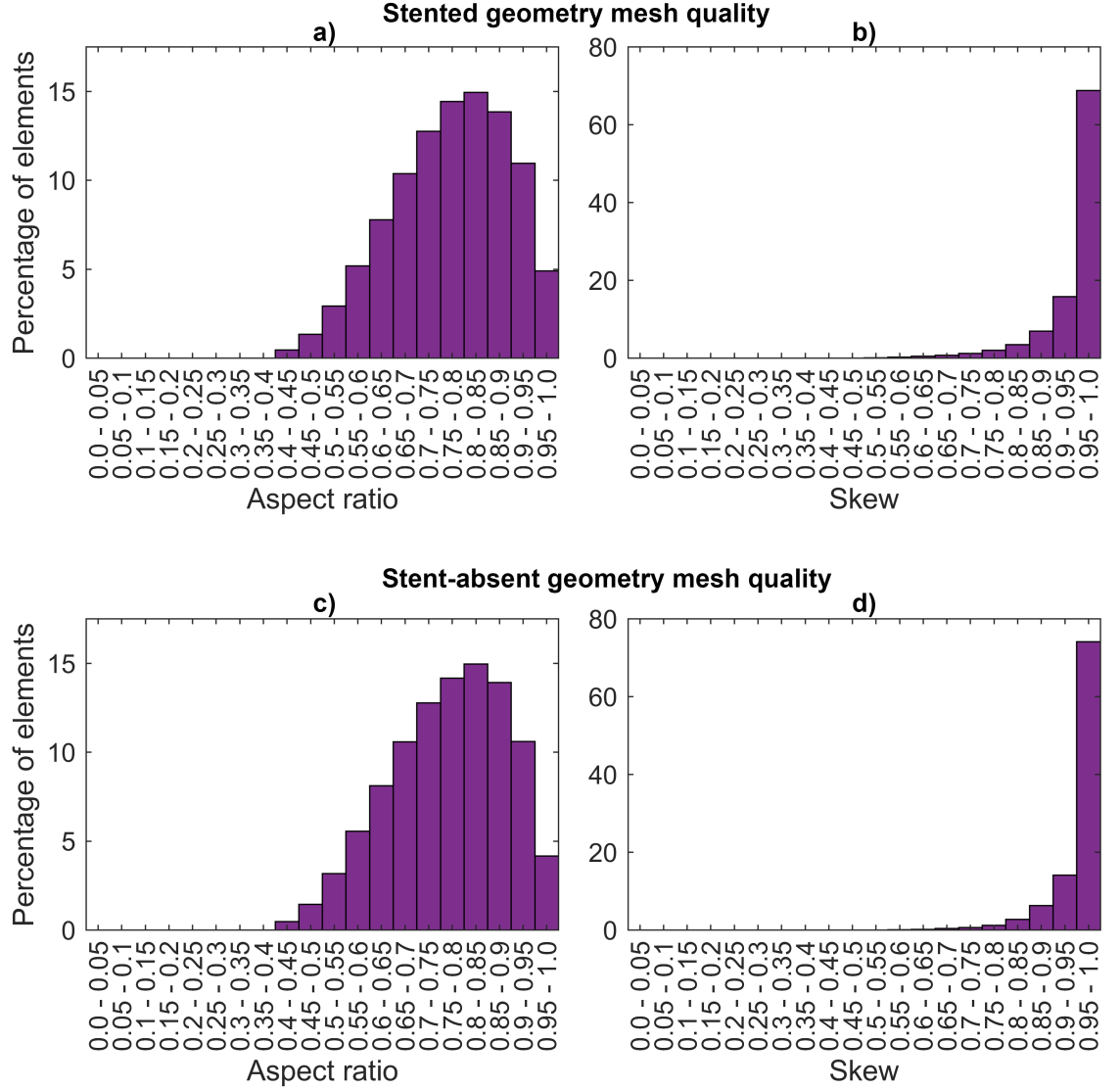


Figure A.1: Mesh quality statistics of the stented (top row) and stent-absent (bottom row) geometries. Sub-figures **a)** and **c)** show the spread of the mesh elements with the corresponding aspect ratios while sub-figures **b)** and **d)** show the spread of the mesh elements with the corresponding skew values.

A.2 Grid Convergence Index assessment

In order to verify that the mesh element sizes were sufficiently resolved for the Reynolds-averaged Navier-Stokes (RANS) simulations, the Grid Convergence Index (GCI) was calculated based on average velocity across slices along the vein (Celik et al., 2008). The location of the slices has been illustrated in figure A.2. Three mesh sizes for the stented

model (9.65 million, 19.75 million, 43.48 million elements) and the stent-absent model (2.95 million, 4.89 million, 6.85 million elements) were created and the velocity values obtained at the maximum inlet time point were used. The slice-averaged velocity values and the resulting GCI%, shown in tables A.1 and A.2, confirm that the grid spacing of the intermediate meshes (of size 19.75 million and 6.85 million elements) was sufficient for the RANS simulations.

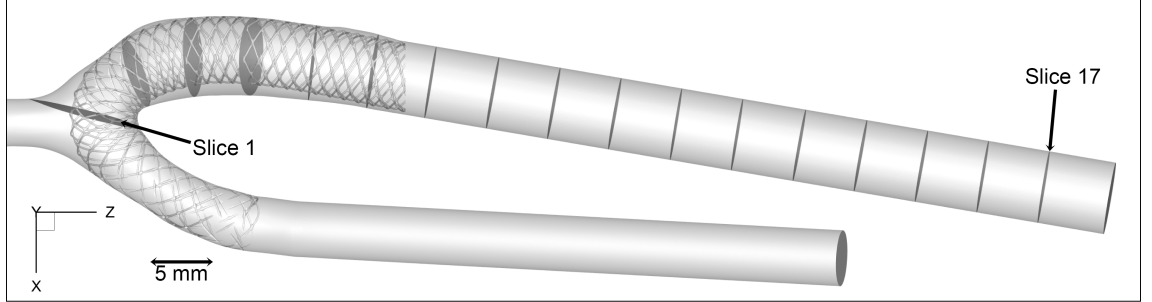


Figure A.2: Locations of slice planes in the vein of the AVF.

Table A.1: Slice averaged velocity magnitude values used for the GCI calculation of the stented case.

	Coarse Mesh	Intermediate Mesh	Fine Mesh	GCI (%)
Slice 1	0.5845	0.5120	0.5031	0.2339
Slice 2	0.7112	0.6674	0.6698	0.0186
Slice 3	0.4985	0.4618	0.4633	0.0118
Slice 4	0.4484	0.4136	0.4137	0.0000
Slice 5	0.5001	0.4628	0.4639	0.0058
Slice 6	0.5801	0.5360	0.5367	0.0021
Slice 7	0.5896	0.5435	0.5441	0.0012
Slice 8	0.5876	0.5424	0.5427	0.0002
Slice 9	0.5866	0.5418	0.5419	0.0000
Slice 10	0.5864	0.5414	0.5416	0.0002
Slice 11	0.5864	0.5414	0.5416	0.0001
Slice 12	0.5861	0.5411	0.5412	0.0000
Slice 13	0.5854	0.5409	0.5411	0.0002
Slice 14	0.5857	0.5407	0.5411	0.0005
Slice 15	0.5858	0.5409	0.5411	0.0002
Slice 16	0.5853	0.5406	0.5408	0.0001
Slice 17	0.5854	0.5407	0.5410	0.0002
Average				0.016

Table A.2: Slice averaged velocity magnitude values used for the GCI calculation of the stent-absent case.

	Coarse Mesh	Intermediate Mesh	Fine Mesh	GCI (%)
Slice 1	0.5100	0.5047	0.5022	2.160
Slice 2	0.6356	0.6311	0.6292	0.792
Slice 3	0.4575	0.4595	0.4634	0.270
Slice 4	0.4160	0.4238	0.4224	0.176
Slice 5	0.4489	0.4482	0.4488	2.008
Slice 6	0.5189	0.5189	0.5192	0.001
Slice 7	0.5414	0.5414	0.5416	0.001
Slice 8	0.5412	0.5412	0.5413	0.002
Slice 9	0.5409	0.5407	0.5408	0.072
Slice 10	0.5408	0.5407	0.5410	0.016
Slice 11	0.5410	0.5409	0.5411	0.173
Slice 12	0.5404	0.5405	0.5409	0.017
Slice 13	0.5406	0.5406	0.5408	0.000
Slice 14	0.5407	0.5408	0.5408	0.001
Slice 15	0.5406	0.5407	0.5411	0.004
Slice 16	0.5406	0.5405	0.5409	0.002
Slice 17	0.5406	0.5405	0.5410	0.003
Average				1.95

A.3 Time-step verification

To ensure that the time-step of the RANS simulations was fine enough to capture unsteady features, simulations were run with a time-step an order of magnitude smaller. The circumferential averaged WSS values along the vein were very similar between the two time-steps (0.001 s and 0.0001 s) as seen in figure A.3 verifying the choice of using a time-step of 0.001 s for the RANS simulations.

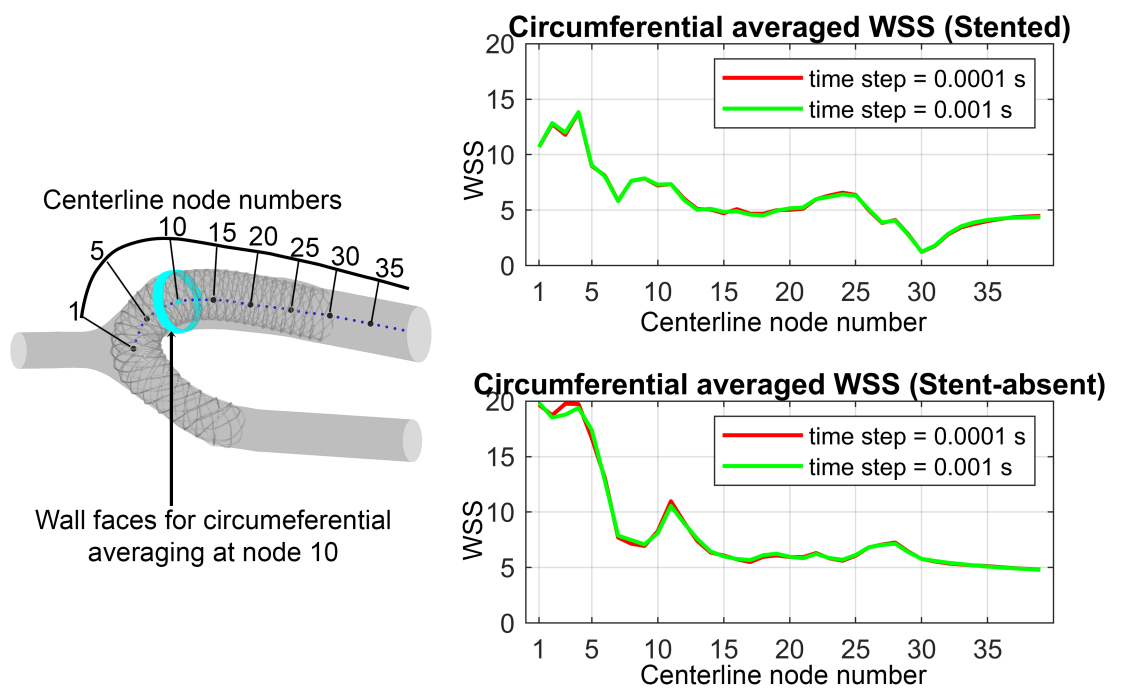


Figure A.3: Circumferential averaged WSS values at the peak inlet timepoint along the vein.